CARBON MOLECULAR SIEVE (CMS) MEMBRANES STRUCTURE-PROPERTY RELATIONSHIPS

A Dissertation
Presented to
The Academic Faculty

By

Shilu Fu

In Partial Fulfillment
Of the Requirements for the Degree
Doctor of Philosophy in the
School of Chemical & Biomolecular Engineering

Georgia Institute of Technology

December 2015

CARBON MOLECULAR SIEVE (CMS) MEMBRANES STRUCTURE-PROPERTY RELATIONSHIPS

Approved by:

Dr. William J. Koros, Advisor
School of Chemical & Biomolecular Engineering
Georgia Institute of Technology

Dr. John Reynolds
School of Chemistry & Biochemistry
School of Materials Science & Engineering
Georgia Institute of Technology

Dr. Dennis W. Hess
School of Chemical & Biomolecular Engineering
Georgia Institute of Technology

Dr. Edgar S. Sanders
Delaware Research and Technology Center
American Air Liquide

Dr. Yulin Deng
School of Chemical & Biomolecular Engineering
Georgia Institute of Technology

Date Approved: Oct. 23, 2015

Dedication

To my supporting and loving parents

To my dearest advisor, Dr. William J. Koros

ACKNOWLEDGEMENTS

I had a life changing experience at Georgia Tech. During the past four years of graduate study, innumerable people have influenced me and deserve my sincere gratitude.

First and foremost I would like to thank my advisor, Dr. Koros. I learnt about Dr. Koros from my former advisor back in China when I was undergoing my undergraduate study. I still remember how anxious and nervous I was before my first meeting with Dr. Koros. However, right after the meeting, his relentless energy, enthusiasm, and sense of humor made me determined to join his group and devote all my energy into the membrane research we both love. To me, he has been a "big- daddy", not only teaching me to be an ethical researcher, but more importantly, an honest person. I can honestly say the biggest motivation for me to work hard and creatively in my Ph.D. life is to make him proud.

Funding support from the American Air Liquide company is also greatly appreciated. I'm so lucky to have Dr. Edgar Sanders and Dr. Sudhir Kulkarni by my side. They came up with this great project, offered insightful suggestions along the way to help me accomplish it.

I would also like to thank my committee members Dr. Dennis Hess, Dr. Yulin Deng and Dr. John Reynolds for their constructive feedback. They have been as always supportive and helpful in spite of their extremely busy schedule.

It has been a great experience working in Koros group. All members deserve thanks. Several people have played key role in my completion of this work. In particular,

I would like to thank our former lab manager Dr. J. R. Johnson. Although we only worked together for one short year, but his incredible mechanical skills and creative problem-solving ability makes him my always mentor. Former group members: Dr. Liren Xu, Dr. Meha Rungta and Dr. Nitesh Bhuwania have set me great models to follow. I've learnt valuable skills from them, including ways of thinking and ways of conveying messages. Dr. Lucy Lu has been a great office mate. We discuss, chat and laugh every day. Current group members: Dr. Wulin Qiu, Dr. Ying Dai and Dr. Kuang Zhang have been kind and patient in sharing their valuable experience with me. I must thank Dr. Chen Zhang for teaching me basic experimental skills when I first joined the group. Graham Wenz and Yu-han Chu are both great friends, they always cheer me up when I feel low.

I am also grateful to have my family and friends supporting me during these four years. My parents, they have been unconditionally loving me and supporting me. My significant other, Ho Yee Hui, has been my great support and I learnt so much from his incredible perseverance and mental-toughness. He has been my source of happiness during my Ph.D. life. I also feel so blessed to have so many friends in Georgia Tech. We always shopping, dining, and playing badminton together, which all make my life so much joyful.

TABLE OF CONTENTS

LIST OF TABLES

LIST OF FIGURES

SUMMARY

Membrane technology is an attractive alternative to energy-intensive traditional thermally-driven gas separation processes with lower energy requirement. Polymer membranes are attractive separation materials because of economical processability into hollow fiber modules with desirable morphology and high surface area per unit volume. Despite many advantages, solution processable polymer membranes face an "upper bound" limitation, involving an inverse relationship between separation factor for gas pairs and permeability of the more permeable gas. On the other hand Carbon Molecular Sieve (CMS) membranes, formed by careful selective thermal decomposition of a precursor polymer, are known to have outstanding separation performance and surpass the upper bound limit.

The goal of this work is to develop a framework to understand the material science options to fabricate novel, high performing separation CMS membranes. The transport and sorption properties of CMS membranes formed by pyrolysis under argon at 550 ^{o}C for four novel polyimide precursors referred to as 6FDA/DETDA, 6FDA:BPDA(1:1)/DETDA, 6FDA/DETDA:DABA(3:2) and 6FDA/1,5-ND:ODA(1:1) were reported and compared. Considering the separation performance, 6FDA/DETDA: DABA(3:2) and 6FDA/1,5-ND:ODA(1:1) CMS membranes showed the greatest potential for further optimization study. The smallest T_d-T_g of 6FDA/DETDA: DABA(3:2) made it favorable in the formation of hollow fiber membranes. Thus, 6FDA/DETDA: DABA(3:2) CMS membrane is chosen for later studies.

The effects of pyrolysis conditions, including pyrolysis temperature; O_2 doping; and precrosslinking, on the separation performance of 6FDA/DETDA:DABA(3:2) derived CMS membranes were reported. It was revealed that increased pyrolysis temperatures tend to give lower permeable but higher selective membranes. Oxygen doping provides a fine tuning method for altering the separation performance of CMS membranes by increasing the selectivity without a significant loss in permeability. Finally, CMS membranes derived from a novel method proposed in this study, referred to as precrosslinking, was proven to be very attractive with significantly improved gas permeability and slightly drop in selectivity. The results reported in this study serves as a guide for future optimization study on CMS membranes; the combination of different tuning methods might be attractive for some specific applications.

Temperature dependences of gas transport and sorption properties on CMS membranes were also examined over the temperature range from 35 ^{o}C to 50 ^{o}C. The permeability, sorption and diffusivity of CMS membranes are reported, and activation energies of permeation and diffusion as well as heats of sorption for gases CO_2, CH_4, O_2, and N_2 are compared. The temperature dependence study of the four similar yet diverse CMS materials derived from 6FDA-based precursor polyimides provides a tool to identify structural characteristics that affect permeability and selectivity. On the other hand, the study on the three CMS membranes derived from 6FDA/DETDA:DABA(3:2) under different pyrolysis protocols provides fundamental insights into the reason for CMS membranes to outperform polymeric membranes.

The viability of extending the promising separation performance obtained from 550 ^{o}C and inert argon pyrolyzed 6FDA/DETDA:DABA(3:2) CMS dense film into

hollow fiber morphology was also explored in this work. The 6FDA/DETDA:DABA(3:2) polymeric hollow fiber membranes were successfully spun and pure gas permeation tests showed defect-free polymeric fibers were achieved. Through pyrolysis of the defect-free polymeric hollow fibers, good performance CMS hollow fibers were also obtained.

CHAPTER 1

INTRODUCTION

1.1 Natural gas processing

Natural gas is the fastest-growing fossil fuel throughout the world, with consumption rising about 0.8% each year from 2012 to 2040. Figure 1.1 shows the primary energy use by fuel from 1980 to 2040 [1]. Raw natural gas varies in composition from source to source, containing methane with significant amount of impurities such as hydrocarbons, water, carbon dioxide, nitrogen, and hydrogen sulfide [2]. In order to be delivered to commercial pipeline grids, raw natural gas needs to be treated. Typical U.S. natural gas pipeline specifications are shown in Table 1.1.

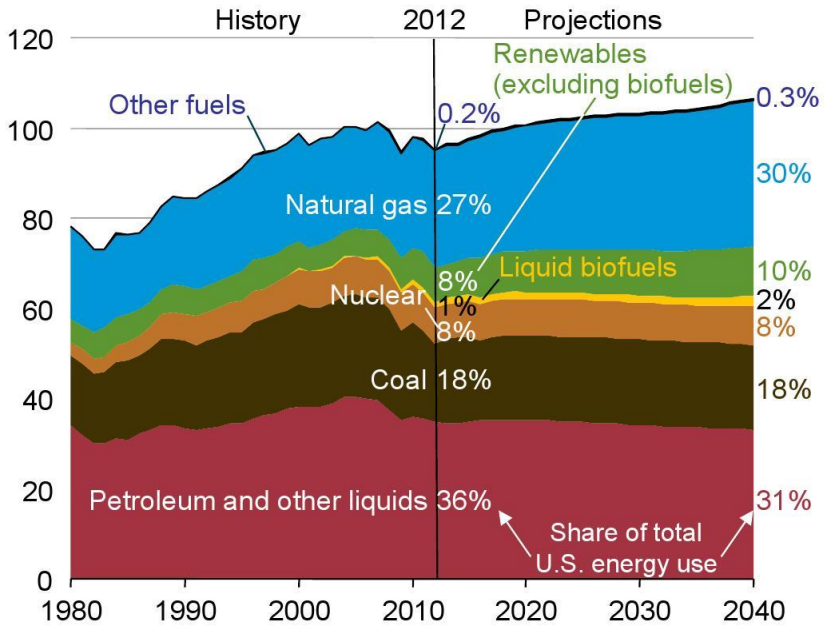

Figure 1.1: Primary energy use by fuel, 1980-2040 (quadrillion Btu) [1].

Table 1.1: Composition specifications for natural gas delivery to the U.S. national pipeline grids [2].

Component	Specification
CO_2	<2%
Total water	<120ppm
H_2S	<4ppm
Total	950-1050 Btu/scf; dew
C_{3+} content	point< -20 ℃
Total inert gases (N_2,He)	<4%

Among the various impurities, CO_2 is usually the most abundant contaminant, present at levels > 50mol% in some cases. The presence of CO_2 may cause pipeline corrosion. What's more as a non-fuel gas, CO_2 decreases the heating value of natural gas, hence increasing the compression cost required for gas transportation; therefore, CO_2/CH_4 separation is a high priority topic [3].

Currently the standard technique for CO_2 removal is amine absorption [4]. Amine absorption can almost completely remove CO_2, moreover, the lower hydrocarbon losses, in the range of 2%-5%, is hardly beatable by other techniques. Having said this, the absorber tower is an expensive, large and heavy vessel, which associates with high capital and maintenance cost. Also, considering the large amount of CO_2 that needs to be removed, huge amount of absorbent fluid must be used. Additional costs are anticipated associated with the regeneration and disposal of solvents.

The high CO_2 content in raw natural gas, which is adverse for amine absorption technique, on the other hand provides membranes an opportunity. The first membrane systems for natural gas treatment were introduced in 1980s using anisotropic cellulose

acetate membrane. During the last two decades newer types of membranes, derived from polyimide and perfluoropolymer also emerged into the market [5, 6].

1.2 Membrane-based gas separation

A membrane is a selective barrier. It separates a feed (mixture) into two streams by preferably allowing one stream (permeate) to pass through while retaining the other (retentate). The faster permeating component is enriched in the permeate side and the slower component is gathered in the retentate side. Membrane technology is an attractive alternative to energy-intensive traditional thermally-driven processes with lower energy requirement due to the economical driving force: trans-membrane pressure difference [7, 8]. It can also offer some key advantages including: environmental friendliness, smaller installation foot-print, lower capital and maintenance cost, adaptability and flexibility.

Since Permea launched the hydrogen-separating Prism membrane, the first large industrial application of gas separation membranes, membrane-based gas separation has grown dramatically [7-10]. The membrane market for gas separation is envisioned to steadily increase each year at an average rate of 7-8%, and it is expected to reach $760 million by year 2020. Table 1.2 below shows the predicted membrane market share for gas separation in 2020.

Table 1.2: Projected future membrane market share in 2020 for gas separation [7].

Separation	Membrane market share ($ million, 2000 dollars)
Nitrogen from air	125
Oxygen from air	30
Hydrogen	100
Natural gas	220
Vapor/nitrogen	60
Vapor/vapor	125
Other	100
total	760

Polymer membranes are attractive separation materials because of economical processability into hollow fiber modules with desirable morphology and high surface area per unit volume [11]. Despite many advantages, solution processable polymer membranes face an "upper bound" limitation, involving an inverse relationship between separation factor for gas pairs and permeability of the more permeable gas as shown in Figure 1.2 [12]. On the other hand CMS materials, formed by careful selective thermal decomposition of a precursor polymer, are known to have outstanding separation performance and surpass the upper bound limit [13, 14]. Moreover, due to high chemical and thermal stability, CMS membranes maintain their performance in adverse environments with aggressive high pressure feeds of high CO_2 concentrations that would undermine polymer membranes performance [15, 16].

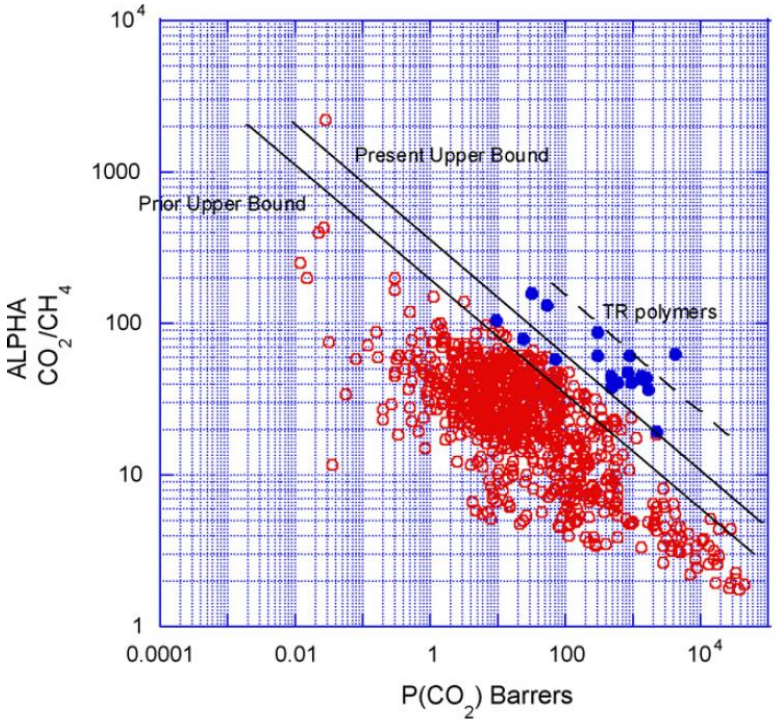

Figure 1.2: Robeson's upper bound for CO_2/CH_4 separation [12].

Nevertheless, despite many advantages, the biggest hurdle to CMS membrane production and implementation may currently be economic feasibility. The cost of CMS membranes is estimated to be between 2-5 X that of polymeric membranes, as compared to estimated 50-100 X higher for standard zeolite and ceramic membranes [17, 18]. This research aims to develop a framework to understand the material science options to fabricate novel, high performing separation CMS membranes.

1.3 Challenges of membrane technology

In order to directly compete with conventional techniques like cryogenic distillation and amine absorption, four practical requirements must be met before the introduction of a new type of membrane process [19]: 1) development of high efficiency modules with desirable morphologies and high surface area per unit volume; 2) creation

of advanced materials capable of separating molecularly similar components; 3) development of morphology control at multiple levels along the membrane cross section; and 4) development of high speed manufacturing methods which integrate the above three elements into economical industrial large-scale membrane systems.

1.3.1 High efficiency modules

Different membrane module configurations have been investigated including: plate and frame, spiral wound, tubular and hollow fiber modules. Nowadays most of the gas separation membranes are formed into hollow fiber modules. The schematic of hollow fiber modules and some parameters controlling which type is preferred for a specific application are shown in Figure 1.3.

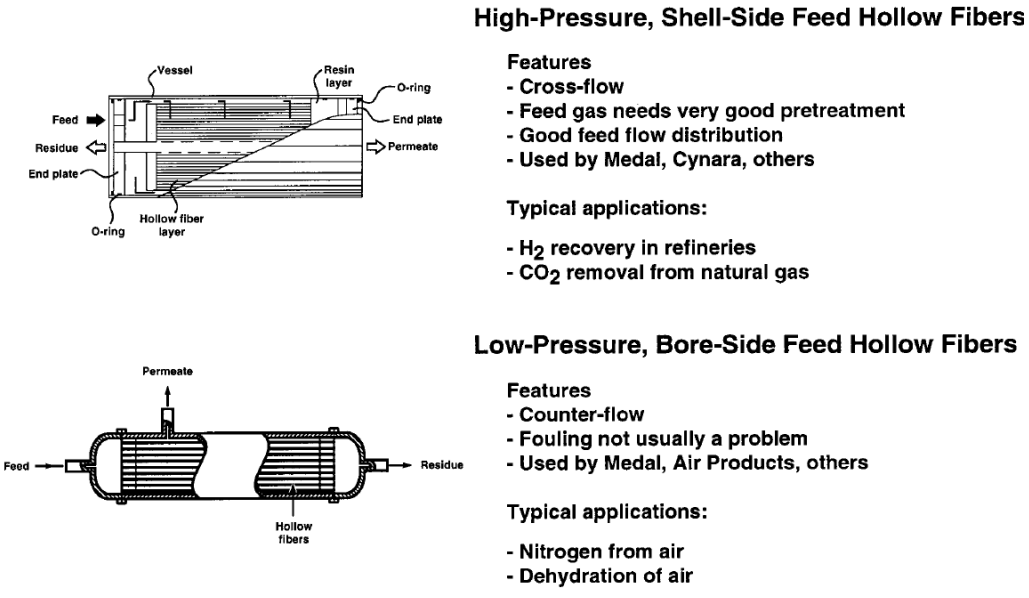

Figure 1.3: Gas separation hollow fiber membrane module configurations [7].

There are several reasons why hollow fiber membrane configuration is industrially preferred for large scale gas separation. First, with small diameter and cylindrical morphology, hollow fibers provide significantly high surface area to volume

ratio and packing densities. Hollow fibers can also provide high fluxes, which results from the asymmetric geometry consisting of thin separating layer supported on a microporous layer [20]. Moreover, low production cost is another major advantage of hollow fiber modules since mass production can be scaled up easily. Typical hollow fiber spinning can be operated on an around-the-clock basis; production of hollow fibers is in the range of \$2-5/m^2, which is 5X – 20X lower than spiral-wound modules [7].

1.3.2 Advanced materials

As mentioned in the above section, polymer membranes face the issues of upper bound limit. As a result, investigating advanced membrane materials with tunable capabilities becomes a key factor.

Facilitated transport membranes have been widely studied for olefin/paraffin separations and showed exceptional selectivities due to the ions which selectively binding with olefin, favoring its transport across the membrane. Nevertheless, the intrinsic instability of these membranes hinders their practical applications [21-23].

Molecular sieving inorganic materials including zeolites and carbon molecular sieve (CMS) membranes have attracted extensive attention due to their ability to overcome the polymeric upper bound. The underlying reason is because they have rigid and tailorable pore structures, which enable subtle size and shape discriminations [24]. On the other hand, in the case of zeolite membranes, the difficulty in fabricating a sufficiently coherent and robust membrane limits their practical application. In this study, I focused on the study of CMS membranes. In many studies, carbon molecular sieve (CMS) membranes have shown attractive gas separation performance for challenging gas pairs, including CO_2/CH_4, O_2/N_2, C_2H_4/C_2H_6, and C_3H_6/C_3H_8 [9, 25].

1.3.3 Morphology control

The intrinsic pore structure of CMS membranes must be effectively tuned for a specific application. Several tuning parameters have been extensively studied including the starting polymer precursor, the pretreatment on the polymer, the pyrolysis conditions, and the post-treatment on the CMS membrane [9].

After translating to hollow fiber form, it is also crucial to engineer the asymmetric morphology in hollow fiber CMS membranes. As shown in Figure 1.4, the microporous support structure is meant for supporting without exerting noticeable resistance to the penetrants. However the densification of micropore support layer during excessive heat treatment, which thickens the ultra-thin dense separation layer, drastically reduces the flux. Lower flux is a major concern from a practical stand point since it requires more membrane surface area and thus higher cost. Hence, effective methods to suppress this substructure collapse are critical for practical application of hollow fiber CMS membranes.

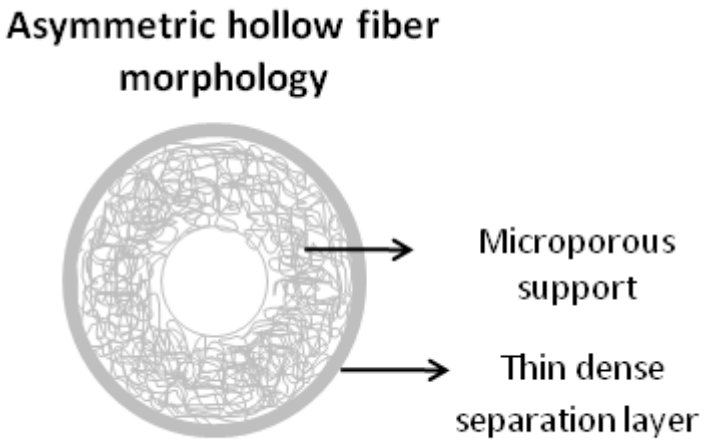

Figure 1.4: Asymmetric hollow fiber morphology [26].

1.3.4 High speed manufacturing

The biggest hurdle to CMS membrane production and implementation may currently be economic feasibility. Thus, scale-up and high speed manufacturing become crucial for membrane technology to be competitive with conventional techniques.

In this work, the four key elements described above are addressed for production of attractive CMS membranes. Advanced material, CMS membranes, and the tuning of their pore structures were developed based on fundamental studies with homogeneous dense film morphology. This fundamental study provides insights into structure-property relationships. To further address the issues of module efficiency and commercial viability, this study was advanced by applying the method for dense films to asymmetric hollow fiber morphology. The following section shows the main research objectives in this dissertation.

1.4 Research objectives

The overarching goal of this work is to develop a framework to understand the material science options to fabricate novel, high performing separation CMS membranes. In order to achieve this goal, we have worked on the following objectives:

Research objective 1: Analysis of different polymers as precursors to CMS dense film membranes for pure gas CO_2/CH_4 and O_2/N_2 separation (Chapters 4).

Former studies have shown that the specific polymer precursor has significant effects on the separation performance of the resulting CMS membranes [27-29]. Here, we report transport and sorption properties of CMS membranes fabricated from a novel set of polymer precursors: 6FDA/DETDA, 6FDA:BPDA(1:1)/DETDA, 6FDA/DETDA:

DABA(3:2) and 6FDA/1,5-ND:ODA(1:1), under a well-controlled pyrolysis protocol. Separation performance of polymer precursor films formed from these polymers was examined using pure gases CO_2, CH_4, O_2 and N_2. The pyrolyzed polymer precursor films to create dense CMS membranes produced separation performance that significantly exceeded the polymer precursor performance in all cases. Separation performance of the CMS membranes was studied as a function of time, with storage under vacuum between tests to assess physical aging. The 6FDA/DETDA:DABA(3:2) derived CMS membranes showed the highest permeability and offered the greatest practical potential among the various precursors.

Research objective 2: Investigation of pyrolysis conditions on gas separation properties of 6FDA/DETDA:DABA(3:2) derived carbon molecular sieve membranes for both pure and mixed gases (Chapter 5).

Several parameters have been studied to tailor the pore structures of CMS membranes including the pyrolysis temperature, pyrolysis atmosphere and heating protocol. 6FDA/DETDA:DABA(3:2) polyimide was pyrolyzed under different protocols to produce carbon molecular sieve (CMS) dense film membranes for separation of important gas pairs including pure gases CO_2/CH_4, O_2/N_2 and mixture gases 50% CO_2/50% CH_4 and 50% C_3H_6/50% C_3H_8. The effects of pyrolysis temperature and atmosphere on CMS separation performance are reported. The CMS dense film pyrolyzed with a novel method, i.e., 800 ^oC with pre-crosslinking, shows very attractive separation performance with CO_2 and O_2 permeability of 4678 Barrer and 683 Barrer, CO_2/CH_4, O_2/N_2 selectivity of 71.5 and 8.0 from pure gas measurements.

Research objective 3: Temperature dependence of gas transport and sorption in carbon molecular sieve membranes derived from four 6FDA based polyimides: entropic selectivity evaluation (Chapter 6).

Temperature dependences of gas transport and sorption properties on carbon molecular sieve (CMS) membranes were examined over the temperature range from 35 ^{o}C to 50 ^{o}C. The permeability, sorption and diffusivity of these materials are reported, and activation energies of permeation and diffusion as well as heats of sorption for gases CO_2, CH_4, O_2, and N_2 of these materials are compared. Permselectivity of these materials at 35 ^{o}C was probed for three gas pairs: CO_2/CH_4, O_2/N_2, and N_2/CH_4, and results show that diffusion selectivity is the dominant factor in providing permselectivity. Diffusion selectivity can be factored further into an energetic selectivity and an entropic selectivity. The temperature dependence of both energetic and entropic selectivity and their contributions to overall diffusion selectivity are discussed in detail in this study. All CMS membranes showed larger than unity entropic selectivity factors. Analysis of the selectivity factors provides insights into the effects of polymer precursor backbone structures on key transport and sorption properties in CMS materials.

Research objective 4: Create "first generation" asymmetric hollow fiber CMS membrane with 6FDA/DETDA:DABA(3:2) (Chapter 7).

As noted earlier, asymmetric hollow fiber membranes are industrial favored membrane morphology considering the high surface area to volume ratio they can provide. This part of study serves as a guide for future study by showing the viability of

spinning the first generation of 6FDA/DETDA:DABA(3:2) hollow fiber membranes and efficacy in achieving defect-free CMS hollow fiber membranes.

1.5 Dissertation overview

Including this introductory chapter, this dissertation contains 9 chapters. Chapter 2 presents background and theory to facilitate understanding of this dissertation. Chapter 3 describes the material development, experimental setup and characterization techniques used in this work. Chapters 4 to 7 are the main body part, covering the four research objectives discussed in the previous section. Chapter 8 summarizes the key results of this work and recommendations for further study. Finally, several appendices provide supplemental information.

1.6 References

[1] Annual Energy Outlook 2014 with projections to 2040, in: U.S.E.I. Administration (Ed.), 2014.

[2] R.W. Baker, K. Lokhandwala, Natural Gas Processing with Membranes: An Overview, Ind. Eng. Chem. Res., 47 (2008) 2109-2121.

[3] R.W. Baker, K. Lokhandwala, Natural Gas Processing with Membranes: An Overview, Ind. Eng. Chem. Res. , 47 (2008) 2109-2121.

[4] A.L. Kohl, R.B. Nielsen, Gas Purification, 5th edition ed., Gulf Professional Publishing, Houston, TX, 1997.

[5] R.W. Baker, I. Pinnau, Z. He, K.D. Amo, A.R.D. Costa, R. Daniels, Nitrogen Gas Separation Using Organic-Vapor-Resistant Membranes, in, U.S. Patent 6579341, June 17, 2003.

[6] J. Simmons, S. Kulkarni, O. Ekiner, Method for Separating Hydrocarbon-Containing Gas Mixtures Using Hydrocarbon-Resistant Membranes, in, U.S. Patent 20040159233, August 19, 2004.

[7] R.W. Baker, Future directions of membrane gas separation technology, Ind. Eng. Chem. Res., 41 (2002) 1393-1411.

[8] J.C. Davis, R.J. Valus, R. Eshraghi, A.E. Velikoff, Facilitated transport membrane hybrid systems for olefin purification, Separ. Sci. Technol., 28 (1993) 463-476.

[9] S.M. Saufi, A.F. Ismail, Fabrication of carbon membranes for gas separation—a review, Carbon, 42 (2004) 241-259.

[10] H.B. Jeazet, C. Staudt, C. Janiak, A method for increasing permeability in O_2/N_2 separation with mixed-matrix membranes made of water-stable MIL-101 and polysulfone, Chem. Commun., 48 (2012) 2140-2142.

[11] M. Kiyono, P.J. Williams, W.J. Koros, Effect of pyrolysis atmosphere on separation performance of carbon molecular sieve membranes, J. Membr. Sci., 359 (2010) 2-10.

[12] L.M. Robeson, The upper bound revisited, J. Membr. Sci., 320 (2008) 390-400.

[13] M. Das, J.D. Perry, W.J. Koros, Gas-Transport-Property Performance of Hybrid Carbon Molecular Sieve-Polymer Materials, Ind. Eng. Chem. Res., 49 (2010) 9310-9321.

[14] K.M. Steel, W.J. Koros, Investigation of porosity of carbon materials and related effects on gas separation properties, Carbon, 41 (2003) 253-266.

[15] P.S. Tin, T.S. Chung, A.J. Hill, Advanced Fabrication of Carbon Molecular Sieve Membranes by Nonsolvent Pretreatment of Precursor Polymers, Ind. Eng. Chem. Res., 43 (2004) 6476-6483.

[16] L.-J. Wang, F. Chau-Nan Hong, Effects of surface treatments and annealing on carbon-based molecular sieve membranes for gas separation, Appl. Surf. Sci., 240 (2005) 161-174.

[17] W.J. Koros, R. Mahajan, Pushing the limits on possibilities for large scale gas separation: which strategies?, J. Membr. Sci., 175 (2000) 181-196.

[18] M. Kiyono, Carbon molecular sieve membranes for natural gas separations, in, Georgia Institute of Technology, Atlanta, Georgia, 2010.

[19] W.J. Koros, Evolving beyond the thermal age of separation processes: Membranes can lead the way, AlChE J., 50 (2004) 2326-2334.

[20] W.J. Koros, R.P. Lively, Water and beyond: Expanding the spectrum of large-scale energy efficient separation processes, AlChE J., 58 (2012) 2624-2633.

[21] M. Azhin, T. Kaghazchi, M. Rahmani, A review on olefin/paraffin separation using reversible chemical complexation technology, Journal of Industrial and Engineering Chemistry, 14 (2008) 622-638.

[22] R. Faiz, K. Li, Olefin/paraffin separation using membrane based facilitated transport/chemical absorption techniques, Chem. Eng. Sci., 73 (2012) 261-284.

[23] M. Teramoto, S. Shimizu, H. Matsuyama, N. Matsumiya, Ethylene/ethane separation and concentration by hollow fiber facilitated transport membrane module with permeation of silver nitrate solution, Sep. Purif. Technol., 44 (2005) 19-29.

[24] A. Singh, W.J. Koros, Significance of entropic selectivity for advanced gas separation membranes, Ind. Eng. Chem. Res., 35 (1996) 1231-1234.

[25] M. Rungta, L. Xu, W.J. Koros, Carbon molecular sieve dense film membranes derived from Matrimid® for ethylene/ethane separation, Carbon, 50 (2012) 1488-1502.

[26] N. Bhuwania, Engineering the morphology of carbon molecular sieve (CMS) hollow fiber membranes, in, Georgia Institute of Technology, 2013.

[27] Y.K. Kim, J.M. Lee, H.B. Park, Y.M. Lee, The gas separation properties of carbon molecular sieve membranes derived from polyimides having carboxylic acid groups, J. Membr. Sci., 235 (2004) 139-146.

[28] H.B. Park, Y.K. Kim, J.M. Lee, S.Y. Lee, Y.M. Lee, Relationship between chemical structure of aromatic polyimides and gas permeation properties of their carbon molecular sieve membranes, J. Membr. Sci., 229 (2004) 117-127.

[29] M. Kiyono, P.J. Williams, W.J. Koros, Effect of polymer precursors on carbon molecular sieve structure and separation performance properties, Carbon, 48 (2010) 4432-4441.

CHAPTER 2

BACKGROUND AND THEORY

2.1 Overview

This chapter provides background, theory and terminology relevant to this dissertation. Section 2.2 provides background on the structures of carbon molecular sieve (CMS) membranes. The formation of CMS membrane and factors affecting its transport properties are outlined in section 2.3. Finally, section 2.4 outlines fundamental gas transport and sorption theory in both polymeric and CMS membranes including permeation, sorption and diffusion.

2.2 Structure of CMS membranes

CMS materials are formed by thermal decomposition of a precursor polymer to produce a carbon rich material [1, 2]. Being heated in an inert atmosphere, polymers go through carbonization and residual materials of coke or char tend to be formed [3, 4]. During carbonization, if the precursor goes through a liquid phase, the polymer chains tend to form aromatic lamellae resulting in crystalline anisotropic coke; otherwise, isotropic char is formed. Two dimensional drawings represent anisotropic vs. isotropic carbons are shown in Figure 2.1.

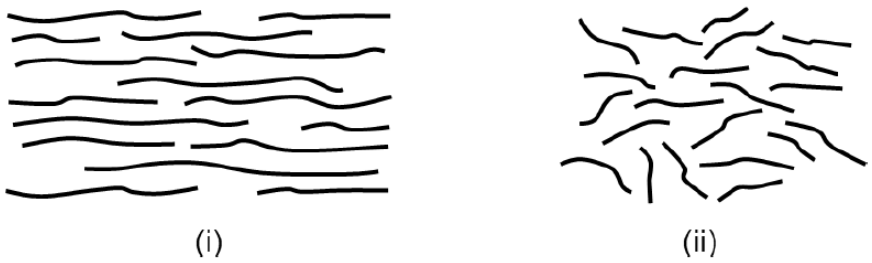

Figure 2.1: Carbon lamellae drawings representative of structure: (i) anisotropic; (ii) isotropic [5].

Coke can be further heated to form graphite at temperatures between 2500 ^{o}C and 3000 ^{o}C, resulting in a layer of graphene sheets stacked in a hexagonal ABA sequence as depicted in Figure 2.2 [4]. Within the layers, the C-C bond, which forms a two-dimensional extended electronic structure, is sp^2-hybrid sigma-bonds with delocalized pi-bonds within the layer [6]. Between the layers, the graphene layers are connected with van der Waals force without any chemical bond. The graphite density is ~2.25 g/cm^3 at 300K with the interlayer distance as 0.335 nm and C-C distance as 0.142 nm [7].

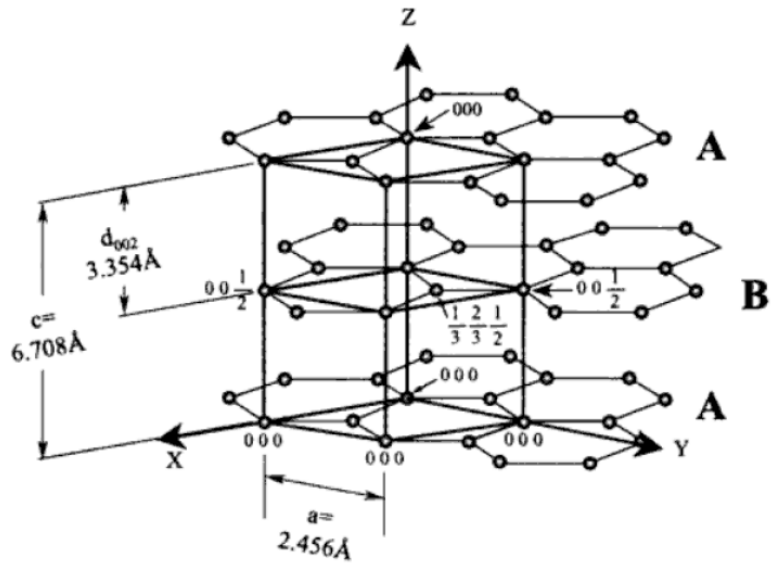

Figure 2.2: The structure of graphite with ABA stacking of graphene sheets [4].

Unlike coke, which can form crystalline graphite structure, char remains in an amorphous form [3, 4]. Most CMS membranes used for gas separation show a turbostratic nature with little long-range order and can be viewed as amorphous and isotropic. Over the long range, this amorphous form contains lamellae arranged randomly, bent and twisted. Over the short range, the sp^2-hybridized carbon sheets can align parallel to each other and form somewhat ordered structure, as shown in Figure 2.3.

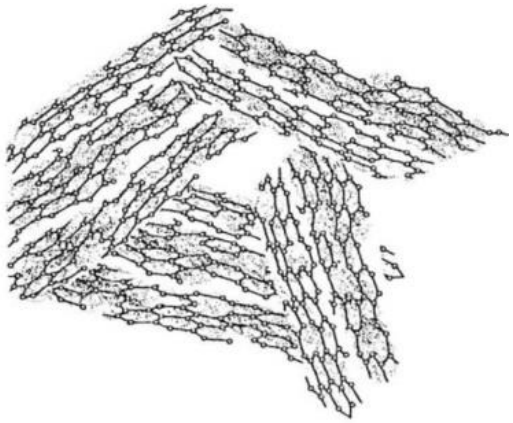

Figure 2.3: Structure of CMS membranes over a short range: the sp^2-hybridized carbon sheets [3, 4].

An idealized pore structure, as shown in Figure 2.4, can be described as "slit-like", and can be represented by a bimodal pore size distribution with larger micropores (~ 7-20 Å) connected by smaller ultramicropores (< 7 Å) [1, 8-10]. Micropores provide sorption sites, while ultramicropores enable molecular sieving, thereby making CMS materials both highly permeable and highly selective, with properties lying above the upper-bound limit of polymers [8, 11].

i) ii)

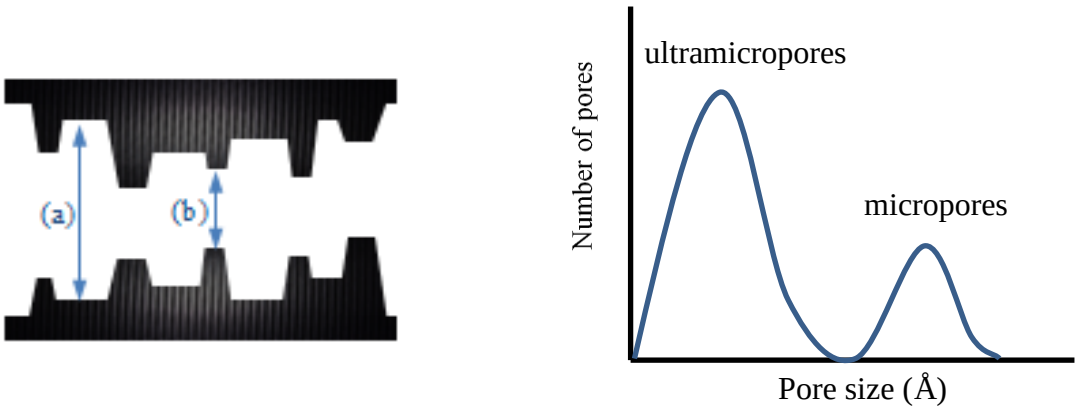

Figure 2.4: i) A simplified idealized slit-like pore structures in CMS membranes. (a): micropores with sizes of 7-20 Å; (b): ultramicropores with sizes < 7 Å; ii) bimodal distribution of pores.

2.3 Formation of CMS membranes

CMS membranes are formed from the pyrolysis of polymer precursors under controlled conditions. During the complicated pyrolysis process, various reactions can occur at the same time including cleavage, dehydrogenation, condensation etc. [12, 13]. In the early steps of the pyrolysis, bonds cleavage takes place and results in free radicals. The free radicals can further go through intramolecular coupling and intermolecular crosslinking, resulting in a loose structure network. At the same time, small molecules as volatile materials in the form of water, methane, carbon dioxide, carbon monoxide, etc. are eliminated and microporosity within the rigid macromolecular system is generated. When temperature reaches around 550 ^{o}C, almost all aliphatic carbon is converted to aromatic C-H, resulting in rich carbon structure [5].

The pore size distribution of CMS membranes, which determines its separation performance, can be influenced by several key parameters including precursor selection, polymer pretreatment, pyrolysis conditions, post treatment, and module construction [14].

In this section, these parameters are reviewed and presented below following the sequence of CMS membrane fabrication process as shown in Figure 2.5.

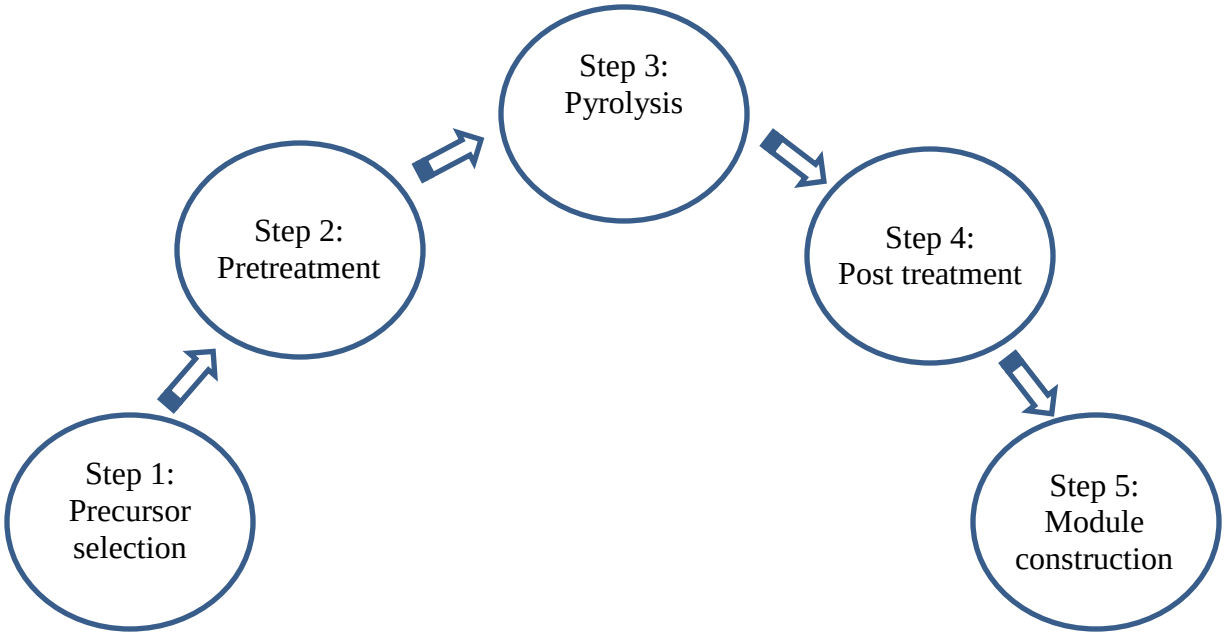

Figure 2.5: CMS membrane fabrication process [14].

2.3.1 Precursor selection

Precursor selection is the first important factor, since different precursor polymers may bring about different kinds of CMS membranes. Since the pioneering work on cellulose CMS hollow fibers introduced by Koresh and Soffer [15], numerous synthetic polymers have been used for CMS membrane study. Most often studied polymers include polyacrylonitrile [16, 17], phenolic resins [18-20], polyfurfuryl alcohol [21, 22], poly (vinylidene)-based polymers [23], and polyimides [24-26]. Polyimides are among the most stable classes of polymers. They tend to decompose near their softening points, so they do not lose shape during the intense heat. Moreover, polyimides exhibit high glass

transitional temperature, good processability and good mechanical strength. Based on these features, polyimides have been the preferred precursor.

Former studies have shown that the polymer precursor has significant effects on the separation performance of the resulting CMS membranes [27-29]. The intrinsic properties including fractional free volume (FFV), chain structure and chain mobility may be somewhat preserved in the resulting CMS membranes.

Park et al. studied CMS membranes derived from various polyimides containing different numbers of methyl substituent groups, and results indicated that the increase of FFV in the polyimides by methyl substituents led to higher permeability in the resulting CMS membranes [28].

Kiyono studied the separation performance of CMS membranes derived from two different polymers: Matrimid® vs. 6FDA/BPDA-DAM [29]. Results showed 6FDA/BPDA-DAM derived CMS membranes exhibit higher permeability but lower selectivity than Matrimid® derived ones. Apart from a higher FFV, 6FDA/BPDA-DAM also contains two CF_3 groups. The bulky CF_3 group tends to hinder chain packing and promotes higher free volume by inhibiting segmental packing. What's more, the evolution of larger fluorinated compounds such as CHF_3 further provides higher microporosity in the resulting CMS membrane.

These studies indicate the importance of choosing the right precursor polymer to fabricate CMS membranes for a specific gas separation. In this study, the separation performance of CMS membranes formed by pyrolysis of four novel polyimide precursors referred to as 6FDA/DETDA, 6FDA:BPDA(1:1)/DETDA, 6FDA/DETDA:DABA(3:2) and 6FDA/1,5-ND:ODA(1:1) are considered and will be discussed in detail in Chapter 5.

2.3.2 Polymer pretreatment

To ensure the stability of the polymeric precursor and the preservation of its structure during pyrolysis, polymeric membranes are often subject to pretreatment before

pyrolysis. Pretreatment has also been proven to be able to change chain packing and alter chain segmental mobility.

Thermal stabilization is a commonly applied method to enhance the structure stability and uniformity of pore formation during pyrolysis. David showed in his study that oxidative thermastabilization atmosphere produced more stable CMS membranes and longer soaking time brought about more selective while less permeable membranes [30]. Similarly, Kusuki et al. prevented softening and collapse and maintained the asymmetric morphology of the fibers during pyrolysis by heating the polymer in air at 400 ^{o}C for 30 minutes prior to pyrolysis [31].

Some researchers used a non-solvent or chemical agent to modify the precursor before pyrolysis. Tin et al. investigated the effects of non-solvent pretreatment [32]. The precursor films were soaked in methanol, ethanol, propanol and butanol for one day. It was claimed that by doing so, the intermolecular interactions were weakened and the structure reorganization was promoted. Results proved that this method reduced the pore size and increased gas selectivity of CMS membranes.

For the purpose of this study, a pretreatment method referred to as pre-crosslinking was probed. 6FDA/DETDA:DABA(3:2) dense films were thermally treated at 370 ^{o}C under pure argon purge for 90 mins. By doing so, the DABA moiety tends to thermally crosslink and opens up the resulting CMS structure.

2.3.3 Pyrolysis

Pyrolysis or carbonization is a process in which a precursor is heated in a controlled inert atmosphere to a final pyrolyzing temperature at a specific heating rate and soaked at the final temperature for a sufficiently long time. The pyrolysis process is conventionally meant for the production of porous material with microporosity of molecular dimensions that is responsible for molecular sieving [33]. The pore structure of CMS membranes are envisioned to be comprised of micropores connected with

ultramicropores. The pore distribution can be tuned by adjusting some key parameters: pyrolysis temperature, pyrolysis atmosphere, ramp rate and thermal soak time.

a) Pyrolysis temperature

Pyrolysis temperature is the highest temperature to which the precursor is heated. It is usually chosen to lie in between the decomposition temperature of the precursor and its graphitization temperature [1, 34]. Pyrolysis temperature is closely related to the membrane structure and separation performance. Generally speaking, a higher pyrolysis temperature leads to carbon membranes with more compact structure, more turbostratic structure, higher crystallinity and density [35].

Rungta et al. reported pyrolysis of Matrimid® dense films at several temperatures between 500 ^{o}C and 800 ^{o}C and tested them for pure gas C_2H_4 and C_2H_6 at 35 ^{o}C and 50 psia [36]. The results are shown in Figure 2.6. In going from 500 ^{o}C to 800 ^{o}C, the membrane permeability drops with a corresponding increase in selectivity. The authors also characterized the different-temperature-pyrolyzed CMS membranes with XRD and CO_2 sorption measurements. They found the XRD peak was more pronounced for higher temperature pyrolyzed membranes, indicating an increase in structure ordering with an increase in pyrolysis temperature. From CO_2 sorption measurements, they found the pore size distribution showed an overall shift towards the smaller end. These findings explained the loss of permeability and the gain of selectivity as pyrolysis temperature increases.

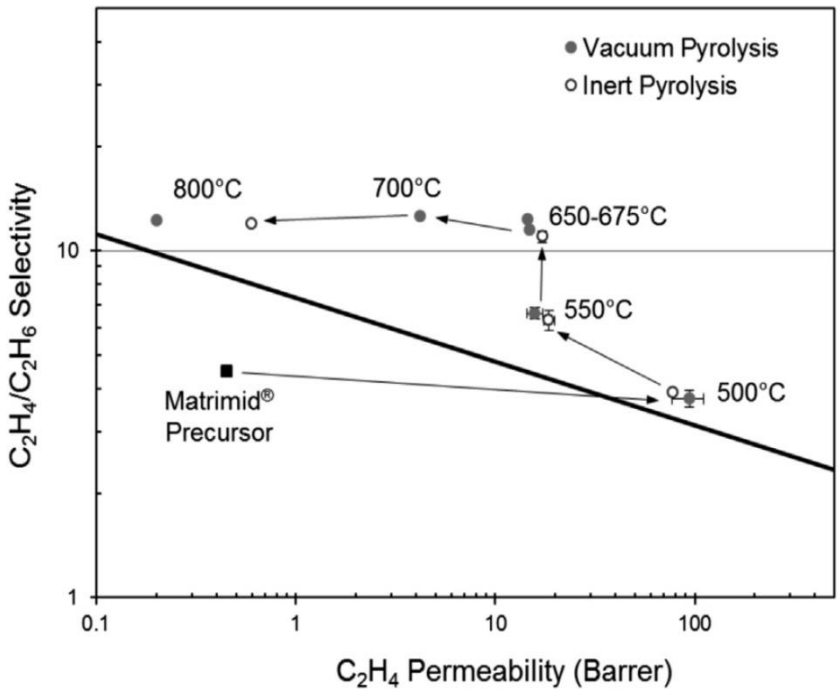

Figure 2.6: Pure gas C_2H_4/C_2H_6 separation performance (35 ^oC, 50 psia) of CMS dense films derived from Matrimid® at different pyrolysis temperatures [36].

Steel and Koros [37] studied CMS membranes derived from Matrimid® and 6FDA/BPDA-DAM by pyrolysis at two temperatures: 550 ^oC and 800-^oC. The results for CO_2/CH_4 and O_2/N_2 separation are shown in Figure 2.7. A decrease in both O_2 and CO_2 permeability along with an increase in CO_2/CH_4 and O_2/N_2 selectivity due to increasing the pyrolyzing temperature can be observed in both CMS membranes.

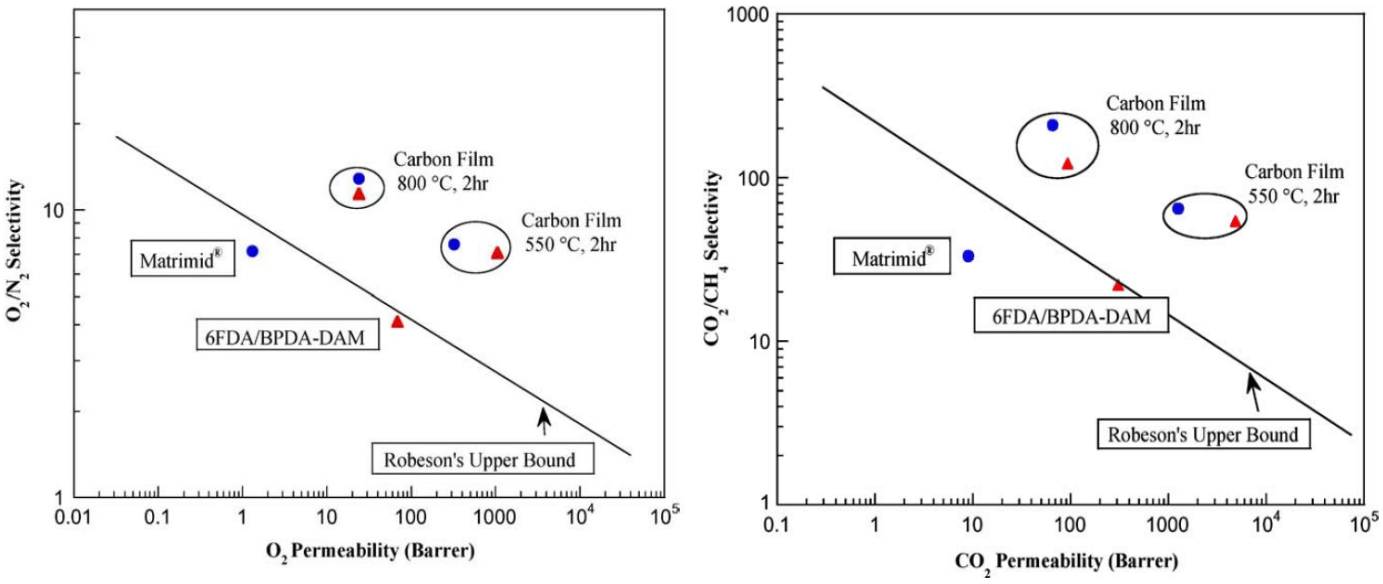

(i) (ii)

Figure 2.7: Effects of final pyrolysis temperature on: (i) CO_2/CH_4; (ii) O_2/N_2 separation of CMS membranes derived from Matrimid® and 6FDA/BPDA-DAM [37].

b) Pyrolysis atmosphere

In order to prevent undesired burn off and chemical damage of the membrane precursor during pyrolysis, a vacuum or inert pyrolysis atmosphere needs to be controlled.

Geiszler and Koros studied the separation performance of 6FDA/BPDA-DAM asymmetric hollow fiber CMS membranes pyrolyzed at different atmosphere: under vacuum (0.01-0.03 mtorr); under inert atmosphere of helium, argon, and carbon dioxide with gas flow rates of 20 and 200 sccm [38, 39]. They found CMS membranes produced by vacuum pyrolysis shower higher gas selectivity than those produced in inert atmosphere. On the other hand, considering the uncertainty of the experimental data, little difference was observed among the membranes pyrolyzed under the three different inert purge gases: helium, argon, and carbon dioxide.

Kiyono et al. [40] investigated a method referred to as oxygen doping with 6FDA/BPDA-DAM derived CMS membranes and found a strong relationship exists between the amount of oxygen and the transport properties of the membranes. At elevated temperature, the oxygen present in the inert gas selectively chemisorb at the ultramicropores, thus allowing subtle tuning of the membrane separation performance. Figure 2.8 below illustrates this oxygen doping hypothesis [41]. Results, as shown in Figure 2.9, demonstrated that CMS membranes pyrolyzed under O_2 doped inert gases perform as attractively as those obtained from vacuum pyrolyzing. Hence, the need for highly-cost vacuum pyrolyzing to achieve high selectivities can be avoided by utilizing O_2 doping.

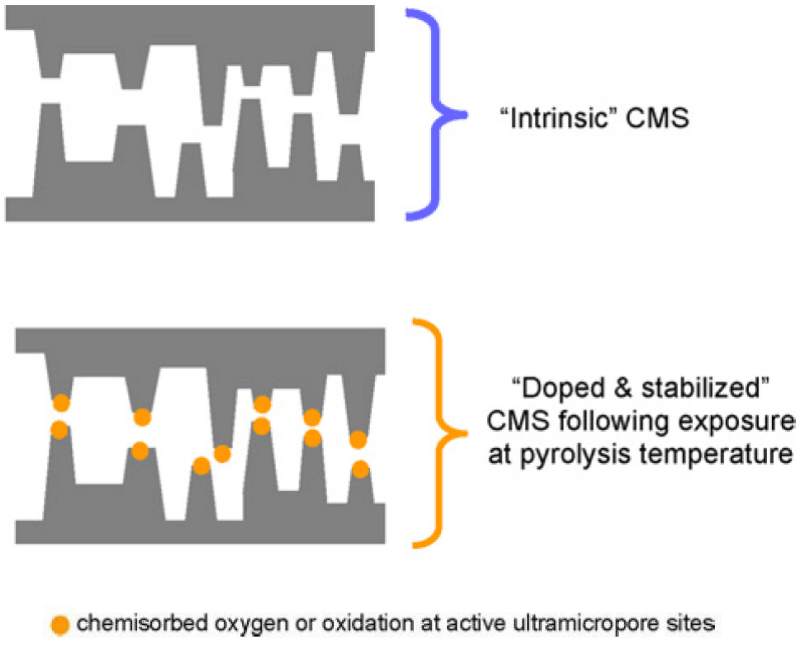

Figure 2.8: Schematic of oxygen doping process [40].

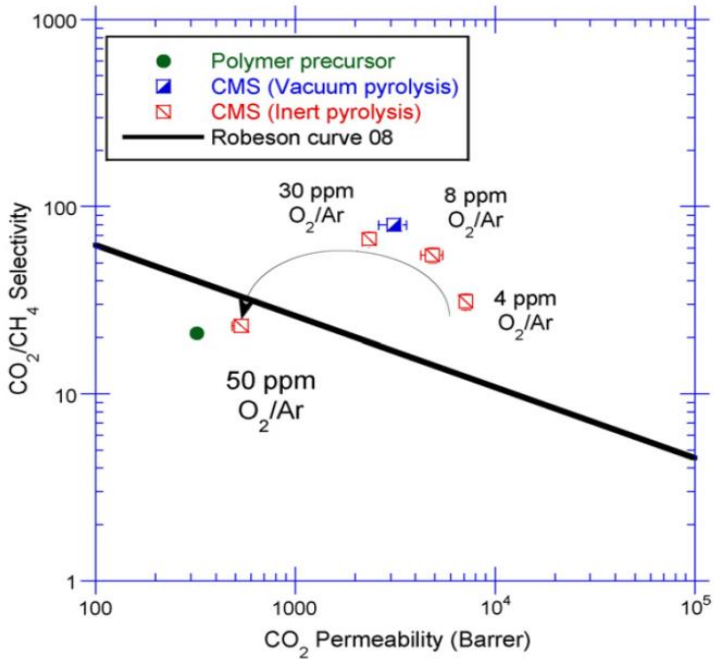

Figure 2.9: Oxygen doping effect on CO_2/CH_4 separation performance for CMS dense films derived from 6FDA/BPDA-DAM [40].

Nevertheless, there is a cut-off point in the benefit of O_2 doping method. As can be seen in Figure 2.9, 50 ppm O_2 doped CMS membrane showed both lower permeability and lower selectivity. It is believed that the excessive amount of O_2 may have filled most of the "active" ultramicropore sites. Essentially, O_2 doping method is useful in tuning the separation performance for membranes with intrinsically open morphology [42].

c) Ramp rate

Ramp rate or heating rate determines the evolution rate of volatile components from the polymer matrix. Lower heating rate is typically preferred since it allows the production of smaller pores and consequently higher selectivity [24, 43]. Excessively

high heating rate might result in pinholes, microscopic crack, blisters and distortion. In Suda and Haraya's work [24], the ramp rate during pyrolysis was varied from 1.33 K/min to 13.3 K/min. Results showed CMS membranes fabricated under a higher ramp rate exhibit higher permeability for several gases.

d) Soak time

Different soaking time would be preferred corresponding to different pyrolysis temperature [33]. Numerous studies have shown that a prolonged soaking time would increase selectivity since longer baking time promotes pore sintering [24, 37, 40, 44]. As shown in Figure 2.10, Steel demonstrated that soaking time has a larger effect on permeability compared with selectivity. Moreover, as the pyrolysis temperature increases from 550 ^{o}C to 800 ^{o}C, the effect of soaking time is less pronounced.

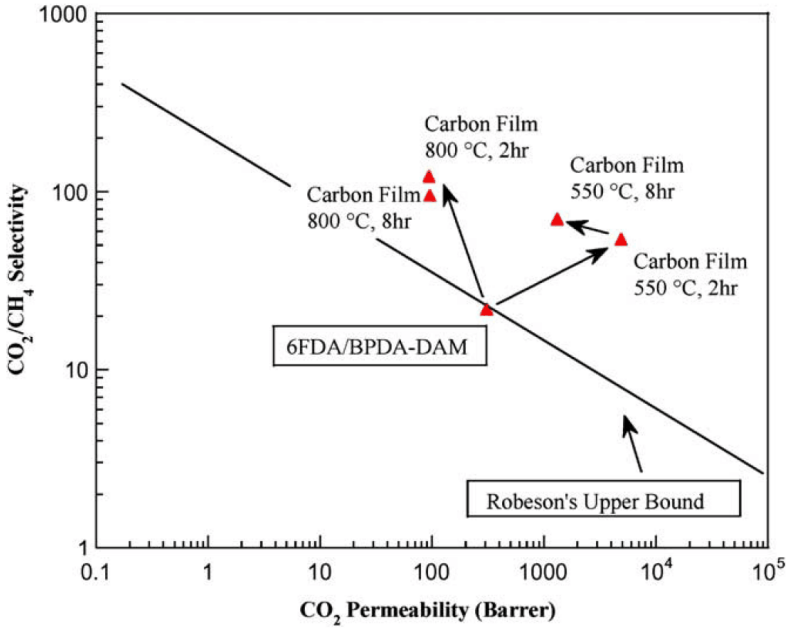

Figure 2.10: Effects of thermal soaking time on CMS dense films derived from 6FDA/BPDA-DAM [37].

2.3.4 Post-treatment

After pyrolyzing, polymeric membranes are transformed into carbon membranes. Afterward, various post-treatment methods have been applied to finely adjust the membrane porosity or even fix defects and cracks. Commonly used post-treatment methods are post-oxidation, chemical vapor deposition (CVD), post-pyrolysis and coating [14, 45].

A successful example of post-treatment is referred to as "Dual Temperature Secondary Oxygen Doping (DTSOD)" developed by Singh and Koros [46]. In this post-treatment, the 6FDA/BPDA-DAM derived CMS membrane was exposed to trace amount of O_2 by briefly taking it to a temperature higher than the final pyrolysis temperature. This treatment is believed to allow selective doping at the ultramicropore edges and as can be seen from Figure 2.11, it dramatically increases the membrane selectivity.

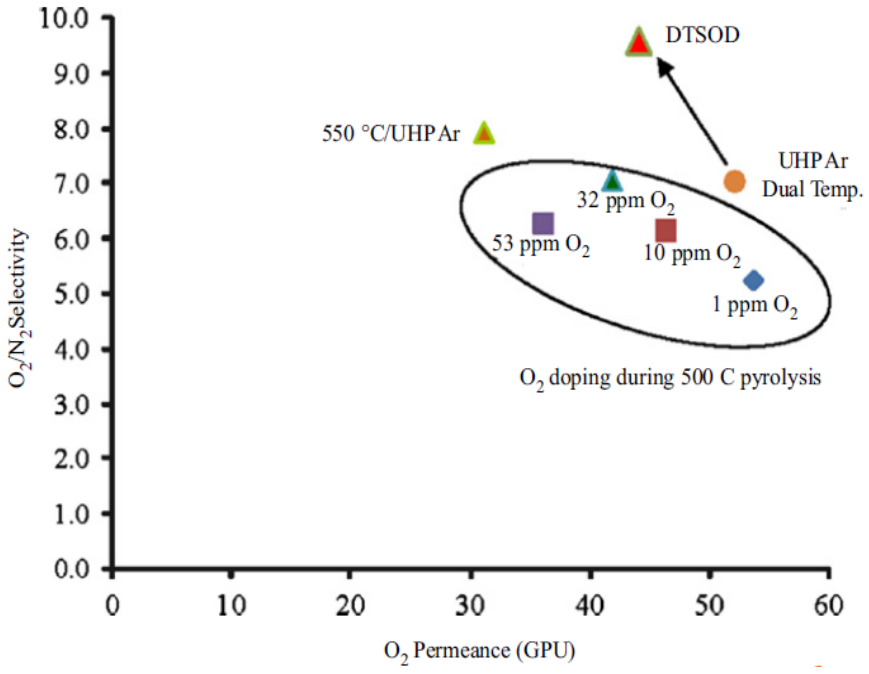

Figure 2.11: Effects of DTSOD post-treatment on CMS dense films derived from 6FDA/BPDA-DAM [46].

2.3.5 Module construction

As mentioned in previous section, asymmetric structure or hollow fiber configuration is preferred for commercial application in order to achieve high permeation rates of the products. A suitable module is critical to ensure the successful application of the membranes [47]. The general and basic requirement for a module to be practical is that it is capable of achieving high productivity and efficiency while keeping operational and maintenance cost low. Two selected examples of modules are shown in Figure 2.12.

a)

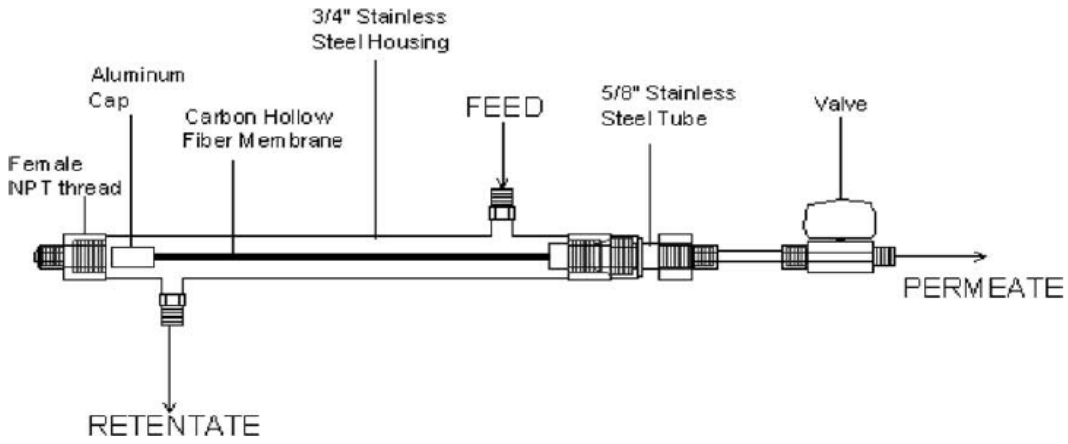

b)

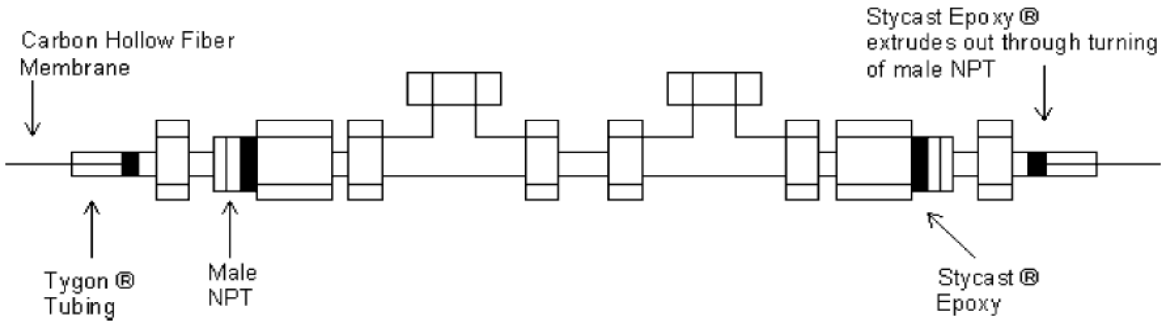

Figure 2.12: Two selected modules fabricated by various researchers [48-50].

2.4 Gas transport and sorption in membranes

Membranes are selective barriers between two phases [51]. They physically separate a gas mixture into two streams by allowing one or more component to pass through, forming a permeate stream while retaining the remaining penetrants at the retentate stream. Several mechanisms can be associated to describe the transport of penetrants through membranes: 1) Knudsen diffusion transport; 2) selective surface adsorption with surface diffusion; 3) molecular sieving transport, and 4) sorption-diffusion transport [52]. These mechanisms are shown in Figure 2.13.

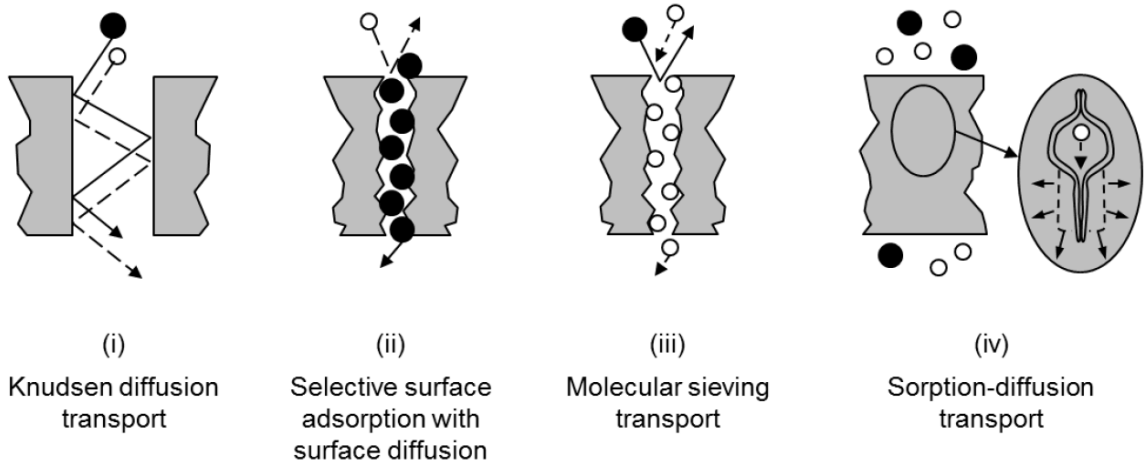

Figure 2.13: Four general mechanisms for selective membranes [52].

Knudsen diffusion transport

When the pore radius is smaller than the mean free paths of the penetrants, Knudsen flow occurs, and the selectivity between gas species can be related with their molecular weights as [53]:

$$\alpha_{A/B} = \sqrt{\frac{M_A}{M_B}} \tag{2.1}$$

where $\alpha_{A/B}$ is the Knudsen selectivity for gas penetrant A vs. B, M_A and M_B are the molecular weight of penetrant A and B. Since popular gas pairs such as: CO_2/CH_4, O_2/N_2, and C_3H_6/C_3H_8 all have relatively similar molecular weight, Knudsen selectivity for these gas pairs are fairly low.

Selective adsorption separation

When one gas penetrant is preferably adsorbed into the membrane over the other, Selective adsorption separation happens. The absorbed gas molecule afterward surface diffuse across the membrane from one sorbed site to the next [54].

Molecular sieving transport

Molecular sieving transport is a selective mechanism based on the size and shape difference between the penetrants. Smaller gas species can diffuse faster than the bigger ones, so the membrane allows the passage of the smaller molecule through resulting in effective separation [55].

Sorption-diffusion transport

In this selective mechanism, both of the size and condensability of the penetrant determine which species goes through the membrane faster. Gas transport through CMS membranes is believed to follow sorption-diffusion mechanism. Micropores provide sorption sites, gases hop from one site to another due to the concentration gradient between upstream and downstream side. Ultramicropores provide diffusion restrictions, requiring the penetrant to overcome repulsive interactions from the walls. This combination of micropores and ultramicropores provide CMS membranes with both high permeability and high selectivity. In fact, one can have molecular sieving and sorption diffusion together in CMS materials.

The following sections will discuss about the detailed transport, including permeation and diffusion, and sorption theory for membrane gas separation.

2.4.1 Permeation

Permeation through membranes follows sorption-diffusion mechanism. Gas molecules sorb into the high pressure upstream side of the membrane, and diffuse through it due to the chemical potential gradient, and desorb at the low pressure downstream side [56]. This membrane separation process mechanism is shown in Figure 2.14.

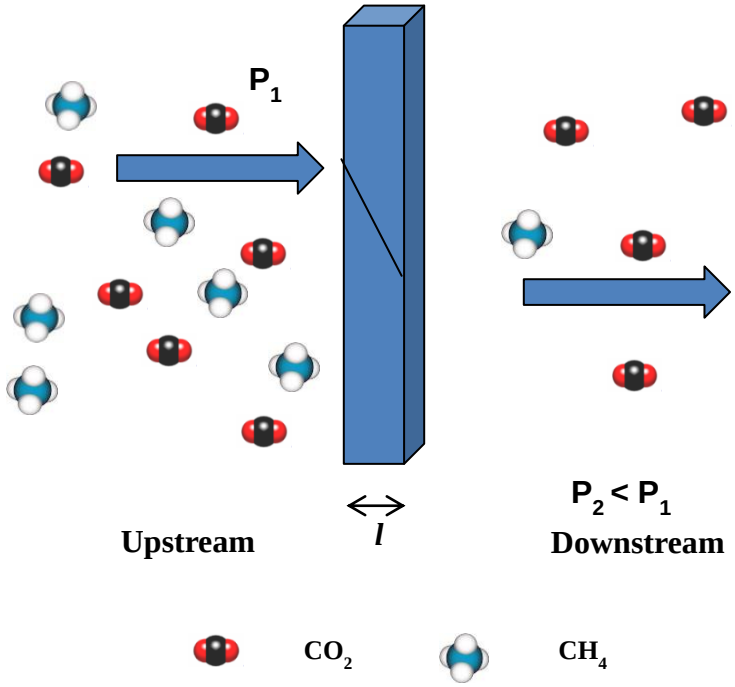

Figure 2.14: Schematic representation of CO_2/CH_4 separation by a sorption-diffusion process.

Two terms, "permeability" and "selectivity", are commonly used to describe the most important properties of membranes—productivity and separation efficiency respectively. Permeability (P_i) is equal to the transmembrane pressure and thickness normalized flux:

$$P_i = \frac{N_i * l}{\Delta p_i} \tag{2.2}$$

where N_i is the penetrant flux through the membrane of thickness (l) under a transmembrane partial pressure difference(Δp_i). The most frequently used unit for permeability, Barrer, is defined as below:

$$1\ \text{Barrer}\ [=]\ 10^{-10}\ \frac{\text{cc(STP)*cm}}{\text{cm}^2\text{*s*cmHg}} \tag{2.3}$$

For homogeneous dense film membrane, the membrane thickness (l) can be measured directly; however in the case of asymmetric hollow fibers, which will be discussed later, the actual membrane thickness is not readily known. Thus the term of permeance, which is simply the pressure normalized flux, is commonly used to describe the productivity as defined below:

$$\frac{P_i}{l} = \frac{N_i}{\Delta p_i} \tag{2.4}$$

and the unit for permeance is GPU and defined as :

$$1\ \text{GPU}\ [=]\ 10^{-6}\ \frac{\text{cc(STP)}}{\text{cm}^2\text{*s*cmHg}} \tag{2.5}$$

The flux of gas molecules through membranes is governed by Fick's law, and the diffusion coefficient is assumed to be independent of the concentration. Thus, the one-dimensional diffusion is given by:

$$N_i = -D_i \frac{dC_i}{dx} \tag{2.6}$$

where D_i and C_i are the diffusion coefficient and the concentration of component i respectively, x is the coordinate in the direction of permeation.

Combining Eqs. 2.2 and 2.6, one can get:

$$P_i = \frac{N_i * l}{\Delta p_i} = -D_i \frac{dC_i}{dx} * \frac{l}{\Delta p_i} \tag{2.7}$$

The diffusion coefficient often depends on local concentration, and in this case, an average diffusion coefficient can be obtained as:

$$\overline{D}_i = \frac{\int_{C_{i,d}}^{C_{i,u}} D_i(C_i)dC_i}{\int_{C_{i,d}}^{C_{i,u}} (C_i)dC_i} \tag{2.8}$$

where $C_{i,u}$ and $C_{i,d}$ represent the upstream and downstream gas concentrations respectively.

Eqs. 2.7 and 2.8 together gives:

$$P_i = \overline{D}_i \frac{(C_{i,u} - C_{i,d})}{\Delta p_i} \tag{2.9}$$

The average sorption coefficient is:

$$\overline{\mathbb{S}}_i = \frac{\int_{C_{i,d}}^{C_{i,u}} dC_i}{\int_{P_{i,d}}^{P_{i,u}} dP_i} = \frac{(C_{i,u} - C_{i,d})}{\Delta p_i} \tag{2.10}$$

Substituting Eq. 2.10 into Eq. 2.9, the permeability can be expressed as the product of a kinetic factor of average diffusion coefficient, and a thermodynamic factor of average sorption coefficient:

$$P_i = \overline{D}_i * \overline{\mathbb{S}}_i \tag{2.11}$$

The separation factor, which characterizes a membrane's ability to separate different penetrants, is equal to the ratio of the upstream and downstream mole fraction of two components. When the downstream pressure is negligible, as in this study, one can write:

$$\alpha_{A/B} = \frac{P_A}{P_B} = \left(\frac{D_A}{D_B}\right)\left(\frac{\mathbb{S}_A}{\mathbb{S}_B}\right) \tag{2.12}$$

For mixed gas feeding, separation factor is a practical measurement of the separation efficiency. Again, in the case where downstream pressure is negligible compared to upstream, selectivity can calculated by Eq. 2.13:

$$\alpha_{A/B} = \frac{(y_A / y_B)}{(x_A / x_B)} \tag{2.13}$$

where x_i is the mole fraction of component i on the feed side and y_i is the mole fraction on the permeate side. x_i is controlled by the specific composition in the feed gas cylinder and y_i is measured by gas chromotography (GC).

2.4.2 Sorption

The sorption coefficient describes the amount or concentration of gas taken up by a membrane at a given pressure at equilibrium as expressed in Eq. 2.14 [56].

$$\mathbb{S}_i = \frac{C_i}{p_i} \tag{2.14}$$

In glassy polymers, the dual mode sorption model is often used since gas penetrants may sorb into both dense polymer matrix and the molecular scale holes or microvoids. Those molecules sorbed into the dense polymer matrix by ordinary dissolution process follow Henry's law:

$$C_{Di} = k_{Di} * p_i \tag{2.15}$$

where k_{Di} is the Henry's law constant. On the other hand, those molecules sorbed into the limited number of microvoids in the polymer matrix follow Langmuir sorption:

$$C_{Hi} = \frac{C'_{Hi} b_i p_i}{1 + b_i p_i} \tag{2.16}$$

where $C'_{Hi'}$ is the Langmuir hole filling capacity and b_i is the Langmuir affinity constant. Thus the total concentration of dissolved gas at a given pressure and temperature in the polymer is given as the sum of Eqs. 2.15 and 2.16 as shown in Eq. 2.17 and Figure 2.15:

$$C_i = C_{Di} + C_{Hi} = k_{Di} * p_i + \frac{C'_{Hi} b_i p_i}{1 + b_i p_i} \tag{2.17}$$

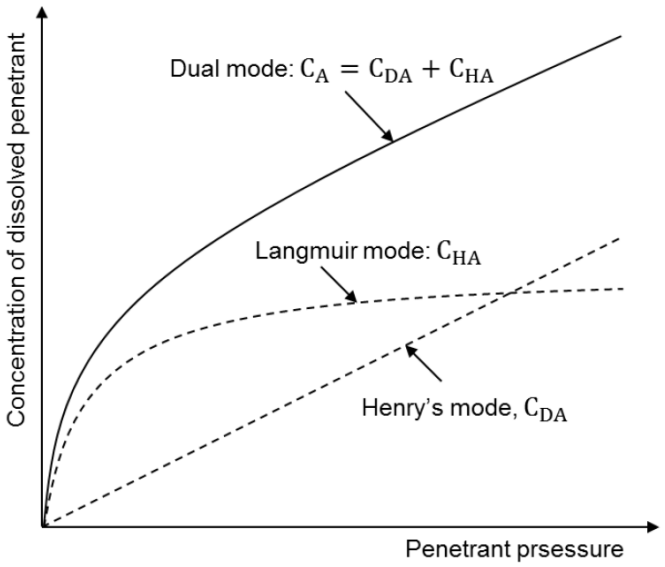

Figure 2.15: Typical sorption isotherm.

For molecular sieving materials, such as zeolites and CMS membrane, there is no dilation of the rigid CMS structure with a finite number of sorption sites, the Langmuir isotherm is typically used alone to describe the sorption process:

$$C_i = C_{Hi} = \frac{C'_{Hi} b_i p_i}{1 + b_i p_i} \tag{2.18}$$

In CMS materials, the majority of the penetrants are believed to be sorbed into larger micropores since the repulsive interaction energy of these molecules is lower than

those residing in the critical ultramicropores. Figure 2.16 is a simplified cartoon showing this idea.

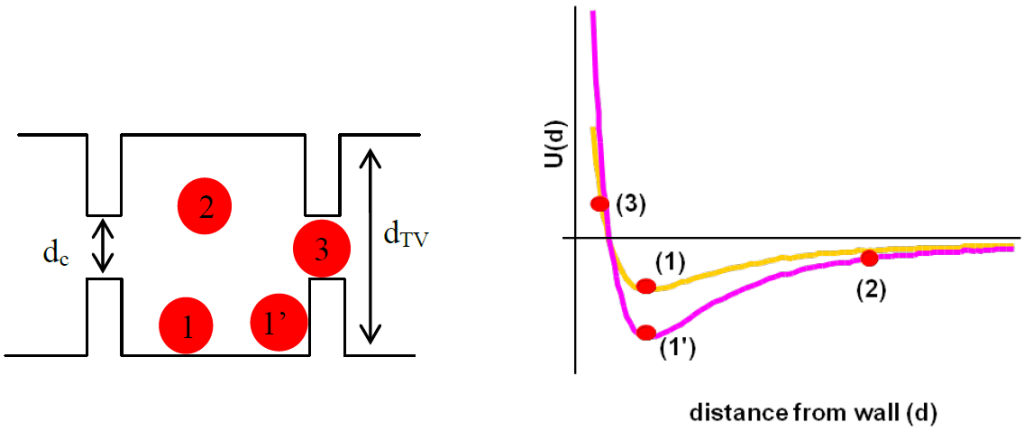

Figure 2.16: (a) Idealized equilibrium positions inside the pore structure; (b) potential energy of penetrants sorbed at different locations [41].

2.4.3 Diffusion

The diffusion coefficient measures the mobility of a gas penetrant through the membrane. In polymeric and CMS membranes, gas molecules diffuse through the membrane along the direction of the concentration gradient by making random jump from one site to another. Quantitatively, diffusion coefficient can be expressed as below:

$$D_i = \frac{f_i \lambda_i^2}{6} \tag{2.19}$$

where f_i is the frequency of jumps the molecule i makes and λ_i is the average diffusion jump length [57].

In polymer membranes, there are fluctuating gaps that are continuously created and redistributed by thermally stimulated polymer chain segmental motions. A sufficient-

sized transient gap enables an adjacent sorbed gas molecule to execute a diffusive jump, as shown in Figure 2.17. The molecules sitting in a sorption site are considered to be in the normal state and those going through the transient gap are considered in the activated state. The diffusion discrimination of polymer membranes results from the difference in the sizes and condensabilities between the penetrants.

CMS membranes, on the other hand, contain rigid micropore and ultramicropore structures. The gas molecules need to make effective diffusive jumps from one sorption site (micropore) to another through a narrow window (ultramicropore). This process is also depicted in Figure 2.17. Gas molecules sitting in micropores are considered to be in the normal state while those going through the ultramicropores are in the activated state. When going through the ultramicropore window, gas molecules need to overcome the repulsive interaction energy from the rigid carbon wall. "Energetic selectivity" takes place due to the difference in the activation energies required to make effective diffusive jump between different penetrants. Moreover, the rigid ultramicropore windows can effectively discriminate the shapes and sizes of different penetrants, referred to as "entropic selectivity". Detailed discussion of energetic selectivity and entropic selectivity will be provided in the later chapters. Entropic selectivity is believed to be the reason for CMS membranes to outperform polymeric membranes.

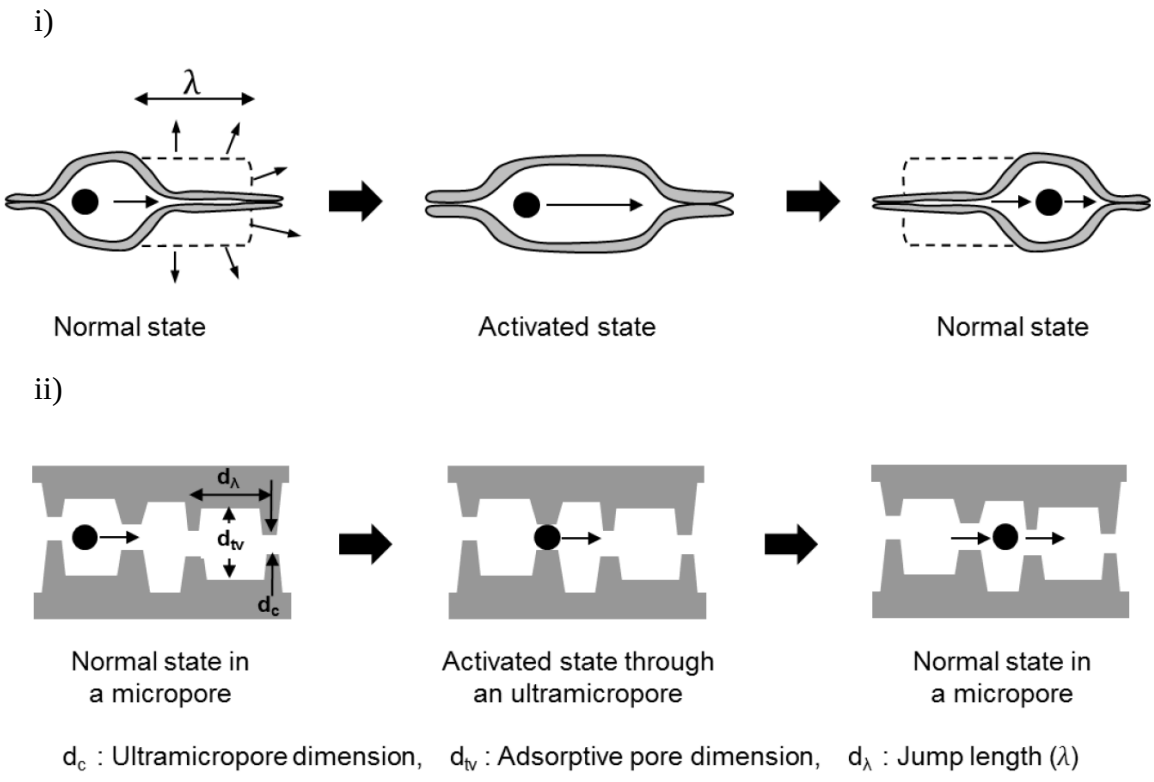

Figure 2.17: Conceptual depiction of a diffusion step in: i): polymeric membranes; (ii) CMS membranes [58].

The average diffusion coefficient has been widely used to characterize CMS membranes in literature [59-62]; however, it can be highly dependent on concentration. In some cases, especially when highly adsorbing gases are considered, a thermodynamically corrected diffusivity – Maxwell-Stefan diffusivity is useful.

Unlike the conventional Fickian transport diffusivity D_f, the Maxwell-Stefan diffusivity Đ accounts for the amount of gas taken up by the media [63, 64] in its interpretation. The two coefficients can be mathematically related as Eq. 2.20:

$$Đ = D_f \frac{d \ln C(p)}{d \ln p} \tag{2.20}$$

where p is the single component gas phase equilibrium pressure and C(p) is the gas sorbed by the media at equilibrium pressure of p. In combination with a Langmuir isotherm model shown in Eq. 2.16, for gas i, one finds:

$$Đ_i = D_{fi}(1-\theta_i) \tag{2.21}$$

where θ_i is the fractional site saturation factor defined as below:

$$\theta_i = \frac{b_i p_i}{1+b_i p_i} \tag{2.22}$$

The average diffusivity can be calculated by integrating the local Fickian diffusivity between a given upstream and downstream (vacuum in this study) concentration in the membrane. Thus, from Eqs. 2.20-2.22, one finds:

$$D_i = \frac{\int_{C_i}^{0} D_f dC_i}{\int_{C_i}^{0} dC_i} \approx \frac{\int_{\theta_i}^{0} \frac{Đ_i}{(1-\theta_i)} d\theta_i}{\int_{\theta_i}^{0} d\theta_i} = \frac{Đ_i}{\theta_i} \ln\left(\frac{1}{1-\theta_i}\right) \tag{2.23}$$

Eq. 2.23 provides a bridge to connect the average diffusivity, which can be easily obtained from permeation and sorption measurements, to the Maxwell-Stefan diffusivity.

2.4.4 Temperature dependence of permeation, diffusion, and sorption

Gas permeation and diffusion through membranes are typically activated processes, and an Arrhenius relationship describes the temperature dependence of gas permeation and diffusion [57, 65], viz.,

$$P_i = P_{0i} \exp\left(\frac{-E_{Pi}}{RT}\right) \tag{2.24}$$

$$D_i = D_{0i} \exp\left(\frac{-E_{Di}}{RT}\right) \tag{2.25}$$

On the other hand, a van't Hoff expression describes gas sorption in membranes:

$$\mathbb{S}_i = \mathbb{S}_{0i} \exp\left(\frac{-H_{\mathbb{S}i}}{RT}\right) \tag{2.26}$$

where P_{0i} , D_{0i} and $\mathbb{S}_{0i}$ are pre-exponential factors, E_{Pi} is the activation energy for permeation, E_{Di} is the activation energy for diffusion, and $H_{\mathbb{S}i}$ is the heat of sorption. R is the universal gas constant, and T is the absolute temperature.

Combination of Eqs. 2.11 and 2.24-2.26 states that permeation activation energy is the sum of diffusion activation energy and heat of sorption, so it is a more complex parameter than either of the individual energetic factors.

$$E_{Pi} = E_{Di} + H_{\mathbb{S}i} \tag{2.27}$$

Moreover, the pre-exponential factors can be arranged to yield:

$$P_{0i} = D_{0i} * \mathbb{S}_{0i} \tag{2.28}$$

2.4.5 Energetic and entropic factors in diffusion selectivity

According to the Eyring theory of rate processes [66]:

$$D = \lambda^2 \frac{kT}{h} e^{S_D/R} e^{-H_D/RT} \tag{2.29}$$

where λ is the average diffusive jump length in the diffusion medium, S_D is the activation entropy of diffusion, k is Boltzmann's constant, h is Planck's constant and the activation enthalpy of diffusion H_D , if assuming negligible volume change in the diffusion process, can be expressed as below:

$$H_D = E_D + PV \approx E_D + RT \tag{2.30}$$

Combining Eqs. 2.29 and 2.30, one can get

$$D = e\lambda^2 \frac{kT}{h} e^{S_D/R} e^{-E_D/RT} \tag{2.31}$$

For gas pairs concerned in this study, λ may be considered equivalent since the average distance between equilibrium micropores should be same. The diffusion selectivity then becomes:

$$\frac{D_A}{D_B} = \underbrace{\left[\exp\left(\frac{S_{DA}-S_{DB}}{R}\right)\right]}_{\text{Entropic selectivity}} \underbrace{\left[\exp\left(-\frac{E_{DA}-E_{DB}}{RT}\right)\right]}_{\text{Energetic selectivity}} \tag{2.32}$$

Eq. 2.32 shows clearly that the diffusion selectivity can be factored into an "energetic selectivity" and an "entropic selectivity". Energetic selectivity stems from the difference in the diffusion activation energies of the two penetrants, while entropic selectivity primarily reflects the difference in the diffusion activation entropies of the two penetrants. Singh and Koros [67] have discussed the significance of entropic selectivity in molecular sieving materials for the O_2/N_2 pair. They also showed that in polymeric membranes, entropic selectivity is close to unity, while in CMS membranes, a much higher entropic selectivity is observed. The high entropic selectivity in CMS membrane is enabled by the rigid CMS pore structures, which polymer membranes lack. This fundamental fact is the main reason for CMS and zeolite membranes to surpass the polymeric upper bound. Entropic selectivity reflects differences in penetrant shape and subtle configurational differences experienced by penetrants transversing the diffusion-limiting ultramicropores. This entropic configurational control can be engineered by controlling differences in rotational and internal vibrational degrees of freedom between the diffusing components.

2.5 References

[1] H. Suda, K. Haraya, Gas permeation through micropores of carbon molecular sieve membranes derived from Kapton polyimide, J. Phys. Chem. B, 101 (1997) 3988-3994.

[2] D.Q. Vu, W.J. Koros, S.J. Miller, High Pressure CO2/CH4Separation Using Carbon Molecular Sieve Hollow Fiber Membranes, Industrial & Engineering Chemistry Research, 41 (2002) 367-380.

[3] G.M. Jenkins, K. Kawamura, Polymeric carbons- carbon fibre, glass and char., Cambridge University Press, London, 1976.

[4] H.O. Pierson, Handbook of carbon, graphite, diamond, and fullerenes, Noyes Publications, New Jersey, 1993.

[5] H. Marsh, Introduction to carbon science, Butterworths, 1989.

[6] T. Enoki, M. Endo, M. Suzuki, Graphite intercalation compounds and applications, Oxford University Press, New York, 2003.

[7] H. Marsh, F.R. Reinoso, Activated carbon, Elsevier, Great Britain, 2006.

[8] K.M. Steel, W.J. Koros, Investigation of porosity of carbon materials and related effects on gas separation properties, Carbon, 41 (2003) 253-266.

[9] Y. Xiao, T.-S. Chung, M.L. Chng, S. Tamai, A. Yamaguchi, Structure and properties relationships for aromatic polyimides and their derived carbon membranes: Experimental and simulation approaches, J. Phys. Chem. B, 109 (2005) 18741-18748.

[10] L. Shao, T. Chung, G. Wensley, S. Goh, K. Pramoda, Casting solvent effects on morphologies, gas transport properties of a novel 6FDA/PMDA?TMMDA copolyimide membrane and its derived carbon membranes, Journal of Membrane Science, 244 (2004) 77-87.

[11] M. Das, J.D. Perry, W.J. Koros, Gas-Transport-Property Performance of Hybrid Carbon Molecular Sieve-Polymer Materials, Ind. Eng. Chem. Res., 49 (2010) 9310-9321.

[12] G.F.L. Ehlers, K.R. Fisch, W.R. Powell, Thermal degradation of polymers with phenylene units in the chain. IV. Aromatic polyamides and polyimides, Journal of Polymer Science Part A-1: Polymer Chemistry, 8 (1970) 3511-3527.

[13] H. Hatori, Y. Yamada, M. Shiraishi, M. Yoshihara, T. Kimura, The mechanism of polyimide pyrolysis in the early stage, Carbon, 34 (1996) 201-208.

[14] S.M. Saufi, A.F. Ismail, Fabrication of carbon membranes for gas separation—a review, Carbon, 42 (2004) 241-259.

[15] J.E. Koresh, A. Sofer, Molecular Sieve Carbon Permselective Membrane. Part I. Presentation of a New Device for Gas Mixture Separation, Sep. Sci. Technol., 18 (1983) 723-734.

[16] V.M. Linkov, R.D. Sanderson, E.P. Jacobs, Carbon membranes from precursors containing low-carbon residual polymers, Polym. Int., 35 (1994) 239-242.

[17] V.M. Linkov, R.D. Sanderson, E.P. Jacobs, Highly asymmetrical carbon membranes, J. Membr. Sci., 95 (1994) 93-99.

[18] A.B. Fuertes, I. Menendez, Separation of hydrocarbon gas mixtures using phenolic resin-based carbon membranes, separ. Sci. Technol., 28 (2002) 29-41.

[19] W. Wei, G. Qin, H. Hu, L. You, G. Chen, Preparation of supported carbon molecular sieve membrane from novolac phenol–formaldehyde resin, Journal of Membrane Science, 303 (2007) 80-85.

[20] T.A. Centeno, A.B. Fuertes, Supported carbon molecular sieve membranes based on a phenolic resin, J. Membr. Sci., 160 (1999) 201-211.

[21] M. Acharya, H.C. Foley, Spray-coating of nanoporous carbon membranes for air separation, J. Membr. Sci., 161 (1999) 1-5.

[22] M. Acharya, B.A. Raich, H.C. Foley, M.P. Harold, J.J. Lerou, Metal-Supported Carbogenic Molecular Sieve Membranes: Synthesis and Applications, Industrial & Engineering Chemistry Research, 36 (1997) 2924-2930.

[23] T.A. Centeno, A.B. Fuertes, Carbon molecular sieve gas separation membranes based on poly(vinylidene chloride-co-vinyl chloride), Carbon, 38 (2000) 1067-1073.

[24] H. Suda, K. Haraya, Gas Permeation through Micropores of Carbon Molecular Sieve Membranes Derived from Kapton Polyimide, The Journal of Physical Chemistry B, 101 (1997) 3988-3994.

[25] J. Barsema, S. Klijnstra, J. Balster, N. Vandervegt, G. Koops, M. Wessling, Intermediate polymer to carbon gas separation membranes based on Matrimid PI, Journal of Membrane Science, 238 (2004) 93-102.

[26] M. Kiyono, P.J. Williams, W.J. Koros, Generalization of effect of oxygen exposure on formation and performance of carbon molecular sieve membranes, Carbon, 48 (2010) 4442-4449.

[27] Y.K. Kim, J.M. Lee, H.B. Park, Y.M. Lee, The gas separation properties of carbon molecular sieve membranes derived from polyimides having carboxylic acid groups, J. Membr. Sci., 235 (2004) 139-146.

[28] H.B. Park, Y.K. Kim, J.M. Lee, S.Y. Lee, Y.M. Lee, Relationship between chemical structure of aromatic polyimides and gas permeation properties of their carbon molecular sieve membranes, J. Membr. Sci., 229 (2004) 117-127.

[29] M. Kiyono, P.J. Williams, W.J. Koros, Effect of polymer precursors on carbon molecular sieve structure and separation performance properties, Carbon, 48 (2010) 4432-4441.

[30] L.I.B. David, A.F. Ismail, Influence of the thermastabilization process and soak time during pyrolysis process on the polyacrylonitrile carbon membranes for O2/N2 separation, J. Membr. Sci., 213 (2003) 285-291.

[31] Y. Kusuki, H. Shimazaki, N. Tanihara, S. Nakanishi, T. Yoshinaga, Gas permeation properties and characterization of asymmetric carbon membranes prepared by pyrolyzing asymmetric polyimide hollow fiber membrane, J. Membr. Sci., 134 245-253.

[32] P.S. Tin, T.S. Chung, A.J. Hill, Advanced Fabrication of Carbon Molecular Sieve Membranes by Nonsolvent Pretreatment of Precursor Polymers, Ind. Eng. Chem. Res., 43 (2004) 6476-6483.

[33] E. Schindler, F. Maier, Manufacture of porous carbon membranes, in, US patent 4919860, 1990.

[34] V.C. Geiszler, W.J. Koros, Effects of Polyimide Pyrolysis Conditions on Carbon Molecular Sieve Membrane Properties, Ind. Eng. Chem. Res., 35 (1996) 2999-3003.

[35] N. Tanihara, H. Shimazaki, Y. Hirayama, S. Nakanishi, T. Yoshinaga, Y. Kusuki, Gas permeation properties of asymmetric carbon hollow fiber membranes prepared from asymmetric polyimide hollow fiber, J. Membr. Sci, 160 (1999) 179-186.

[36] M. Rungta, L. Xu, W.J. Koros, Structure–performance characterization for carbon molecular sieve membranes using molecular scale gas probes, Carbon, 85 (2015) 429-442.

[37] K.M. Steel, W.J. Koros, An investigation of the effects of pyrolysis parameters on gas separation properties of carbon materials, Carbon, 43 (2005) 1843-1856.

[38] V.C. Geiszler, W.J. Koros, Effects of polyimide pyrolysis conditions on carbon molecular sieve membrane properties, Ind. Eng. Chem. Res., 35 (1996) 2999-3003.

[39] V.C. Geiszler, Polyimide precursors for carbon molecular sieve membranes., in, University of Texas at Austin, 1997.

[40] M. Kiyono, P.J. Williams, W.J. Koros, Effect of pyrolysis atmosphere on separation performance of carbon molecular sieve membranes, J. Membr. Sci., 359 (2010) 2-10.

[41] M. Kiyono, Carbon molecular sieve membranes for natural gas separations, in, Georgia Institute of Technology, Atlanta, Georgia, 2010.

[42] M. Rungta, C. Zhang, W.J. Koros, L. Xu, Membrane-based ethylene/ethane separation: The upper bound and beyond, AlChE J., 59 (2013) 3475-3489.

[43] J. Petersen, Masaji Matsuda, K. Haraya, Capillary carbon molecular sieve membraens derived from Kapton for high temperature gas separation, J. Membr. Sci., 131 (1997) 85-94.

[44] A. Singh-Ghosal, W.J. Koros, Air separation properties of flat sheet homogeneous pyrolytic carbon membranes, J. Membr. Sci., 174 (2000) 177-188.

[45] K. Kusakabe, M. Yamamoto, S. Morooka, Gas permeation and micropore structure of carbon molecular sieving membranes modified by oxidation, J. Membr. Sci., 149 (1998) 59-67.

[46] R. Singh, W.J. Koros, Carbon molecular sieve membrane performance tuning by dual temperature secondary oxygen doping (DTSOD), Journal of Membrane Science, 427 (2013) 472-478.

[47] M.G. Buonomenna, Membrane processes for a sustainable industrial growth, RSC Advances, 3 (2013) 5694.

[48] L.I.B. David, A.F. Ismail, Influence of the thermastabilization process and soak time during pyrolysis process on the polyacrylonitrile carbon membranes for O2/N2 separation, Journal of Membrane Science, 213 (2003) 285-291.

[49] D.Q. Vu, W.J. Koros, S.J. Miller, High pressure CO_2/CH_4 separation using carbon molecular sieve hollow fiber membranes, Ind. Eng. Chem. Res., 41 (2002) 367-380.

[50] S.M. Saufi, A.F. Ismail, Development and characterization of polyacrylonitrile (PAN) based carbon hollow fiber membrane, Songklanakarin J. Sci. Technol., 24(Suppl.) (2002) 843-854.

[51] M. Mulder, Basic principles of membrane technology, second ed., Kluwer Academic Publishers, Dordrecht Netherlands, 1997.

[52] W.J. Koros, Evolving beyond the thermal age of separation processes: Membranes can lead the way, AlChE J., 50 (2004) 2326-2334.

[53] A.L. Hines, R.N. Maddox, Mass Transfer: Fundamentals and Applications, Prentice Hall, Englewood Cliffs, New Jersey, 1985.

[54] W.J. Koros, Membranes: Learning a lesson from nature, Chem. Eng. Prog., 91 (1995) 68-81.

[55] W.J. Koros, G.K. Fleming, Membrane-based gas separation, J. Membr. Sci., 83 (1993) 1-80.

[56] H.F. Mark, Encyclopedia of Polymer Science and Technology, 3rd ed., Wiley-interscience, 2004.

[57] W.J. Koros, Barrier polymers and structures, American Chemical Society, Washington DC, 1990.

[58] M. Rungta, Carbon molecular sieve dense film membranes for ethylene/ethane separations, in, Georgia Institute of Technology, Atlanta, GA, 2012.

[59] Y.D. Chen, R.T. Yang, Preparation of Carbon Molecular Sieve Membrane and Diffusion of Binary Mixtures in the Membrane, Ind. Eng. Chem. Res., 33 (1994) 3146-3153.

[60] K. Wang, H. Suda, K. Haraya, Permeation Time Lag and the Concentration Dependence of the Diffusion Coefficient of CO_2 in a Carbon Molecular Sieve Membrane, Ind. Eng. Chem. Res., 40 (2001) 2942-2946.

[61] J. Su, A.C. Lua, Experimental and theoretical studies on gas permeation through carbon molecular sieve membranes, Sep. Purif. Technol., 69 (2009) 161-167.

[62] S. Lagorsse, Carbon molecular sieve membranesSorption, kinetic and structural characterization, Journal of Membrane Science, 241 (2004) 275-287.

[63] J. Karger, D.M. Ruthven, Diffusion in zeolites and other microporous solids, John Wiley, New York, USA, 1992.

[64] D.W. Breck, Zeolite Molecular Sieves, Structure, Chemistry and Use, John Wiley & Sons, New York, London, Sydney, Toronto, 1974.

[65] G.J. Van Amerongen, The permeability of different rubbers to gases and its relation to diffusivity and solubility, J. Appl.Phys., 17 (1946) 972-985.

[66] S. Glasstone, K.J. Laidler, H. Eyring, The Theory of Rate Processes, 1st ed., McGraw-Hill Book Co., Inc., New York, 1941.

[67] A. Singh, W.J. Koros, Significance of entropic selectivity for advanced gas separation membranes, Ind. Eng. Chem. Res., 35 (1996) 1231-1234.

CHAPTER 3

MATERIALS AND EXPERIMENTAL PROCEDURES

3.1 Overview

This chapter provides a description of the materials and experimental methods used in this study. Section 3.2 discusses the polymers and gases used for membrane formation and testing. The membrane fabrication methods for both polymeric and carbon molecular sieve (CMS) membranes in the morphologies of dense films as well as hollow fibers are provided in section 3.3. Section 3.4 presents the various characterization techniques and equipment.

3.2 Materials

3.2.1 Polymers

In this study, two dianhydride monomers and four diamine monomers were investigated to consider CMS precursors that have not been studied previously. 4,4′-(hexafluoroisopropylidene) diphthalic anhydride (6FDA), 3,3′,4,4′-biphenyltetracarboxylic dianhydride (BPDA), 3,5-diaminobenzoic acid (DABA), 4,4′-oxydianiline (ODA), and 1,5-diaminonaphthalene (1,5-ND) were purchased from Sigma Aldrich. Diethyltoluenediamine (DETDA) was purchased from Albemarle Corporation under the listing name of Ethacure 100. All monomers were used without further purification, and were stored in high vacuum prior to use in synthesis.

Table 3.1 shows the structures of the four 6FDA-based polyimides used in this study, all of which were synthesized in-house.

Table 3.1 – Chemical structures of the polyimides discussed in this study

Polymer	Chemical structure
6FDA/DETDA	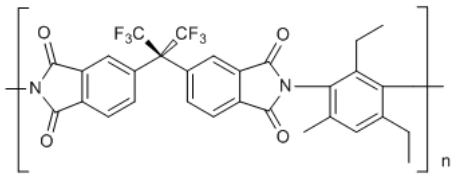
6FDA:BPDA(1:1)/DETDA	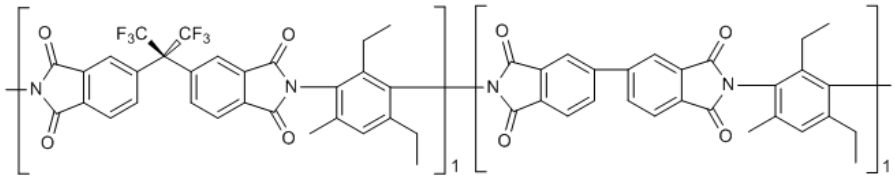
6FDA/DETDA:DABA(3:2)	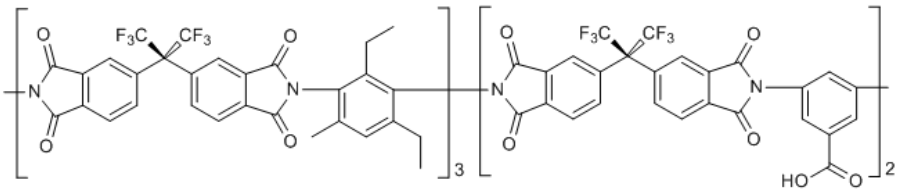
6FDA/1,5-ND:ODA(1;1)	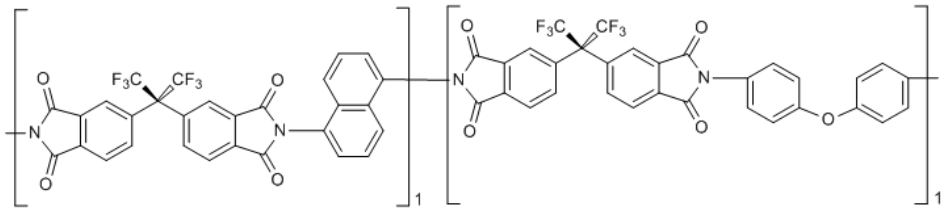

A great deal of prior work has been done by researchers on the synthesis of polyimides. The most widely practiced procedure is a two-step polyamic acid (PAA) process. This process was pioneered by workers at Dupont in 1950's and remains the primary route [1]. Another synthesis method is commonly referred to as "one step high temperature solution polymerization" as reported by McGrath et al. [2-4]. In this study, the synthesis of all polyimides follows the two-step method, as Figure 3.1 illustrates for the 6FDA/DETDA:DABA(3:2) case [5]. The detailed synthesis procedure is provided in Appendix A. In the first step, stoichiometric amounts of dianhydride and diamine monomers were dissolved in NMP (N-Methyl-2-pyrrolidone), forming a 20 wt% solution. Under N_2 purging and stirring, a high molecular weight polyamic acid was produced after 24 hours at low temperature (~5 ^{o}C), and in the second step, the imide ring was closed by releasing water molecules. In this study, chemical imidization was pursued with the presence of beta picoline (9.6g/0.1mol 6FDA) as a catalyst, and acetic anhydride (96g/0.1mol 6FDA) as a dehydrating agent at ambient temperature for 24 hours. Polycondensation reactions are sensitive to water, so to ensure minimal moisture exposure, all reactants and solvents were dried before synthesis. The resulting polyimide was phase separated and washed in methanol, and the polyimide powder was finally dried at 210 ^{o}C under vacuum for 24 hours.

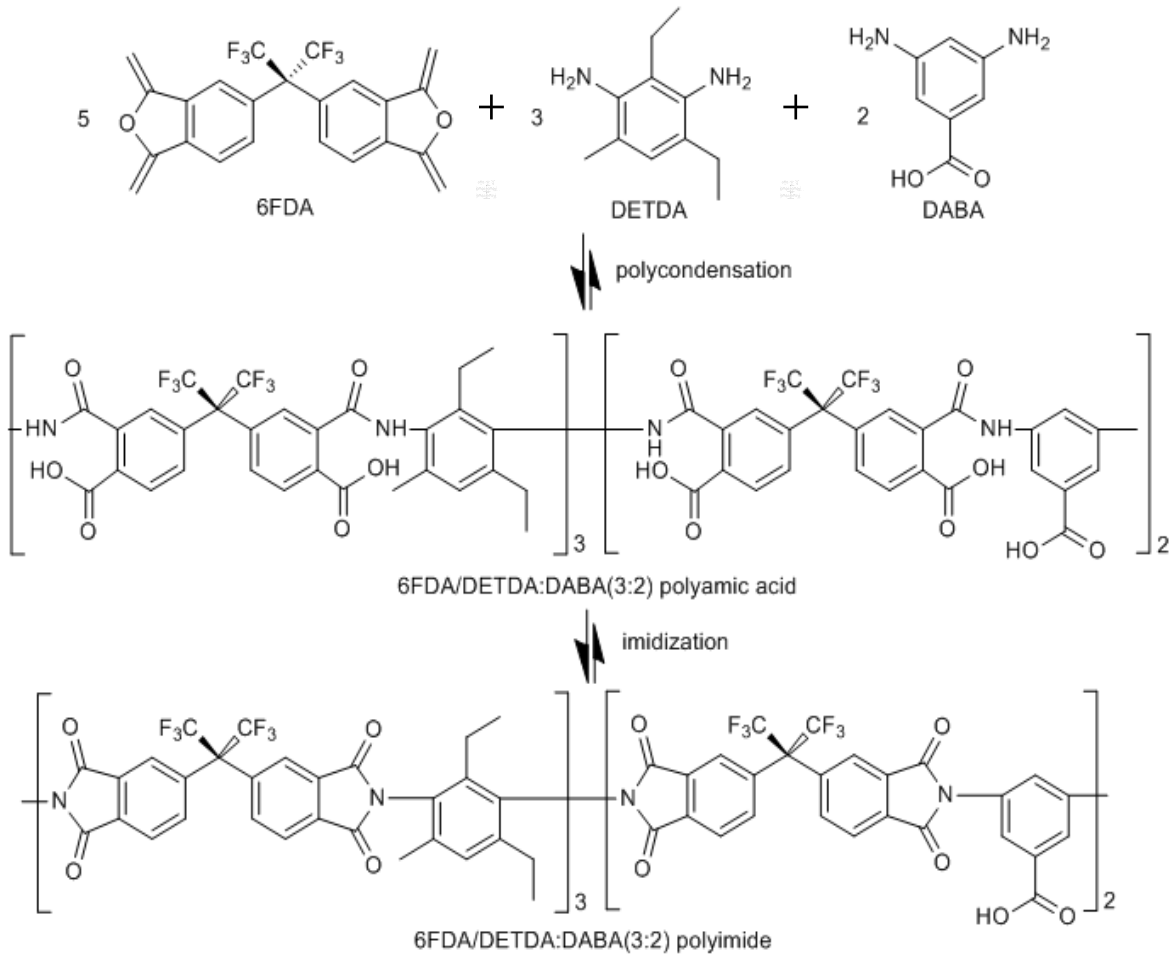

Figure 3.1: Reaction scheme for 6FDA/DETDA:DABA(3:2) synthesis [5].

3.2.2 Solvents and non-solvents

For dense film formation, solvents of tetrahydrofuran (THF) and N-Methyl-2-pyrrolidone (NMP) were purchased from Sigma Aldrich. For asymmetric hollow fiber formation, chemicals of ethanol and lithium nitrate ($LiNO_3$) were purchased from Sigma Aldrich. Solvent exchange agents of methanol and hexane were purchased from VWR.

3.2.3 Gases

In this study, all pure gases including: CO_2, CH_4, O_2, and N_2 for permeation and sorption tests, and argon for pyrolysis, were purchased from Airgas with purity higher than 99.97%. Mixture gases including: 50% CO_2/50% CH_4 and 50% C_3H_6/50% C_3H_8 for permeation tests, and "ppm" levels of O_2 (30ppm and 50 ppm) with balanced argon were purchased from NexAir.

The molecular size of penetrants is usually represented by kinetic diameters, which based on the minimum equilibrium cross-sectional diameters, or the collision diameters calculated from Lennard-Jones potential. For light gases including CO_2, CH_4, O_2, and N_2, kinetic diameters are more often used and are listed in Table 3.2; however, for higher hydrocarbons like C_3H_6 and C_3H_8, the kinetic diameter may no longer provide a reasonable estimation, thus the Lennard-Jones diameter are used and listed in Table 3.2. The critical temperatures of these gases are also shown in Table 3.2 [6-8].

Table 3.2: Molecular size and critical temperatures of gases studied.

Gases	Diameter(Å)	Critical temperature (K)
CO_2	3.30	304
CH_4	3.80	191
O_2	3.46	155
N_2	3.64	126
C_3H_6	4.68	365
C_3H_8	5.06	370

3.3 Membrane formation

The formation of CMS membranes requires two steps: 1) formation of the polymeric membranes; 2) pyrolysis of the polymeric membranes formed from step 1.

This section describes the procedure to prepare dense film and asymmetric hollow fiber polymeric membranes as well as the corresponding resulting CMS membranes.

3.3.1 Formation of polymeric membranes

3.3.1.1 Formation of homogeneous dense film membranes

Before dissolving in a specific casting solvent to form a 3-5wt% polymer solution, the polymer powder was first dried in a vacuum oven for at least 12 hours at 120 ℃ to remove moisture. The solution, contained in a 40 ml ICHEM vial (Fisher Scientific), was then placed on a roller for about 6 hours to form a homogeneous solution. The choice of solvents was based on the solubility of different polyimides, i.e. a relatively more volatile solvent, THF, is preferred for polyimides 6FDA/DETDA, 6FDA:BPDA(1:1)/DETDA and 6FDA/DETDA:DABA(3:2) in which they can be easily solubilized. Since 6FDA/1,5-ND:ODA (1:1) was not soluble in THF, NMP was chosen as the solvent for this polymer. Our preliminary work (as shown in Appendix B) confirmed that precursor films cast from different solvents gave CMS membranes with essentially equivalent gas separation performance, since essentially all solvent is removed during the film-formation and subsequent pyrolysis processes.

The polymer precursor dense films were prepared from a homogeneous solution in a Teflon® casting dish based on a previously reported method as shown in Figure 3.2 [9]. For polymer solutions using THF, the film casting was completed inside a glovebag (Cole Parmer) kept in a fume hood. Inside the glovebag there were: the polymer solution contained in a vial, a leveled stage to ensure a flat and uniform surface, a Teflon® disk to serve as casting substrate, a 30 ml syringe with a Millex®-RH 0.45 micro PTFE filter

(Millipore Corporation), a crystallization dish (VWR), and two jars containing THF. The glovebag was then sealed and purged with nitrogen. After 3 hours of THF saturation time, the polymer solution was then transferred from the vial to the syringe and slowly pushed through the filter onto the Teflon® disk. Afterwards, the Teflon® disk was covered with the crystallization dish to ensure a 3-5 days slow evaporation rate. For polymer solutions with NMP, a hot plate with moderate temperature of 50 ^{o}C was used to accelerate the evaporation process, while avoiding curling due to excessively fast evaporation rate.

The dense film was subsequently annealed at a temperature above the boiling point of the solvent to further remove any residual solvent. The annealing temperatures used for dense films cast from solvents THF and NMP were both set as 210 ℃ for consistency.

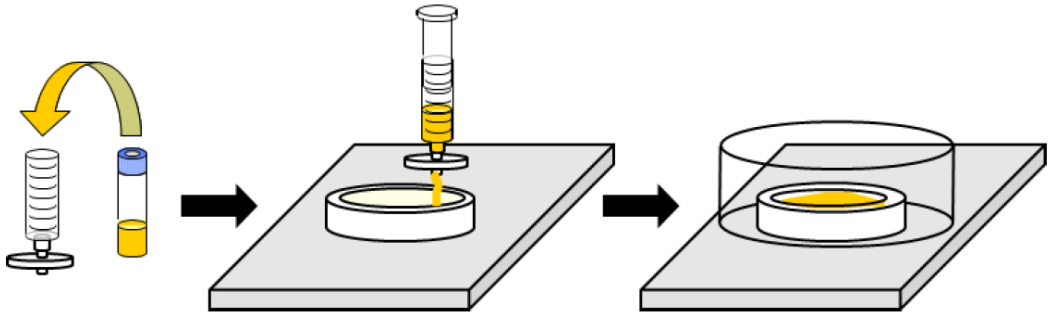

Figure 3.2: Schematic showing the solution-casting method for dense film preparation [9].

3.3.1.2 Formation of asymmetric hollow fiber membranes

a. Dope formulation

The polymer solution used for hollow fiber formation is often referred to as a "dope". A dope typically consists of the polymer, solvents and non-solvents. NMP was

chosen as the non-volatile solvent because it dissolves many of the polyimides and is relatively environmentally friendly. THF was chosen as the volatile solvent to assist skin layer formation. Ethanol was used as a non-solvent to bring the polymer solution close to the two phase region on a ternary phase diagram, shown in Figure 3.3, to promote phase separation. Moreover, the high volatility of ethanol can also assist the formation of skin layer within the air gap. Additives such as lithium nitrate ($LiNO_3$) were sometimes used to enhance viscosity, phase separation, and pore formation. Figure 3.4 shows the ternary phase diagram of polymer 6FDA/DETDA:DABA(3:2), one of the polymers of interest in this study. Figure 3.4 is the base of our hollow fiber study, which will be discussed in detail in Chapter 7.

A suitable dope composition has been proven to be crucial for the solution spinning process [10-12]. High enough viscosity is the first important factor for a successful spinning. Thus, a polymer with sufficiently high molecular weight or a dope with sufficient high polymer concentration should be controlled. A suitable ratio of solvents to non-solvents should also be adjusted. The binodal line was determined via a cloud point technique [13]. At a fixed polymer concentration, a series of dope samples with increasing non-solvent to solvent ratio were prepared. At a certain point, referred to as “cloud point”, the dope becomes cloudy since as the concentration of non-solvent increases, the dope changes from one-phase into two-phase. Cloud points under different polymer concentration together form the binodal line. A good dope composition should be in the one-phase region but close enough to the binodal line as shown in Figure 3.3.

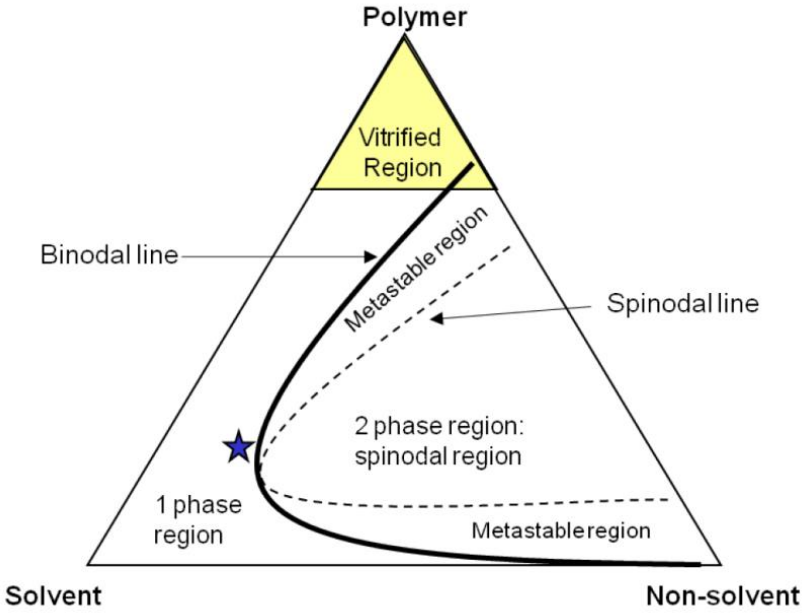

Figure 3.3: Ternary phase diagrams of polymer, solvents, and non-solvents. The star marks a desired dope composition [14].

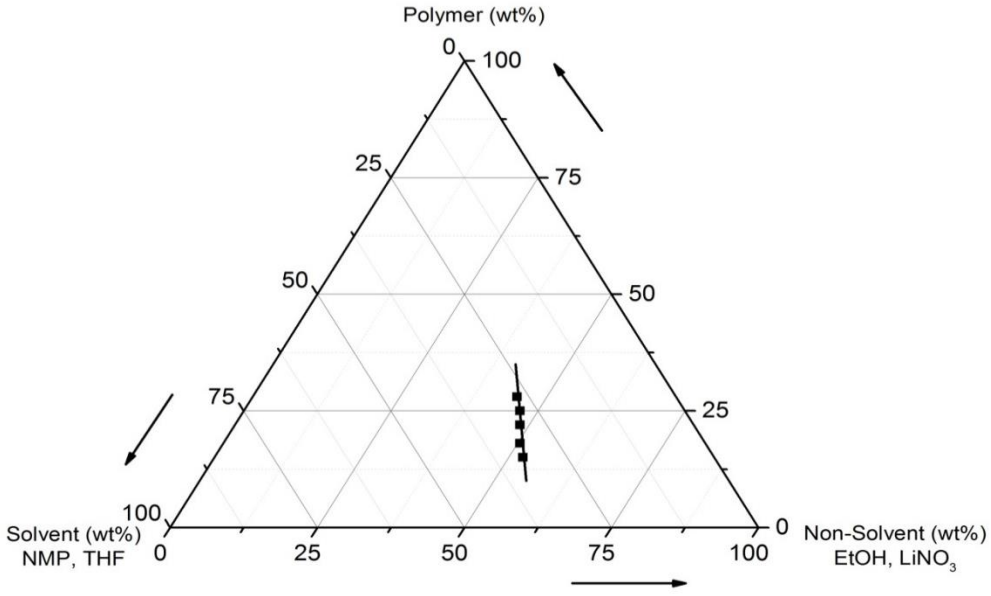

Figure 3.4: Ternary phase diagrams of 6FDA/DETDA:DABA(3:2), solvents, and non-solvents.

b. Asymmetric hollow fiber spinning

A dry-jet/wet-quench spinning process was used to spin hollow fibers, and a schematic of this technique is depicted in Figure 3.5 [15]. The polymer powder was first dried in a vacuum oven for at least 12 hours at 120 ℃ to remove moisture and residual organics. The dope, contained in a Qorpak® glass bottle sealed with a Teflon® cap, was placed on the roller for 2-4 weeks until homogeneous dope was obtained. Afterwards, the dope was loaded into a 500 ml syringe pump (ISCO Inc. Lincoln, NE) and degassed overnight. Bore fluid was loaded into another 100 ml syringe pump. The dope and the bore fluid were co-extruded through a spinneret with in-line filtrations between the pumps and the spinneret. The temperature of the spinneret, dope line, and dope pump were carefully controlled by thermocouples. The co-extruded dope, along with bore fluid, passed through an air gap and was immersed into a water quench bath. The phase-separated fiber line was collected on a 0.32 m diameter rotating polyethylene drum with a Teflon® guide. After being collected, the fibers were rinsed in water baths at least three times during 48 hours. The fibers were then solvent exchanged with three separate 20 min methanol baths followed by three separate 20 min hexane baths and finally dried under vacuum at 75 ^{o}C for about 3 hours.

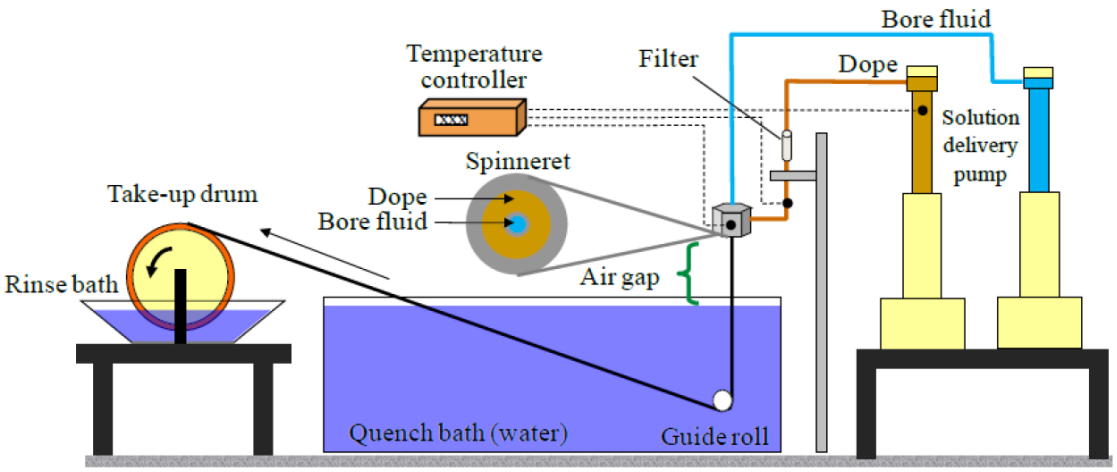

Figure 3.5: A dry-jet/wet-quench spinning process for hollow fiber spinning [15, 16].

3.3.2 Formation of CMS membranes

3.3.2.1 Pyrolysis set up

CMS dense films were formed by pyrolyzing the corresponding precursor polymer films in a pyrolysis set-up updated from a previous reported apparatus, as shown in Figure 3.6 [17]. Dried polymer films were cut into small discs, placed on a custom made quartz plate (United Silica Products, Franklin, NJ, USA) with grooves to allow for easy efflux of pyrolysis by-products. The quartz plate is depicted in Figure 3.7. The plate, along with the films, was put into a quartz tube (National Scientific Company, GE Type 214 quartz tubing, Quakertown, PA) before being loaded into a pyrolysis furnace (Thermocraft, Inc., model 23-24-1ZH, Winston-Salem, NC, USA). The quartz tube was sealed on each side with an assembly of metal flanges with silicon O-rings (MTI Corporation, Richmond, CA). An oxygen analyzer (Cambridge Sensotec Ltd., Rapidox 2100 series, Cambridge, England) was integrated into the system to monitor the O_2 cencentration during pyrolysis.

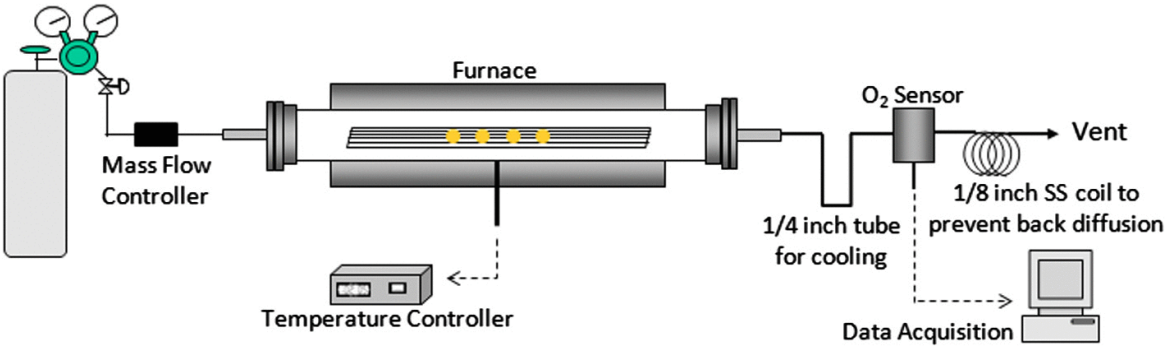

Figure 3.5: Schematic representation of the pyrolysis system used for CMS dense film membranes formation [18].

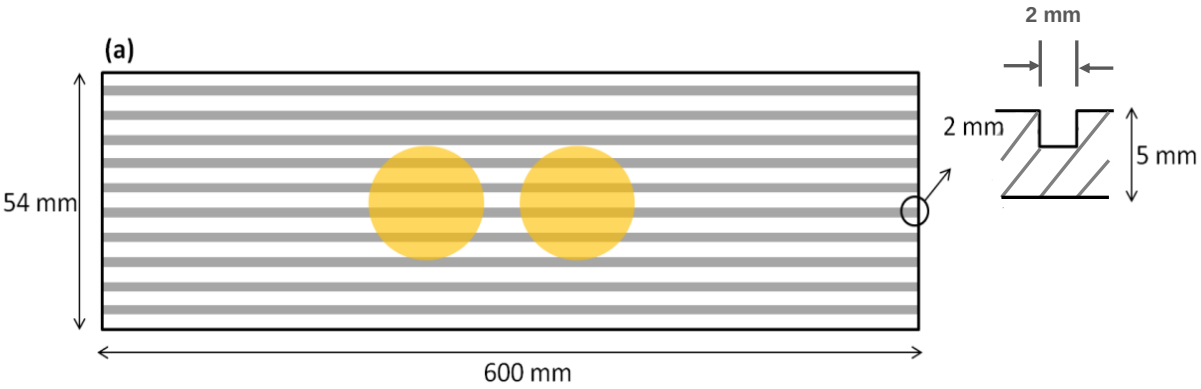

Figure 3.7: Schematic representation of a quartz plate used for CMS dense film membranes formation [18].

On the other hand, CMS hollow fibers were pyrolyzed in a three-zone furnace (Thermocraft, Inc., Model # XST-3-0-24-3C, Winston-Salem, NC) [9] in order to achieve a uniform temperature profile along the length of the hollow fibers. The setup is shown in Figure 3.8. Also, instead of the quartz plate, a stainless steel wire mesh plate (McMaster Carr, Robbinsville, NJ), as shown in Figure 3.9, was chosen for CMS hollow fiber pyrolysis. Stainless steel wires were loosely threaded through openings in the wire mesh plate at several axial positions. When fibers were being pyrolyzed, this design can ensure that the fibers were separate from each other.

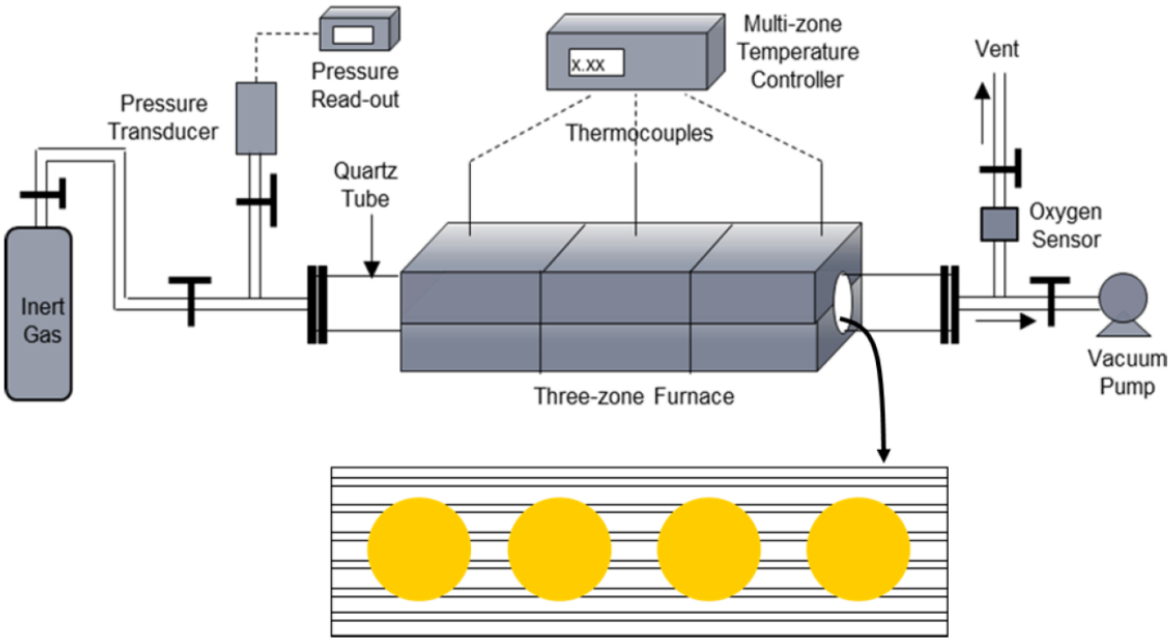

Figure 3.8: Schematic representation of the pyrolysis system used for CMS hollow fiber membranes formation [9].

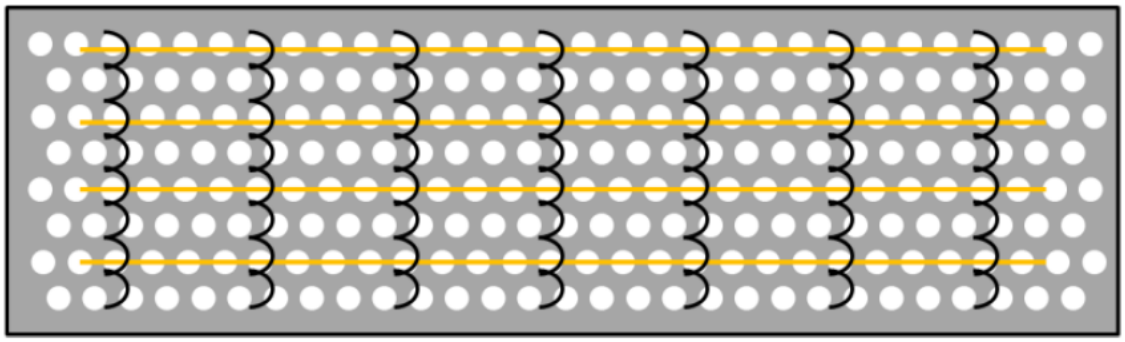

Figure 3.9: Schematic representation of mesh plate used for CMS hollow fiber membranes formation [18].

3.3.2.2 Pyrolysis protocols

Several different pyrolyzing protocols that were used in this study are listed below.

a. Formation of different temperature pyrolyzed CMS dense films

Dense films were pyrolyzed under UHP argon purge at three different final pyrolysis temperatures of 550 ^{o}C, 675 ^{o}C, and 800 ^{o}C. The inert atmosphere was achieved after purging the tube with UHP Argon for at least 12h, and the typical oxygen level was measured to be below 1ppm as sensed by the oxygen analyzer. The oxygen analyzer was typically calibrated with ppm levels of O_2 doped argon mixtures at an interval of 3-6 months. The UHP argon purge was maintained during pyrolysis at 200 scc/min to remove pyrolysis by-products using the heating protocol below:

Protocol 1: for 550 ^{o}C-pyrolyzed CMS membranes:

1) 50-250 ℃ at a ramp rate of 13.3 ℃ /min.
2) 250 ℃-535 ℃ (T_{max} -15) at a ramp rate of 3.85 ℃ /min.
3) 535 ℃-550 ℃ at a ramp rate of 0.25 ℃ /min.
4) Soak for 2 hours at 550 ℃.

Protocol 2: for 675 ^{o}C- and 800 ^{o}C-pyrolyzed CMS membranes:

1) 50-250 ℃ at a ramp rate of 13.3 ℃ /min.
2) 250 ℃-535 ℃ at a ramp rate of 3.85 ℃ /min.
3) 535 ℃-550 ℃ at a ramp rate of 0.25 ℃ /min.
4) 550 ℃-(T_{max} -15) ℃ at a ramp rate of 3.85 ℃ /min.
5) (T_{max} -15) ℃- T_{max} ℃ at a ramp rate of 0.25 ℃ /min.
6) Soak for 2 hours at T_{max} ℃.

b. Formation of different amounts of O_2-doped CMS dense films

All O_2-doped CMS membranes were pyrolyzed with a final temperature of 550 ^{o}C following the temperature protocol 1 listed above. Instead of using continuous pure argon as a purge gas, mixtures of argon and various amounts of oxygen in ppm levels were used. The whole system was purged with the mixture at a flow rate of 200 scc/min for at least 12 hours before each pyrolysis experiment. When this extended purge was not used, scatter between samples was sometimes observed. The oxygen analyzer was used to monitor the oxygen concentration levels.

c. Formation of precrosslinked CMS dense films

All precrosslinked CMS membranes were pyrolyzed with a final temperature of 800 ^{o}C under UHP argon following a temperature protocol 3 listed below:

Protocol 3: for 800 ^{o}C-pyrolyzed and pre-crosslinked CMS membranes:

1) 50-250 ℃ at a ramp rate of 13.3 ℃ /min.
2) 250 ℃-370 ℃ at a ramp rate of 3.85 ℃ /min.
3) Soak for 90 min at 370 ℃.
4) 370 ℃-785 ℃ (T_{max} -15) ℃ at a ramp rate of 3.85 ℃ /min.
5) 785 ℃- 800 ℃ at a ramp rate of 0.25 ℃ /min.
6) Soak for 2 hours at 800 ℃.

When a complete heating cycle was finished, the furnace was allowed to cool down naturally while maintaining UHP argon purging. When temperature dropped below 100 ^{o}C, typically after three hours, the CMS dense films were unloaded from the furnace and loaded into permeation or sorption systems [19]. After each pyrolysis, the quartz plate and quartz tube were rinsed with acetone and baked at 800 ^{o}C with 500 scc/min air flow to burn out residue which could influence subsequent runs.

3.4 Membrane characterization

3.4.1 Permeation

3.4.1.1 Dense film masking

After fabrication, both polymeric and CMS dense films were mounted into a permeation cell to run permeation measurements. The films were first masked by sandwiching between impermeable aluminum tapes with a known area (~1 cm^2) exposed

for permeation. Epoxy was then applied at the interface of the tape and membrane for sealing integrity in the permeation cell. Five minute epoxy (3M, DP-100) worked well for sealing the CMS film and tape interface; however, this epoxy sometimes failed on precursor films, so Duralco 4525 epoxy was used for mounting these films. The film, together with the aluminum tape, was then mounted on a double O-ring flange permeation cell. A typical assembly of the film and the permeation cell is shown in Figure 3.10.

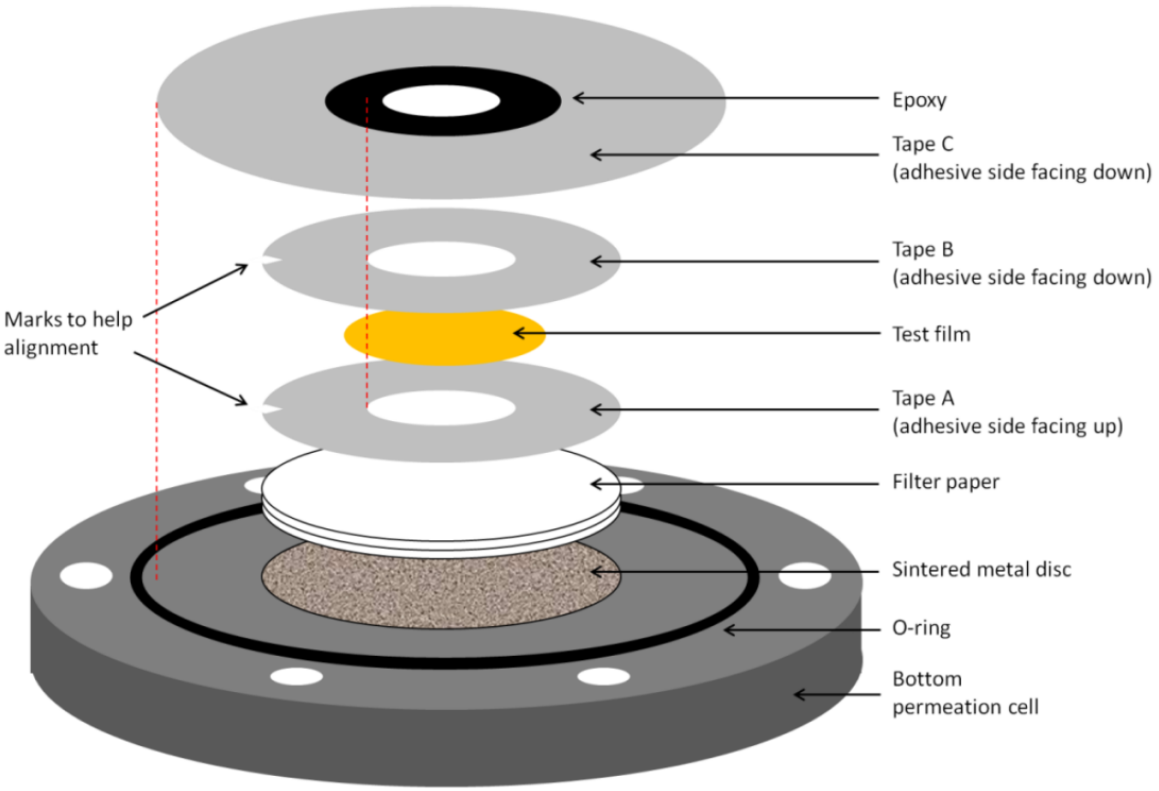

Figure 3.10: Schematic representation of masking a dense film on a permeation cell [20].

3.4.1.2 Hollow fiber module formation

Figure 3.11 represents a typical lab-scale membrane hollow fiber module for permeation tests [21]. Five minute epoxy (3M, DP-100) was used to seal the ends of modules. When testing polymeric hollow fibers, multiple fibers, usually 4 to 6, were required to build up the flux. On the other hand, due to their less flexible nature, single-fiber CMS fiber modules were often prepared for the measurement of carbon fibers.

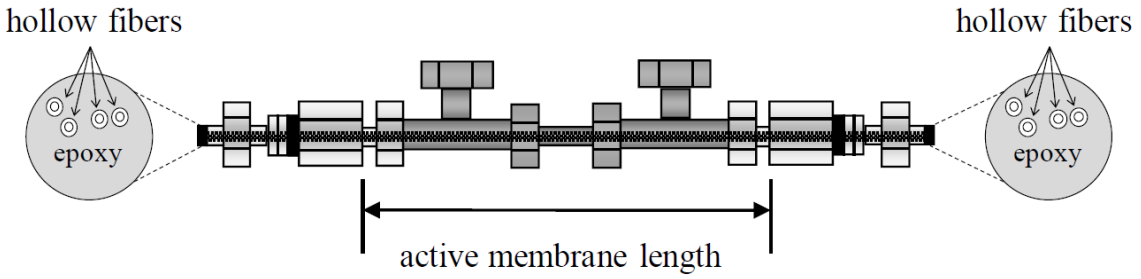

Figure 3.11: Schematic representation of a lab-scale hollow fiber module [21].

3.4.1.3 Constant volume permeation measurement

After formation, the dense film permeation cell or the hollow fiber module was connected into a constant volume permeation box to evaluate the membrane separation properties. Figure 3.12 shows a typical constant volume permeation box with a dense film permeation cell inside. When testing hollow fibers, a “module tree” shown on the right was used by replacing part #12.

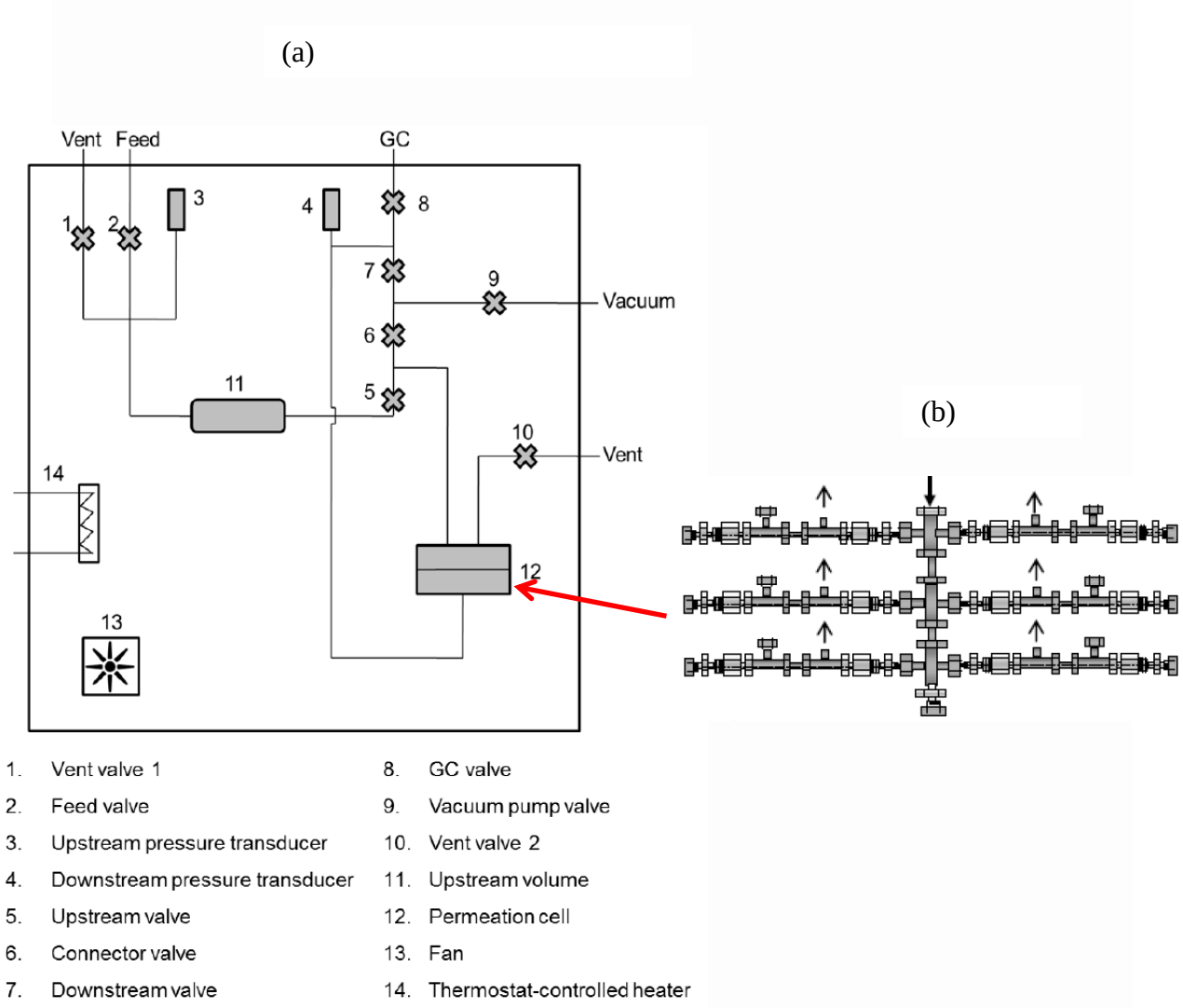

Figure 3.12: Schematic representation of: (a) a constant volume permeation box; (b) a module tree consisting of 6 hollow fiber modules.

Both upstream and downstream cell chambers were typically evacuated for at least six hours and the outgassing rate was less than 1% of the test gas permeate rate. Then the upstream was pressurized on the shell side with the test gas, and the pressure rise in the downstream was recorded using LabView (National Instruments, Austin, TX, USA) until at least 10 times of time lag were reached. If a different testing gas was to be

applied, the whole system was evacuated again until the outgassing rate met the above criteria. Mixed gas permeation experiments were performed with a binary mixture containing 50 mol% CO_2 and 50 mol% CH_4 or 50 mol% C_3H_6 and 50 mol% C_3H_8. Stage cut, referred to as the percentage of feed permeating through the membrane, was controlled by a needle valve and set to be lower than 1% to avoid concentration polarization. Permeate composition was analyzed using a gas chromatograph, as described earlier [19]. At least two replicate runs were made for each measurement. Results reported in this study represent the average with variance within 10%.

Permeability of dense films was calculated using the following equation:

$$P = \frac{1.77*10^6*(\frac{dp}{dt})*V*l}{T*A*\Delta p} \tag{3.1}$$

where P is the permeability with a unit of Barrer, $1.77*10^6$ accounts for the conversion of units; $\frac{dp}{dt}$ is the downstream pressure changing rate recorded from the Labview with a unit of torr/s; V is the downstream volume in cm^3; l is the membrane thickness in units of mils; T in K is the absolute testing temperature inside the permeation box; A is the exposed area of the membrane in cm^2, and Δp is the testing pressure in psia.

Permeance of hollow fiber membranes was calculated based on the following equation:

$$\frac{P}{l} = \frac{2.46*10^7*(\frac{dp}{dt})*V}{T*OD*L*n*\Delta p} \tag{3.2}$$

where $\frac{P}{l}$ is the permeance with a unit of GPU; $2.46*10^7$ considers the unit conversion, OD is the outer diameter of fibers; L is the active fiber length and n is the number of fibers inside the module. V is the downstream volume in cm^3; T in K is the absolute testing temperature inside the permeation box; and Δp is the testing pressure in psia.

3.4.2 Sorption

Sorption was studied using a pressure decay sorption system, as shown in Figure 3.13 [22], with samples held in a porous stainless steel filter holder (0.5μm, Swagelok). The entire system was degassed overnight, and to start a run, the reservoir cell was filled with a known amount of sorption gas and equilibrated thermally for 10 to 15 minutes. The valve between the reservoir and sample cell was then opened to charge the sample cell with gas, and LabView recorded the pressure decay in both cells. When the pressure reached equilibrium (typically 10 times of the sorption time lag was waited), the run was stopped and the amount of sorbed gas was calculated based on a mole balance [22].

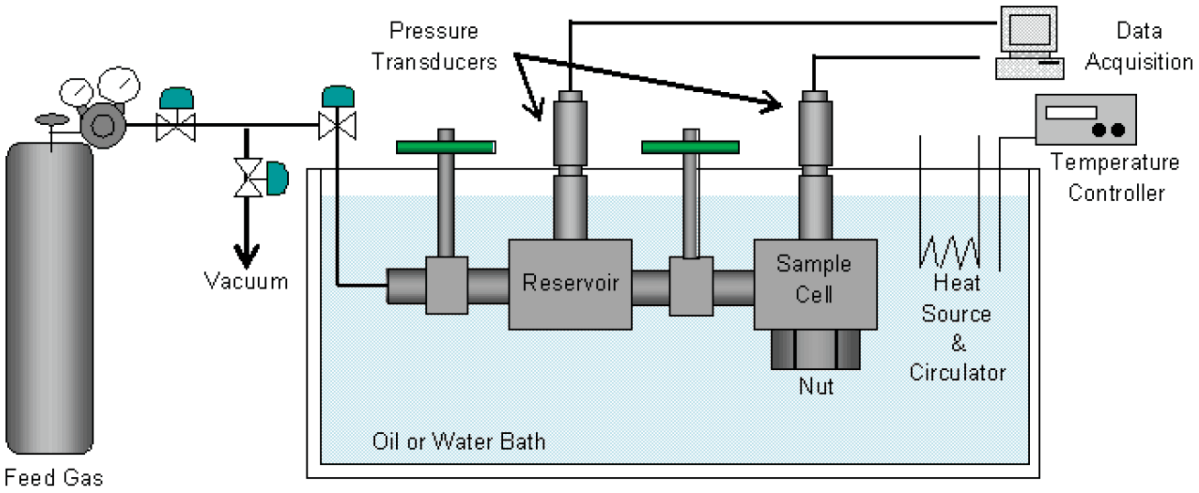

Figure 3.13: Schematic representation of the pressure decay sorption system.

3.4.3 Other characterization techniques

3.4.3.1 FTIR

Fourier transform infrared spectroscopy (FTIR) was done using a Bruker Tensor 27 FTIR spectrometer. For polymer powder, a Harrick MVP2 micro ATR with 512 scans was used.

3.4.3.2 TGA

Thermal stability and polymer degradation during the heating were investigated using a thermogravimetric analysis (TGA: Q5000, TA Instrument) under N_2 inert atmosphere at a heating rate of 10 ℃/min. The maximum temperature was 900 ℃.

3.4.3.3 DSC

Differential scanning calorimetry (DSC) was applied to measure the glass-rubber transition temperature of polymers. A TA Q200 instrument was used. The heating and cooling rates were 10 ^{o}C /min. The sample was first heated to 420 ^{o}C (a temperature beyond its expected glass transition temperature but below its decomposition temperature determined from TGA) and then cooled down to -50 ^{o}C before another heating cycle was done. The double heating cycle eliminated the effects of heat history of the materials. The transition temperature was taken to be the inflection point of the change in the heat flow during the second heating cycle.

3.4.3.4 XRD

Wide-angle X-ray diffraction (WAXD) was applied to study the average d-spacing in both polymeric and CMS materials. A Phillips Panalytical X-ray diffractometer with a CuKα radiation of wavelength 1.54 Å was used. The measurement angle ranged from 5-50 degree. Bragg's law $d=\lambda/2\sin\theta$ can be applied here.

3.4.3.5 SEM

A high resolution scanning electron microscope (Zeiss Ultra FE-SEM) was used to examine the geometry and morphology of pristine and pyrolyzed fiber membranes. Pristine fiber samples, soft in nature, were soaked in hexane and then shear fractured in liquid nitrogen to help maintain the morphology in the cross section area. CMS fiber samples, on the other hand, hard and brittle, were directly shear fractured.

3.4.3.6 Density column

Density is another important physical property of polymers. In this study, a density gradient column (Model DC-4, Techne, New Jersey) was used to measure the polymer density. The column was prepared with calcium nitrate ($Ca(NO_3)_2$) solution. First of all, two solutions were prepared, one with a density 10% below the lowest density required and the other one having a density 10% above the highest density required. Then the two solutions were degased and filled into the density column. Column filling is a critical step in order to get a linear gradient column. A density gradient column filler (V2.9, H&D Fitzgerald Ltd.), which can accurately control the flowrates of two inlet solutions, was applied to fill in the low density and high density $Ca(NO_3)_2$ solutions. After the solutions being stabilized overnight, calibrated density standards, in the form of glass floats, were introduced into the column and a graph of position against density can be plotted. Finally, both polymer and CMS samples were wetted and submerged into the column. The sample descended until reaching the level where the density of the liquid was equal to that of the sample's. From the measurement of height, the sample density can be read off from the graph. All measurements were conducted at 23 ^{o}C.

Appendix C shows the densities of the polymeric and CMS membranes investigated in this study. As for CMS samples, uncertainty may exist in the tested

density since water vapor may sorb from the aqueous salt bath. To assess the potential impact of this hypothetical effect, separate moisture vapor sorption studies were done, and uptake at the approximate moisture activity were assessed. For this study, corrections due to this possible second order effect were estimated, but adjustments to apparent densities were not attempted. This issue is under detailed study by Graham Wenz and Yu-han Chu and will be reported in their dissertations

3.4.3.7 CO_2 uptake measurement

The surface area and pore distributions of CMS membranes were achieved based on the CO_2 sorption uptakes analyzed with a Micromeritics ASAP 2020 Accelerated Surface Area and Porosimetry System. Density functional theory was used to analyze the CO2 adsorption isotherms in order to characterize the micropore distribution of the CMS materials [23, 24]..

3.5 References

[1] C.E. Sroog, A.L. Endrey, S.V. Abramo, C.E. Berr, W.M. Edwards, K.L. Olivier, Aromatic polypyromellitimides from aromatic polyamic acids, J. Polym. Sci. Polym. Chem. Ed., 34 (1996) 2069-2086.

[2] C.A. Arnold, J.D. Summers, Y.P. Chen, R.H. Bott, D. Chen, J.E. McGrath, Structure-property behaviour of soluble polyimide-polydimethylsiloxane segmented copolymers, Polymer, 30 (1989) 986-995.

[3] T.M. Moy, C.D. DePorter, J.E. McGrath, Synthesis of soluble polyimides and functionalized imide oligomers via solution imidization of aromatic diester-diacids and aromatic diamines, Polymer, 34 (1993) 819-824.

[4] A.E. Eichstadt, T.C. Ward, M.D. Bagwell, I.V. Farr, D.L. Dunson, J.E. McGrath, Synthesis and Characterization of Amorphous Partially Aliphatic Polyimide Copolymers Based on Bisphenol-A Dianhydride, Macromolecules, 35 (2002) 7561-7568.

[5] S. Fu, E.S. Sanders, S.S. Kulkarni, W.J. Koros, Carbon molecular sieve membrane structure–property relationships for four novel 6FDA based polyimide precursors, J. Membr. Sci., 487 (2015) 60-73.

[6] D.W. Breck, Zeolite Molecular Sieves, Structure, Chemistry and Use, John Wiley & Sons, New York, London, Sydney, Toronto, 1974.

[7] D.R. Lide, Handbook of Chemistry and Physics, 71st ed., CRC Press, Boca Raton, FL, 1980.

[8] R.L. Burns, W.J. Koros, Defining the challenges for C3H6/C3H8 separation using polymeric membranes, J. Membr. Sci., 211 (2003) 299-309.

[9] M. Rungta, Carbon molecular sieve dense film membranes for ethylene/ethane separations, in, Georgia Institute of Technology, Atlanta, GA, 2012.

[10] C.-C. Chen, W. Qiu, S.J. Miller, W.J. Koros, Plasticization-resistant hollow fiber membranes for CO_2/CH_4 separation based on a thermally crosslinkable polyimide, J. Membr. Sci., 382 (2011) 212-221.

[11] I.C. Omole, S.J. Miller, W.J. Koros, Increased Molecular Weight of a Cross-Linkable Polyimide for Spinning Plasticization Resistant Hollow Fiber Membranes, Macromolecules, 41 (2008) 6367-6375.

[12] D.T. Clausi, W.J. Koros, Formation of defect-free polyimide hollow fiber membranes for gas separations, J. Membr. Sci., 167 (2000) 79-89.

[13] M.R. Kosuri, W.J. Koros, Defect-free asymmetric hollow fiber membranes from Torlon®, a polyamide–imide polymer, for high-pressure CO2 separations, Journal of Membrane Science, 320 (2008) 65-72.

[14] M. Kiyono, Carbon molecular sieve membranes for natural gas separations, in, Georgia Institute of Technology, Atlanta, Georgia, 2010.

[15] C. Zhang, Zeolitic imidazolate framework (ZIF)-based membranes and sorbens for advanced olefin/paraffin separations, in, Georgia Institute of Technology, 2014.

[16] N. Bhuwania, Engineering the morphology of carbon molecular sieve (CMS) hollow fiber membranes, in, Georgia Institute of Technology, 2013.

[17] M. Kiyono, P.J. Williams, W.J. Koros, Effect of pyrolysis atmosphere on separation performance of carbon molecular sieve membranes, J. Membr. Sci., 359 (2010) 2-10.

[18] X. Ning, W.J. Koros, Carbon molecular sieve membranes derived from Matrimid® polyimide for nitrogen/methane separation, Carbon, 66 (2014) 511-522.

[19] L. Xu, M. Rungta, J. Hessler, W. Qiu, M. Brayden, M. Martinez, G. Barbay, W.J. Koros, Physical aging in carbon molecular sieve membranes, Carbon, 80 (2014) 155-166.

[20] X. Ning, Carbon molecualr sieve membranes for nitrogen/methane separation, in, Georgia Institute of Technology, 2014.

[21] L. Xu, Carbon molecular sieve hollow fiber membranes for olefin/paraffin separations, in, Georgia Institute of Technology, 2012.

[22] W.J. Koros, D.R. Paul, Design considerations for measurement of gas sorption in polymers by pressure decay, J. Polym. Sci. Polym. Phys. Ed., 14 (1976) 1903-1907.

[23] K.M. Steel, W.J. Koros, Investigation of porosity of carbon materials and related effects on gas separation properties, Carbon, 41 (2003) 253-266.

[24] M. Rungta, L. Xu, W.J. Koros, Structure–performance characterization for carbon molecular sieve membranes using molecular scale gas probes, Carbon, 85 (2015) 429-442.

CHAPTER 4

CHARACTERIZATION OF POLYMER PRECURSORS AND ANALYSIS OF DIFFERENT POLYMERS AS PRECURSORS FOR CARBON MOLECULAR SIEVE (CMS) DENSE FILM MEMBRANES

4.1 Overview

Ultimate CMS properties are strongly influenced by polymer precursor properties. This chapter focuses on the objective 1 of this thesis to consider the separation performance of CMS membranes formed by pyrolysis under argon at 550 ^{o}C for four novel polyimide precursors referred to as 6FDA/DETDA, 6FDA:BPDA(1:1)/DETDA, 6FDA/DETDA:DABA(3:2) and 6FDA/1,5-ND:ODA(1:1). Section 4.2 discusses the characterization of these four polymer precursors. Separation performances of polymeric and CMS dense film membranes formed from these polymers were examined using pure gases CO_2, CH_4, O_2 and N_2 in sections 4.3 and 4.4 respectively. Section 4.4 also assesses the effects of physical aging on the separation performance of CMS membranes, and considers a practical method to suppress physical aging.

4.2 Polymer precursors for CMS membranes fabrication

4.2.1 Polymers

Table 3.1, shows here again to facilitate discussion, shows the structures of the four 6FDA-based polyimides used in this study, all of which were synthesized in-house following the procedure discussed in section 3.2.1. The inhibited chain packing introduced by the bulky 6F group provides high free volume and promotes increased solubility to enable facile processing and high permeability in the precursor polymers and resultant CMS materials [1]. Extensive earlier work on 6FDA-DAM, 6FDA:BPDA/DAM, and 6FDA/DAM:DABA CMS films [2-6] showed DAM to be useful in forming high-performance CMS films; however DETDA, resulting from replacement of two methyl groups in DAM by two ethyl groups, has not been studied previously for CMS applications. Thus, including 6FDA/DETDA, 6FDA:BPDA(1:1)/DETDA, and 6FDA/DETDA:DABA(3:2) in this work provides a systematic analogy between DAM- vs. DETDA-based membranes to explore effects of the ethyl vs. methyl substituents. Also, 1,5-ND, due to its rigid structure, has attracted attention in the area of polymer film study for H_2/CH_4 separation [7, 8]; however, it also had not been explored previously in CMS applications. A 1,5-ND copolymer membrane was expected to be highly permeable due to the chain packing inhibition effect, thereby leading to highly permeable CMS materials. Prior studies have shown that BPDA-ODA derived CMS membranes displayed attractive size distinguishing performance for CO_2/CH_4, C_2H_4/C_2H_6 and C_3H_6/C_3H_8 [9, 10]; therefore, including polymer 6FDA/1,5ND:ODA (1:1), which contains the packing favoring ODA unit with the packing disruptive 1-5ND unit, seemed like a useful strategy to potentially provide both high selectivity and high permeability.

Table 3.1 – Chemical structures of the polyimides discussed in this study

Polymer	Chemical structure
6FDA/DETDA	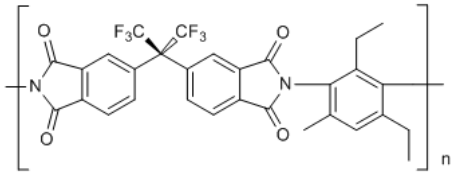
6FDA:BPDA(1:1)/DETDA	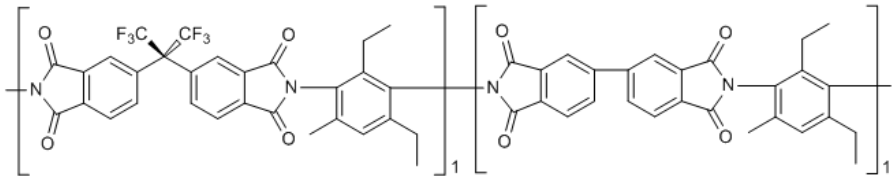
6FDA/DETDA:DABA(3:2)	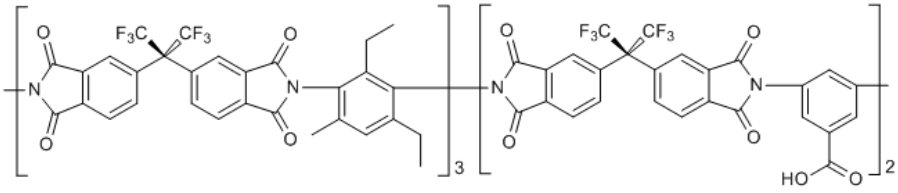
6FDA/1,5-ND:ODA(1;1)	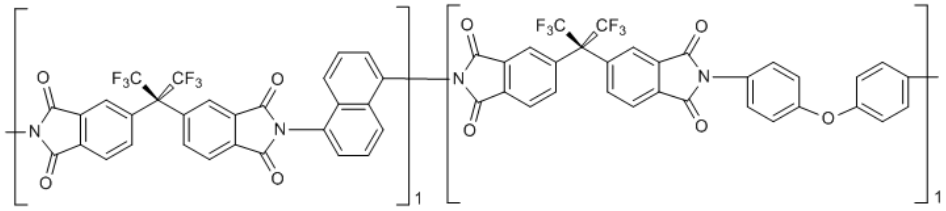

4.2.2 Polymer characterizations

The four polyimide precursors: 6FDA/DETDA, 6FDA:BPDA(1:1)/DETDA, 6FDA/DETDA:DABA(3:2) and 6FDA/1,5-ND:ODA(1:1) were characterized using various techniques including: Gel Permeation Chromatography (GPC) (The GPC tests were done by Dr. Park Doh-Yeon in Professor Beckham's Group in Georgia Institute of Technology), Fourier Transform Infrared Spectroscopy (FTIR), Thermogravimetric Analysis (TGA), Differential Scanning Calorimetry (DSC), and Wide-angle X-ray Diffraction (WAXD).

4.2.2.1 ATR-IR

ATR-IR was used to confirm the imidization of polyamic acid and to determine the chemical structures of the 4 polymers, as shown in Figure 4.1.

Amide groups in polyamic acids have characteristic peaks at 1660 cm^{-1} and 1550 cm^{-1} corresponding to the carbonyl (CONH) and C-NH groups. After the imidization step, the peak at 1550 cm^{-1} disappeared as N-H group disappeared. In the meantime, the absorption band at 1660 cm^{-1} transformed into two characteristic bands at 1780 cm^{-1} and 1730 $cm^{-1}$of the imide C=O stretching linkage. These peaks clearly indicated the existence of imide groups and confirmed the success of imidization process.

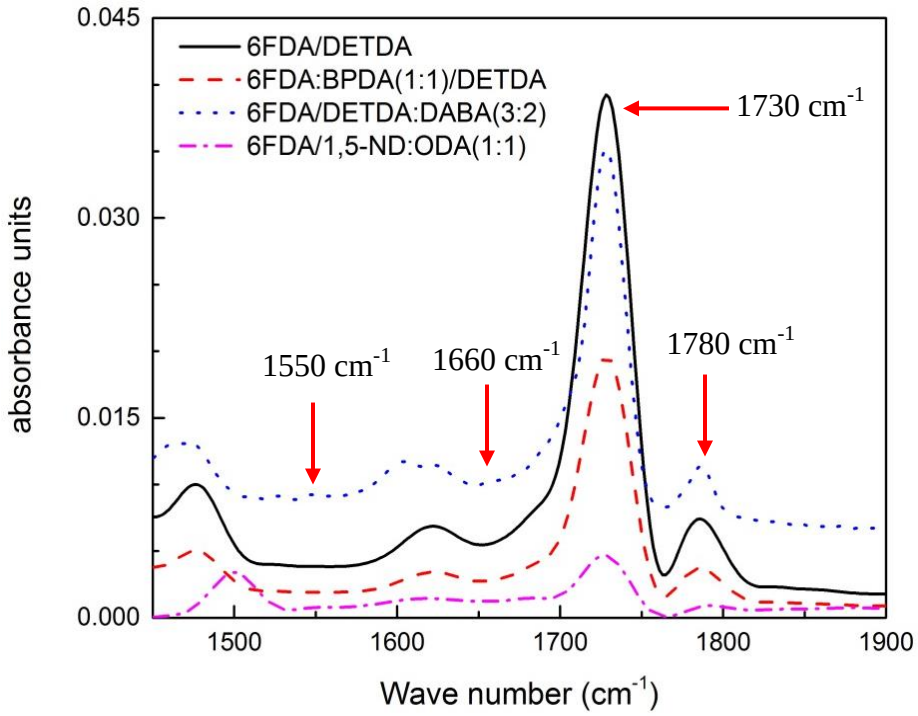

Figure 4.1: ATR-IR spectrum of polymers: 6FDA/DETDA, 6FDA:BPDA(1:1)/DETDA, 6FDA/DETDA:DABA(3:2), and 6FDA/1,5-ND:ODA(1:1).

Figure 4.2 shows the IR spectrum of 6FDA/DETDA:DABA(3:2) and 6FDA/DETDA as well as 6FDA/DAM:DABA(3:2), which has been reported previously [6], in the region of wave number between 2000 cm^{-1} to 4000 cm^{-1}. The broad weak absorption peak at 3200 to 3500 cm^{-1}, which can only be observed in 6FDA/DETDA:DABA(3:2) and 6FDA/DAM:DABA(3:2), is attributed to the vibration band of –OH in DABA moiety [6]. This peak proves the existence of –OH group in the 6FDA/DETDA:DABA(3:2) polymer, which may provide potential crosslinking sites during the pyrolysis step.

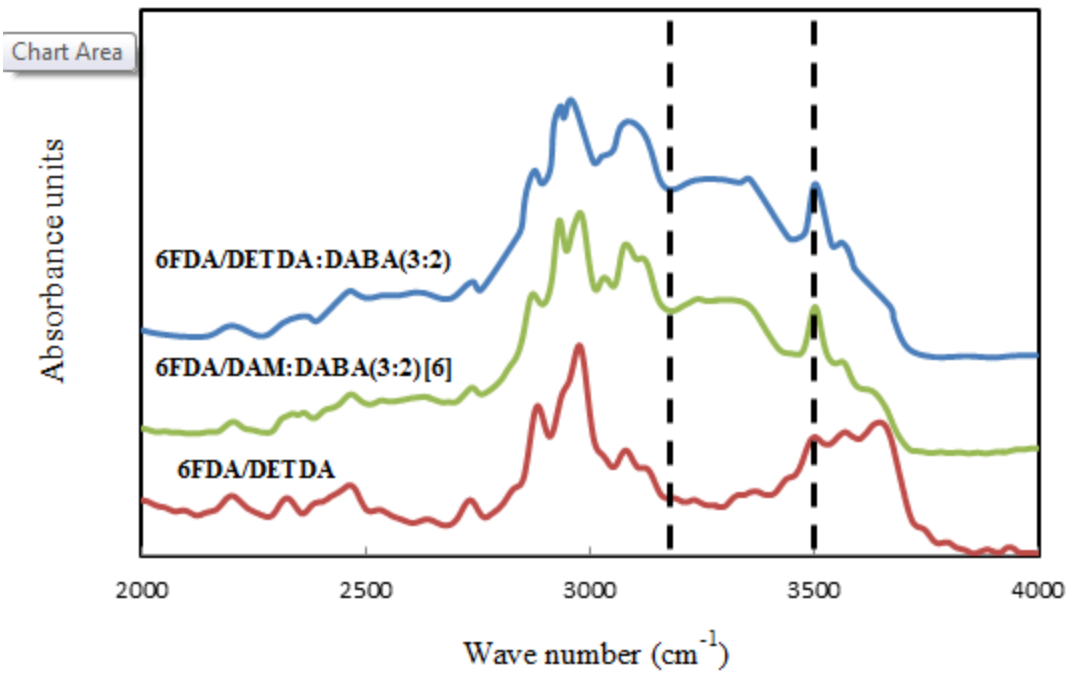

Figure 4.2: ATR-IR spectrum of 6FDA/DETDA:DABA(3:2) and 6FDA/DETDA in the region of wave number between 2000 cm^{-1} to 4000 cm^{-1}.

4.2.2.2 TGA

The TGA thermal decomposition behaviors and weight variations of the 4 polymers during heating are shown in Figure 4.3. The TGA results show that except for polymer 6FDA/DETDA:DABA(3:2), from room temperature to about 400 ^{o}C, the other 3 polymers lost only 2% of their original weight, presumably mainly due to the removal of small amounts of water vapor and/or residual solvent [11]. For 6FDA/DETDA:DABA(3:2) polymer, a larger abrupt weight drop was observed at around 400 ^{o}C. Qiu et al. have demonstrated a weight loss occurs from 350 ^{o}C to 500 ^{o}C in a related DABA-containing polymer 6FDA/DAM:DABA(3:2) [5, 12]. The weight drop is

believed to be decarboxylation of –COOH group in the DABA unit, which ultimately leads to crosslinking. Above 490 ^{o}C, polymer backbones begin to degrade, with differing amounts of weight losses for four polymers. The degradation temperatures T_d (defined here for convenience to be the temperature where 5% of the original weight has lost) and the final percent weight loss of the four polymers are listed in Table 4.1, along with other physical properties that will be discussed in the following sections. Inspection of Figure 4.3 shows that 6FDA/1,5-ND:ODA(1:1) exhibited the highest thermal stability (T_d=520 ^{o}C) and 6FDA: BPDA(1:1)/DETDA the highest residual weight percent (58%).

It is noted that there is an alternative way to determine the T_d of the polymer 6FDA/DETDA:DABA(3:2) as the temperature where 5% of the residue weight after decarboxylation has lost. Nevertheless, it is believed that this T_d reflects a new materials, referred to as precrosslinked-6FDA/DETDA:DABA(3:2), of which the T_g and T_d is not of concern in the scope of this work. For consistency, the T_d reported in Table 4.1 is based on the first method defined in the previous paragraph.

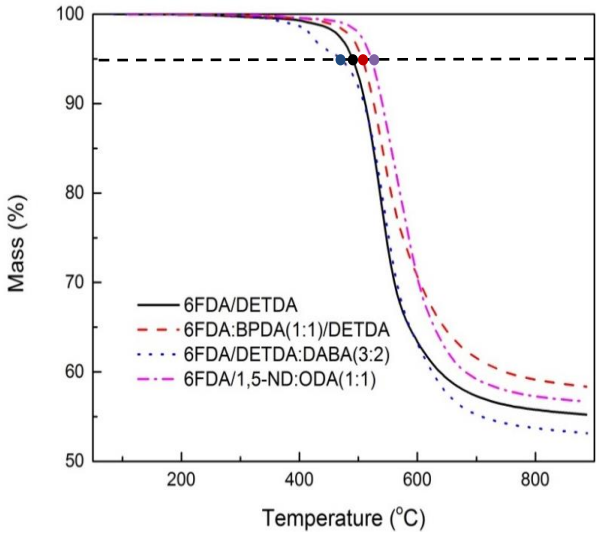

Figure 4.3: Thermal degradation of polymers: 6FDA/DETDA, 6FDA:BPDA(1:1)/DETDA, 6FDA/DETDA:DABA(3:2), and 6FDA/1,5-ND:ODA(1:1).

Table 4.1: Physical properties of the polyimide polymers.

Polymer	Weight loss %	T_d (^oC)	T_g(^oC)	$\Delta = T_d - T_g$ (^oC)
6FDA/DETDA	45	495	378	117
6FDA:BPDA(1:1)/DETDA	42	505	401	104
6FDA/DETDA:DABA(3:2)	47	470	388	82
6FDA/1,5-ND:ODA(1:1)	43	520	356	164
6FDA:BPDA/DAM	-	492	424	68 [13]

Polymer	Mw (kDa)	PDI	d-spacing (Å)	Density (g/cm^3)	FFV
6FDA/DETDA	~77	2.5	6.6	1.3126	0.174
6FDA:BPDA(1:1)/DETDA	~93	2.1	6.9	1.2319	0.182
6FDA/DETDA:DABA(3:2)	~ 95	2.3	6.1	1.3764	0.169
6FDA/1,5-ND:ODA(1:1)	-	-	5.8	1.4471	0.147

4.2.2.3 DSC

Differential Scanning calorimetry (DSC) was applied to measure the glass transition temperature (T_g) of polymers, which is related to polymer chain flexibility, polarity and packing. In general, higher T_g tends to indicate higher backbone rigidity. Figure 4.4 shows the DSC thermograms of the four polyimides and the T_gs are listed in Table 4.1.

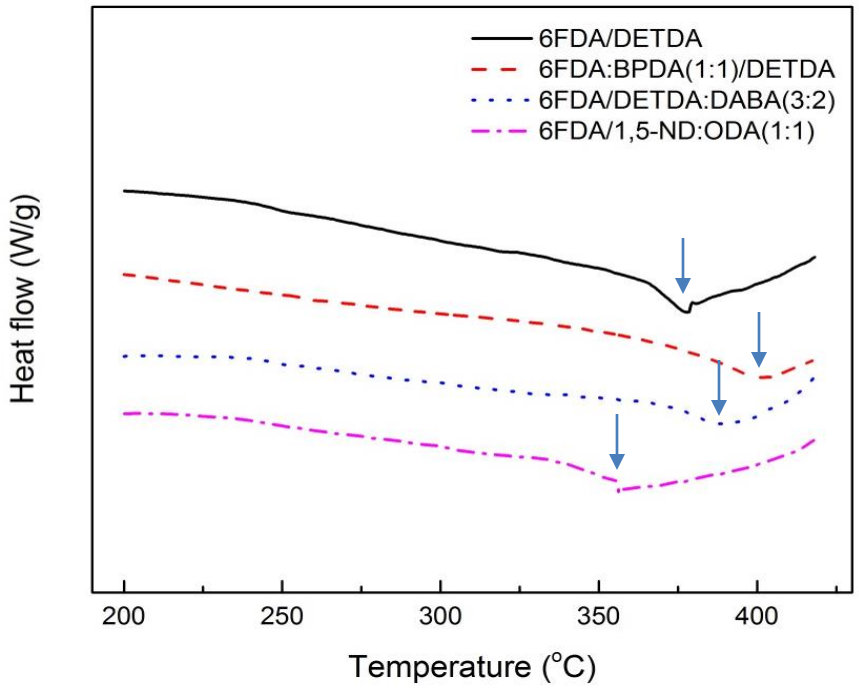

Figure 4.4: DSC thermograms of polymers: 6FDA/DETDA, 6FDA:BPDA(1:1)/DETDA, 6FDA/DETDA:DABA(3:2), and 6FDA/1,5-ND:ODA(1:1).

Defect-free hollow fibers with high gas permeability and selectivity must ultimately be spun for practical CMS membranes applications. Unfortunately, some undesirable fiber substructure collapse can occur between T_g and T_d, which can cause increased separation layer thickness and decreased permeance [13]. On this basis, polymers with smaller Δ in Table 4.1, defined as the difference between T_d and T_g, are attractive as CMS precursors. For example, the well-studied hollow fiber precursor 6FDA:BPDA/DAM has a Δ=68 ^{o}C [13]. From this perspective, without considering the intrinsic permeability and selectivity, 6FDA/DETDA: DABA(3:2) with Δ=82 ^{o}C is the best choice for hollow fiber formation and 6FDA/1,5-ND:ODA(1:1) is the least favored

among the polymers of this study. Fortunately, as will be shown later, when the intrinsic properties of the CMS are considered, the 6FDA/DETDA:DABA(3:2) also emerges as the most promising of the four precursors, a fortunate coincidence.

4.2.2.4 XRD

Wide-angle X-ray diffraction (WAXD) was used to study the average d-spacing in both polymeric and CMS membranes. As noted earlier, the d-spacing reflects the average spacing between chain segment centers in the molecular matrix. The results roughly reflect interchain spacing if one applies Bragg's law, $d=\lambda/2\sin\theta$, where d is the d-spacing, and λ is the wavelength that has been applied in the XRD equipment (here for CuKα 1.54Å). The broad WAXD patterns in Figure 4.5 verify the amorphous nature of the CMS.

Table 4.1 summarizes d-spacing values of the precursor polymers films of 6FDA/DETDA, 6FDA:BPDA(1:1)/DETDA, 6FDA/DETDA:DABA(3:2) and 6FDA/1, 5-ND: ODA(1:1). The d-spacing values of the resulting CMS films, although cannot be explicitly calculated from WAXD because of their amorphous nature, still can be observed to be smaller than those of their precursor polymers.

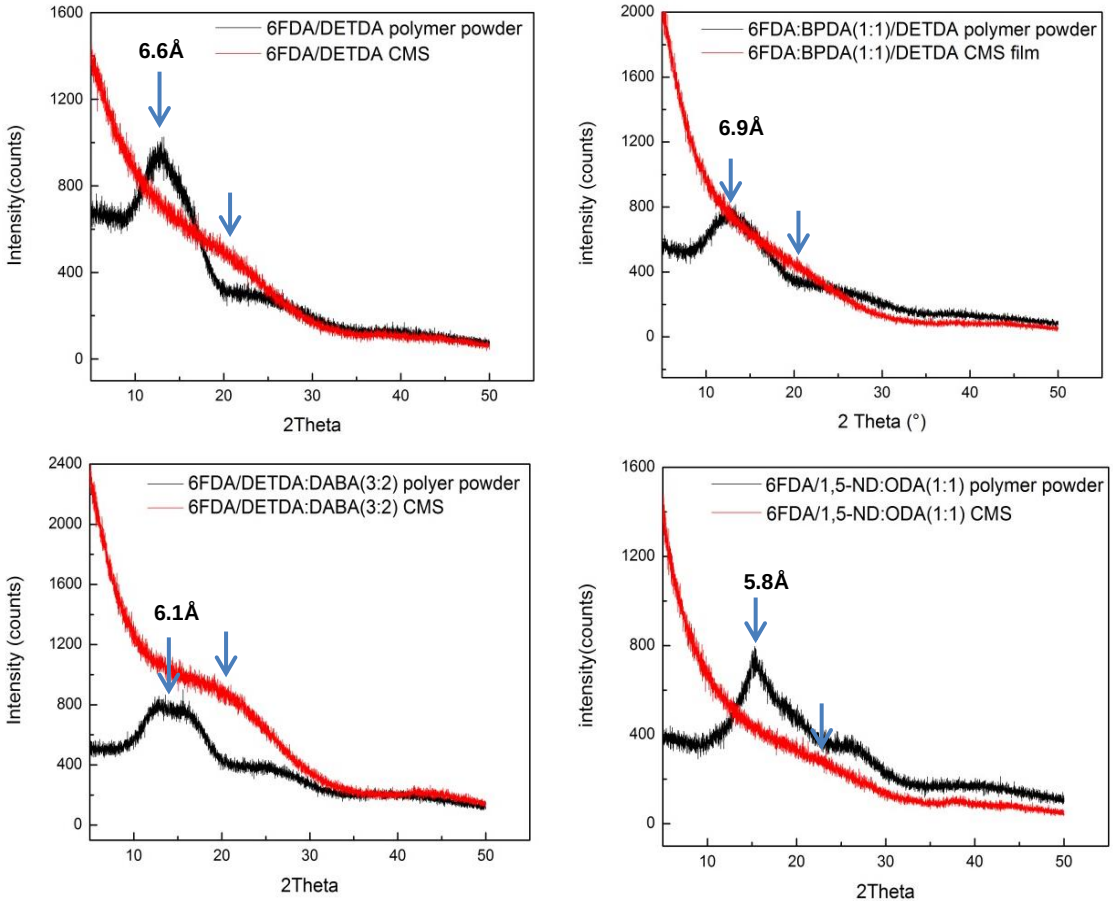

Figure 4.5: WAXD of polymer powder and CMS dense films derived from polymers: 6FDA/DETDA, 6FDA:BPDA(1:1)/DETDA, 6FDA/DETDA:DABA(3:2), and 6FDA/1,5-ND:ODA(1:1).

4.2.2.5 Density and FFV of polymeric membranes

The density values of the four polymeric films are listed in Table 4.1. Density values of the polymeric films varied between 1.2319g/cm^3 for 6FDA:BPDA(1:1)/DETDA to 1.4471g/cm^3 for 6FDA/1,5-ND:ODA(1:1).

For polymer precursors, the concept of fractional free volume (FFV) is helpful for correlation and prediction of transport properties. FFV is defined as Eq. 4.1:

$$FFV = (V - V_o)/V \tag{4.1}$$

in which, V is the specific volume of the polymer (defined as volume per repeat unit in this study), so:

$$V = \frac{M}{\rho} \tag{4.2}$$

here, M is the molecular weight of a repeat unit, ρ is the measured density listed above, and V_o is the volume occupied by the polymer chains. Bondi's group contribution method is commonly used to estimate V_o with the following equation:

$$V_o = 1.3\sum_{K=1}^{K}(V_W)_K \tag{4.3}$$

V_W represents the van der Waals volume for each group, and K represents the total number of groups into which the repeat functioning groups the polymer is divided. In this study, the density and the V_W of each group, estimated by the method of Park and Paul [14], were used to calculate the fractional free volume, FFV. These FFV values are summarized in Table 4.1 with other properties of the polymers. In a later section, the relationship between polymer FFV and gas permeability will be discussed in detail. As noted with respect to the lack of correlation of d-spacing with CMS transport properties, FFV is not expected to be as useful for correlating CMS transport properties as it is for polymers, since it does not probe the most important morphological features. Moreover, the estimation of V_o is not currently possible since the detailed natures of CMS structural components are complex and still somewhat ambiguous.

4.3 Pure gas separation performance of the precursor polyimide dense film membranes

Precursor polyimide dense film membranes derived from 6FDA/DETDA, 6FDA:BPDA(1:1)/DETDA, 6FDA/DETDA:DABA(3:2) and 6FDA/1,5-ND:ODA(1:1) were fabricated following the solution-casting method described in section 3.3.1. The permeability and selectivity for pure gas pairs CO_2/CH_4 and O_2/N_2 of these polymeric membranes were examined at 35 ^oC and 30 psia using equipment described previously [15].

Table 4.2 below summarizes the different gas permeation and separation properties of the four polyimide membranes synthesized here. Since polymeric membranes are not the focus of this work, only one sample of 6FDA/DETDA, 6FDA:BPDA(1:1)/DETDA, and 6FDA/1,5-ND:ODA(1:1) polymeric membranes were tested. We did replicated tests on 6FDA/DETDA:DABA(3:2) polymeric membranes and the uncertainty of the results are listed in Table 4.2. As can be seen, all the uncertainties were subtle. It is clear that in all cases, as with most glassy polymers, the permeability decreases in the following order:

$$CO_2\ (3.3\ Å) > O_2\ (3.46\ Å) > N_2\ (3.64\ Å) > CH_4\ (3.8\ Å)$$

The numbers in parenthesis are the kinetic diameters of the gases [16] and permeability decreases as the gas kinetic diameters increase, so the polymeric films in this study clearly have size discriminating capabilities. Unlike CMS materials, FFV and chain rigidity in the polymer membrane affect the permeability of penetrants and size sieving capabilities. Figure 4.6 shows the relation between gas permeability and the reciprocal of FFV of each polyimide. The CO_2, O_2, N_2, and CH_4 permeabilities of polymer films all decrease as the FFV of the polymer decreases. For example, 6FDA:BPDA(1:1)/DETDA,

as shown in Table 4.1 has the highest FFV and the highest permeability for all four pure gases, while 6FDA/1,5-ND:ODA(1:1), with the lowest FFV, has the lowest permeability for all gases. On the other hand, CO_2/CH_4 and O_2/N_2 ideal selectivity follow the opposite order apparent for permeability, i.e. polymers with lower FFV show higher selectivity for both gas pairs. Figure 4.7, which plots data vs. T_g of the various precursors also shows a correlation, although the opposite trend is seen for the 1/FFV relationship in Figure 4.6.

.

Table 4.2: Pure gas permeation and separation properties of polyimide membranes (measured at 35°C, 30 psia).

Polymer	**Permeability (Barrer)**				**Selectivity**	
	CO_2	**CH_4**	**O_2**	**N_2**	**CO_2/CH_4**	**O_2/N_2**
6FDA/DETDA	354	19	76	22	18.6	3.5
6FDA:BPDA(1:1)/DETDA	560	34	107	35	16.2	3.1
6FDA/DETDA:DABA(3:2)	238±13	11±1	54±4	16±1	22.0±2	3.5±0.4
6FDA/1,5-ND:ODA(1:1)	45	1	11	2	45.0	5.5

1 Barrer [=] $10^{-10}\ \frac{cc(STP)*cm}{cm^2*s*cmHg}$

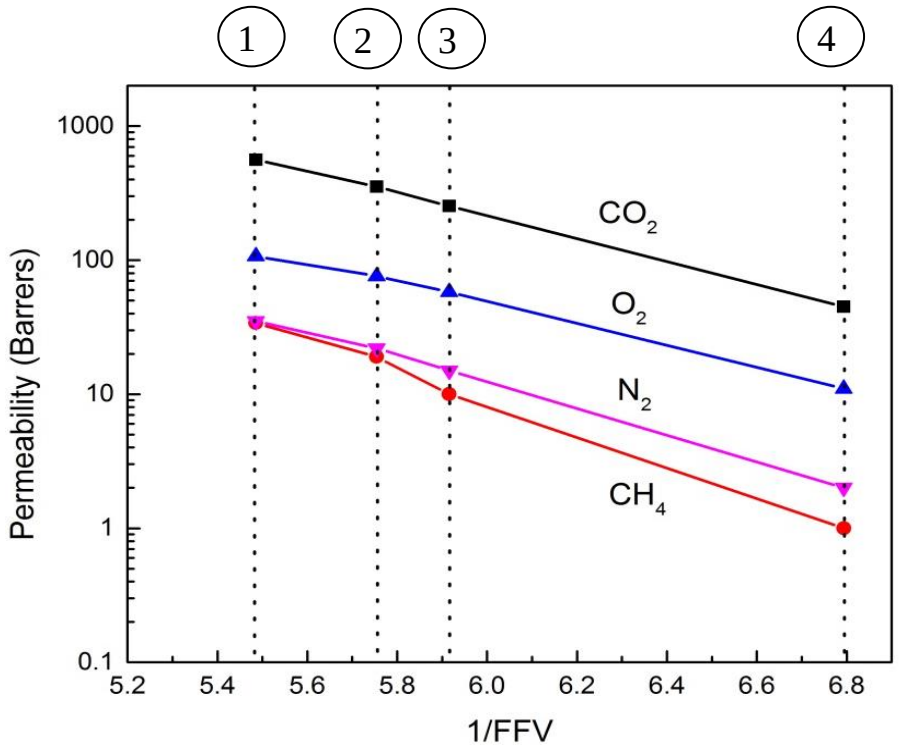

Figure 4.6: Pure gas permeability of polymeric films as a function of their reciprocal FFV. Numbers on top of the figure each represents one polymer. 1: 6FDA:BPDA(1:1)/DETDA; 2: 6FDA/DETDA; 3: 6FDA/DETDA:DABA(3:2); 4: 6FDA/1,5-ND:ODA(1:1). Permeabilities were measured at 35 ^{o}C with a feed pressure of 30 psia.

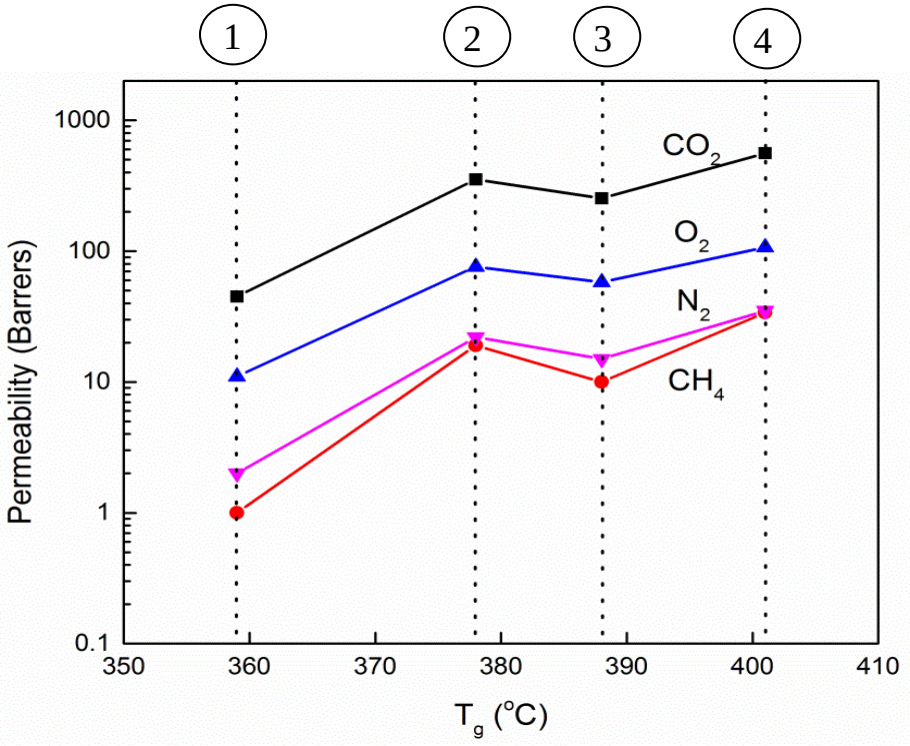

Figure 4.7: Pure gas permeability of polymeric films as a function of their glass transition temperatures T_g. Numbers on top of the figure each represents one polymer. 1: 6FDA/1,5-ND:ODA(1:1); 2: 6FDA/DETDA; 3: 6FDA/DETDA:DABA(3:2); 4: 6FDA:BPDA(1:1)/DETDA. Permeabilities were measured at 35 ^{o}C with a feed pressure of 30 psia.

4.4 Pure gas separation performance of the CMS dense film membranes

For this preliminary investigation, all CMS membranes were pyrolyzed up to 550 ^{o}C in ultra-high purity argon following the protocol 1 listed in section 3.3.2.2. Permeability and selectivity for pure gas pairs CO_2/CH_4 and O_2/N_2 of CMS membranes

derived from 6FDA/DETDA, 6FDA:BPDA(1:1)/DETDA, 6FDA/DETDA:DABA(3:2) and 6FDA/1,5-ND:ODA(1:1) were examined. Testing for CMS films was conducted one day after the films being pyrolyzed.

4.4.1 Physical aging study of pure gases permeation for four CMS materials

As noted in Chapter 2, contrary to simple polymers, with diffusional jumps moderated by segmental motions, in CMS material, conventional properties such as FFV are less useful for understanding transport property differences. Prior to discussing and interpreting the observed trends for the CMS materials, another important concept, "physical aging" is needed to avoid confounding the discussion. "Physical aging" refers to changes in the physical properties of a non-equilibrium glassy material as it approaches equilibrium via structural relaxation [17, 18]. Such aging results from a gradual decrease in sample volume and, even in simpler glassy polymers, leads to lower permeability and higher selectivity versus time. Recent studies found that the separation performance of amorphous CMS films derived from glassy polymer precursors showed time dependence and exhibited somewhat similar physical aging phenomenon to that seen in glassy polymers [19]. Unlike simple glassy polymers, glassy carbons do not have well-defined glass transitions. This important distinction means that, once formed, a glassy carbon cannot be rejuvenated by heating above T_g as can be done for simple glassy polymers [20].

In this study, four pure gases: CO_2, CH_4, O_2 and N_2 were used to probe the changes in transport properties of CMS membranes over time. The permeability and selectivity for CO_2/CH_4 and O_2/N_2 of 550 ^oC pyrolyzed CMS dense films derived from all four polymers were tested under 35 ^oC with feed pressure of 30 psia during a month of time and the membranes were stored *under vacuum* during the testing intervals inside the

sorption cell to avoid any artificial errors from mounting or processing. Vacuum storage is the most rigorous aging mode based on prior studies [19]. Figures 4.8-4.11 show the time dependence of gas permeability and selectivity.

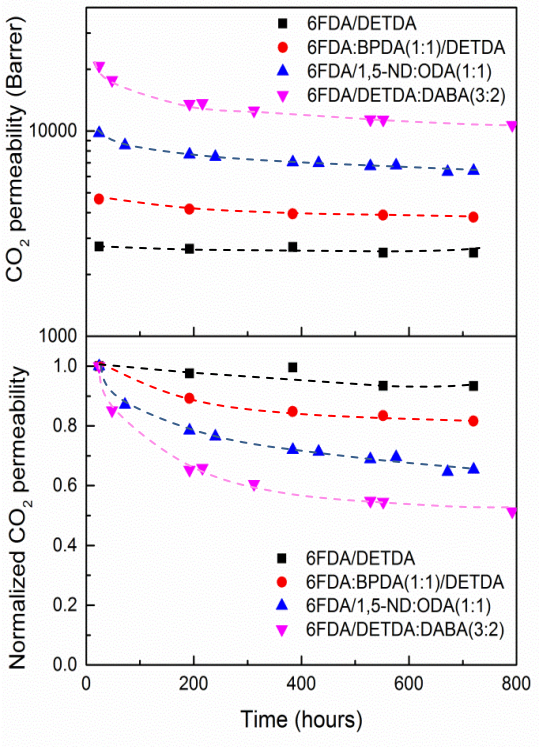

Figure 4.8: Pure gas aging study of CMS films pyrolyzed at 550 ^{o}C: CO_2 permeability changes (35 ^{o}C with a feed pressure of 30 psia, and membranes stored in vacuum). The lines are added to aid the reader's eye.

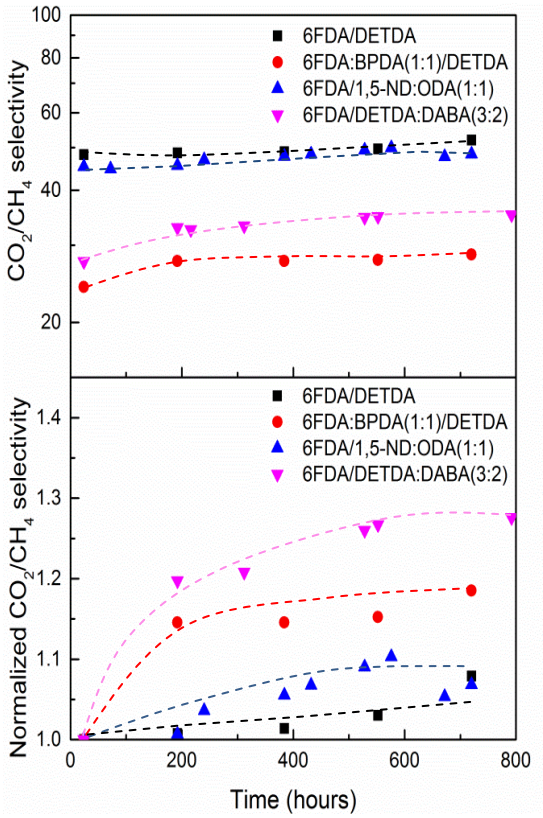

Figure 4.9: Pure gas aging study of CMS films pyrolyzed at 550 ^{o}C: CO_2/CH_4 selectivity changes (35 ^{o}C with a feed pressure of 30 psia, and membranes stored in vacuum). The lines are added to aid the reader's eye.

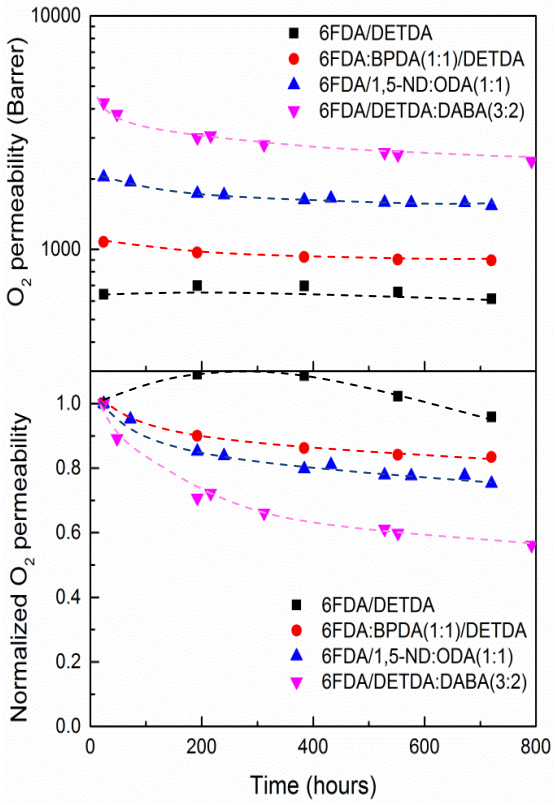

Figure 4.10: Pure gas aging study of CMS films pyrolyzed at 550 ^{o}C: O_2 permeability changes (35 ^{o}C with a feed pressure of 30 psia, and membranes stored in vacuum). The lines are added to aid the reader's eye.

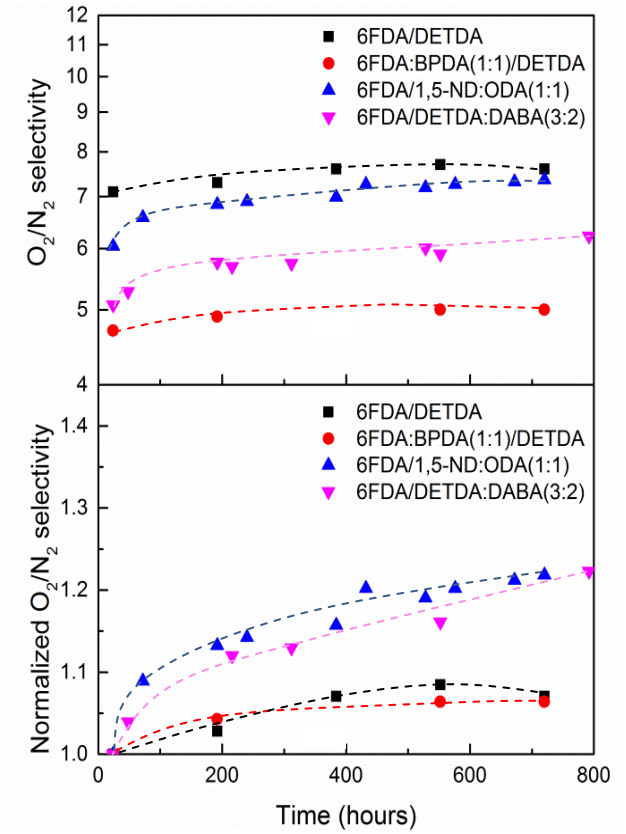

Figure 4.11: Pure gas aging study of CMS films pyrolyzed at 550 ^{o}C: O_2/N_2 selectivity changes (35 ^{o}C with a feed pressure of 30 psia, and membranes stored in vacuum). The lines are added to aid the reader's eye.

The permeability for the four gases of the four CMS films showed a decreasing trend with only a few exceptions and the exceptions were only observed in 6FDA/DETDA CMS membrane as can be seen in Figure 4.8 and 4.10. The possible reason for this data scattering might be: as will be discussed in the next paragraph, 6FDA/DETDA CMS membrane showed the least physical aging among the four CMS materials with both permeability and selectivity change within 15% after one month.

More specifically, the permeability increase in Figure 4.8 represents a CO_2 permeability increase from 2667 to 2723 Barrer (2%), and Figure 4.10 showed an O_2 permeability increase from 640-698 Barrer (9%). Thus we believe this discrepancy might be a result of experimental uncertainty. To prove this, replicate tests will be needed; however considering the extensive amount of time and work that need to be consumed, we didn't do the replicate tests here. On the other hand, selectivity showed an increasing trend for all samples with aging time. The changing rate was the highest in the first few days, which was as expected, since the free volume of the material was the highest initially, and aging is a self-retarding process.

Although the property changes for four different CMS materials showed a similar trend, from Figures 4.8 to 4.11, it is clear that different CMS structures have significant impacts on the aging phenomena. The 6FDA/DETDA:DABA(3:2) CMS membrane, which started with the highest permeability (above 20,000 Barrer for CO_2 and above 4000 Barrer for O_2), showed the fastest and most extensive aging, with permeability reductions of roughly 50% during the one month testing time before approaching a more or less stable point. On the other hand, the most compact CMS film derived from 6FDA/DETDA (~2700 Barrer for CO_2 and ~660 Barrer for O_2) showed permeability reductions of less than 15%. The 6FDA:BPDA(1:1)/DETDA and 6FDA/1,5-ND: ODA(1:1) CMS membranes showed intermediate aging.

For long term membrane applications, the stabilized separation performance is the most important property to consider and Figures 4.8 to 4.11 show that gas permeabilities and selectivities are essentially stabilized after vacuum aging for a month. This is a small period in the "life" of a practical membrane, and among the four CMS materials, although showing the largest percentage aging, the 6FDA/DETDA: DABA(3:2) CMS membrane *still maintained the highest permeability after stabilization*.

Different responses from different gases to physical aging in the materials are also of interest. In fact, gas selectivity increases moderately with aging since aging affects the

larger gases more than smaller ones. The 6FDA/DETDA:DABA(3:2) CMS membrane clearly illustrates this trend. The smaller penetrants (CO_2 and O_2) show permeability reductions of 43% and 48% respectively, while for larger penetrants as CH_4 and N_2, the changes were 59% and 54%, suggesting that the CMS pore distribution shifts as time proceeds.

Table 4.3 summarizes the separation performance of the four CMS membranes before and after one month's aging. Each data point is the average of at least two tests, and shows permeability reductions as the gas kinetic diameters increase. Moreover, comparing to the precursor membranes, separation performance of the resulting CMS films improves significantly in all cases with both higher permeability and selectivity. We were somewhat surprised to note that the performance of the polymeric precursors and the final CMS membranes *were not simply correlated*. Specifically, 6FDA/DETDA:DABA(3:2) CMS showed the highest permeability; however, its precursor showed only the third highest among the four polymers. Similarly, the 6FDA/1,5-ND:ODA(1:1) CMS, while maintaining the second highest selectivity among all, showed more dramatic permeability increases compared to 6FDA:BPDA(1:1)/DAM and 6FDA/DETDA CMS films. This disconnection between polymeric and CMS films was alluded to in the earlier discussion of FFV and the fundamentally different nature of the activated diffusion steps in the case of polymeric vs. CMS matrices. The simultaneously high permeability and high selectivity of 6FDA/1,5-ND:ODA(1:1) CMS may reflect packing disrupted regions that are serially communicating with more tightly packed and selective domains. Clearly, 6FDA/1,5-ND:ODA(1:1) has a stiff part 1,5-ND and a flexible more easily packed ODA part; however, it is not clear how or if these features might be preserved in the massively transformed final CMS morphology. In any case, it would be helpful to explore whether this trend can be generalized using other packable co-monomers such as methylene dianiline. The 6FDA/DETDA:DABA(3:2) precursor, itself has a relatively flexible backbone, but the carboxylic group in DABA

provides a crosslinking position, which also appears to open up the CMS structures compared to the DABA-free precursor case. The suggested mechanism of decarboxylation-induced crosslinking is presented in Figure 4.12 [21], in which two –COOH groups in DABA moieties react and form an anhydride by releasing one water molecule followed by creation of phenyl free radicals by decarboxylation of the anhydride. The phenyl radicals are capable of crosslinking with formation of the bulky crosslinked structure that may strongly inhibit chain packing and provides high permeability. It appears that this feature is carried forward somehow into the properties of the final CMS derived from the DABA precursor.

The separation performance of the well-studied 6FDA/BPDA-DAM CMS membranes is listed in Table 4.4 for direct comparison with 6FDA:BPDA(1:1)/DETDA derived CMS membranes. Moreover through personal communication, Dr. Wulin Qiu in Koros group kindly provided the gas separation performance of 6FDA-DAM:DABA(3:2) CMS membranes, which is also listed for direct comparison with 6FDA/DETDA:DABA(3:2) derived ones. These pieces of information can provide insight into the analogy between DAM- vs. DETDA-based CMS membranes. As it can be seen, both 6FDA/BPDA-DAM and 6FDA-DAM:DABA(3:2) CMS membranes show lower permeability but higher selectivity compared with 6FDA:BPDA(1:1)/DETDA and 6FDA/DETDA:DABA(3:2) CMS membrane. This might due to the slightly more bulky ethyl group in DETDA- based membranes, compared with the methyl group in DAM-based membranes, which appears to help open up the pore structures. We believe this trend is also true in the analogy between 6FDA/DETDA vs. 6FDA/DAM; however, because of the lack of data from literature, we cannot yet provide the proof. This also means for DETDA- based CMS membranes to achieve as high selectivity as DAM-based ones, higher pyrolysis temperature or other treatment methods need to be applied.

Table 4.3: Pure gas permeation and separation properties of CMS membranes (measured at 35 ^{o}C, 30 psia). (a) before one month's aging; (b) after one month's aging;

(a) Before one month's aging

Polymer	**Permeability (Barrer)**			
	CO_2	**CH_4**	**O_2**	**N_2**
6FDA/DETDA	2779 ±43	60 ±3	663 ±18	91 ±1
6FDA:BPDA(1:1)/DETDA	4663 ±72	194 ±12	1074 ±21	229 ±17
6FDA/DETDA:DABA(3:2)	21740 ±944	723 ±32	4293 ±45	868 ±31
6FDA/1,5-ND:ODA(1:1)	9791 ±113	217 ±8	2038 ±97	337 ±19
6FDA/BPDA-DAM	***3110***	***57***	***647***	***101[2]***
6FDA-DAM:DABA(3:2)	***16823***	***490***	***-***	***-***

Polymer	**Selectivity**	
	CO_2/CH_4	**O_2/N_2**
6FDA/DETDA	46.3 ±1.1	7.3 ±0.3
6FDA:BPDA(1:1)/DETDA	24.0 ±1.8	4.7 ±0.4
6FDA/DETDA:DABA(3:2)	30.1 ±1.7	4.9 ±0.1
6FDA/1,5-ND:ODA(1:1)	45.1 ±3.8	6.0 ±0.2
6FDA/BPDA-DAM	***54.9***	***6.4 [2]***
6FDA-DAM:DABA(3:2)	***34.5***	***-***

(b) After one month's aging

Polymer	**Permeability (Barrer)**				**Selectivity**	
	CO_2	**CH_4**	**O_2**	**N_2**	**CO_2/CH_4**	**O_2/N_2**
6FDA/DETDA	2552	49	614	81	52.0	7.6
6FDA:BPDA(1:1)/DETDA	3805	133	896	179	28.5	5.0
6FDA/DETDA:DABA(3:2)	10689	304	2384	383	34.8	6.2
6FDA/1,5-ND:ODA(1:1)	6243	128	1517	206	48.6	7.4

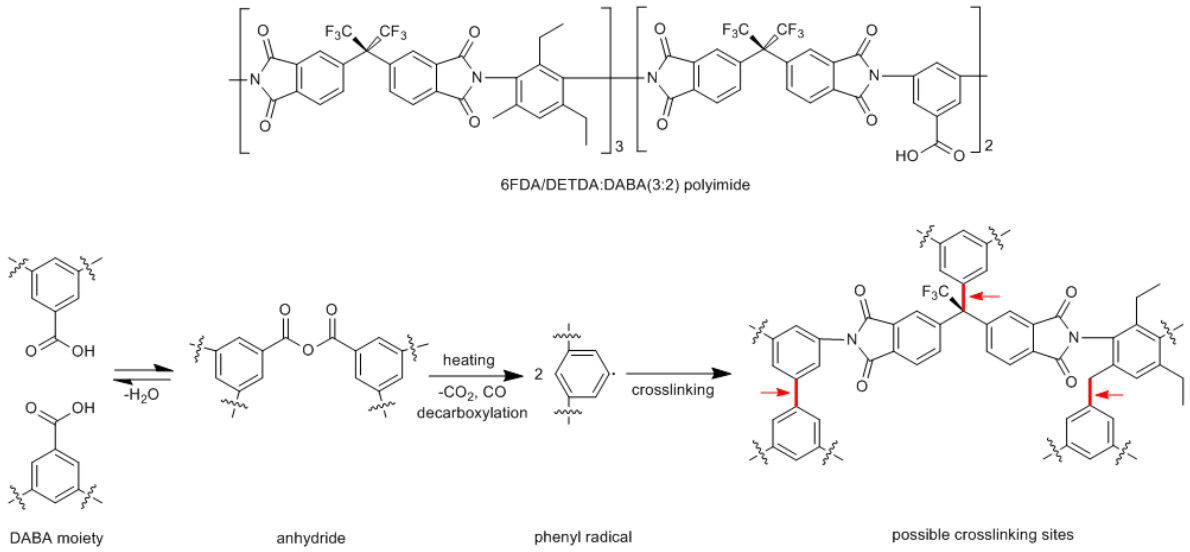

Figure 4.12: Chemical structure of 6FDA/DETDA:DABA (3:2) and crosslinking mechanism of decarboxylation-induced crosslinking. Possible crosslinking sites are noted with an arrow.

While the performance of all of the polymer precursors fall below the so-called polymer "upper bounds" in Figure 4.13, after pyrolysis, all CMS samples show properties well beyond these polymer limits for both CO_2/CH_4 and O_2/N_2, even after aging for one month. Separation performance of various CMS membranes is also given in Figure 4.13 for comparison.

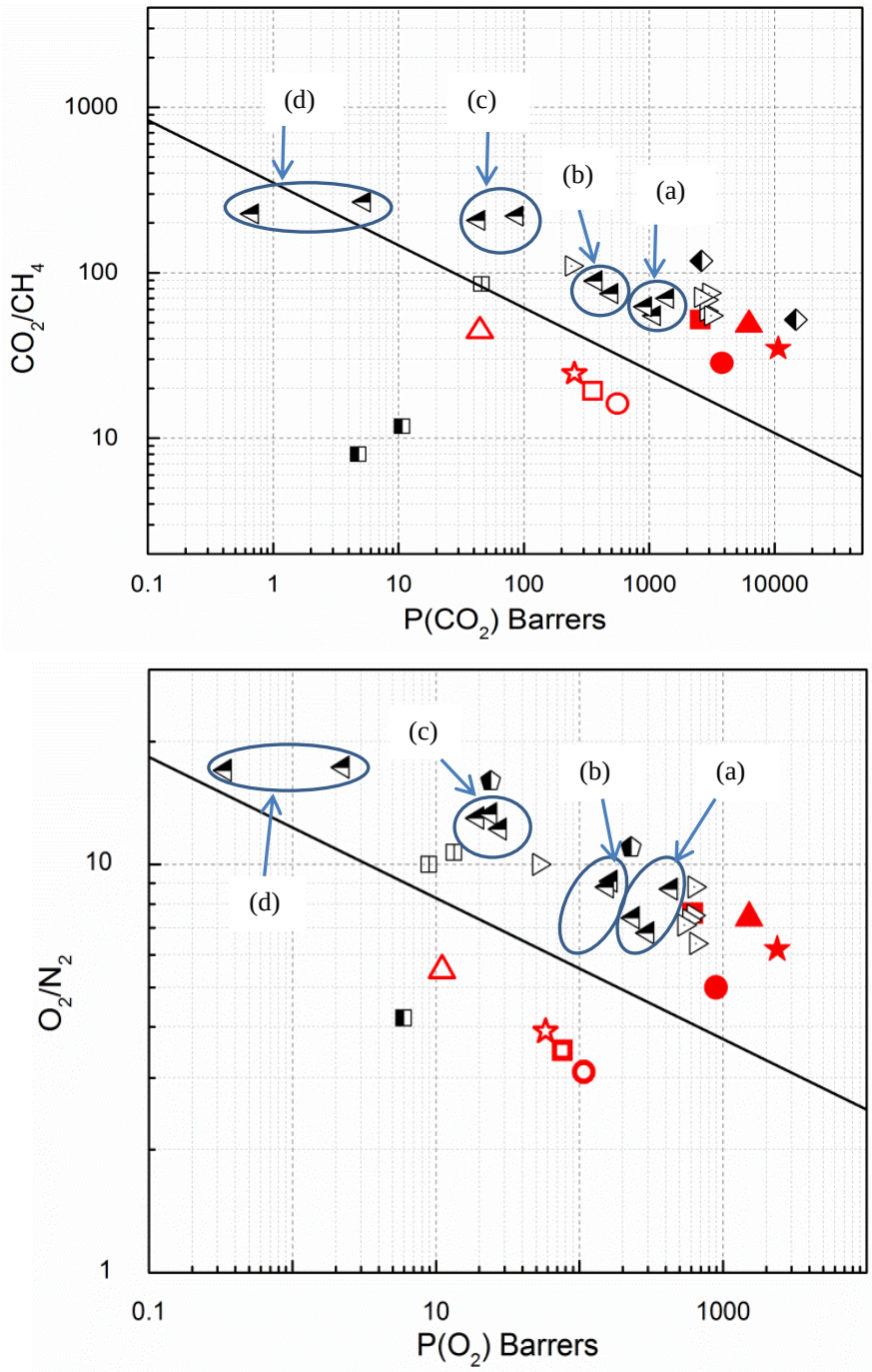

Figure 4.13: Pure gas separation performance of polymer and one month-aged CMS films derived from: a) ☐ 6FDA/DETDA; b) ○ 6FDA:BPDA(1:1)/DETDA; c)△ 6FDA/1,5-ND:ODA(1:1); d)☆6FDA/DETDA:DABA(3:2); red open symbols for polymer films and red solid symbols for CMS films investigated in this study. Measurements were made at

35 ^{o}C with feed pressure of 30 psia. Separation performance of various CMS membranes are shown for comparison: ◅ are Matrimid® CMS membranes pyrolyzed at: a) 550 ^{o}C with soaking time of 2 hrs; b) 550 ^{o}C with soaking time of 8 hrs; c) 800 ^{o}C with soaking time of 2 hrs; d) 800 ^{o}C with soaking time of 8 hrs; [4], ◫ are flat phenolic-resin-based CMS pyrolyzed at 700 ^{o}C supported on porous ceramic tubes [22, 23], ▷ are various homogeneous 6FDA/BPDA-DAM CMS membranes produced at 550 ^{o}C under different pyrolysis atmosphere including He, Ar, and vacuum [2], ◧ are supported PVDC-PVC coated CMS membranes with one or two layers of coating [24], ◐ are BTDA-*m*-TMPD CMS membranes pyrolyzed at 600 ^{o}C or 800 ^{o}C [25], and ◆ are 550 ^{o}C or 800 ^{o}C pyrolyzed 6FDA-mPDA/DABA (3:2) CMS membranes [26].

4.4.2 Physical aging study of pure gases sorption on four CMS materials

To further probe microstructure and its evolution over time, pure gas sorption tests were conducted. Since the majority of gas molecules are believed to be sorbed in micropores in the CMS material, sorption isotherms offer a quite useful probe of the micropore structures. The CMS samples were fabricated using the same protocols and polymers used in the permeation studies. Samples were loaded into two sorption cells after being unloaded from the pyrolysis furnace, one for CO_2 and CH_4 sorption and the other for O_2 and N_2 sorption. After overnight evacuation (day 1), the samples were immediately put into pure gas sorption tests. Then the membranes were kept in the cell under vacuum for one month, and tested on the same gases again on day 30.

Unlike glassy polymers, CMS materials, with a finite number of sorption sites and rigid saturable capacities, the Langmuir isotherm is typically used to describe gas sorption where sorption occurs in microvoids only [27]. The experimental data were

fitted to Langmuir isotherms shown in Figure 4.14 and Figure 4.15 below, and the fitting parameters are listed in Table 4.4 and Table 4.5.

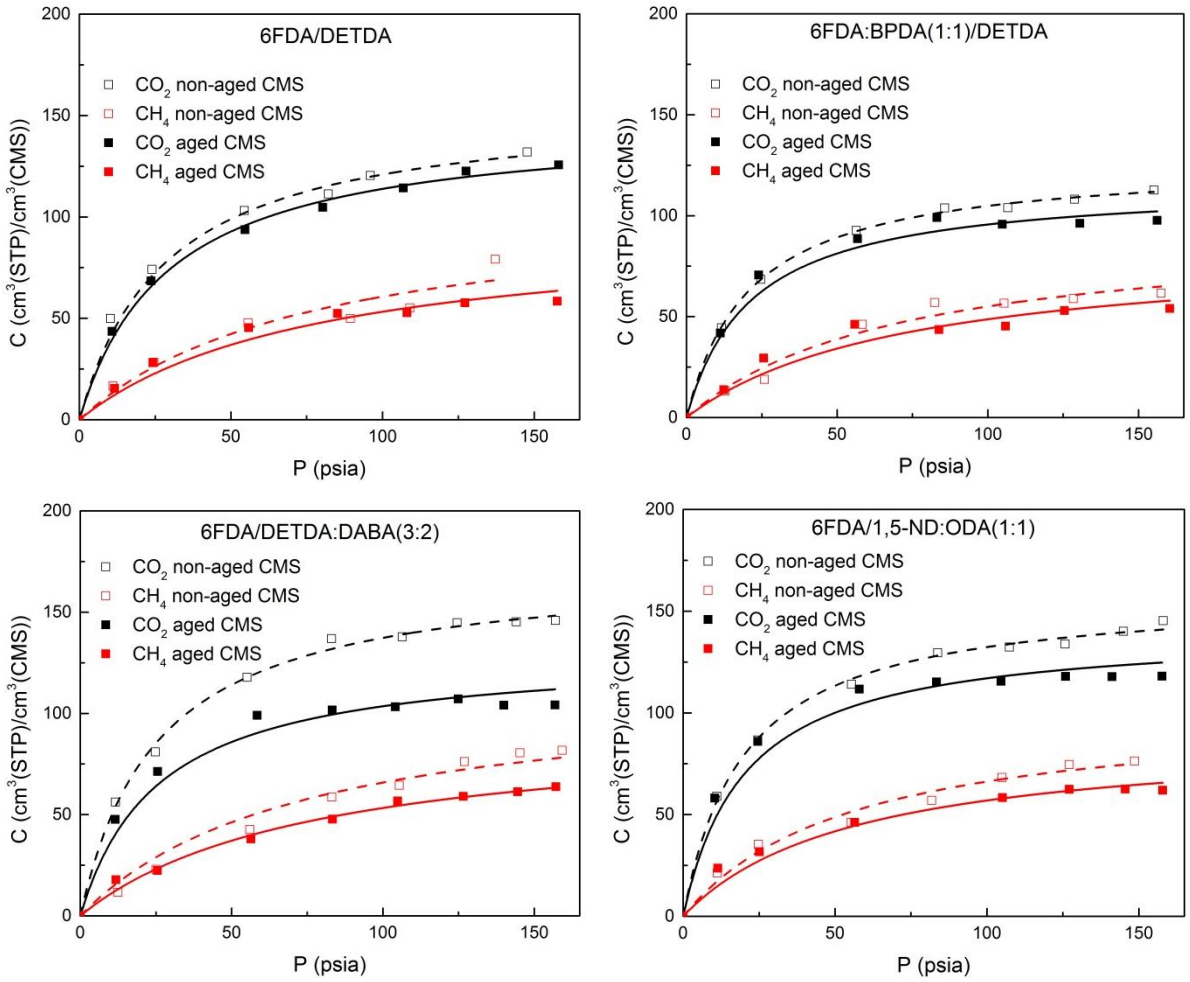

Figure 4.14: CO_2 and CH_4 sorption isotherms at 35 ^oC for fresh and 30-day-aged CMS films derived from 6FDA/DETDA, 6FDA:BPDA(1:1)/DETDA, 6FDA/DETDA:DABA(3:2), and 6FDA/1,5-ND:ODA(1:1) pyrolyzed at 550 ^oC and UHP Ar.

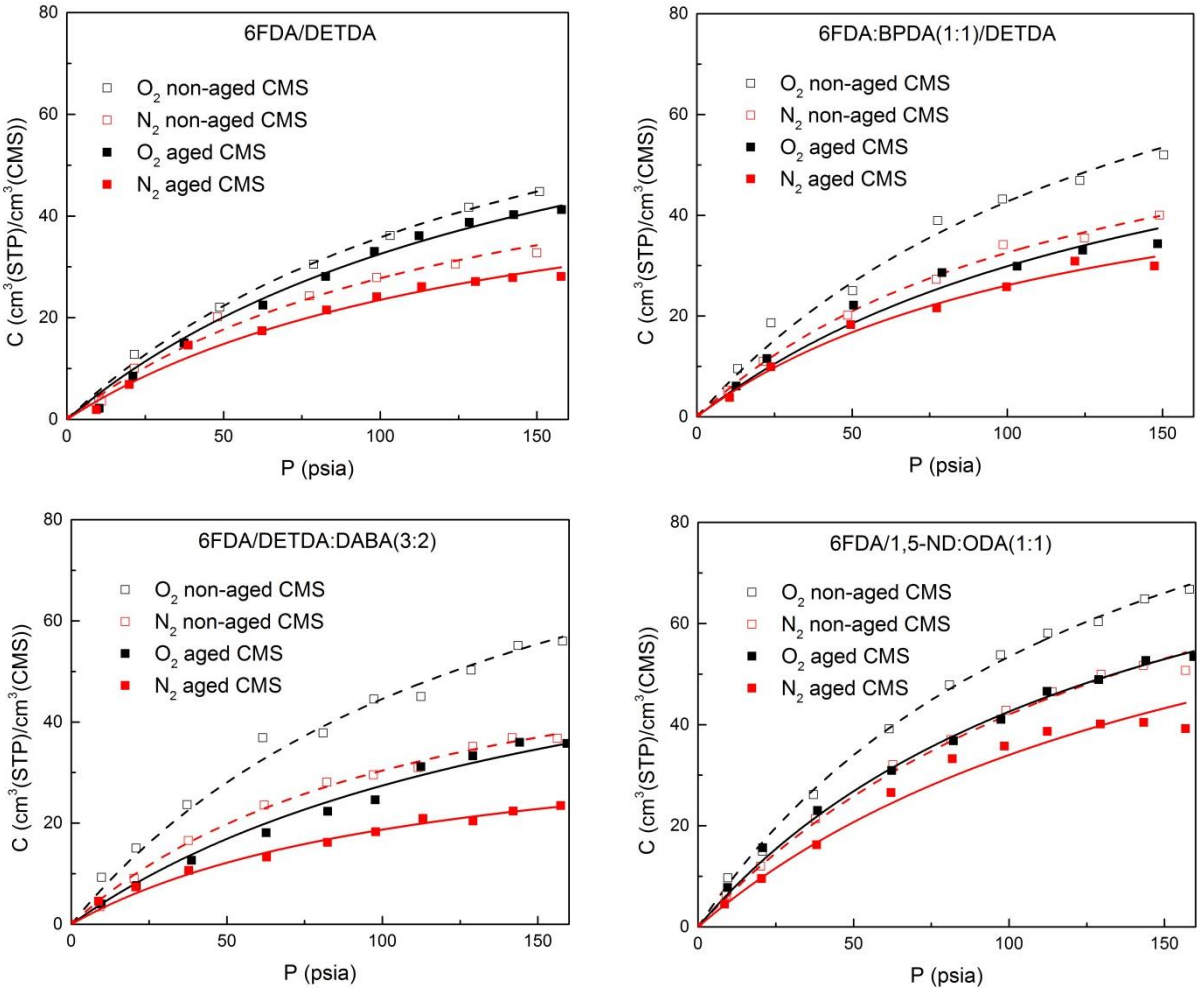

Figure 4.15: O_2 and N_2 sorption isotherms at 35 ^oC for fresh and 30-day-aged CMS films derived from 6FDA/DETDA, 6FDA:BPDA(1:1)/DETDA, 6FDA/DETDA:DABA(3:2), and 6FDA/1,5-ND:ODA(1:1) pyrolyzed at 550 ^oC and UHP Ar.

Table 4.4: CO_2 and CH_4 Langmuir isotherm parameters at 35 ^oC for fresh and 30-day-aged CMS films derived from 6FDA/DETDA, 6FDA:BPDA(1:1)/DETDA, 6FDA/DETDA:DABA(3:2), and 6FDA/1,5-ND:ODA(1:1) pyrolyzed at 550 ^oC and UHP Ar.

		6FDA/DETDA				6FDA:BPDA(1:1)/DETDA			
		Non-aged CMS		Aged CMS		Non-aged CMS		Aged CMS	
		CO_2	CH_4	CO_2	CH_4	CO_2	CH_4	CO_2	CH_4
$C_H^{'}$	[cm^3(STP)/cm^3]	155.5	107.4	147.3	95.6	127.0	94.4	116.2	84.5
b	[1/psia]	0.0350	0.0130	0.0340	0.0126	0.0473	0.0140	0.0466	0.0136

		6FDA/DETDA:DABA(3:2)				6FDA/1,5-ND:ODA(1:1)			
		Non-aged CMS		Aged CMS		Non-aged CMS		Aged CMS	
		CO_2	CH_4	CO_2	CH_4	CO_2	CH_4	CO_2	CH_4
$C_H^{'}$	[cm^3(STP)/cm^3]	172.2	114.3	130.3	94.3	158.9	103.2	140.9	89.3
b	[1/psia]	0.0393	0.0136	0.0386	0.0130	0.0498	0.0179	0.0490	0.0176

Table 4.5: O_2 and N_2 Langmuir isotherm parameters at 35 ^oC for fresh and 30-day-aged CMS films derived from 6FDA/DETDA, 6FDA:BPDA(1:1)/DETDA, 6FDA/DETDA:DABA(3:2), and 6FDA/1,5-ND:ODA(1:1) pyrolyzed at 550 ^oC and UHP Ar.

		6FDA/DETDA				6FDA:BPDA(1:1)/DETDA			
		Non-aged CMS		Aged CMS		Non-aged CMS		Aged CMS	
		O_2	N_2	O_2	N_2	O_2	N_2	O_2	N_2
$C_H^{'}$	[cm^3(STP)/cm^3]	90.1	64.4	83.1	56.7	107.5	73.0	77.4	58.7
b	[1/psia]	0.0066	0.0076	0.0065	0.0071	0.0066	0.0081	0.0063	0.0080

		6FDA/DETDA:DABA(3:2)				6FDA/1,5-ND:ODA(1:1)			
		Non-aged CMS		Aged CMS		Non-aged CMS		Aged CMS	
		O_2	N_2	O_2	N_2	O_2	N_2	O_2	N_2
$C_H^{'}$	[cm^3(STP)/cm^3]	108.3	65.2	73.1	40.5	125.2	112.1	112.1	94.8
b	[1/psia]	0.0070	0.0087	0.0060	0.0086	0.0074	0.0060	0.0060	0.0056

The dashed lines represent isotherms for non-aged CMS materials and solid lines represent isotherms for aged CMS materials which have been held under vacuum for one month. The figures show the sorption capacity for CO_2/CH_4 and O_2/N_2 of all CMS materials decreased over time, and the decrease in $C_H^{'}$ indicates some reduction of Langmuir sorption sites relative to non-aged to aged CMS. These sites are presumably direct reflections of the so-called microvoids, as opposed to the size-sieving ultramicropores that provide the diffusion selectivity responsible for the high selectivity of CMS vs. polymers. The value of b remains almost unchanged during the aging, implying that the intrinsic nature of CMS did not change dramatically during aging. The

micropores in CMS are believed to be formed due to packing imperfections between graphene-like sheets, which can settle somewhat to a more stable state through structure relaxation as time proceeds. As a result, a somewhat lower Langmuir capacity remains.

The 6FDA/DETDA:DABA(3:2) CMS membrane, which started with the highest permeability and showed the fastest and most permeation aging, also showed the most sorption capacity loss for all gases. On the other hand, the 6FDA/DETDA CMS, which showed less permeation aging, also showed the least sorption aging with all sorption capacity losses of $\leq$ 10%. 6FDA:BPDA(1:1)/DETDA and 6FDA/1,5-ND:ODA(1:1) CMS membranes showed intermediate sorption aging once again, as was seen for the case of permeability.

Eq. 2.12 shows that permselectivity is comprised of diffusion selectivity and sorption selectivity. Diffusion selectivity $\frac{D_A}{D_B}$ is governed by the size and shape of the gas molecules, and sorption selectivity $\frac{\mathbb{S}_A}{\mathbb{S}_B}$ is dependent on the condensability of the gases and their interaction with the membrane material. Table 4.6 and 4.7 list 35 ^oC and 30 psia, the permeability P, the sorption coefficient $\mathbb{S}$, the diffusion coefficient D, the overall membrane permselectivity $\alpha_{A/B}$, the sorption selectivity $\frac{\mathbb{S}_A}{\mathbb{S}_B}$, and the diffusion selectivity $\frac{D_A}{D_B}$ of two gas pairs CO_2/CH_4 and O_2/N_2 for four fresh and one month-aged CMS materials. The P, $\mathbb{S}$, $\alpha_{A/B}$ and $\frac{\mathbb{S}_A}{\mathbb{S}_B}$ are determined using the permeation measurements and sorption measurements, while D and $\frac{D_A}{D_B}$ is calculated according to Eq. 2.11 and 2.12 ($P_i = \overline{D}_i * \overline{\mathbb{S}}_i$ and $\alpha_{A/B} = \frac{P_A}{P_B} = \left(\frac{D_A}{D_B}\right)\left(\frac{\mathbb{S}_A}{\mathbb{S}_B}\right)$). Clearly, for both fresh and one month-aged CMS materials, diffusion selectivity is the main contributing factor to the overall

permselectivity for both gas pairs. The sorption selectivity for CO_2/CH_4 and O_2/N_2 separation is only around 2.7 and 1.3 respectively, regardless of the different CMS structures. These factors show that higher diffusion selectivity is essential to achieve higher separation efficiency and the adjustment of diffusion selectivity is the key tool to improve separation performance of CMS membranes. To further pursue this issue, different pyrolyzing protocols, which have been proven to be quite useful in tuning the pore structures of CMS materials [4], will be investigated in Chapter 5 to study their effects on the resulting CMS material properties.

Table 4.6: The permeability P, the sorption coefficient $\mathbb{S}$, the diffusion coefficient D, the overall membrane permselectivity $\alpha_{A/B}$, the sorption selectivity $\frac{\mathbb{S}_A}{\mathbb{S}_B}$, and the diffusion selectivity $\frac{D_A}{D_B}$ of pure gas pairs CO_2/CH_4 for four fresh and one month-aged CMS materials at 35 ^oC and 30 psia.

CMS membrane	P_{CO_2} [Barrers]		$\mathbb{S}_{CO_2}$ [cc(STP)/cm^3/psia]		D_{CO_2} [cm^2/s] ($*10^{-8}$)	
	Non-aged CMS	Aged CMS	Non-aged CMS	Aged CMS	Non-aged CMS	Aged CMS
6FDA/DETDA	2779	2552	2.7	2.5	53.3	52.8
6FDA:BPDA(1:1)/DETDA	4663	3805	2.5	2.3	96.5	85.6
6FDA/DETDA:DABA(3:2)	21740	10689	3.1	2.3	363.0	240.5
6FDA/1,5-ND:ODA(1:1)	9791	6243	3.2	2.8	158.3	115.4

CMS membrane	P_{CH_4} [Barrers]		$\mathbb{S}_{CH_4}$ [cc(STP)/cm^3/psia]		D_{CH_4} [cm^2/s] ($*10^{-8}$)	
	Non-aged CMS	Aged CMS	Non-aged CMS	Aged CMS	Non-aged CMS	Aged CMS
6FDA/DETDA	60	49	1.0	0.9	3.1	2.8
6FDA:BPDA(1:1)/DETDA	194	133	0.9	0.8	11.2	8.6
6FDA/DETDA:DABA(3:2)	723	304	1.1	0.9	34.0	17.5
6FDA/1,5-ND:ODA(1:1)	217	128	1.2	1.0	9.4	6.6

CMS membrane	α_{CO_2/CH_4}		$\frac{\mathbb{S}_{CO_2}}{\mathbb{S}_{CH_4}}$		$\frac{D_{CO_2}}{D_{CH_4}}$	
	Non-aged CMS	Aged CMS	Non-aged CMS	Aged CMS	Non-aged CMS	Aged CMS
6FDA/DETDA	46.3	52.1	2.7	2.8	17.2	18.8
6FDA:BPDA(1:1)/DETDA	24.0	28.6	2.8	2.9	8.6	10.0
6FDA/DETDA:DABA(3:2)	30.1	35.2	2.8	2.6	10.7	13.8
6FDA/1,5-ND:ODA(1:1)	45.1	48.8	2.7	2.8	17.0	17.4

Table 4.7: The permeability P, the sorption coefficient $\mathbb{S}$, the diffusion coefficient D, the overall membrane permselectivity $\alpha_{A/B}$, the sorption selectivity $\frac{\mathbb{S}_A}{\mathbb{S}_B}$, and the diffusion selectivity $\frac{D_A}{D_B}$ of pure gas pairs O_2/N_2 for four fresh and one month-aged CMS materials at 35 ^oC and 30 psia.

CMS membrane	P_{O_2} [Barrers]		$\mathbb{S}_{O_2}$ [cc(STP)/cm^3/psia]		D_{O_2} [cm^2/s] (*10^{-8})	
	Non-aged CMS	Aged CMS	Non-aged CMS	Aged CMS	Non-aged CMS	Aged CMS
6FDA/DETDA	663	614	0.5	0.5	68.6	63.6
6FDA:BPDA(1:1)/DETDA	1074	896	0.6	0.4	115.9	92.6
6FDA/DETDA:DABA(3:2)	4293	2384	0.6	0.4	370.3	308.4
6FDA/1,5-ND:ODA(1:1)	2038	1517	0.8	0.6	131.8	130.8

CMS membrane	P_{N_2} [Barrers]		$\mathbb{S}_{N_2}$ [cc(STP)/cm^3/psia]		D_{N_2} [cm^2/s] (*10^{-8})	
	Non-aged CMS	Aged CMS	Non-aged CMS	Aged CMS	Non-aged CMS	Aged CMS
6FDA/DETDA	91	81	0.4	0.3	14.0	11.8
6FDA:BPDA(1:1)/DETDA	229	179	0.5	0.4	23.7	23.2
6FDA/DETDA:DABA(3:2)	868	383	0.4	0.3	112	66.1
6FDA/1,5-ND:ODA(1:1)	337	206	0.6	0.5	29.1	21.3

CMS membrane	α_{CO_2/CH_4}		$\frac{\mathbb{S}_{CO_2}}{\mathbb{S}_{CH_4}}$		$\frac{D_{CO_2}}{D_{CH_4}}$	
	Non-aged CMS	Aged CMS	Non-aged CMS	Aged CMS	Non-aged CMS	Aged CMS
6FDA/DETDA	7.3	7.6	1.3	1.7	5.8	4.5
6FDA:BPDA(1:1)/DETDA	4.7	5.0	1.2	1.0	3.9	5.0
6FDA/DETDA:DABA(3:2)	4.9	6.2	1.5	1.3	3.3	4.7
6FDA/1,5-ND:ODA(1:1)	6.0	7.4	1.3	1.2	4.5	6.1

4.4.3 Physical aging study of active mixed gas feed on 6FDA/DETDA:DABA(3:2) CMS membrane

To address the issue of time changes in CMS membrane separation performance, in this section, we consider a practical way to suppress physical aging. This approach has been considered previously for V-treated Matrimid® hollow fiber membranes, but we wanted to see if the same trend would be observed for the CMS membranes investigated in this study. 6FDA/DETDA:DABA(3:2) CMS material was chosen in this part of the study out of two reasons. First, it has been proven to be the most promising CMS material with significantly high permeability amongst the four CMS materials of interest. Second, it showed the highest degree of physical aging in pure gas permeation stored under vacuum as discussed earlier. If the method probed here can efficiently suppress its physical aging, it is reasonable to believe that this method can also help stabilize the separation performance of the other CMS materials as well.

The time dependent stability of 6FDA/DETDA:DABA(3:2) CMS membrane under continuous active feed of 50 psia of mixed gas 50% CO_2/50% CH_4 was observed during a month's time and is presented in Figure 4.16. Comparing to a 50% CO_2 permeability loss and a 30% CO_2/CH_4 selectivity gain in the pure gas and vacuum storage study, the results obtained here *showed much lower time dependence* with only 4% CO_2 permeability loss and 6% CO_2/CH_4 selectivity gain. The reason for this aging suppression is believed to be that as the CMS structure approaches a more stable and lower free volume state, the highly condensable CO_2 in the mixed gas feed sorbs in the micropores and inhibits large-scale relaxation. From this sense, a higher feed pressure can help suppress physical aging even more since at higher pressure, CO_2 absorption would be further favored – a highly desirable situation for separation of aggressive feeds.

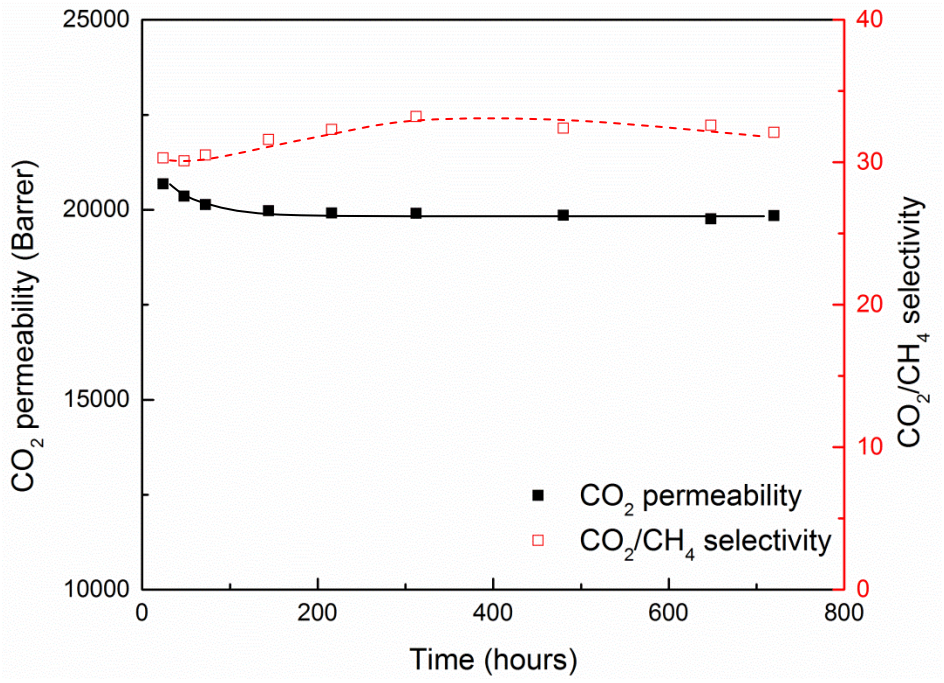

Figure 4.16: Aging study of 6FDA/DETDA:DABA(3:2)CMS membrane pyrolyzed at 550 ^{o}C and UHP Argon under continuous active feed of 50 psia of mixed gas 50% CO_2/50% CH_4 and testing temperature was 35 ^{o}C. The lines are added to aid the reader's eye.

4.5 Summary

Four novel polyimides, 6FDA/DETDA, 6FDA:BPDA(1:1)/DETDA, 6FDA/DETDA:DABA(3:2) and 6FDA/1,5-ND:ODA(1:1), were prepared and characterized with different techniques. The separation performance of precursor polymer films formed from these polymers was studied using CO_2, CH_4, O_2 and N_2 pure gases. As expected, higher FFV in the polyimide led to higher permeability of the polymeric film. The separation performance, as well as its time dependent behavior, of the resulting CMS

membranes pyrolyzed under pure argon at 550 ^{o}C was also examined. 6FDA/DETDA and 6FDA:BPDA(1:1)/DETDA carbon membranes showed somewhat lower permeability, but moderate aging tendencies. On the other hand, 6FDA/DETDA:DABA(3:2) and 6FDA/1,5-ND:ODA(1:1) CMS films displayed much higher permeability and comparable selectivity but were subject to larger aging-related phenomenon. The 6FDA/DETDA:DABA(3:2) derived CMS membranes showed the highest permeability (above 20,000 Barrer for CO_2 and above 4000 Barrer for O_2 at 35 ^{o}C), however, its highly time-dependent issue needs to be addressed before using in practical applications. An active feed of mixed gas 50% CO_2/50% CH_4 was shown to suppress physical aging in 6FDA/DETDA: DABA(3:2) CMS, with only 4% CO_2 permeability loss and 6% CO_2/CH_4 selectivity gain.

Considering the separation performance, 6FDA/DETDA: DABA(3:2) and 6FDA/1,5-ND:ODA(1:1) CMS membranes showed great potential for future study. The smallest T_d-T_g of 6FDA/DETDA: DABA(3:2) makes it favorable in the formation of hollow fibers. Thus, 6FDA/DETDA: DABA(3:2) CMS membrane is proposed for later studies including: 1) Chapter 5: effects of different pyrolysis protocols, including different pyrolyzing temperatures and atmospheres; 2) Chapter 7: hollow fiber studies.

4.6 References

[1] T.L. Cottrell, Strengths of Chemical Bonds Second Edition, Butterworths, London, 1958.

[2] M. Kiyono, P.J. Williams, W.J. Koros, Effect of pyrolysis atmosphere on separation performance of carbon molecular sieve membranes, J. Membr. Sci., 359 (2010) 2-10.

[3] V.C. Geiszler, W.J. Koros, Effects of polyimide pyrolysis conditions on carbon molecular sieve membrane properties, Ind. Eng. Chem. Res., 35 (1996) 2999-3003.

[4] K.M. Steel, W.J. Koros, An investigation of the effects of pyrolysis parameters on gas separation properties of carbon materials, Carbon, 43 (2005) 1843-1856.

[5] W. Qiu, C.-C. Chen, M.R. Kincer, W.J. Koros, Thermal analysis and its application in evaluation of fluorinated polyimide membranes for gas separation, Polymer, 52 (2011) 4073-4082.

[6] W. Qiu, C.-C. Chen, L. Xu, L. Cui, D.R. Paul, W.J. Koros, Sub-Tg Cross-Linking of a Polyimide Membrane for Enhanced CO_2 Plasticization Resistance for Natural Gas Separation, Macromolecules, 44 (2011) 6046-6056.

[7] M. Moe, W.J. Koros, H.H. Hoehn, G.R. Husk, Effects of film history on gas transport in a fluorinated aromatic polyimide, J. Appli. Polym. Sci., 36 (1988) 1833-1846.

[8] M. Khalil, C.-S. Ha, S. Saeed, I.M. Khan, Z. Ahmad, Polyimide molecular composites containing a stiff-chain polymer derived from 1,5-diaminonaphathalene and pyromellitic dianhydride, Polym. Compos., 31 (2009) 645-652.

[9] J.-i. Hayashi, M. Yamamoto, K. Kusakabe, S. Morooka, Effect of Oxidation on Gas Permeation of Carbon Molecular Sieving Membranes Based on BPDA-pp‘ODA Polyimide, Ind. Eng. Chem. Res., 36 (1997) 2134-2140.

[10] J.-i. Hayashi, H. Mizuta, M. Yamamoto, K. Kusakabe, S. MorookaE, Separation of Ethane/Ethylene and Propane/Propylene Systems with a Carbonized BPD, Ind. Eng. Chem. Res., 35 (1996) 4176-4181.

[11] P.S. Tin, T.-S. Chung, A.J. Hill, Advanced Fabrication of Carbon Molecular Sieve Membranes by Nonsolvent Pretreatment of Precursor Polymers, Ind. Eng. Chem. Res., 43 (2004) 6476-6483.

[12] C.-C. Chen, W. Qiu, S.J. Miller, W.J. Koros, Plasticization-resistant hollow fiber membranes for CO_2/CH_4 separation based on a thermally crosslinkable polyimide, J. Membr. Sci., 382 (2011) 212-221.

[13] L. Xu, M. Rungta, M.K. Brayden, M.V. Martinez, B.A. Stears, G.A. Barbay, W.J. Koros, Olefins-selective asymmetric carbon molecular sieve hollow fiber membranes for hybrid membrane-distillation processes for olefin/paraffin separations, J. Membr. Sci., 423-424 (2012) 314-323.

[14] J.Y. Park, D.R. Paul, Effects of CO_2 exposure and physical aging on the gas permeability of thin 6FDA-based polyimide membranes - Part 1. Without crosslinking, J. Membr. Sci., 125 (1997) 23-39.

[15] M. Rungta, L. Xu, W.J. Koros, Carbon molecular sieve dense film membranes derived from Matrimid® for ethylene/ethane separation, Carbon, 50 (2012) 1488-1502.

[16] D.W. Breck, Zeolite Molecular Sieves, Structure, Chemistry and Use, John Wiley & Sons, New York, London, Sydney, Toronto, 1974.

[17] L. Cui, W. Qiu, D.R. Paul, W.J. Koros, Physical aging of 6FDA-based polyimide membranes monitored by gas permeability, Polymer, 52 (2011) 3374-3380.

[18] T.M. Murphy, D.S. Langhe, M. Ponting, E. Baer, B.D. Freeman, D.R. Paul, Physical aging of layered glassy polymer films via gas permeability tracking, Polymer, 52 (2011) 6117-6125.

[19] L. Xu, M. Rungta, J. Hessler, W. Qiu, M. Brayden, M. Martinez, G. Barbay, W.J. Koros, Physical aging in carbon molecular sieve membranes, Carbon, 80 (2014) 155-166.

[20] Y. Huang, D.R. Paul, Effect of temperature on physical aging of thin glassy polymer films, Macromolecules, 38 (2005) 10148-10154.

[21] A.M. Kratochvil, W.J. Koros, Decarboxylation-Induced Cross-Linking of a Polyimide for Enhanced CO_2 Plasticization Resistance, Macromolecules, 41 (2008) 7920-7927.

[22] T.A. Centeno, A.B. Fuertes, Supported carbon molecular sieve membranes based on a phenolic resin, J. Membr. Sci., 160 (1999) 201-211.

[23] T.A. Centeno, A.B. Fuertes, Carbon molecular sieve membranes derived from a phenolic resin supported on porous ceramic tubes, Sep. Purif. Technolo., 25 (2001) 379-384.

[24] T.A. Centeno, A.B. Fuertes, Carbon molecular sieve gas separation membranes based on poly(vinylidene chloride-co-vinyl chloride), Carbon, 38 (2000) 1067-1073.

[25] H.B. Park, Y.K. Kim, J.M. Lee, S.Y. Lee, Y.M. Lee, Relationship between chemical structure of aromatic polyimides and gas permeation properties of their carbon molecular sieve membranes, J. Membr. Sci., 229 (2004) 117-127.

[26] W. Qiu, K. Zhang, F.S. Li, K. Zhang, W.J. Koros, Gas separation performance of carbon molecular sieve membranes based on 6FDA-mPDA/DABA (3:2) polyimide, ChemSusChem, 7 (2014) 1186-1194.

[27] J. Karger, D.M. Ruthven, Diffusion in zeolites and other microporous solids, John Wiley, New York, USA, 1992.

CHAPTER 5

EFFECTS OF PYROLYSIS CONDITIONS ON GAS SEPARATION PROPERTIES OF 6FDA/DETDA:DABA(3:2) DERIVED CARBON MOLECULAR SIEVE DENSE FILM MEMBRANES

5.1 Overview

Separation performance of CMS membranes depends on the critical pore size and the pore size distribution, which can be tuned by several factors [1-9]. In Chapter 4, of the four precursors considered, 6FDA/DETDA:DABA(3:2) CMS membrane pyrolyzed at 550 ^{o}C was shown to offer extraordinary practical potential with the highest permeability, i.e., above 20,000 Barrer for CO_2 and above 4000 Barrer for O_2 at 35 ^{o}C. As an extension study, in this chapter, 6FDA/DETDA:DABA(3:2) polyimide was pyrolyzed under different protocols to produce carbon molecular sieve (CMS) dense film membranes for separation of important gas pairs, including pure gases CO_2/CH_4, O_2/N_2 and mixture gases 50% CO_2/50% CH_4 and 50% C_3H_6/50% C_3H_8. The effects of pyrolysis temperature and atmosphere on CMS separation performance are reported. Section 5.2, 5.3, and 5.4 investigated the effects of pyrolysis temperature, O_2 doping, and precrosslinking, respectively, on the separation performance of 6FDA/DETDA:DABA(3:2) CMS membranes. Sorption measurements provide insight into the pore size distributions among these CMS membranes. Section 5.5 summarizes and compares the effects of these three parameters during pyrolysis on the CMS membranes gas separation performance. Moreover, speculative hypotheses regarding the structure changes brought about by changing these parameters were also provided.

5.2 Effect of pyrolysis temperature on 6FDA/DETDA:DABA(3:2) CMS membrane separation performance

5.2.1 Permeation

6FDA/DETDA:DABA(3:2) CMS dense films were formed from pyrolysis of precursor films under UHP argon at three final pyrolysis temperatures: 550 ^{o}C, 675 ^{o}C, and 800 ^{o}C using the applicable pyrolysis protocol 1 or protocol 2 listed in Chapter 3. The CMS dense films obtained were tested on 6 gases, including 4 pure gases: CO_2, CH_4, O_2, and N_2 at 35 ^{o}C and 30 psia, and 2 mixture gases: 50% CO_2/50% CH_4 and 50% C_3H_6/50% C_3H_8 at 35 ^{o}C and 60 psia.

The steady state gas separation performance of these three different final temperature pyrolyzed CMS membranes are listed in Table 5.1. The pure gas CO_2, O_2 permeability and CO_2/CH_4, O_2/N_2 selectivity results are plotted in Figure 5.1. As seen from Figure 5.1, both permeabilities and selectivities of CMS membranes are significantly higher than those of the precursor membranes and surpass the polymeric upper bound. As pyrolysis temperature increases, permeability drops dramatically, while corresponding selectivity increases. It is also interesting to see from Table 5.1 that CO_2 permeability is lower and CO_2/CH_4 selectivity is higher in the case of mixture gas separation in comparison to the case of pure gas feeds. These observations may reflect the so-called dual mode competition effects between CO_2 and CH_4 molecules [10, 11]. The competition between both molecules reduces sorption and hinders diffusion of both gases, resulting in lower permeabilities. On the other hand, CO_2 sorption might be favored over CH_4 sorption during the competition due to its higher critical temperature, with a resultant increase in mixed gas selectivity.

Table 5.1: Pure and mixture gases permeation results of three different final temperature pyrolyzed CMS membranes as well as polymeric membranes derived from 6FDA/DETDA:DABA(3:2). Pure gas permeations were measured at 35 ^{o}C and 30 psia, mixture gas permeations were measured at 35 ^{o}C and 60 psia.

Membranes	**Pure gases**			
	P_{CO_2} (Barrer)	α_{CO_2/CH_4}	P_{O_2} (Barrer)	α_{O_2/N_2}
Polymeric-	238 ±13	22.0 ±2	54 ±4	3.5 ±0.4
550 ^{o}C-CMS	21740 ±944	30.1 ±1.7	4293 ±45	4.9 ±0.1
675 ^{o}C-CMS	5569 ±9	55 ±4.1	928 ±105	7.5 ±0.4
800 ^{o}C-CMS	1812 ±204	88.3 ±1.5	300 ±43	7.6 ±0.5

Membranes	**Mixture gases**			
	50% CO_2/50% CH_4		50% C_3H_6/50% C_3H_8	
	P_{CO_2} (Barrer)	α_{CO_2/CH_4}	$P_{C_3H_6}$ (Barrer)	$\alpha_{C_3H_6/C_3H_8}$
Polymeric-	-	-	-	-
550 ^{o}C-CMS	20073 ±1627	37.6 ±5.0	2444 ±99	12.7 ±0.8
675 ^{o}C-CMS	4107 ±287	66.4 ±1.0	401 ±9	30.2 ±0
800 ^{o}C-CMS	1397 ±132	102.7 ±0.9	71 ±1	63.7 ±0.2

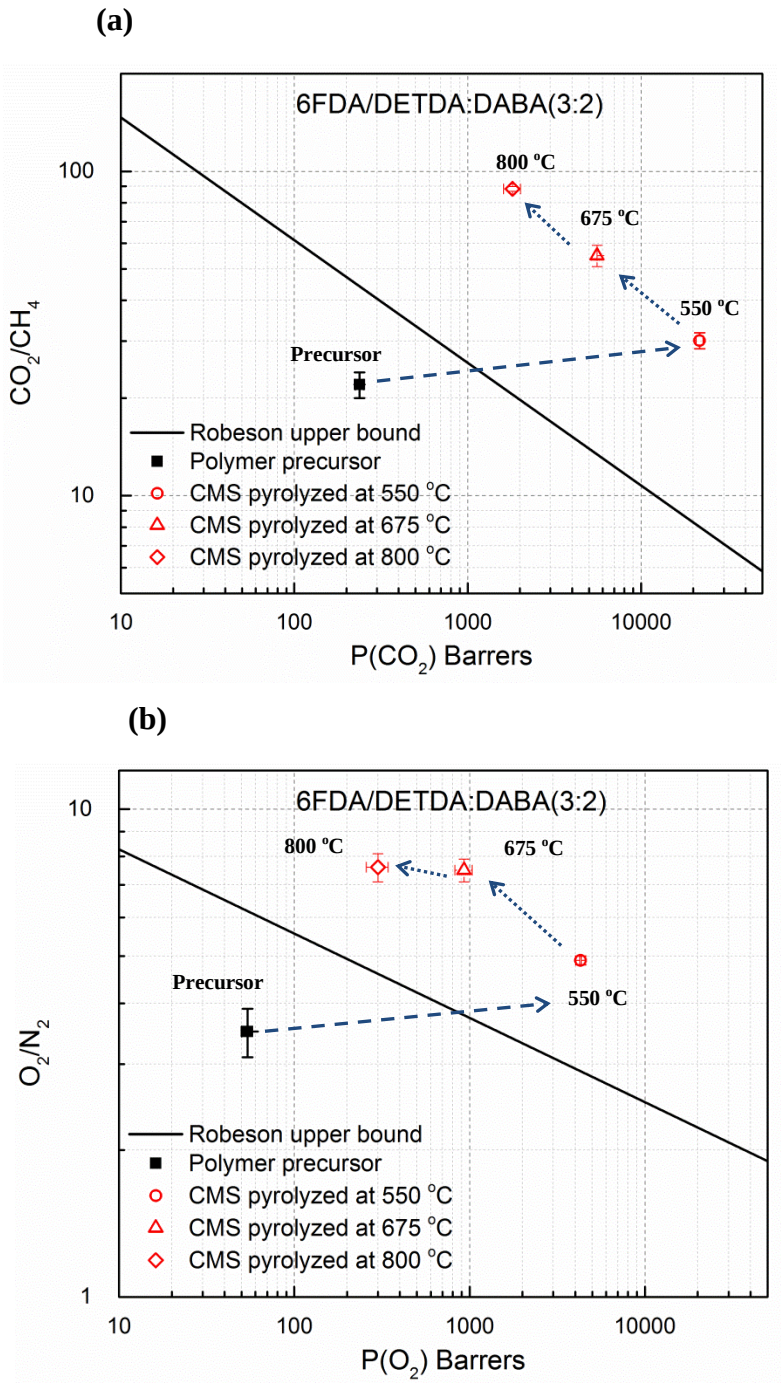

Figure 5.1: (a) Pure CO_2 permeability and CO_2/CH_4 selectivity; (b) pure O_2 permeability and O_2/N_2 selectivity of 6FDA/DETDA:DABA(3:2) precursor and CMS dense films pyrolyzed at 550 °C, 675 °C, and 800 °C. Robeson's CO_2/CH_4 and O_2/N_2 upper bound lines are shown for references [12].

Figure 5.2 represents an idealized, bimodal pore distribution in CMS membranes, with larger micropores (7-20 Å), connected with smaller ultramicropores (< 7 Å) [13-16]. It is believed that micropores provide high permeability and ultramicropores function as molecular sieving sites which provide high selectivity. We envision that as pyrolysis temperature increases, CMS structure becomes more tightly packed, and both micropores and ultramicropores distributions shift to smaller sizes. As a result for all gases, permeabilities decrease and selectivities increase.

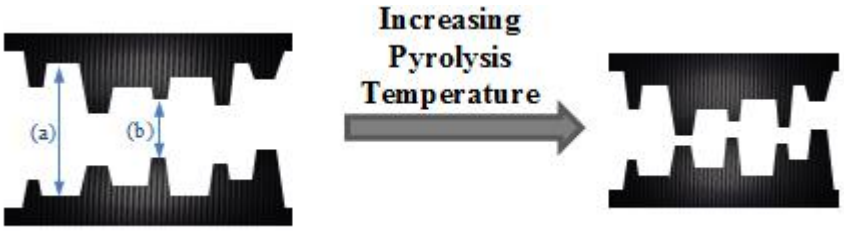

Figure 5.2: A simplified idealized slit-like pore structures in CMS membranes. (a): micropores with sizes of 7-20 Å; (b): ultramicropores with sizes < 7 Å.

5.2.2 Sorption

To further probe changes in micropores, pure gas CO_2, CH_4, O_2, and N_2 sorption capacities at 35 ^oC of 550 ^oC-, 675 ^oC-, and 800 ^oC- pyrolyzed 6FDA/DETDA:DABA(3:2) CMS dense films were measured and are shown in Figure 5.3. Only one sorption measurement was carried out for each sample without replicates considering the huge amount of time the sorption tests consumed, and moreover, we believe comparing with permeation and diffusion, sorption is a parameter of secondary importance. The experimental data were fitted to Langmuir isotherms and the fitted

parameters are listed in Table 5.2. The majority of the gas molecules are believed to be sorbed in micropores, thus sorption isotherms offer a useful probe of the CMS micropore structures. Figure 5.3 shows as final pyrolysis temperature increases, the sorption capacity for all gases of the corresponding CMS membrane decreases. From Table 5.2, it can be seen the loss of sorption capacity mainly results from the decrease of $C_H^{'}$, which implies a reduction of Langmuir sorption sites and tightened micropore structures. The relatively constancy of the affinity coefficient (b) with increasing temperature, however, suggests relatively small changes in the micropore distribution, with primarily a reduction in overall number of microvoids.

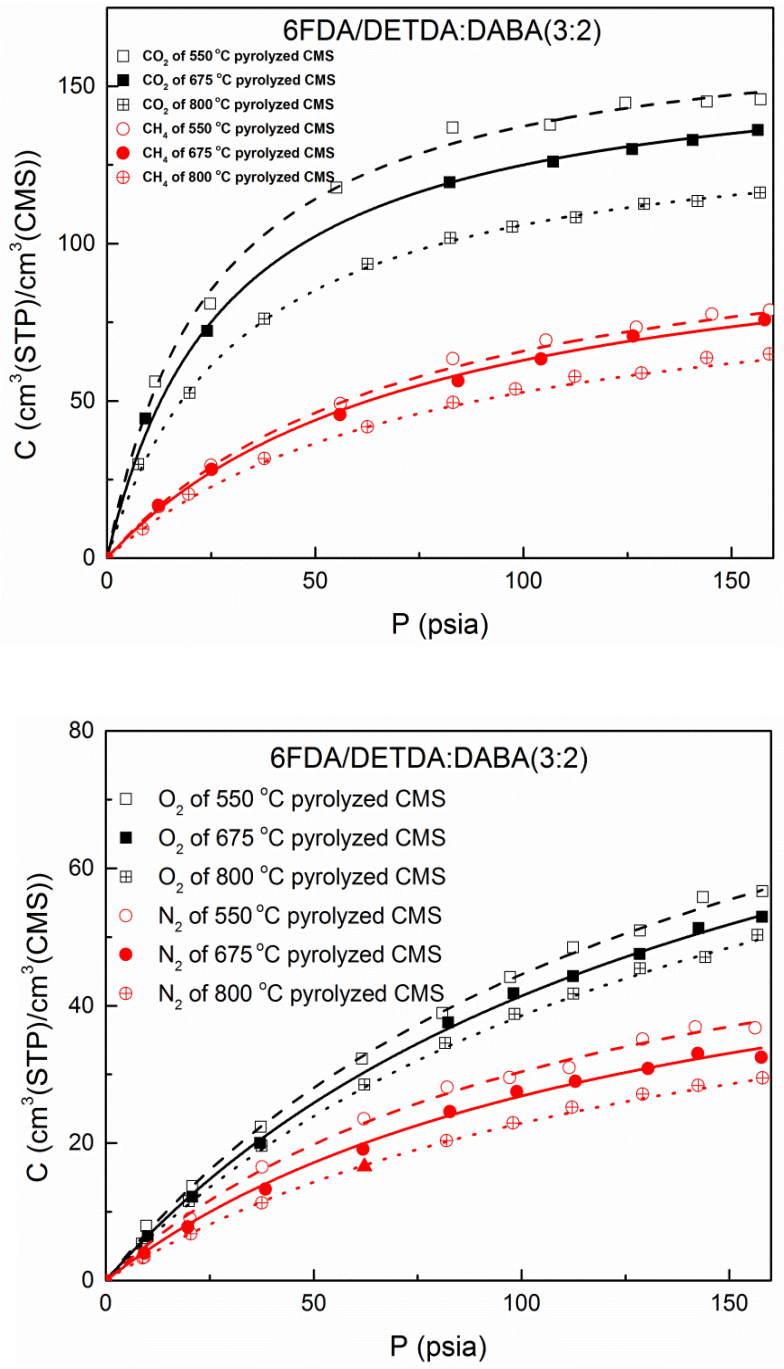

Figure 5.3: Pure gas CO_2, CH_4, O_2, and N_2 sorption isotherms at 35 ^oC of 550 ^oC-, 675 ^oC-, and 800 ^oC- pyrolyzed 6FDA/DETDA:DABA(3:2) CMS dense films.

Table 5.2: Pure gas CO_2, CH_4, O_2, and N_2 Langmuir isotherm parameters at 35 ^oC of 550 ^oC-, 675 ^oC-, and 800 ^oC- pyrolyzed 6FDA/DETDA:DABA(3:2) CMS dense films

		550 ^oC-CMS		675 ^oC-CMS		800 ^oC-CMS	
		CO_2	CH_4	CO_2	CH_4	CO_2	CH_4
C_H'	[cm^3(STP)/cm^3]	172.2	114.3	160.7	111.3	140.1	94.7
b	[1/psia]	0.039	0.014	0.035	0.013	0.031	0.013
		O_2	N_2	O_2	N_2	O_2	N_2
C_H'	[cm^3(STP)/cm^3]	108.3	65.2	104.2	61.7	99.7	57.0
b	[1/psia]	0.0070	0.0087	0.0066	0.0077	0.0063	0.0067

Table 5.3 below summarizes the CO_2, O_2 permeabilities, sorption coefficients, diffusion coefficients and the corresponding CO_2/CH_4, O_2/N_2 selectivities of 550 ^oC-, 675 ^oC-, and 800 ^oC- pyrolyzed 6FDA/DETDA:DABA(3:2) CMS dense films at 35 ^oC and 30 psia. The permeability P_A, overall membrane selectivity $\alpha_{A/B}$, sorption coefficients $\mathbb{S}_A$ and sorption selectivity $\mathbb{S}_A/\mathbb{S}_B$ are determined directly from permeation and sorption measurements. The sorption coefficient, $\mathbb{S}$ = C/P, is determined to be the secant slope of the isotherm at a given pressure, and for consistency, the sorption coefficients reported here correspond to a sorption pressure of 30 psia, which equals the permeation feed pressure. The diffusion coefficients D_A, and diffusion selectivity D_A/D_B are calculated according to Eq. 2.11 and Eq. 2.12. Both sorption and diffusion coefficients follow a similar trend to that for permeability, decreasing with increase in pyrolysis temperature. Diffusion coefficients in CMS reflect the packing of a material matrix and a decreased diffusion coefficient represents an overall tightened matrix, which is consistent with our hypothesis regarding the structure evolution as shown in Figure 5.2. On the other hand, sorption selectivity and diffusion selectivity show different responses in comparison to

the overall selectivity for gas pairs CO_2/CH_4 vs. O_2/N_2. For CO_2/CH_4 separation, the great enhancement in overall selectivity mainly results from the increase in diffusion selectivity (from ~12 to ~35) while sorption selectivity remains in the range of 2.8-2.5. Nevertheless for O_2/N_2 separation, the contributions from sorption selectivity and diffusion selectivity are similar. More pronounced O_2/N_2 diffusion selectivity enhancement might be achieved if higher pyrolysis temperature, 900 ^oC for instance, were explored; however, this was beyond the scope of this study.

Table 5.3: The permeability P_A, overall membrane selectivity $\alpha_{A/B}$, sorption coefficient $\mathbb{S}_A$, sorption selectivity $\mathbb{S}_A / \mathbb{S}_B$, diffusion coefficient D_A, and diffusion selectivity D_A / D_B of gas pairs CO_2/CH_4 and O_2/N_2 for 550 ^oC-, 675 ^oC-, and 800 ^oC- pyrolyzed 6FDA/DETDA:DABA(3:2) CMS dense films at 35 ^oC and 30 psia. Permeation results represent the average with variance within 15%.

Membranes	P_{CO_2} **Barrer**	α_{CO_2/CH_4}	$\mathbb{S}_{CO_2}$ **cc(STP)/cm^3/psia**	$\mathbb{S}_{CO_2}/\mathbb{S}_{CH_4}$	D_{CO_2} **10^{-7}cm^2/s**	D_{CO_2} / D_{CH_4}
550 ^oC-CMS	**21740**	30.1	**3.1**	2.8	**36.3**	10.8
675 ^oC-CMS	**5569**	55.0	**2.7**	2.6	**10.7**	21.2
800 ^oC-CMS	**1812**	88.3	**2.3**	2.5	**4.1**	35.3
	P_{O_2} **Barrer**	α_{O_2/N_2}	$\mathbb{S}_{O_2}$ **cc(STP)/cm^3/psia**	$\mathbb{S}_{O_2}/\mathbb{S}_{N_2}$	D_{O_2} **10^{-7}cm^2/s**	D_{O_2} / D_{N_2}
550 ^oC-CMS	**4293**	4.9	**0.6**	1.4	**37.0**	3.5
675 ^oC-CMS	**928**	7.5	**0.6**	1.5	**8.0**	5.0
800 ^oC-CMS	**300**	7.6	**0.5**	1.7	**3.1**	4.5

5.3 Effect of O_2 doping on 6FDA/DETDA:DABA(3:2) CMS membrane separation performance

Kiyono et al. [2, 3] developed a fine tuning method referred to as "oxygen doping", in which a trace amount of oxygen was introduced into the pyrolysis atmosphere. By studying the separation performance of 6FDA/BPDA-DAM CMS membranes pyrolyzed in 4, 8, 30 and 50 ppm O_2 doped argon, they found a strong correlation between the amount of oxygen available during pyrolysis and separation performance. In this study, 6FDA/DETDA:DABA(3:2) precursor dense films were pyrolyzed at 550 ^{o}C using protocol 1 listed in Chapter 3 except that instead of purging pure argon, a mixture of argon and 30 ppm or 50 ppm oxygen was used.

5.3.1 Permeation

The gas separation performance for pure and mixture gases of these two O_2 doped samples, along with the original 550 ^{o}C-undoped CMS membranes are listed in Table 5.4. The pure gas CO_2, O_2 permeability and CO_2/CH_4, O_2/N_2 selectivity results are plotted in Figure 5.4. It is clear that as the doping amount of O_2 increases, gas selectivity increases with a moderate reduction in permeability. It is noteworthy that comparing to pyrolysis temperature, O_2 doping exerts smaller effects on the gas transport property in CMS membranes, i.e., smaller permeability and selectivity changes are witnessed. This finding supports the claim by Kiyono that O_2 doping is a fine tuning method in adjusting the separation performance of CMS membranes [17].

Table 5.4: Pure and mixture gases permeation results of 550 ^{o}C-, 550 ^{o}C-30 ppm O_2 doped and 550 ^{o}C-50 ppm O_2 doped CMS membranes as well as polymeric membranes derived from 6FDA/DETDA:DABA(3:2). Pure gas permeations were measured at 35 ^{o}C and 30 psia, mixture gas permeations were measured at 35 ^{o}C and 60 psia.

Membranes	**Pure gases**			
	P_{CO_2} (Barrer)	α_{CO_2/CH_4}	P_{O_2} (Barrer)	α_{O_2/N_2}
Polymeric-	238 ±13	22.0 ±2	54 ±4	3.5 ±0.4
550 ^{o}C-CMS	21740 ±944	30.1 ±1.7	4293 ±45	4.9 ±0.1
550 ^{o}C-30 ppm O_2 doped-CMS	9679 ±847	41.8 ±3.5	1908 ±145	6.7 ±0.4
550 ^{o}C-50 ppm O_2 doped -CMS	3213 ±283	60.9 ±5.1	450 ±39	6.3 ±0.3
Membranes	**Mixture gases**			
	50% CO_2/50% CH_4		50% C_3H_6/50% C_3H_8	
	P_{CO_2} (Barrer)	α_{CO_2/CH_4}	$P_{C_3H_6}$ (Barrer)	$\alpha_{C_3H_6/C_3H_8}$
Polymeric-	-	-	-	-
550 ^{o}C-CMS	20073 ±1627	37.6 ±5.0	2444 ±99	12.7 ±0.8
550 ^{o}C-30 ppm O_2 doped-CMS	7972 ±938	48.5 ±3.1	941 ±89	23.1 ±1.8
550 ^{o}C-50 ppm O_2 doped -CMS	2163 ±189	70.3 ±4.2	101 ±8	50.7 ±2.3

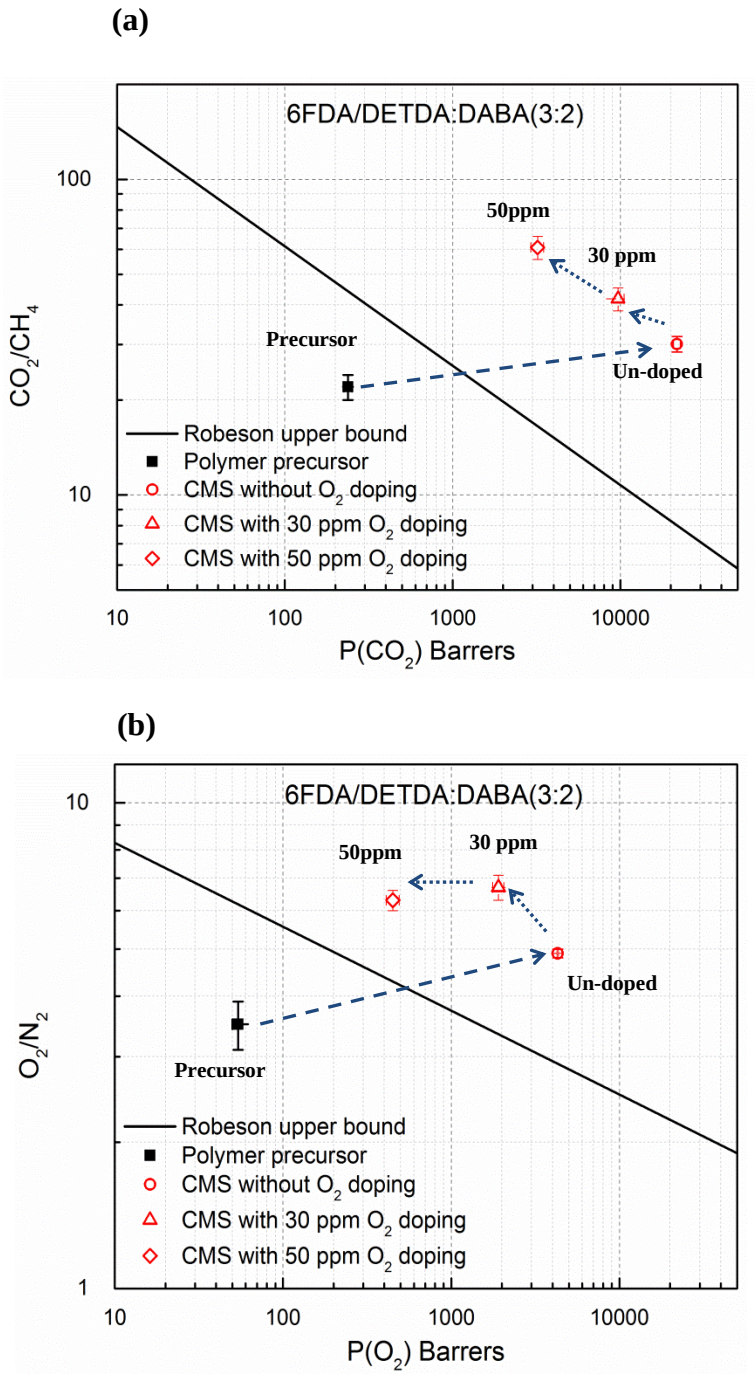

Figure 5.4: (a) Pure CO_2 permeability and CO_2/CH_4 selectivity; (b) pure O_2 permeability and O_2/N_2 selectivity of 6FDA/DETDA:DABA(3:2) precursor and CMS dense films pyrolyzed at 550 ^oC, 550 ^oC-30 ppm O_2 doped, and 550 ^oC-50 ppm O_2 doped. Robeson's CO_2/CH_4 and O_2/N_2 upper bound lines are shown for references [12].

Figure 5.5 represents a hypothetical schematic illustrating the oxygen doping process during pyrolysis. As a result for all gases, permeabilities decrease and selectivities increase. Kiyono et al. [3] envisioned that the majority of the oxygen molecules would react and bind to the ultramicropores in CMS membranes. Former studies on the electrochemical oxidation of carbon have shown that with more reactive unpaired sigma electrons prone to oxidation, the carbon on edge plane has a 17 times greater gas-phase oxidation rate than on the basal plane [18-20]. This process narrows the ultramicropore windows, and as a result, lowers the membrane permeability and enhances the selectivity. Nevertheless in Kiyono's study [3], they demonstrated the existence of a cut-off point. If exceedingly amount of oxygen molecules is available in the pyrolysis environment and most highly reactive edge sites are oxidized and filled, faster penetrants would also be hindered and as a result, both lower permeability and lower selectivity would be observed. In this work, we have not reached such a point, since selectivity was not found to decrease at any of the O_2 doping levels that showed "over-doping" in Kiyono's work with intrinsically less packing resistance precursors such as Matrimid® and 6FDA:BPDA/DAM [17].

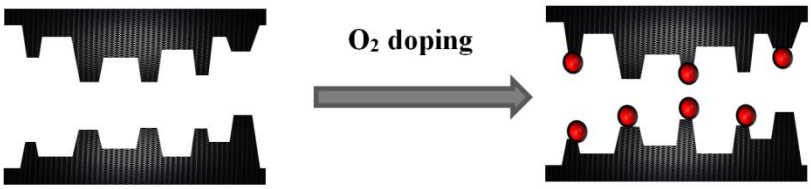

Figure 5.5: A hypothetical schematic of oxygen doping process during pyrolysis. ● represents chemisorbed O_2 molecule.

5.3.2 Sorption

The sorption isotherms of pure gas CO_2, CH_4, O_2, and N_2 at 35 ^oC of 550 ^oC-, 550 ^oC-30 ppm O_2 doped, and 550 ^oC-50 ppm O_2 doped 6FDA/DETDA:DABA(3:2) CMS dense films are shown in Figure 5.6. The fitted Langmuir isotherms parameters are listed in Table 5.5. The almost unchanged sorption capacity and C_H' for all gases leads us to the conclusion that the oxygen doping process has little influence on the micropore structure.

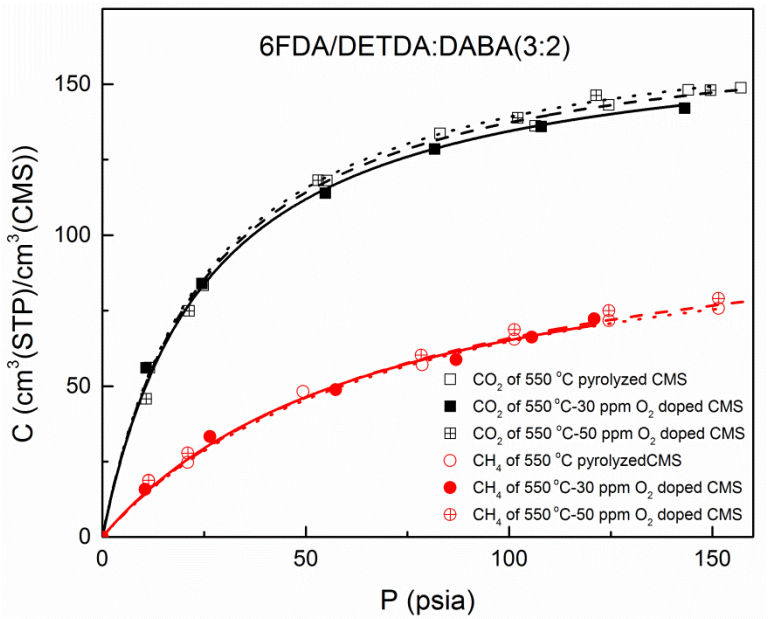

Figure 5.6: Pure gas CO_2, CH_4, O_2, and N_2 sorption isotherms at 35 ^oC of 550 ^oC-, 550 ^oC-30 ppm O_2 doped, and 550 ^oC-50 ppm O_2 doped 6FDA/DETDA:DABA(3:2) CMS dense films.

Table 5.5: Pure gas CO_2, CH_4, O_2, and N_2 Langmuir isotherm parameters at 35 ^oC of 550 ^oC-, 550 ^oC-30 ppm O_2 doped, and 550 ^oC-50 ppm O_2 doped 6FDA/DETDA:DABA(3:2) CMS dense films.

		550 ^oC-		550 ^oC- 30 ppm O_2 doped		550 ^oC- 50 ppm O_2 doped	
		CO_2	CH_4	CO_2	CH_4	CO_2	CH_4
C_H'	[cm^3(STP)/cm^3]	172.2	114.3	168.4	109.9	174.8	112.4
b	[1/psia]	0.039	0.014	0.040	0.015	0.039	0.014
		O_2	N_2	O_2	N_2	O_2	N_2
C_H'	[cm^3(STP)/cm^3]	108.3	65.2	109.0	66.4	108.1	66.4
b	[1/psia]	0.007	0.009	0.007	0.009	0.007	0.008

Table 5.6 below summarizes the CO_2, O_2 permeabilities, sorption coefficients, diffusion coefficients and the corresponding CO_2/CH_4, O_2/N_2 selectivities of 550 ^oC-, 550 ^oC-30 ppm O_2 doped, and 550 ^oC-50 ppm O_2 doped 6FDA/DETDA:DABA(3:2) CMS dense films at 35 ^oC and 30 psia. Sorption coefficient remains almost unchanged while diffusion coefficients drop as the amount of oxygen doping increases, which is the main reason for permeability drop. On the other hand, the gain in overall selectivity also mainly stems from the increase in diffusion selectivity, which is in agreement with what have been found in the study on different temperature pyrolyzed CMS membranes.

Table 5.6: The permeability P_A, overall membrane selectivity $\alpha_{A/B}$, sorption coefficient $\mathbb{S}_A$, sorption selectivity $\mathbb{S}_A / \mathbb{S}_B$, diffusion coefficient D_A, and diffusion selectivity D_A / D_B of gas pairs CO_2/CH_4 and O_2/N_2 for 550 ^oC-, 550 ^oC-30 ppm O_2 doped, and 550 ^oC-50 ppm O_2 doped 6FDA/DETDA:DABA(3:2) CMS dense films.at 35 ^oC and 30 psia. Permeation results represent the average with variance within 15%.

Membranes	P_{CO_2} **Barrer**	α_{CO_2/CH_4}	$\mathbb{S}_{CO_2}$ **cc(STP)/cm^3/psia**	$\mathbb{S}_{CO_2}/\mathbb{S}_{CH_4}$	D_{CO_2} **10^{-7}cm^2/s**	D_{CO_2} / D_{CH_4}
550 ^oC-CMS	**21740**	30.1	**3.1**	2.8	**36.3**	10.8
550 ^oC-30 ppm O_2 doped-CMS	**9679**	41.8	**3.1**	2.7	**16.2**	15.5
550 ^oC-50 ppm O_2 doped -CMS	**3213**	60.9	**3.1**	2.9	**5.4**	21.0
	P_{O_2} **Barrer**	α_{O_2/N_2}	$\mathbb{S}_{O_2}$ **cc(STP)/cm^3/psia**	$\mathbb{S}_{O_2}/\mathbb{S}_{N_2}$	D_{O_2} **10^{-7}cm^2/s**	D_{O_2} / D_{N_2}
550 ^oC-CMS	**4293**	4.9	**0.6**	1.4	**37.0**	3.5
550 ^oC-30 ppm O_2 doped-CMS	**1908**	6.7	**0.6**	1.3	**16.5**	5.2
550 ^oC-50 ppm O_2 doped -CMS	**450**	6.3	**0.6**	1.4	**3.8**	4.5

5.4 Effect of precrosslinking during pyrolysis on 6FDA/DETDA:DABA(3:2) CMS membrane separation performance

5.4.1 Permeation

Qiu et al. developed a new decarboxylation-induced thermal crosslinking in DABA containing polymeric membranes at temperature below the material's T_g (glass transition temperature) [9, 21]. They demonstrated that the membrane was highly-crosslinked after being thermally annealed at 370 ^oC for an hour. What's more, this novel method not only stabilizes polymer membranes against swelling and plasticization in aggressive feed streams, it also induces a significant increase in membrane permeability with slight loss in selectivity. In this study we incorporated this method in the application of carbon membranes, and to the best of the authors' knowledge, no former publications have addressed this topic. Since crosslinking tends to open up the membrane structure, a final pyrolysis temperature of 800 ^oC, which has been proven to offer compact CMS membrane, was selected. An adjusted pyrolysis protocol listed as protocol 3 in Chapter 3 was followed. More specifically, 6FDA/DETDA:DABA(3:2) polymer membrane was precrosslinked by soaking in 370 ^oC for 90 minutes before being heated to 800 ^oC. The proposed mechanism of decarboxylation-induced crosslinking is illustrated in Figure 5.7.

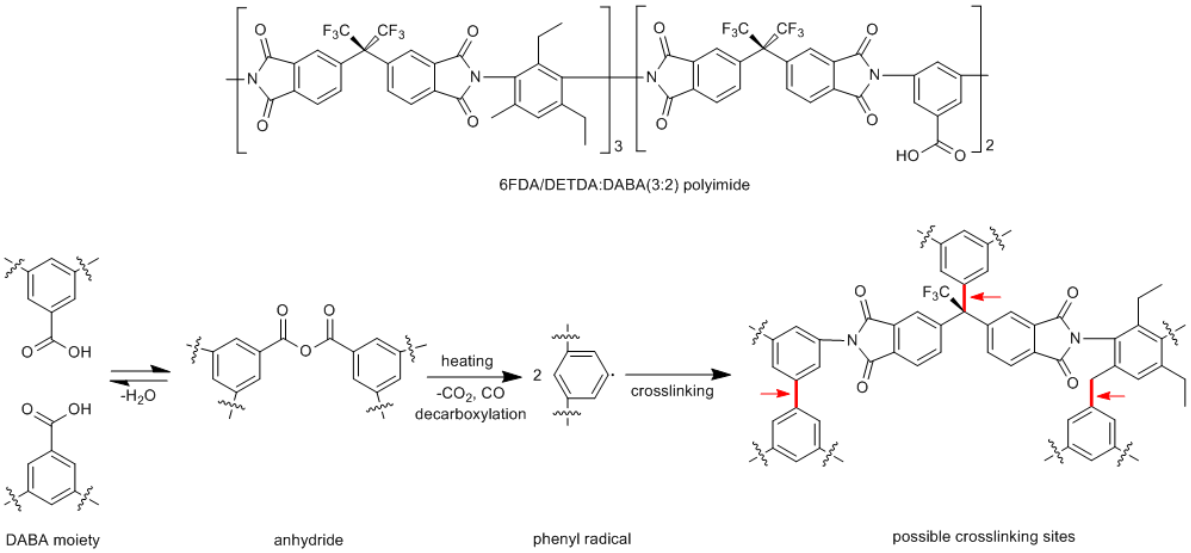

Figure 5.7: Chemical structure of 6FDA/DETDA:DABA (3:2) and crosslinking mechanism of decarboxylation-induced crosslinking. Possible crosslinking sites are noted with an arrow [22].

The precrosslinked CMS membranes were tested for their solubility to serve as an indirect proof of whether crosslinking happened. Polymeric 6FDA/DETDA:DABA (3:2) membranes were thermally treated in the pyrolysis system at 370 ^{o}C for 90 mins and soaked in NMP. The original 6FDA/DETDA:DABA (3:2) polymeric dense film were easily dissolved in NMP at room temperature; however, the thermally treated membranes were insoluble in NMP either at room temperature or elevated temperature, indicating the membranes were highly crosslinked.

The same 4 pure gases and 2 mixture gases were used to examine the separation performance of this novel 800 ^{o}C-precrosslinked CMS and results are shown in Table 5.7, the earlier-illustrated separation performance of 550 ^{o}C- and 800 ^{o}C- pyrolyzed CMS are also listed for comparison purpose. The pure gas CO_2, O_2 permeability and CO_2/CH_4,

O_2/N_2 selectivity results are plotted in Figure 5.8. It can be observed that compared with 800 ^oC- pyrolyzed CMS, the permeabilities of 800 ^oC-precrosslinked CMS were significantly higher, increased by about 158% (pure CO_2), 128% (pure O_2), 92% (CO_2 in mixture gas 50% CO_2/50% CH_4), and 194% (C_3H_6 in mixture gas 50% C_3H_6/50% C_3H_8). It is believed that the higher permeabilities results from the DABA moiety in the precursor polymer. As decarboxylation occurs, microvoids and packing disruptions are created and the polymer chains are locked in. Such a crosslinked structure might thereby be maintained in the subsequent pyrolysis process. What accompany these huge permeability enhancements are slight selectivities losses: 19% (pure CO_2/CH_4), -5% (pure O_2/N_2), 42% (mixture gas 50% CO_2/50% CH_4), 18% (mixture gas 50% C_3H_6/50% C_3H_8). Detailed analysis of diffusion selectivity and sorption selectivity in the following section will provide further explanation of the overall selectivity losses.

Table 5.7: Pure and mixture gases permeation results of 550 ^{o}C-, 800 ^{o}C- and 800 ^{o}C-precrosslinked-6FDA/DETDA:DABA(3:2) CMS membranes. Pure gas permeations were measured at 35 ^{o}C and 30 psia, mixture gas permeations were measured at 35 ^{o}C and 60 psia.

Membranes	**Pure gases**			
	P_{CO_2} (Barrer)	α_{CO_2/CH_4}	P_{O_2} (Barrer)	α_{O_2/N_2}
Polymeric-	238 ±13	22.0 ±2	54 ±4	3.5 ±0.4
550 ^{o}C-CMS	21740 ±944	30.1 ±1.7	4293 ±45	4.9 ±0.1
800 ^{o}C-CMS	1812 ±204	88.3 ±1.5	300 ±43	7.6 ±0.5
800 ^{o}C-precrosslinked-CMS	4678 ±81	71.5 ±4.0	683 ±5	8.0 ±0.1

Membranes	**Mixture gases**			
	50% CO_2/50% CH_4		50% C_3H_6/50% C_3H_8	
	P_{CO_2} (Barrer)	α_{CO_2/CH_4}	$P_{C_3H_6}$ (Barrer)	$\alpha_{C_3H_6/C_3H_8}$
Polymeric-	-	-	-	-
550 ^{o}C-CMS	20073 ±1627	37.6 ±5.0	2444 ±99	12.7 ±0.8
800 ^{o}C-CMS	1397 ±132	102.7 ±0.9	71 ±1	63.7 ±0.2
800 ^{o}C-precrosslinked-CMS	2690 ±223	59.8 ±0.3	200 ±40	52.0 ±5.0

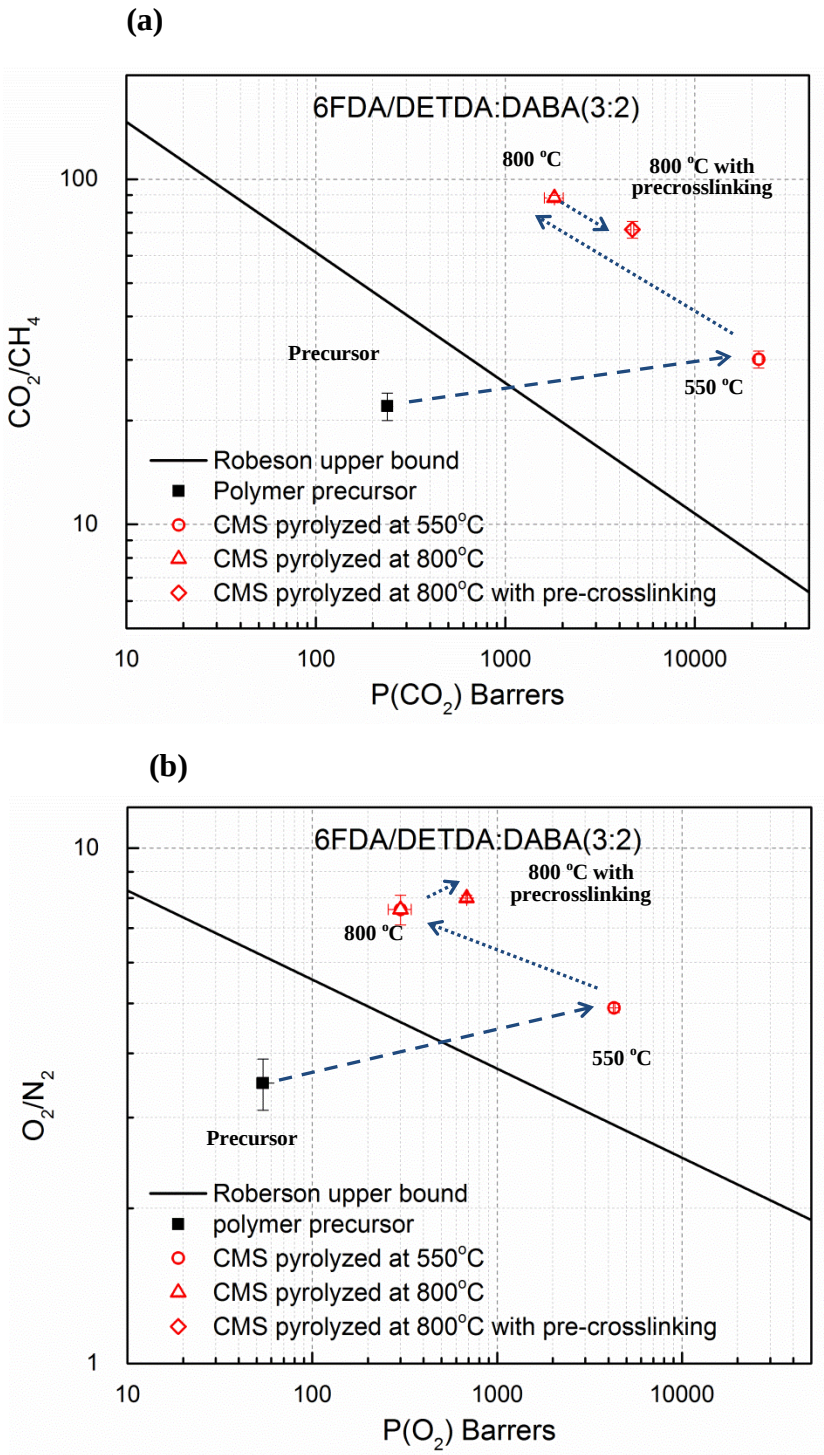

Figure 5.8: (a) Pure CO_2 permeability and CO_2/CH_4 selectivity; (b) pure O_2 permeability and O_2/N_2 selectivity of 6FDA/DETDA:DABA(3:2) precursor and CMS dense films pyrolyzed at 550 °C, 800 °C, and 800 °C-precrosslinked. Robeson's CO_2/CH_4 and O_2/N_2 upper bound lines are shown for references [12].

5.4.2 Sorption

The sorption isotherms of pure gas CO_2, CH_4, O_2, and N_2 at 35 ^oC of 800 ^oC- and 800 ^oC-precrosslinked 6FDA/DETDA:DABA(3:2) CMS dense films are shown in Figure 5.9. The fitted Langmuir isotherms parameters are listed in Table 5.8. After precrosslinking, the sorption capacity for all gases increases. The increase in C_H' suggests a more open micropore structure with more Langmuir sorption sites.

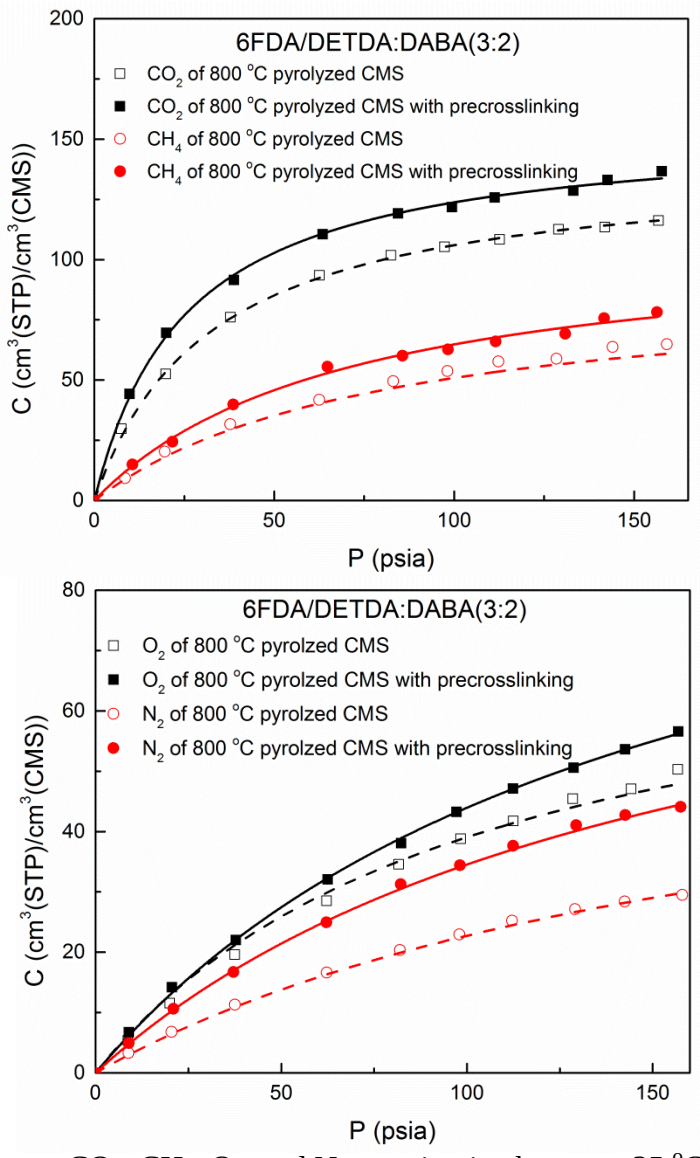

Figure 5.9: Pure gas CO_2, CH_4, O_2, and N_2 sorption isotherms at 35 ^oC of 800 ^oC, and 800 ^oC-precrosslinked 6FDA/DETDA:DABA(3:2) CMS dense films.

Table 5.8: Pure gas CO_2, CH_4, O_2, and N_2 Langmuir isotherm parameters at 35 ^oC of 800 ^oC- and 800 ^oC-precrosslinked- 6FDA/DETDA:DABA(3:2) CMS dense films.

		800 ^oC		800 ^oC with precrosslinking	
		CO_2	CH_4	CO_2	CH_4
C_H'	[cm^3(STP)/cm^3]	140.1	95.2	155.4	110.7
b	[1/psia]	0.031	0.013	0.039	0.014
		O_2	N_2	O_2	N_2
C_H'	[cm^3(STP)/cm^3]	99.7	57.0	110.3	88.9
b	[1/psia]	0.006	0.007	0.007	0.006

The CO_2, O_2 permeabilities, sorption coefficients, diffusion coefficients and the corresponding CO_2/CH_4, O_2/N_2 selectivities of 800 ^oC- and 800 ^oC-precrosslinked 6FDA/DETDA:DABA(3:2) CMS dense films at 35 ^oC and 30 psia are listed in Table 5.9. It can be seen that the increase in permeability results from the increase in both sorption and diffusion coefficient. On the other hand, again sorption selectivity and diffusion selectivity have different contributions to the overall selectivity for different gas pairs CO_2/CH_4 vs. O_2/N_2. For CO_2/CH_4, the overall selectivity decreases after precrosslinking, which solely dues to the drop in diffusion selectivity from ~35 to ~28. Nevertheless O_2/N_2 overall selectivity increases slightly after precrosslinking, which is a combined result from opposing effects from sorption selectivity and diffusion selectivity. Since the diffusion selectivity increase is more prominent than the sorption selectivity decrease, overall O_2/N_2 selectivity increases. The higher diffusion selectivity is hypothesized to due to the more complex and tortuous pore structures in precrosslinked CMS membranes.

Table 5.9: The permeability P_A, overall membrane selectivity $\alpha_{A/B}$, sorption coefficient $\mathbb{S}_A$, sorption selectivity $\mathbb{S}_A / \mathbb{S}_B$, diffusion coefficient D_A, and diffusion selectivity D_A / D_B of gas pairs CO_2/CH_4 and O_2/N_2 for 800 ^oC-, and 800 ^oC-precrosslinked- 6FDA/DETDA:DABA(3:2) CMS dense films at 35 ^oC and 30 psia. Permeation results represent the average with variance within 15%.

Membranes	P_{CO_2} **Barrer**	α_{CO_2/CH_4}	$\mathbb{S}_{CO_2}$ **cc(STP)/cm^3/psia**	$\mathbb{S}_{CO_2}/\mathbb{S}_{CH_4}$	D_{CO_2} **10^{-7}cm^2/s**	D_{CO_2} / D_{CH_4}
550 ^{o}C-CMS	**21740**	30.1	**3.1**	2.8	**36.3**	10.8
800 ^{o}C-CMS	**1812**	88.3	**2.3**	2.5	**4.1**	35.3
800 ^{o}C-precrosslinked-CMS	**4678**	71.5	**2.8**	2.5	**8.6**	28.1
	P_{O_2} **Barrer**	α_{O_2/N_2}	$\mathbb{S}_{O_2}$ **cc(STP)/cm^3/psia**	$\mathbb{S}_{O_2}/\mathbb{S}_{N_2}$	D_{O_2} **10^{-7}cm^2/s**	D_{O_2} / D_{N_2}
550 ^{o}C-CMS	**4293**	4.9	**0.6**	1.4	**37.0**	3.5
800 ^{o}C-CMS	**300**	7.6	**0.5**	1.7	**3.1**	4.5
800 ^{o}C-precrosslinked-CMS	**683**	8.0	**0.6**	1.3	**5.8**	6.2

5.5 The comparison of effects of pyrolysis temperature, O_2-doping, and precrosslinking during pyrolysis on 6FDA/DETDA:DABA(3:2) CMS membrane separation performance

Section 5.2, 5.3, and 5.4 investigated the effects of pyrolysis temperature; O_2 doping; and precrosslinking, respectively, on the separation performance of 6FDA/DETDA:DABA(3:2) CMS membranes. In this section, the effects of these three pyrolyzing parameters are summarized and compared. Moreover, speculative hypotheses regarding the structure changes brought about by changing these parameters were also provided.

Table 5.10 tabulates the permeabilities, sorption coefficients, Langmuir hole filling capacities C_H' and Langmuir affinity constants b of gas CO_2 as well as the CO_2/CH_4 selectivity of polymeric-; 550 ^oC-CMS; 800 ^oC-CMS; 550 ^oC-50 ppm O_2 doped -CMS membranes, and 800 ^oC-precrosslinked-CMS; and derived from 6FDA/DETDA:DABA(3:2). Figure 5.10 summarizes the fitted Langmuir sorption isotherms of pure gas CO_2 at 35 ^oC of these membrane materials. As can be seen compared to the 550 ^oC-CMS membrane: 1) with increased pyrolysis temperature, the 800 ^oC-CMS membrane presents lower CO_2 permeability, sorption coefficient, C_H' and b and higher CO_2/CH_4 selectivity; 2) with O_2 doping, the 550 ^oC-50 ppm O_2 doped -CMS membrane presents lower CO_2 permeability, higher CO_2/CH_4 selectivity, but almost the same sorption coefficient, C_H' and b; compared to the 800 ^oC-CMS membrane, with precrosslinking, the 800 ^oC-precrosslinked-CMS membrane presents higher CO_2 permeability, sorption coefficient, C_H' and b and lower CO_2/CH_4 selectivity. These trends provide information of the membrane pore morphologies. Figure 5.11 is a speculative

scheme showing the comparison of the effects of final pyrolysis temperature, oxygen doping and precrosslinking on the CMS structures.

Table 5.10: Pure and mixture gases permeation results of 550 ^{o}C-, 800 ^{o}C- and 800 ^{o}C-precrosslinked- 6FDA/DETDA:DABA(3:2) CMS membranes. Pure gas permeations were measured at 35 ^{o}C and 30 psia, mixture gas permeations were measured at 35 ^{o}C and 60 psia.

Membranes	**Pure gases**				
	P_{CO_2} (Barrer)	α_{CO_2/CH_4}	$\mathbb{S}_{CO_2}$ cc(STP)/cm^3/psia	C_H' (CO_2) [cm^3(STP)/cm^3]	b (CO_2) [1/psia]
Polymeric-	238 ±13	22.0 ±2	-	-	-
550 ^{o}C-CMS	21740 ±944	30.1 ±1.7	3.1	172.2	0.039
800 ^{o}C-CMS	1812 ±204	88.3 ±1.5	2.3	140.1	0.031
550 ^{o}C-50 ppm O_2 doped - CMS	3213 ±283	60.9 ±5.1	3.1	174.8	0.039
800 ^{o}C-precrosslinked-CMS	4678 ±81	71.5 ±4.0	2.8	155.4	0.039

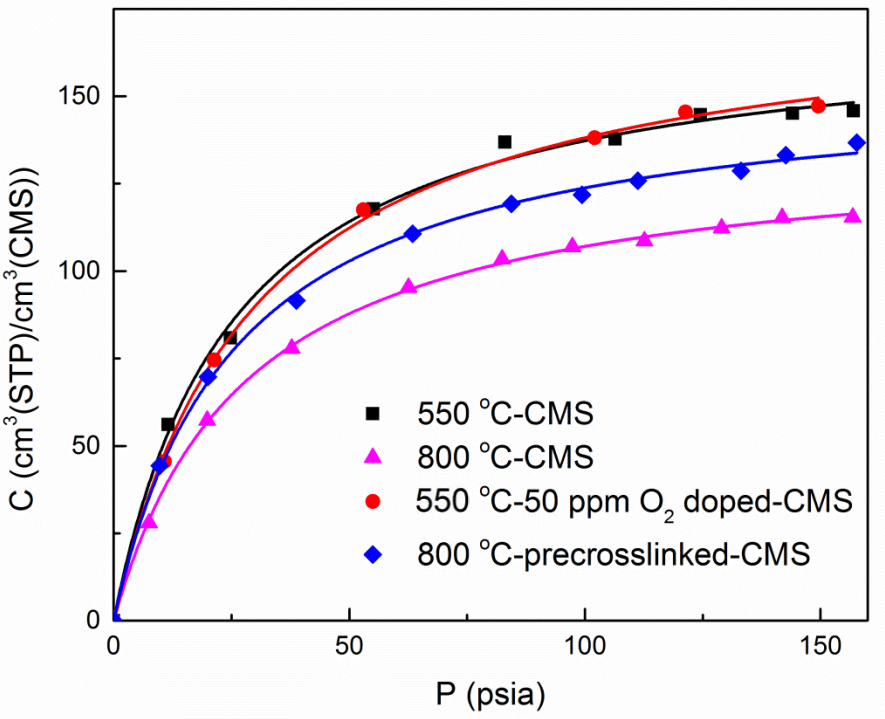

Figure 5.10: Pure gas CO_2 sorption isotherms at 35 ^{o}C of 550 ^{o}C-CMS; 800 ^{o}C-CMS; 550 ^{o}C-50 ppm O_2 doped –CMS; and 800 ^{o}C-precrosslinked-CMS membranes derived from 6FDA/DETDA:DABA(3:2).

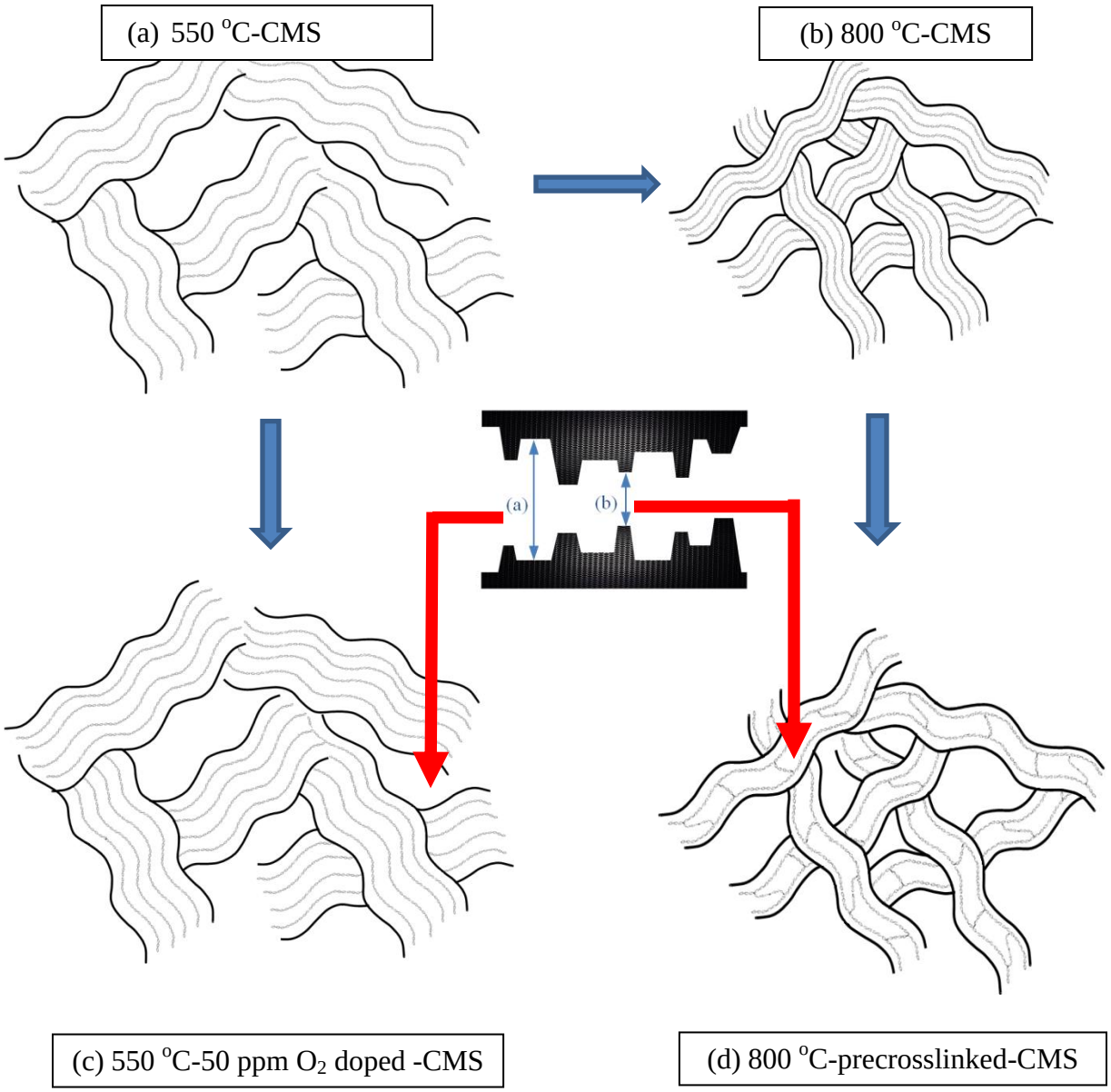

Figure 5.11: Speculative cartoon representation of the effects of the final pyrolysis temperature, oxygen doping, and precrosslinking on CMS structures: (a) 550 °C-CMS; (b) 800 °C-CMS; (c) 550 °C-50 ppm O_2 doped –CMS; and (d) 800 °C-precrosslinked-CMS. (a): micropores with sizes of 7-20 Å; (b): ultramicropores with sizes < 7 Å.

As has been explained in Chapter 2 and shown in Figure 5.11, CMS membranes can be described as amorphous over the long range with turbostratic ribbon-like structures; over the short range, the sp^2-hybridized carbon sheets can align parallel to each other and form somewhat ordered structure. It is hypothesized that the micropores in between the ribbon-like structures, resulting from the packing imperfection, provides sorption sites; while the ultramicropores in between the ordered carbon sheets enable molecular sieving. Pyrolysis at a relatively lower temperature of 550 ^{o}C results in an open intrinsic CMS framework with both large micropores and ultramicropores as can be seen in Figure 5.11 (a). During pyrolysis at a higher temperature of 800 ^{o}C, the CMS framework is condensed with both tightened micropores and ultramicropores as shown in Figure 5.11 (b). The condensed micropore structures result in lowered permeability and sorption while the tightened ultramicropore enhances gas selectivity. For oxygen doping during 550 ^{o}C, shown in Figure 5.11 (c), the intrinsic open framework is not condensed with unchanged micropore structure and thus sorption capacity, however, the ultramicropore is tuned by selective chemisorption of oxygen and results in higher gas selectivity. Figure 5.11 (d) shows the pore morphology of 800 ^{o}C-precrosslinked-CMS membrane, the precrosslinking step opens up the micropores and gives higher permeability and sorption capacity; however in the same time, it disturbs the ordered carbon sheets, and the less anisotropic ultramicropores lose some molecular sieving ability.

5.6 Summary

The effects of pyrolysis conditions including pyrolysis temperature, O_2 doping, and precrosslinking were studied based on 6FDA/DETDA:DABA(3:2) CMS dense film membranes for separation of important gas pairs including pure gases CO_2/CH_4, O_2/N_2 and mixture gases 50% CO_2/50% CH_4 and 50% C_3H_6/50% C_3H_8. It was shown that the increased pyrolysis temperature tends to give lower permeable but more selectivity membranes. The O_2 doping provides a fine tuning method in altering the separation performance of CMS membranes. Finally, CMS membranes derived from a novel method, which was first proposed for another DABA containing precursor and referred to as precrosslinking, was shown in this study to be very attractive with significantly improved gas permeability and slightly drop in selectivity.

The results reported in this chapter serve as a guide for future optimization study on CMS membranes. The optimized pyrolysis conditions will be highly dependent on the type of the CMS membrane used and the targeted gas pairs. For example, an optimized pyrolysis condition effective for CO_2/CH_4 separation is not necessarily ideal for O_2/N_2 separation. Different final pyrolysis temperatures or different amount of O_2 doping might be favored for different gas pair separations. Moreover, the combination of different tuning methods might also be attractive for some specific applications.

5.7 References

[1] V.C. Geiszler, W.J. Koros, Effects of Polyimide Pyrolysis Conditions on Carbon Molecular Sieve Membrane Properties, Ind. Eng. Chem. Res., 35 (1996) 2999-3003.

[2] M. Kiyono, P.J. Williams, W.J. Koros, Generalization of effect of oxygen exposure on formation and performance of carbon molecular sieve membranes, Carbon, 48 (2010) 4442-4449.

[3] M. Kiyono, P.J. Williams, W.J. Koros, Effect of pyrolysis atmosphere on separation performance of carbon molecular sieve membranes, J. Membr. Sci., 359 (2010) 2-10.

[4] M. Rungta, L. Xu, W.J. Koros, Carbon molecular sieve dense film membranes derived from Matrimid® for ethylene/ethane separation, Carbon, 50 (2012) 1488-1502.

[5] X. Ning, W.J. Koros, Carbon molecular sieve membranes derived from Matrimid® polyimide for nitrogen/methane separation, Carbon, 66 (2014) 511-522.

[6] Y.-J. Fu, K.-S. Liao, C.-C. Hu, K.-R. Lee, J.-Y. Lai, Development and characterization of micropores in carbon molecular sieve membrane for gas separation, Microporous Mesoporous Mater., 143 (2011) 78-86.

[7] K.M. Steel, W.J. Koros, An investigation of the effects of pyrolysis parameters on gas separation properties of carbon materials, Carbon, 43 (2005) 1843-1856.

[8] P.S. Tin, T.-S. Chung, Y. Liu, R. Wang, Separation of CO2/CH4 through carbon molecular sieve membranes derived from P84 polyimide, Carbon, 42 (2004) 3123-3131.

[9] W. Qiu, K. Zhang, F.S. Li, K. Zhang, W.J. Koros, Gas separation performance of carbon molecular sieve membranes based on 6FDA-mPDA/DABA (3:2) polyimide, ChemSusChem, 7 (2014) 1186-1194.

[10] M. Rungta, Carbon molecular sieve dense film membranes for ethylene/ethane separations, in, Georgia Institute of Technology, Atlanta, GA, 2012.

[11] X. Ning, Carbon molecualr sieve membranes for nitrogen/methane separation, in, Georgia Institute of Technology, 2014.

[12] L.M. Robeson, The upper bound revisited, J. Membr. Sci., 320 (2008) 390-400.

[13] H. Suda, K. Haraya, Gas permeation through micropores of carbon molecular sieve membranes derived from Kapton polyimide, J. Phys. Chem. B, 101 (1997) 3988-3994.

[14] K.M. Steel, W.J. Koros, Investigation of porosity of carbon materials and related effects on gas separation properties, Carbon, 41 (2003) 253-266.

[15] Y. Xiao, T.-S. Chung, M.L. Chng, S. Tamai, A. Yamaguchi, Structure and properties relationships for aromatic polyimides and their derived carbon membranes: Experimental and simulation approaches, J. Phys. Chem. B, 109 (2005) 18741-18748.

[16] L. Shao, T. Chung, G. Wensley, S. Goh, K. Pramoda, Casting solvent effects on morphologies, gas transport properties of a novel 6FDA/PMDA?TMMDA copolyimide membrane and its derived carbon membranes, Journal of Membrane Science, 244 (2004) 77-87.

[17] M. Kiyono, Carbon molecular sieve membranes for natural gas separations, in, Georgia Institute of Technology, Atlanta, Georgia, 2010.

[18] R.O. Grisdale, The Properties of Carbon Contacts, J. Appl. Phys., 24 (1953) 1288.

[19] H. Marsh, Introduction to Carbon Science, Butterworth & Co. Ltd., Borough Green, 1989.

[20] K. Kinoshita, Carbon: Electrochemical and Physicochemical Properties, Wiley-Interscience, Berkeley, CA, 1988.

[21] W. Qiu, C.-C. Chen, L. Xu, L. Cui, D.R. Paul, W.J. Koros, Sub-Tg Cross-Linking of a Polyimide Membrane for Enhanced CO_2 Plasticization Resistance for Natural Gas Separation, Macromolecules, 44 (2011) 6046-6056.

[22] S. Fu, E.S. Sanders, S.S. Kulkarni, W.J. Koros, Carbon molecular sieve membrane structure–property relationships for four novel 6FDA based polyimide precursors, J. Membr. Sci., 487 (2015) 60-73.

CHAPTER 6

ANALYSIS OF THE EFFECTS OF TESTING TEMPERATURE ON THE GAS SEPARATION PERFORMANCE OF CARBON MOLECULAR SIEVE (CMS) DENSE FILM MEMBRANES

6.1 Overview

CMS fiber membranes have been proven to maintain stability under high pressure up to 1000 psi without undergoing plasticization [1-3]; however, temperature effects on CMS membranes need more systematic investigations. Analysis of the effects of testing temperature on CMS membrane performance is important not just from a practical purpose, but also for a fundamental understanding of this type of material. In this chapter, a more in-depth understanding of the complex separation process is provided by studying the sorptive and diffusive contributions to permeation and permselectivity over a certain range of temperature. Seven types of membranes were studied: four CMS membranes derived from 6FDA-based precursor polyimides: 6FDA/DETDA, 6FDA:BPDA(1:1)/DETDA, 6FDA/1,5-ND:ODA(1:1), and 6FDA/DETDA:DABA(3:2), and three types of membranes derived from 6FDA/DETDA:DABA(3:2) including polymeric-; 800 ^{o}C-; and 800 ^{o}C-precrosslinked CMS membranes. In Section 6.2, analysis of activation energies of permeation and diffusion as well as heats of sorption for CO_2, CH_4, O_2, and N_2 in the four CMS materials derived from the above-mentioned 6FDA-based precursors provides insights regarding the permeability and selectivity

changes at higher temperature. In addition, the study of these related CMS materials provides a tool to identify structural characteristics that affect permeability and selectivity. Finally, the diffusion selectivity is factored into "energetic" and "entropic" selectivity contributions to clarify the importance of entropic factors as tools to tailor membrane performance. In section 6.3, a similar study is conducted on the three membranes derived from 6FDA/DETDA:DABA(3:2). The analysis of the selectivity factors provides fundamental insights into the reason that CMS membranes outperform polymeric membranes.

6.2 Temperature dependence of gas transport and sorption in CMS membranes derived from four 6FDA- based polyimides

6.2.1 Characterization of the four CMS membranes

Prior to discussing the main transport and sorption properties of these carbon membranes, it is useful to probe the difference in their pore structures. In this study, we used sorption-based micropore distribution analysis to provide insight in the pore morphologies of these materials.

The pore distributions (shown in Figure 6.1) of the four CMS membranes pyrolyzed at 550 ^{o}C under UHP argon were characterized using CO_2 sorption uptakes analyzed in terms of density functional theory [4, 5]. Figure 6.1 indicates the presence of a bimodal pore distribution as the authors have noted in the theory and background section. In both micropore and ultramicropore regions, there is no clear pattern observable about the peaks of the pore width distributions of the four membranes. As a matter of fact, the critical molecular sieving ultramicropores are expected to be smaller than 4 Å (in the range of gas sizes as listed in Table 3.2 in Section 3.2). Thus, the

permeability-selectivity trends cannot be conclusively determined based on pore size distributions obtained from CO_2 sorption measurement.

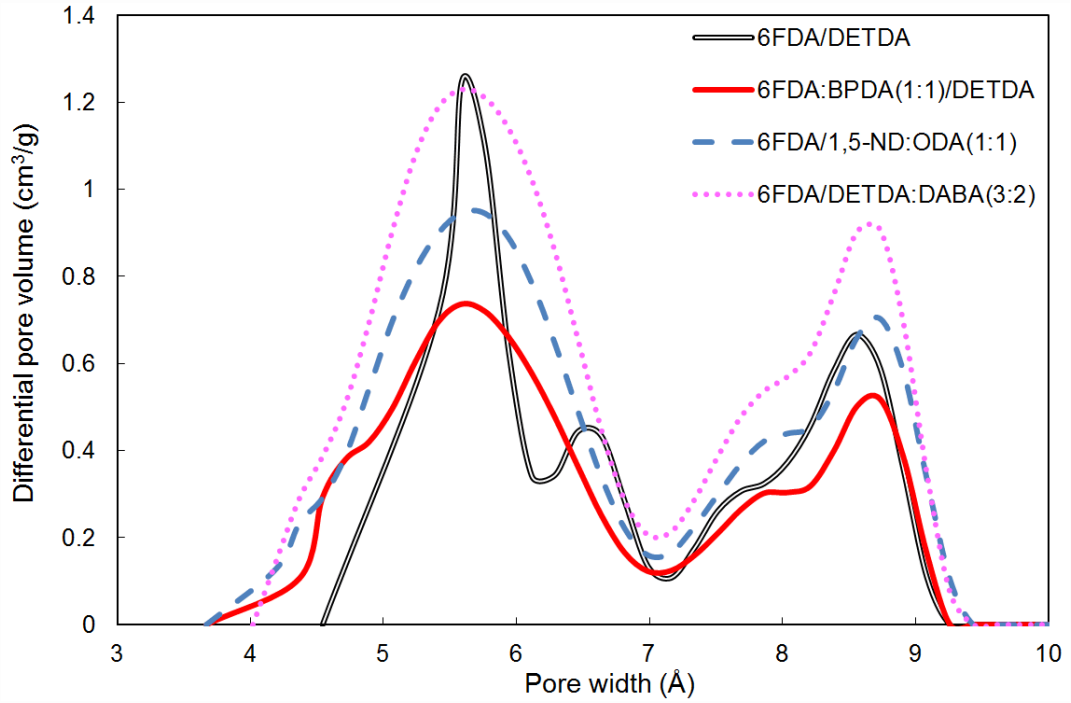

Figure 6.1: Pore distributions of CMS membranes derived from 6FDA/DETDA, 6FDA:BPDA(1:1)/DETDA, 6FDA/1, 5-ND: ODA(1:1) and 6FDA/DETDA:DABA(3:2) pyrolyzed at 550 ^{o}C under UHP argon from CO_2 sorption.

Table 6.1 lists the total pore volume and total surface area per gram of CMS samples, which as well correlates well with gas permeability, i.e., membranes with higher gas permeabilities showed larger pore volume and surface area, indicating a more open porous structure. It is not surprising to see the much larger pore volume and surface area in 6FDA/DETDA:DABA(3:2) CMS membranes considering its extremely high gas permeabilities.

For comparison purposes, the total pore volume and total surface area of 550 ^{o}C pyrolyzed Matrimid® are also listed in Table 6.1 [5]. As can be seen, the total pore volume and surface area of Matrimid® carbon membrane are noticeably smaller than 6FDA- containing polymer derived carbon membranes. This comparison shows that 6FDA- containing polymers derived carbon membranes have more open structures compared with Matrimid® derived ones. It is believed that the inhibited chain packing introduced by the bulky 6F group provides higher free volume in the precursor, which carries over to much higher gas permeabilities observed in 6FDA- carbon than Matrimid® carbon.

Table 6.1: Total pore volume and surface area of CMS films derived from 6FDA/DETDA, 6FDA:BPDA(1:1)/DETDA, 6FDA/1, 5-ND: ODA(1:1) and 6FDA/DETDA:DABA(3:2). The data for Matrimid® is also listed for comparison purpose.

Membranes	Total pore volume ≤10.8 Å (cm^3/g)	Total surface area (m^2/g)
6FDA/DETDA	0.1342	570.3
6FDA:BPDA(1:1)/DETDA	0.1385	598.0
6FDA/1,5-ND:ODA(1:1)	0.1898	804.5
6FDA/DETDA:DABA(3:2)	0.2458	1060.3
Matrimid®	0.1041	478.1 [5]

6.2.2 Temperature dependence of permeability

In this study, CO_2, CH_4, O_2, and N_2 permeability of CMS membranes derived from 6FDA/DETDA, 6FDA:BPDA(1:1)/DETDA, 6FDA/1,5-ND:ODA(1:1), and 6FDA/DETDA:DABA(3:2) were obtained at 30 psia and 35 ^{o}C, 42.5 ^{o}C, and 50 ^{o}C. Measurements at higher temperatures were avoided to prevent artifacts due to possible degradation of the adhesive on the foil used to define the permeation area. Permeation results reported in this study represent the average of 2-3 samples each with variance within 15%.

Figure 6.2 shows least squares fit of the permeability of four gases versus inverse absolute temperature for four CMS materials. As with studies on polymeric membranes [6, 7], the gas permeability of CMS membranes increases with temperature. According to Eq. 2.11, the permeability temperature dependence is a combination of diffusion and sorption coefficient temperature dependencies. Diffusion coefficients increase with temperature, because of positive diffusion activation energies, while sorption coefficients decrease due to typical negative heats of sorption. The change in diffusion coefficients usually outweighs the change in sorption coefficients as has been proven in literature [8, 9] and can be seen in the later section, as a result, permeability generally increases with temperature. The detailed temperature dependence of diffusion and sorption coefficients will be discussed in later sections.

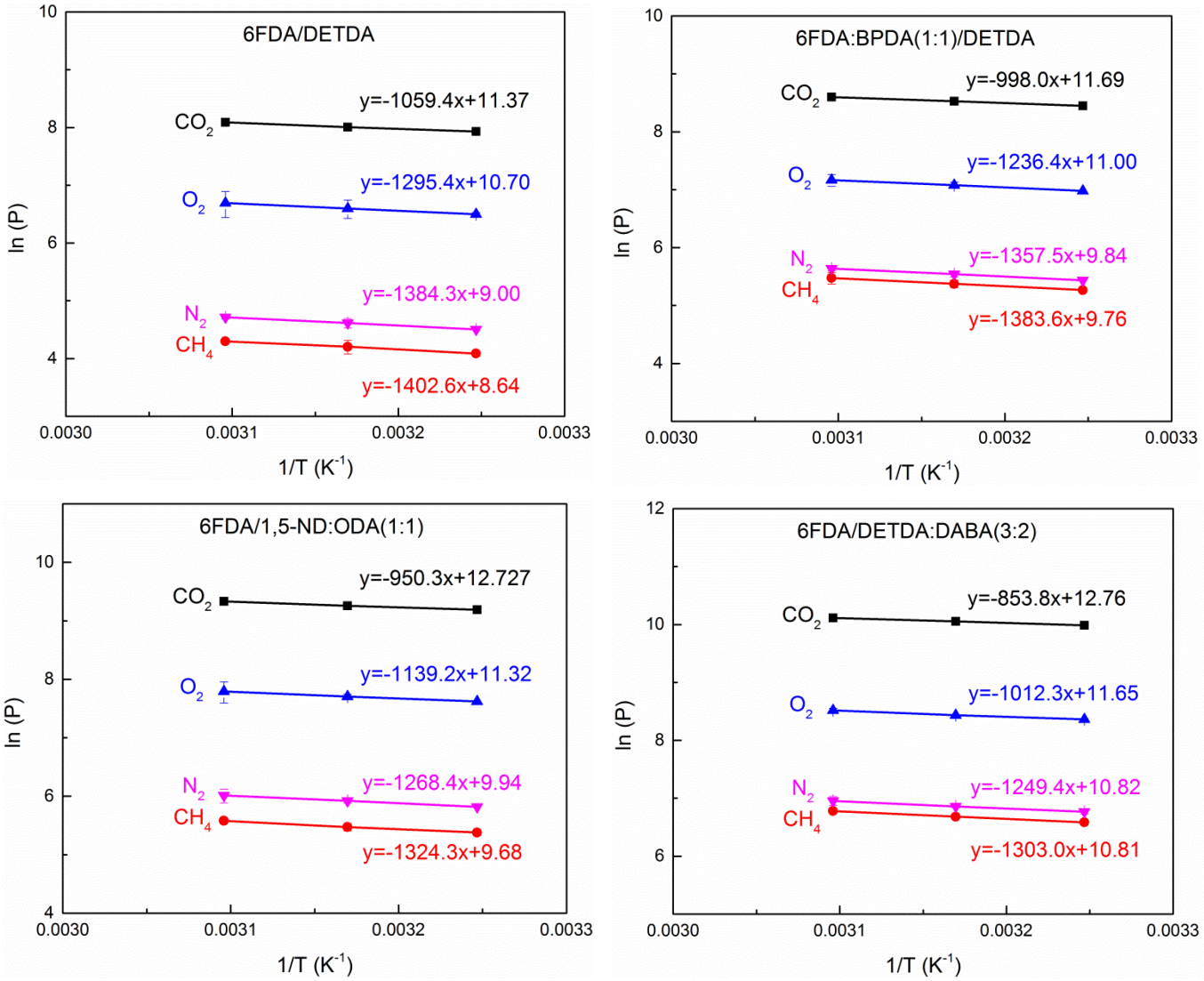

Figure 6.2: Temperature dependence of permeability for various gases in CMS membranes derived from 6FDA/DETDA, 6FDA:BPDA(1:1)/DETDA, 6FDA/1,5-ND:ODA(1:1), and 6FDA/DETDA:DABA(3:2) at 30 psia in the temperature range from 35 ^{o}C to 50 ^{o}C. (All data points are presented with error bars, some of the error bars are too small to be seen. Equations are shown with $y=\ln P=\frac{-E_p}{R}x+\ln P_0$)

The permeation activation energies and the corresponding permeation pre-exponential factors for CO_2, CH_4, O_2, and N_2 of the four CMS materials are tabulated in Table 6.2 and Table 6.3. The calculated uncertainty of the permeation activation energies are also listed. The method of calculation of these uncertainties, which is also applied for the calculations of the uncertainties of the diffusion activation energies as well as heats of sorption that will be seen in the following sections, is described in the Appendix E. From Table 6.2 one can see the difference in permeation activation energies is not huge, possibly because of the similar structures of these four CMS membranes resulted from the same pyrolysis protocol; but still some patterns can be observed. Permeation activation energy depends on both penetrant sizes and CMS types. The permeation activation energies increase with penetrant size in the order $CO_2 < O_2 < N_2 < CH_4$. On the other hand, it is noted that the CMS membrane with higher pore volume and surface area, as shown in Table 6.1, possesses lower gas permeation activation energies for all gases. As shown in Table 4.3, the permeability order of the four CMS membranes at 35 ^oC to be: 6FDA/DETDA< 6FDA:BPDA(1:1)/DETDA< 6FDA/1,5-ND:ODA(1:1)< 6FDA/DETDA:DABA(3:2), while Table 6.2 shows a reverse order for permeation activation energy order. More specifically, 6FDA/DETDA CMS has the highest permeation activation energies for all gases and 6FDA/DETDA:DABA(3:2) CMS has the lowest. Since permeation activation energy is the sum of diffusion activation energy and heat of sorption, a detailed analysis of these factors will be pursued in the following sections.

Table 6.2: Permeation activation energies of four gases for CMS membranes derived from 6FDA/DETDA, 6FDA:BPDA(1:1)/DETDA, 6FDA/1,5-ND:ODA(1:1), and 6FDA/DETDA:DABA(3:2) at 30 psia in the temperature range from 35 ^{o}C to 50 ^{o}C.

CMS membrane	E_P [kJ/mol]			
	CO_2	CH_4	O_2	N_2
6FDA/DETDA	8.8±0.2	11.7±0.1	10.8±0.1	11.5±0.0
6FDA:BPDA(1:1)/DETDA	8.3±0.2	11.5±0.0	10.3±0.2	11.3±0.1
6FDA/1,5-ND:ODA(1:1)	7.9±0.2	11.0±0.2	9.5±0.2	10.5±0.2
6FDA/DETDA:DABA(3:2)	7.1±0.0	10.8±0.1	8.4±0.5	10.4±0.2

Table 6.3: Permeation pre-exponential factors of four gases for CMS membranes derived from 6FDA/DETDA, 6FDA:BPDA(1:1)/DETDA, 6FDA/1,5-ND:ODA(1:1), and 6FDA/DETDA:DABA(3:2) at 30 psia in the temperature range from 35 ^{o}C to 50 ^{o}C.

CMS membrane	P_o [Barrers]			
	CO_2	CH_4	O_2	N_2
6FDA/DETDA	$8.7*10^4$	$5.7*10^3$	$4.4*10^4$	$8.1*10^3$
6FDA:BPDA(1:1)/DETDA	$1.2*10^5$	$1.7*10^4$	$6.0*10^4$	$1.9*10^4$
6FDA/1,5-ND:ODA(1:1)	$2.1*10^5$	$1.6*10^4$	$8.2*10^4$	$2.1*10^4$
6FDA/DETDA:DABA(3:2)	$3.5*10^5$	$5.0*10^4$	$1.1*10^5$	$5.0*10^4$

The permeability pre-exponential factors correspond to the hypothetical intercepts at infinite temperature, so it has a complex physical interpretation associated with the combined nature of the parameters in Eq. 2.28.

6.2.3 Temperature dependence of sorption coefficients

CO_2, CH_4, O_2, and N_2 sorption measurements of CMS membranes derived from 6FDA/DETDA, 6FDA:BPDA(1:1)/DETDA, 6FDA/1,5-ND:ODA(1:1), and 6FDA/DETDA:DABA(3:2) were obtained at 35 ^{o}C, 42.5 ^{o}C, and 50 ^{o}C. The sorption coefficient, $\mathbb{S} = C/P$, can be determined as the secant slope of the isotherm at a given pressure. Figures 6.3-6.6 show the CO_2, CH_4, O_2, and N_2 sorption isotherms of 6FDA/DETDA, 6FDA:BPDA(1:1)/DETDA, 6FDA/1,5-ND:ODA(1:1), and 6FDA/DETDA:DABA(3:2) CMS membranes at the three temperatures along with the Langmuir mode fitting respectively, and the fitted parameters are listed in Tables 6.4-6.7. The non-linear nature of Langmuir causes the sorption coefficient to vary somewhat with pressure. For consistency, the sorption coefficients reported here correspond to a sorption pressure of 30 psia, equals to the permeation feed pressure reported earlier.

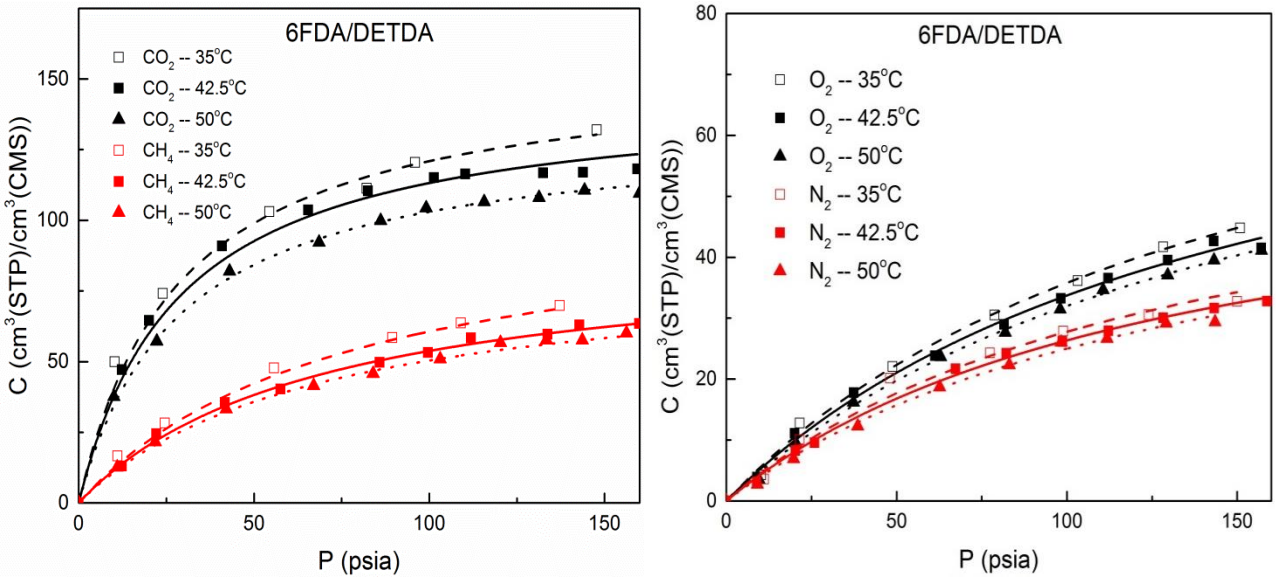

Figure 6.3: CO_2, CH_4, O_2, and N_2 sorption isotherms of 6FDA/DETDA CMS membrane at 35 ^oC, 42.5 ^oC, and 50 ^oC.

Table 6.4: CO_2, CH_4, O_2, and N_2 Langmuir mode parameters of 6FDA/DETDA CMS membrane at 35 ^oC, 42.5 ^oC, and 50 ^oC.

	6FDA/DETDA					
	35°C		42.5°C		50°C	
	CO_2	CH_4	CO_2	CH_4	CO_2	CH_4
C_H' [cm^3 (STP) /cm^3]	155.5	107.3	145.5	90.9	132.5	85.1
b [1/psia]	0.035	0.013	0.035	0.015	0.035	0.015
	O_2	N_2	O_2	N_2	O_2	N_2
C_H' [cm^3 (STP) /cm^3]	90.1	64.4	84.9	61.1	83.9	60.8
b [1/psia]	0.007	0.008	0.007	0.008	0.006	0.007

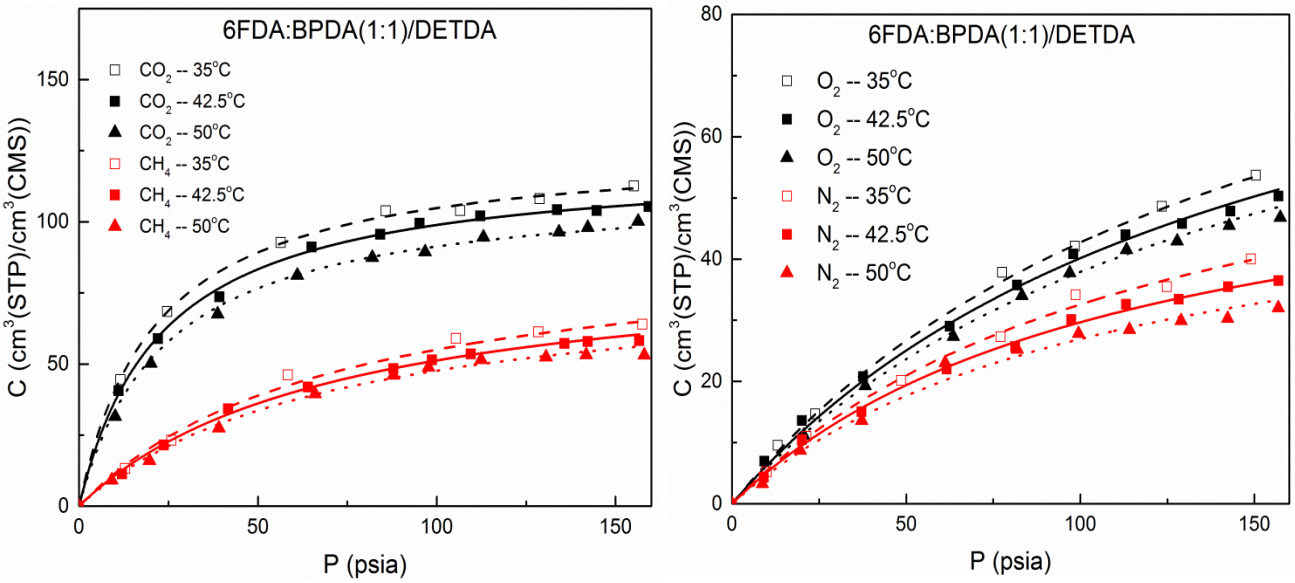

Figure 6.4: CO_2, CH_4, O_2, and N_2 sorption isotherms of 6FDA:BPDA(1:1)/DETDA CMS membrane at 35 ^oC, 42.5 ^oC, and 50 ^oC.

Table 6.5: CO_2, CH_4, O_2, and N_2 Langmuir mode parameters of 6FDA:BPDA(1:1)/DETDA CMS membrane at 35 ^oC, 42.5 ^oC, and 50 ^oC.

	6FDA:BPDA(1:1)/DETDA					
	35°C		42.5°C		50°C	
	CO_2	CH_4	CO_2	CH_4	CO_2	CH_4
C_H' [cm^3 (STP) /cm^3]	127.0	94.4	121.7	88.2	113.1	81.8
b [1/psia]	0.047	0.014	0.043	0.014	0.042	0.014
	O_2	N_2	O_2	N_2	O_2	N_2
C_H' [cm^3 (STP) /cm^3]	107.5	73.0	101.0	63.2	95.4	56.9
b [1/psia]	0.007	0.008	0.007	0.009	0.007	0.009

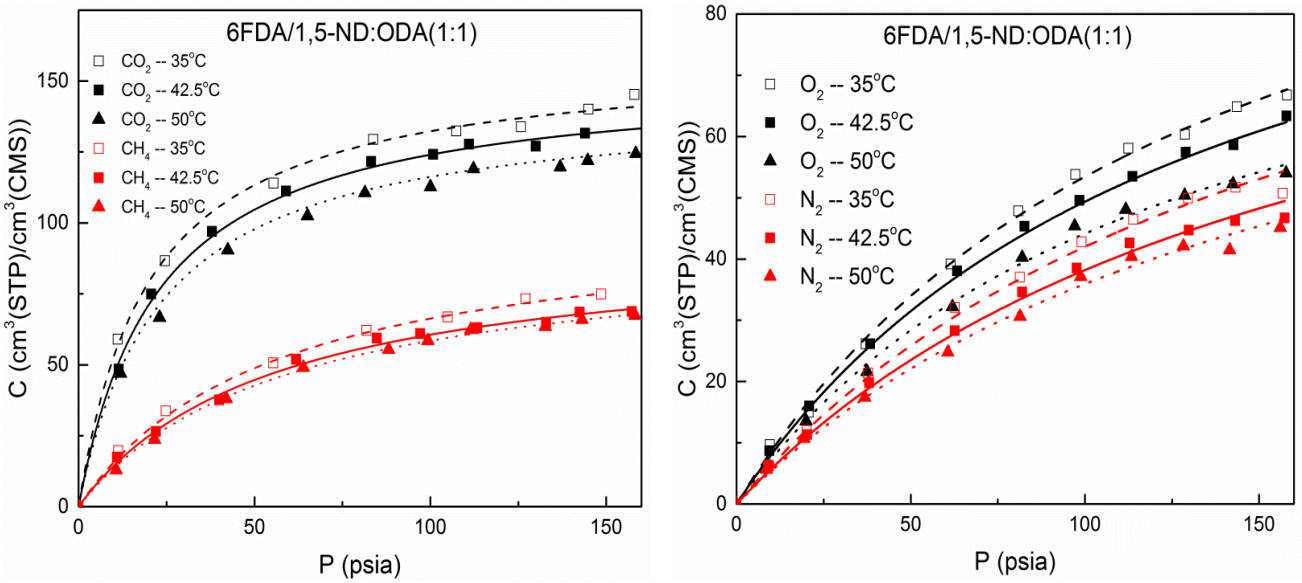

Figure 6.5: CO_2, CH_4, O_2, and N_2 sorption isotherms of 6FDA/1,5-ND:ODA(1:1) CMS membrane at 35 ^oC, 42.5 ^oC, and 50 ^oC.

Table 6.6: CO_2, CH_4, O_2, and N_2 Langmuir mode parameters of 6FDA/1,5-ND:ODA(1:1) CMS membrane at 35 ^oC, 42.5 ^oC, and 50 ^oC.

6FDA/1,5-ND:ODA(1:1)						
	35°C		42.5°C		50°C	
	CO_2	CH_4	CO_2	CH_4	CO_2	CH_4
C_H' [cm^3(STP) /cm^3]	158.9	103.2	152.3	94.3	143.3	92.9
b [1/psia]	0.050	0.018	0.044	0.018	0.043	0.017
	O_2	N_2	O_2	N_2	O_2	N_2
C_H' [cm^3(STP) /cm^3]	125.2	112.1	114.3	101.9	99.4	95.9
b [1/psia]	0.007	0.006	0.008	0.006	0.008	0.006

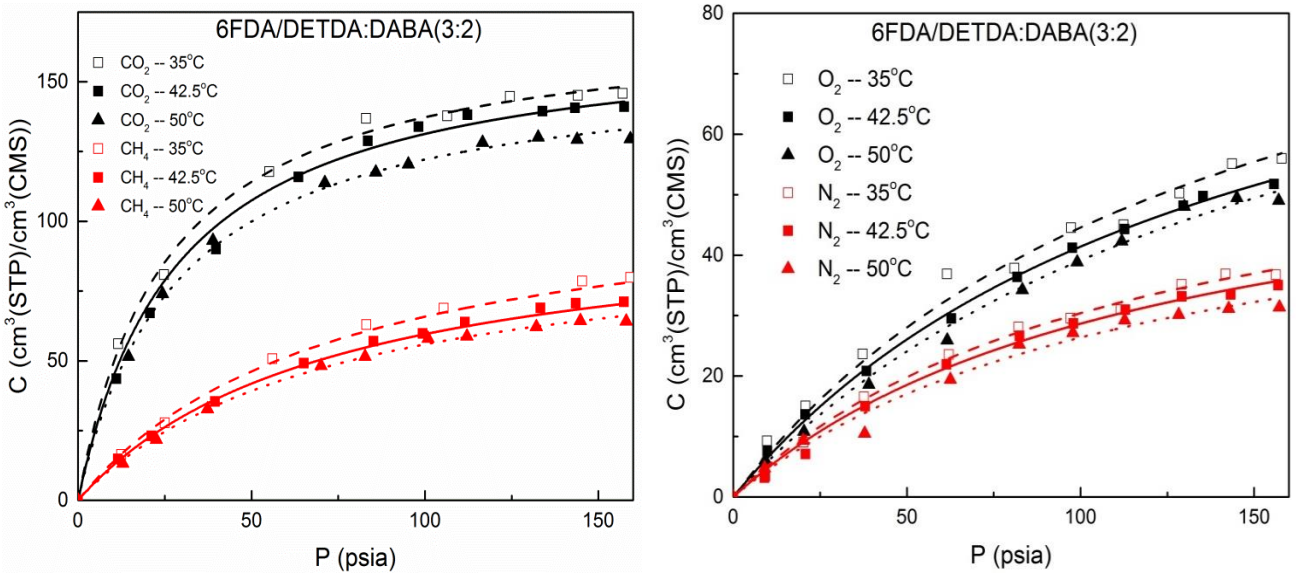

Figure 6.6: CO_2, CH_4, O_2, and N_2 sorption isotherms of 6FDA/DETDA:DABA(3:2) CMS membrane at 35 ^oC, 42.5 ^oC, and 50 ^oC.

Table 6.7: CO_2, CH_4, O_2, and N_2 Langmuir mode parameters of 6FDA/DETDA:DABA(3:2) CMS membrane at 35 ^oC, 42.5 ^oC, and 50 ^oC.

	6FDA/DETDA:DABA(3:2)					
	35°C		42.5°C		50°C	
	CO_2	CH_4	CO_2	CH_4	CO_2	CH_4
$C_H^{'}$ [cm^3(STP)/cm^3]	172.2	114.3	168.8	96.6	157.0	92.8
b [1/psia]	0.039	0.014	0.035	0.014	0.035	0.014
	O_2	N_2	O_2	N_2	O_2	N_2
$C_H^{'}$ [cm^3(STP)/cm^3]	108.3	65.2	100.8	63.1	98.5	58.1
b [1/psia]	0.007	0.009	0.007	0.008	0.007	0.008

Somewhat surprisingly, there is no clear pattern observable by comparing the C_H' s of the various gases of the four CMS membranes. The C_H' s of the four CMS membranes do not correlate well with either gas permeabilities or material pore volume. This discrepancy might due to the fact that permeability and pore volume depends on both of the ultramicropore and micropore of the membrane while C_H' mainly relies on the micropores. Moreover considering the similar structure of these four CMS membranes, the combined effects from ultramicropores and micropores might overlap with each other and complicate the scenario. On the other hand as expected, the C_H' s increase with gas critical temperature in the order: N_2 < O_2< CH_4 < CO_2, and decreases as temperature increases. The drop of C_H' is primarily caused by decreased density of sorbed penetrants at higher temperature at saturation of the CMS microvoids [10].

Van't Hoff relationships (Eq. 2.26) describe the temperature dependence of sorption coefficients, and Figure 6.7 shows the least squares fit of sorption coefficients of four gases versus inverse absolute temperature for the four CMS materials. The apparent heats of sorption and the corresponding sorption pre-exponential factors for CO_2, CH_4, O_2, and N_2 of the four CMS materials are tabulated in Table 6.8 and Table 6.9. As expected, sorption coefficients of all gases decrease with increasing temperature, reflecting a negative heat of sorption. In flexible polymers, the heat of sorption reflects the sum of two energetic contributions: one part represents the enthalpy change when a gas molecule transfers from the gas phase into a more stablized sorbed state. This enthalpy change is mainly governed by the gas critical temperature, which measures the tendency of the molecule to exist in the sorbed state. The other energetic contribution represents the combination of formation of a sorption site and the energy of mixing the sorbed molecule with the formed site [11, 12]. In rigid porous CMS media, the need to form a sorption site is absent. Table 6.8 shows the relationship between gas condensability and the sorption heat. The heat of sorption increases in the order: N_2 <

O_2< CH_4 < CO_2 for the four CMS materials, which follows the order of gas critical temperature listed in Table 3.2. This general trend is consistent with the expectation that the first factor, related to condensibility, controls sorption for these CMS materials. Table 6.8 also shows only moderate differences in the sorption enthalpy between CMS samples, probably showing similar intrinsic micropore natures of the different CMS materials.

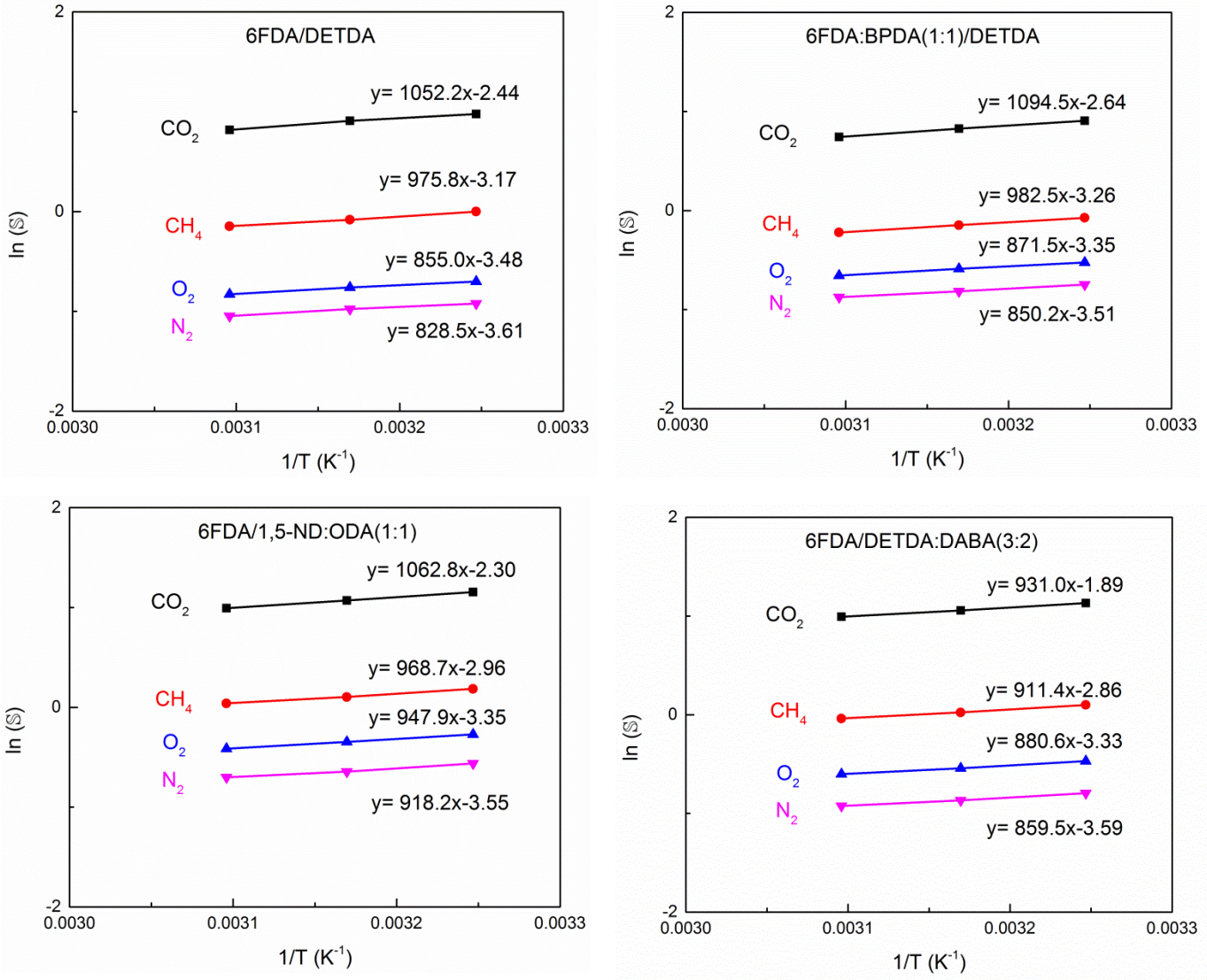

Figure 6.7: Temperature dependence of sorption coefficients for various gases in CMS membranes derived from 6FDA/DETDA, 6FDA:BPDA(1:1)/DETDA, 6FDA/1,5-ND:ODA(1:1), and 6FDA/DETDA:DABA(3:2) at 30 psia in the temperature range from 35 ^{o}C to 50 ^{o}C. (Equations are shown with $y=\ln\mathbb{S}=\frac{-H_{\mathbb{S}}}{R}x+\ln\mathbb{S}_{0}$)

Table 6.8: Apparent heats of sorption of four gases for CMS membranes derived from 6FDA/DETDA, 6FDA:BPDA(1:1)/DETDA, 6FDA/1,5-ND:ODA(1:1), and 6FDA/DETDA:DABA(3:2) at 30 psia in the temperature range from 35 ^{o}C to 50 ^{o}C.

CMS membrane	$H_{\mathbb{S}}$ [kJ/mol]			
	CO_2	CH_4	O_2	N_2
6FDA/DETDA	-8.7 ±0.3	-8.1 ±0.2	-7.1 ±0.1	-6.9 ±0.1
6FDA:BPDA(1:1)/DETDA	-9.1 ±0.3	-8.2 ±0.1	-7.2 ±0.1	-7.1 ±0.0
6FDA/1,5-ND:ODA(1:1)	-8.8 ±0.0	-8.1 ±0.1	-7.9 ±0.0	-7.7 ±0.1
6FDA/DETDA:DABA(3:2)	-7.7 ±0.0	-7.6 ±0.1	-7.3 ±0.2	-7.1 ±0.0

Table 6.9: Sorption pre-exponential factors of four gases for CMS membranes derived from 6FDA/DETDA, 6FDA:BPDA(1:1)/DETDA, 6FDA/1,5-ND:ODA(1:1), and 6FDA/DETDA:DABA(3:2) at 30 psia in the temperature range from 35 ^{o}C to 50 ^{o}C.

CMS membrane	$\mathbb{S}_0$ [cc(STP)/cm^3/psia]			
	CO_2	CH_4	O_2	N_2
6FDA/DETDA	$8.8*10^{-2}$	$4.2*10^{-2}$	$3.1*10^{-2}$	$2.7*10^{-2}$
6FDA:BPDA(1:1)/DETDA	$7.1*10^{-2}$	$3.8*10^{-2}$	$3.5*10^{-2}$	$3.0*10^{-2}$
6FDA/1,5-ND:ODA(1:1)	$1.0*10^{-1}$	$5.2*10^{-2}$	$3.5*10^{-2}$	$2.9*10^{-2}$
6FDA/DETDA:DABA(3:2)	$1.5*10^{-1}$	$5.7*10^{-2}$	$3.6*10^{-2}$	$2.8*10^{-2}$

6.2.4 Temperature dependence of diffusion coefficients

Average diffusion coefficients of CO_2, CH_4, O_2, and N_2 at 35 ^oC, 42.5 ^oC, and 50 ^oC were calculated from the permeability and sorption coefficients according to Eq. 2.11 ($P_i = \overline{D}_i * \overline{\mathbb{S}}_i$). The temperature dependence of diffusion coefficients follows an Arrhenius relationship, reflecting the activated nature of diffusion. Figure 6.8 illustrates the least squares fit of the diffusion coefficients for the four gases versus inverse absolute temperature for four CMS materials. The activation energies of diffusion and the corresponding diffusion pre-exponential factors are calcalated according to Eq. 2.27 and Eq. 2.28, and are tabulated in Table 6.10 and Table 6.11.

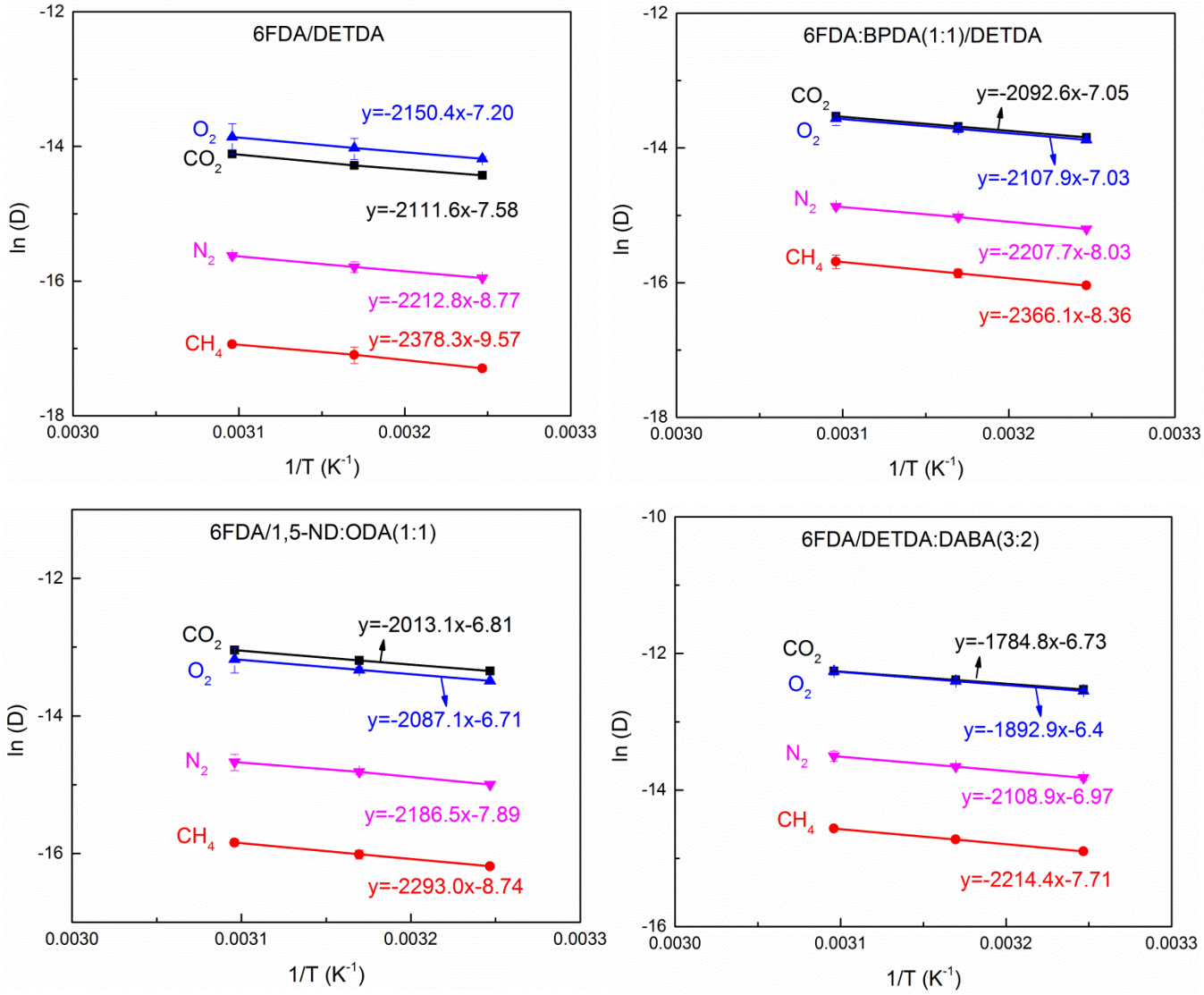

Figure 6.8: Temperature dependence of diffusion coefficients for various gases in CMS membranes derived from 6FDA/DETDA, 6FDA:BPDA(1:1)/DETDA, 6FDA/1,5-ND:ODA(1:1), and 6FDA/DETDA:DABA(3:2) at 30 psia in the temperature range from 35 ^{o}C to 50 ^{o}C. (All data points are presented with error bars, some of the error bars are too small to be seen. Equations are shown with $y=\ln D=\frac{-E_D}{R}x+\ln D_0$)

Table 6.10: Diffusion activation energies of four gases for CMS membranes derived from 6FDA/DETDA, 6FDA:BPDA(1:1)/DETDA, 6FDA/1,5-ND:ODA(1:1), and 6FDA/DETDA:DABA(3:2) at 30 psia in the temperature range from 35 ^{o}C to 50 ^{o}C.

CMS membrane	E_D [kJ/mol]			
	CO_2	CH_4	O_2	N_2
6FDA/DETDA	17.6 ±0.2	19.8 ±0.3	17.9 ±0.0	18.4 ±0.3
6FDA:BPDA(1:1)/DETDA	17.4 ±0.1	19.7 ±0.2	17.5 ±0.0	18.4 ±0.2
6FDA/1,5-ND:ODA(1:1)	16.7 ±0.4	19.1 ±0.1	17.4 ±0.4	18.2 ±0.1
6FDA/DETDA:DABA(3:2)	14.8 ±0.0	18.4 ±0.1	15.7 ±0.5	17.6 ±0.3

Table 6.11: Diffusion pre-exponential factors of four gases for CMS membranes derived from 6FDA/DETDA, 6FDA:BPDA(1:1)/DETDA, 6FDA/1,5-ND:ODA(1:1), and 6FDA/DETDA:DABA(3:2) at 30 psia in the temperature range from 35 ^{o}C to 50 ^{o}C.

CMS membrane	D_0 [cm^2/s]			
	CO_2	CH_4	O_2	N_2
6FDA/DETDA	$5.1*10^{-4}$	$7.0*10^{-5}$	$7.4*10^{-4}$	$1.6*10^{-4}$
6FDA:BPDA(1:1)/DETDA	$8.7*10^{-4}$	$2.3*10^{-4}$	$8.8*10^{-4}$	$3.3*10^{-4}$
6FDA/1,5-ND:ODA(1:1)	$1.1*10^{-3}$	$1.6*10^{-4}$	$1.2*10^{-3}$	$3.7*10^{-4}$
6FDA/DETDA:DABA(3:2)	$1.2*10^{-3}$	$4.5*10^{-4}$	$1.7*10^{-3}$	$9.3*10^{-4}$

Diffusion coefficients increase with temperature (Figure 6.8), reflecting a positive activation energy for diffusion. Diffusion activation energy measures the minimum energy required for a penetrant to make a diffusive jump from one equilibrium site to another, and depends on CMS packing of the matrix, and the penetrant size. Larger penetrants require higher diffusion activation energy to enable passage through the size discriminating ultramicropores responsible for diffusive selectivity. This critical difference between the activation step in rigid CMS vs. flexible polymeric matrices, which relies upon motion of the membrane matrix, is fundamentally related to the higher selectivities achievable in CMS materials vs. flexible polymers. As expected, the diffusion coefficients of a larger penetrant exhibit greater temperature dependence than a smaller penetrant. Our previous statement that diffusion activation energy is expected to outweigh the heat of sorption in affecting permeation activation energy is validated by comparing Table 6.8 and Table 6.10. The increase in diffusion coefficient outweighs the decrease in sorption coefficient, thereby resulting in an increase of permeability with temperature. Clearly, the increase in permeability is lower than that of diffusivity, due to the decreasing tendency of the sorption coefficient

Table 6.10 shows that, similar to the trend observed in permeability, activation energy for 6FDA/DETDA:DABA(3:2) derived CMS membranes, which showed the highest permeability and most open pore structure (as shown in Fig. 6.2) among the four, shows the lowest diffusion activation energy, while the 6FDA/DETDA CMS membrane with the lowest permeability and most compact pore structure, shows the highest diffusion activation energy for all gases. These results, combined with the pore structures discussed in section 6.2.1, indicate that tighter 6FDA/DETDA CMS hindered the ability of all molecules to make a diffusive jump, while in an open structure like 6FDA/DETDA:DABA(3:2) CMS, effective diffusive jumps are easily executed.

Maxwell-Stefan diffusion coefficients were also studied. Unlike the conventional Fickian transport diffusivity D_f, the Maxwell-Stefan diffusivity Đ accounts for the amount of gas taken up by the media [13, 14] in its interpretation. The two coefficients can be mathematically related as Equation 6.1:

$$Đ = D_f \frac{d\ln C(p)}{d\ln p} \tag{6.1}$$

where p is the single component gas phase equilibrium pressure and C(p) is the gas absorbed by the media at equilibrium pressure of p. In combination with a Langmuir isotherm model shown in Equation 6.2, for gas i, one can find equation 6.3:

$$S_A = \frac{C_i}{p_i} = \frac{C'_{Hi} b_i}{1+b_i p_i} \tag{6.2}$$

$$Đ_i = D_{fi}(1-\theta_i) \tag{6.3}$$

where θ_i is the fractional site saturation factor defined as below:

$$\theta_i = \frac{b_i p_i}{1+b_i p_i} \tag{6.4}$$

The average diffusivity can be calculated by integrating the local Fickian diffusivity between a given upstream and downstream (vacuum in this study) concentration in the membrane. Thus, from Eqs. 6.1-6.4, one finds:

$$D_i = \frac{\int_{C_i}^{0} D_f dC_i}{\int_{C_i}^{0} dC_i} \approx \frac{\int_{\theta_i}^{0} \frac{Đ_i}{(1-\theta_i)} d\theta_i}{\int_{\theta_i}^{0} d\theta_i} = \frac{Đ_i}{\theta_i} \ln\left(\frac{1}{1-\theta_i}\right) \tag{6.5}$$

Eq. 6.5 provides a bridge to connect the average diffusivity, which can be easily obtained from permeation and sorption measurements, to the Maxwell-Stefan diffusivity.

Figure 6.9 shows the temperature dependence of Maxwell-Stefan diffusivities for various gases of the four CMS membranes at 30 psia and in the temperature range from 35 ^{o}C to 50 ^{o}C. Table 6.12 and Table 6.13 tabulate the Maxwell-Stefan diffusion

activation energies and the corresponding Maxwell-Stefan diffusion pre-exponential factors for various gas of the four CMS membranes at 30 psia and in the temperature range from 35 ^{o}C to 50 ^{o}C.

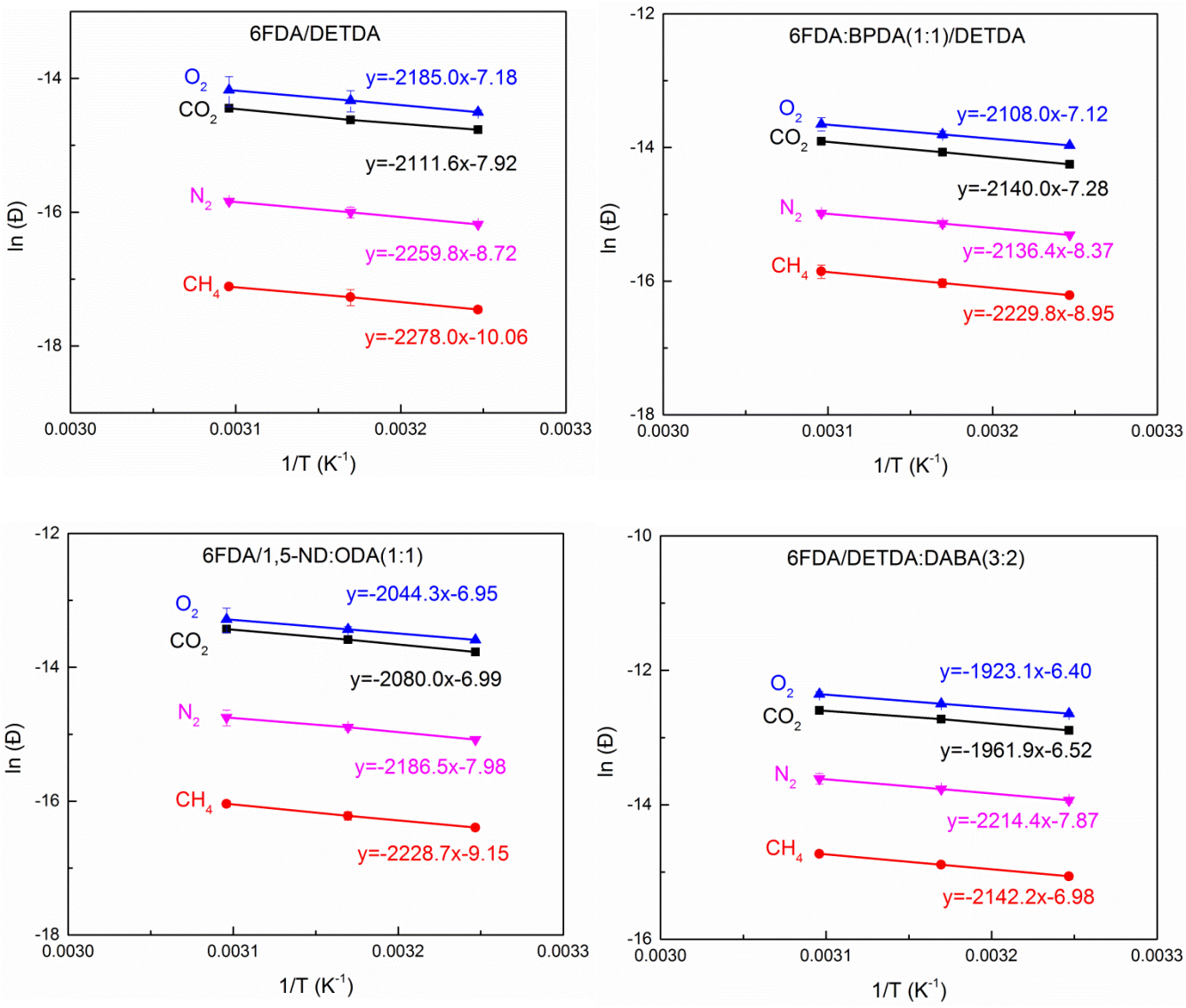

Figure 6.9: Temperature dependence of Maxwell-Stefan diffusivities for various gases in CMS membranes derived from 6FDA/DETDA, 6FDA:BPDA(1:1)/DETDA, 6FDA/1,5-ND:ODA(1:1), and 6FDA/DETDA:DABA(3:2) at 30 psia in the temperature range from 35 ^{o}C to 50 ^{o}C. *(In accordance with Figure 6.8).*

Table 6.12: Diffusion activation energies, based on Maxwell-Stefan diffusivity, of four gases for CMS membranes derived from 6FDA/DETDA, 6FDA:BPDA(1:1)/DETDA, 6FDA/1,5-ND:ODA(1:1), and 6FDA/DETDA:DABA(3:2) at 30 psia in the temperature range from 35 ^{o}C to 50 ^{o}C. *(In accordance with Table 6.10).*

CMS membrane	$E_Đ$ [kJ/mol]			
	CO_2	CH_4	O_2	N_2
6FDA/DETDA	17.6±0.2	18.9±0.3	18.4±0.1	19.0±0.3
6FDA:BPDA(1:1)/DETDA	17.8±0.1	18.5±0.2	17.5±0.1	17.8±0.1
6FDA/1,5-ND:ODA(1:1)	17.3±0.4	18.5±0.1	17.0±0.3	18.1±0.1
6FDA/DETDA:DABA(3:2)	16.3±0.0	18.4±0.0	16.0±0.5	17.8±0.3

Table 6.13: Diffusion pre-exponential factors, based on Maxwell-Stefan diffusivity, of four gases for CMS membranes derived from 6FDA/DETDA, 6FDA:BPDA(1:1)/DETDA, 6FDA/1,5-ND:ODA(1:1), and 6FDA/DETDA:DABA(3:2) at 30 psia in the temperature range from 35 ^{o}C to 50 ^{o}C. *(In accordance with Table 6.11).*

CMS membrane	$Đ_0$ [cm^2/s]			
	CO_2	CH_4	O_2	N_2
6FDA/DETDA	$3.7*10^{-4}$	$4.3*10^{-5}$	$6.6*10^{-4}$	$1.6*10^{-4}$
6FDA:BPDA(1:1)/DETDA	$6.9*10^{-4}$	$1.3*10^{-4}$	$8.1*10^{-4}$	$2.3*10^{-4}$
6FDA/1,5-ND:ODA(1:1)	$9.2*10^{-4}$	$1.1*10^{-4}$	$9.6*10^{-4}$	$3.4*10^{-4}$
6FDA/DETDA:DABA(3:2)	$1.5*10^{-3}$	$9.3*10^{-4}$	$1.7*10^{-3}$	$3.8*10^{-4}$

The general trends we observed from the results based on average diffusion coefficients are also valid for Maxwell-Stefan diffusion coefficients with only minor differences. By comparing Figure 6.9 and Figure 6.8, clearly, as for the average diffusivities (Figure 6.8), the Maxwell-Stefan diffusivities increase with temperature. Table 6.12 shows that, similar to the trend observed in average diffusion activation energy, the 6FDA/DETDA:DABA(3:2) CMS membrane, which shows the highest permeabilities among the four, shows the lowest Maxwell-Stefan diffusion activation energy.

Essentially, Maxwell-Stefan diffusivities represent the diffusivity at zero loading. The more condensable the gas is, the more different the Maxwell-Stefan diffusivity is from the average diffusivity due to the concentration in Equation 6.3. In this case, the results related with CO_2 were altered the most compared to the cases with other less condensable gases.

6.2.5 Selectivity consideration

The permselectivity in Equation 2.12 reflects the combined diffusion selectivity and sorption selectivity. Table 6.14 lists at 35 ^{o}C and 30 psia, the overall membrane permselectivity, $\alpha_{A/B}$; the sorption selectivity, $\frac{\mathbb{S}_A}{\mathbb{S}_B}$; and the diffusion selectivity, $\frac{D_A}{D_B}$, of three gas pairs CO_2/CH_4, O_2/N_2, and N_2/CH_4 for four CMS materials. The $\alpha_{A/B}$ and $\frac{\mathbb{S}_A}{\mathbb{S}_B}$ are determined using the permeation measurements and sorption measurements, while $\frac{D_A}{D_B}$ is calculated according to Equation 2.12 ($\alpha_{A/B} = \frac{P_A}{P_B} = \left(\frac{D_A}{D_B}\right)\left(\frac{\mathbb{S}_A}{\mathbb{S}_B}\right)$). Clearly for all three gas pairs, diffusion selectivity is the dominant contributor to the overall permselectivity, with sorption selectivity for CO_2/CH_4, O_2/N_2 separation is only

contributing around 2.7 and 1.4 respectively, regardless of the different CMS structures. For N_2/CH_4 separation, sorption selectivity is even less than unity due to the higher condensability of CH_4 vs. N_2 reflected by the large difference in $\frac{(T_C)_{CH_4}}{(T_C)_{N_2}}$. The preceding factors show that to achieve higher separation efficiency, tuning of diffusion selectivity is the key tool to improve separation performance of CMS membranes.

Table 6.14: The overall membrane permselectivity $\alpha_{A/B}$, the sorption selectivity $\frac{\mathbb{S}_A}{\mathbb{S}_B}$, and the diffusion selectivity $\frac{D_A}{D_B}$ of gas pairs CO_2/CH_4, O_2/N_2, and N_2/CH_4 for four CMS materials at 35 ^oC 30 psia.

CMS membrane	α_{CO_2/CH_4}	$\frac{\mathbb{S}_{CO_2}}{\mathbb{S}_{CH_4}}$	$\frac{D_{CO_2}}{D_{CH_4}}$
6FDA/DETDA	46.3 ±2.4	2.7	17.2 ±0.9
6FDA:BPDA(1:1)/DETDA	24.0 ±1.5	2.8	8.6 ±0.5
6FDA/1,5-ND:ODA(1:1)	45.1 ±1.7	2.7	17.0 ±0.6
6FDA/DETDA:DABA(3:2)	30.1 ±1.9	2.8	10.7 ±0.7
CMS membrane	α_{O_2/N_2}	$\frac{\mathbb{S}_{O_2}}{\mathbb{S}_{N_2}}$	$\frac{D_{O_2}}{D_{N_2}}$
6FDA/DETDA	7.3 ±0.2	1.3	5.8 ±0.1
6FDA:BPDA(1:1)/DETDA	4.7 ±0.4	1.2	3.9 ±0.3
6FDA/1,5-ND:ODA(1:1)	6.0 ±0.4	1.3	4.5 ±0.3
6FDA/DETDA:DABA(3:2)	4.9 ±0.2	1.5	3.3 ±0.1
CMS membrane	α_{N_2/CH_4}	$\frac{\mathbb{S}_{N_2}}{\mathbb{S}_{CH_4}}$	$\frac{D_{N_2}}{D_{CH_4}}$
6FDA/DETDA	1.5 ±0.0	0.4	3.4 ±0.2
6FDA:BPDA(1:1)/DETDA	1.2 ±0.1	0.5	2.3 ±0.2
6FDA/1,5-ND:ODA(1:1)	1.6 ±0.1	0.5	3.3 ±0.3
6FDA/DETDA:DABA(3:2)	1.2 ±0.0	0.4	2.9 ±0.1

Eq. 2.32 shows clearly that the diffusion selectivity can be factored into an "energetic selectivity" and an "entropic selectivity". Energetic selectivity stems from the difference in the diffusion activation energies of the two penetrants, while entropic selectivity primarily reflects the difference in the diffusion activation entropies of the two penetrants. Singh and Koros [15] have discussed the significance of entropic selectivity in molecular sieving materials for the O_2/N_2 pair. They also showed that in polymeric membranes, entropic selectivity is close to unity, while in CMS membranes, a much higher entropic selectivity can be observed. The high entropic selectivity in CMS membrane is enabled by the rigid CMS pore structures, which polymer membranes lack. This fundamental fact is the main reason CMS and zeolite membranes surpass the polymeric upper bound. Entropic selectivity reflects differences in penetrant shape and subtle configurational differences experienced by penetrants transversing the diffusion-limiting ultramicropores. This entropic configurational control can be engineered by controlling differences in rotational and internal vibrational degrees of freedom between the diffusing components in the activated state.

Table 6.15 summarizes at 30 psia and in the temperature range from 35 ^{o}C to 50 ^{o}C, the energetic and entropic selectivities of gas pairs CO_2/CH_4, O_2/N_2, and N_2/CH_4 for four CMS membranes calculated based on average diffusivity. Energetically for each gas pair, 6FDA/DETDA, 6FDA:BPDA(1:1)/DETDA and 6FDA/1,5-ND:ODA(1:1) CMS membranes showed similar discriminating ability. Based on Equation 2.32, the energetic selectivity shows a small change over the temperature range studied; however, using the average over this range is convenient for discussion purposes. The energetic selectivities for these materials for CO_2/CH_4, O_2/N_2, and N_2/CH_4 are all about 2.4, 1.3 and 1.5 respectively. 6FDA/DETDA:DABA(3:2) CMS membrane showed somewhat higher CO_2/CH_4, O_2/N_2 energetic selectivities as about 4.0 and 2.0. On the other hand, entropically, all four CMS membranes showed larger than unity entropic discriminations for these gas pairs, illustrating that rigid CMS materials are capable of discrimination

between different molecular configurations in the activated state of diffusion. The degree of discrimination must depend highly on the limiting pore size distribution of the CMS materials. The three DETDA-based CMS membranes possessed increasing entropic selectivity for all gas pairs following the order: 6FDA/DETDA:DABA(3:2)< 6FDA:BPDA(1:1)/DETDA< 6FDA/DETDA, which is the opposite of their permeability and pore volume order for the various penetrants. Such a trend for CMS derived from related precursor may arise from progressive tightening of the ultramicropore distribution leading to lower permeability and systematically higher shape and configurational discrimination between different penetrants. Somewhat surprisingly, CMS membranes derived from 6FDA/1,5-ND:ODA(1:1) showed the second highest permeability but also comparable entropic selectivity to the 6FDA/DETDA derived CMS. As noted in our previous paper, the 6FDA/1,5-ND:ODA(1:1) polymer precursor contains a stiff structure of 1,5-ND connected with a flexible structure of ODA. While this combination of features may provide an additional tool to provide CMS materials with both high permeability and high entropic discrimination, the basis for such an effect is not clear at this point, but deserves further exploration with other stiff-flexible pair combinations.

Table 6.15: Summary of energetic and entropic selectivities of gas pairs CO_2/CH_4, O_2/N_2, and N_2/CH_4 for four CMS materials at 30 psia in the temperature range from 35 ^oC to 50 ^oC.

	Energetic selectivity		
CMS membrane	CO_2/CH_4	O_2/N_2	N_2/CH_4
6FDA/DETDA	2.3 ±0.3	1.2 ±0.3	1.7 ±0.4
6FDA:BPDA(1:1)/DETDA	2.4 ±0.2	1.4 ±0.2	1.6 ±0.3
6FDA/1,5-ND:ODA(1:1)	2.5 ±0.4	1.4 ±0.4	1.4 ±0.1
6FDA/DETDA:DABA(3:2)	4.0 ±0.1	2.1 ±0.5	1.4 ±0.3
	Entropic selectivity		
CMS membrane	CO_2/CH_4	O_2/N_2	N_2/CH_4
6FDA/DETDA	7.4 ±1.2	4.8 ±0.3	2.0 ±0.2
6FDA:BPDA(1:1)/DETDA	3.6 ±0.4	2.8 ±0.4	1.4 ±0.1
6FDA/1,5-ND:ODA(1:1)	6.8 ±1.1	3.3 ±0.2	2.3 ±0.2
6FDA/DETDA:DABA(3:2)	2.7 ±0.2	1.6 ±0.4	2.1 ±0.1

Table 6.16 summarizes at 30 psia and in the temperature range from 35 ^oC to 50 ^oC, the energetic and entropic selectivities of gas pairs CO_2/CH_4, O_2/N_2, and N_2/CH_4 for the four CMS membranes calculated based on Maxwell-Stefan diffusivity. Again, the general trends we observed from the results based on average diffusion coefficients are also valid for those based on Maxwell-Stefan diffusion coefficients.

Table 6.16: Summary of energetic and entropic selectivities of gas pairs CO_2/CH_4, O_2/N_2, and N_2/CH_4 for four CMS materials at 30 psia in the temperature range from 35 ^oC to 50 ^oC, based on Maxwell-Stefan diffusivity. *(In accordance with Table 6.15).*

	Energetic selectivity		
CMS membrane	CO_2/CH_4	O_2/N_2	N_2/CH_4
6FDA/DETDA	1.6 ±0.4	1.3 ±0.3	1.0 ±0.2
6FDA:BPDA(1:1)/DETDA	1.3 ±0.2	1.1 ±0.1	1.3 ±0.2
6FDA/1,5-ND:ODA(1:1)	1.6 ±0.4	1.5 ±0.3	1.2 ±0.1
6FDA/DETDA:DABA(3:2)	2.2 ±0.0	2.0 ±0.5	1.3 ±0.3
	Entropic selectivity		
CMS membrane	CO_2/CH_4	O_2/N_2	N_2/CH_4
6FDA/DETDA	10.5 ±1.2	4.6 ±0.6	3.5 ±0.4
6FDA:BPDA(1:1)/DETDA	6.6 ±0.8	3.4 ±0.5	1.8 ±0.1
6FDA/1,5-ND:ODA(1:1)	10.8 ±1.2	3.0 ±0.4	2.8 ±0.2
6FDA/DETDA:DABA(3:2)	4.8 ±0.3	1.7 ±0.3	2.3 ±0.3

As discussed by Rungta [16], the pyrolysis conditions are useful tools in tuning the CMS material pore structure for CMS samples, and as a result, the entropic discrimination abilities. This finding leads us to the following section of study, in which the effects of testing temperature on several different conditions pyrolyzed CMS membranes derived from 6FDA/DETDA:DABA(3:2) were investigated.

6.3 Temperature dependence of gas transport and sorption in CMS membranes derived from 6FDA/DETDA:DABA(3:2)

Chpater 4 demonstrated that 6FDA/DETDA:DABA(3:2) derived CMS membranes to have the greatest practical potential with high gas permeabilities. Chapter 5 investigated pure and mixed gas separation performance of different types of CMS membranes derived from 6FDA/DETDA:DABA(3:2) with different pyroslysis conditions. To better understand the nature of these membranes and similar to the study listed in Section 6.2, in this section, the temperatrue dependence of pure gas permeaton, sorption, and diffusion of 550 ^{o}C-CMS; 800 ^{o}C-CMS; and 800 ^{o}C-precrosslinked-CMS as well as polymeric membranes derived from 6FDADETDA:DABA(3:2) were studied over the temperature range of 35-50 ^{o}C at 30 psia upstream pressure. Through the study in this section, we are seeking to clarify why CMS membranes can outperform polymeric membranes.

6.3.1 Characterization of the CMS membranes derived from 6FDA/DETDA:DABA(3:2)

Figure 6.10 shows the pore distributions of 550 ^{o}C-CMS; 800 ^{o}C-CMS; and 800 ^{o}C-precrosslinked-CMS derived from 6FDA/DETDA:DABA(3:2) achieved based on the CO_2 sorption uptakes analyzed in terms of density functional theory. Note that the 550 ^{o}C-CMS in this section is the same membrane as the 6FDA/DETDA:DABA(3:2) CMS membrane that has been discussed in Section 6.2. It is listed again in this section to aid the discussion. Recall in Chapter 5, the following conclusions have been reached: 1) compared to the 550 ^{o}C-CMS membrane, with increased pyrolysis temperature, both 800 ^{o}C-CMS and 800 ^{o}C-precrosslinked-CMS membrane present lower CO_2 permeability, sorption coefficient, C_H' and b and higher CO_2/CH_4 selectivity; 2) compared to the 800

^{o}C-CMS membrane, with precrosslinking, the 800 ^{o}C-precrosslinked-CMS membrane presents higher CO_2 permeability, sorption coefficient, C_H' and b and lower CO_2/CH_4 selectivity. From Figure 6.10 one can see: in the ultramicropore region (< 7 Å), the pore sizes of the membranes shift towards the smaller end as the pyrolysis temperature increases from 550 ^{o}C to 800 ^{o}C. This pore shift might help to explain the enhanced gas selectivity of 800 ^{o}C pyrolyzed CMS membranes.

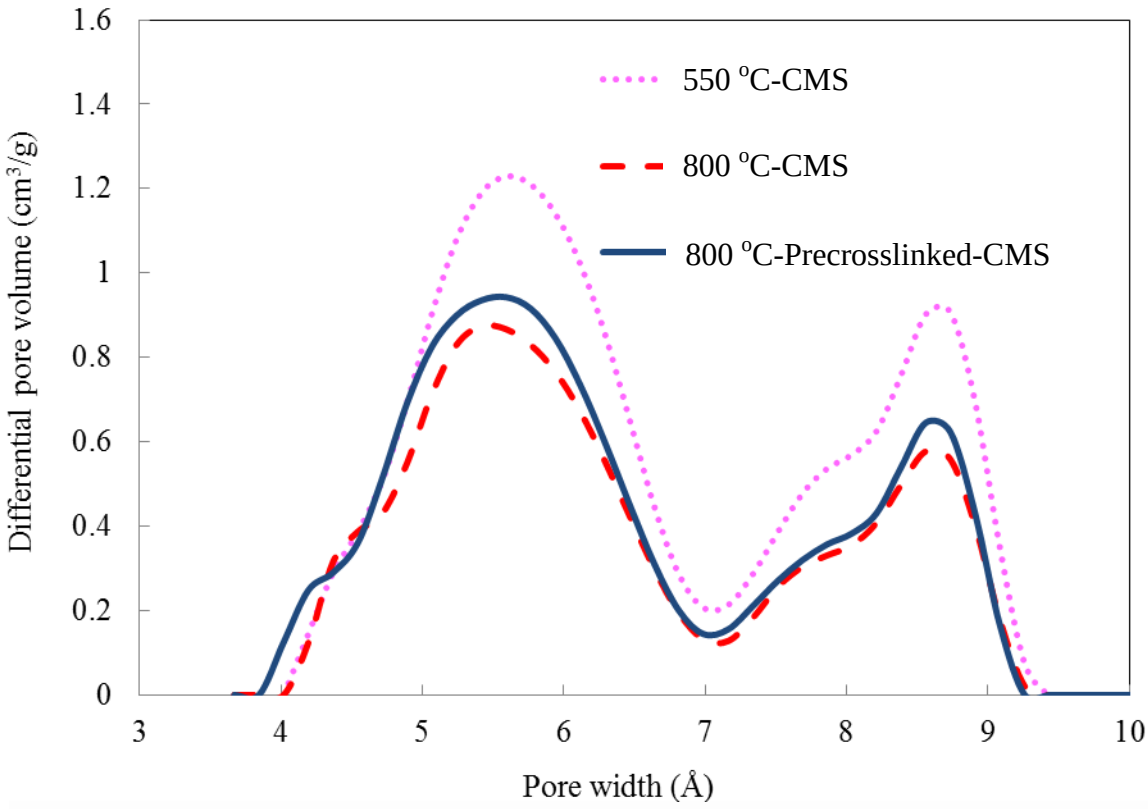

Figure 6.10: Pore distributions of 550 ^{o}C-CMS; 800 ^{o}C-CMS; and 800 ^{o}C-precrosslinked-CMS as well as precursor membranes derived from 6FDA/DETDA:DABA(3:2).

Table 6.17 lists the total pore volume and total surface area per gram of CMS samples, which correlates well with their gas permeabilities, i.e., 6FDA/DETDA:DABA(3:2) derived 550 ^{o}C-CMS membrane, with the highest gas permeabilities, shows the largest pore volume and surface area, indicating a more open porous structure, while the 800 ^{o}C-CMS membrane shows the most compact pore structure.

Table 6.17: Total pore volume and surface area of CMS films derived from 6FDA/DETDA:DABA(3:2).

Membranes	Total pore volume ≤10.8 Å (cm^3/g)	Total surface area (m^2/g)
550 ^{o}C-CMS	0.2458	1060.3
800 ^{o}C-CMS	0.1738	753.6
800 ^{o}C-precrosslinked-CMS	0.1932	755.9

6.3.2 Temperature dependence of permeabilities

CO_2, CH_4, O_2, and N_2 permeability of various CMS membranes derived from 6FDA/DETDA:DABA(3:2) were obtained at 30 psia and 35 ^{o}C, 42.5 ^{o}C, and 50 ^{o}C. Permeation results reported in this study represent the average of at least two measurements with variance within 15%.

Least squares fit of permeability of four pure gases versus inverse absolute temperature for 550 ^{o}C-CMS, 800 ^{o}C-CMS, and 800 ^{o}C-precrosslinked-CMS as well as polymeric membranes derived from 6FDA/DETDA:DABA(3:2) are shown in Figure 6.11. As with studies on polymeric membranes [6, 7] and CMS membranes [17], the gas

permeability increases with temperature. As has been explained in Section 6.2.2, the permeability temperature dependence is a combination of diffusion and sorption coefficient temperature dependencies and the detailed temperature dependence of diffusion and sorption coefficients will be discussed in later sections.

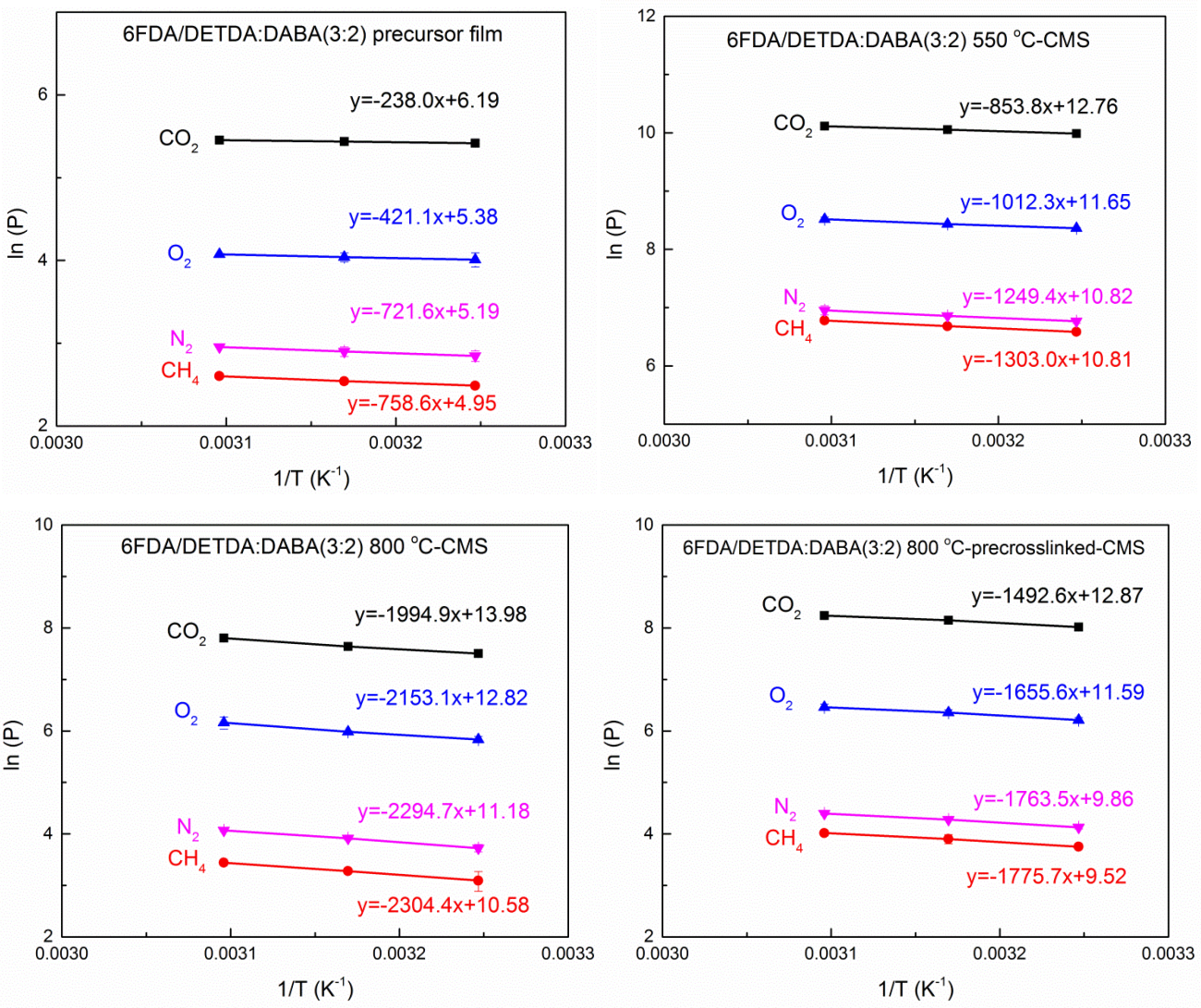

Figure 6.11: Temperature dependence of permeability for various gases in 550 °C-CMS, 800 °C-CMS, and 800 °C-precrosslinked-CMS as well as precursor membranes derived from 6FDA/DETDA:DABA(3:2) at 30 psia in the temperature range from 35 °C to 50 °C. (All data points are presented with error bars, some of the error bars are too small to be seen)

The permeation activation energies and the corresponding permeation pre-exponential factors for CO_2, CH_4, O_2, and N_2 of the four membrane materials are listed in Table 6.18 and Table 6.19. It can be seen that permeation activation energy are related to penetrant sizes and membrane types. Permeation activation energies increase with penetrant size in the order $CO_2 < O_2 < N_2 < CH_4$. On the other hand, the permeation activation energies of CMS membranes are much higher than that of precursor membranes. Among the three types of CMS membranes, the order of permation energy follows the opposite trend of gas permeability. More specifically, from the discussion in Chapter 5, one can conclude that the permeability order of the three CMS membranes at 35 ^{o}C to be: 800 ^{o}C-CMS < 800 ^{o}C-precrosslinked-CMS< 550 ^{o}C-CMS, while Table 6.18 shows a reverse order for permeation activation energy. Since permeation activation energy is the sum of diffusion activation energy and heat of sorption, a detailed analysis of these factors will be pursued in the following sections.

Table 6.18: Permeation activation energies of four gases for 550 °C-CMS, 800 °C-CMS, and 800 °C-precrosslinked-CMS as well as precursor membranes derived from 6FDA/DETDA:DABA(3:2) at 30 psia in the temperature range from 35 °C to 50 °C.

	E_P [kJ/mol]			
	CO_2	CH_4	O_2	N_2
Precursor membrane	2.0 ±0.1	6.3 ±0.0	3.5 ±0.0	6.0 ±0.0
550 °C-CMS	7.1 ±0.0	10.8 ±0.1	8.4 ±0.5	10.4 ±0.2
800 °C-CMS	16.6 ±0.4	19.2 ±0.4	17.9 ±0.5	19.1 ±0.0
800 °C-precrosslinked-CMS	12.4 ±0.5	14.8 ±0.1	13.8 ±0.4	14.7 ±0.1

Table 6.19: Permeation pre-exponential factors of four gases for 550 °C-CMS, 800 °C-CMS, and 800 °C-precrosslinked-CMS as well as precursor membranes derived from 6FDA/DETDA:DABA(3:2) at 30 psia in the temperature range from 35 °C to 50 °C.

	P_o [Barrers]			
	CO_2	CH_4	O_2	N_2
Precursor membrane	488	141	216.3	179.1
550 °C-CMS	$3.5*10^5$	$5.0*10^4$	$1.1*10^5$	$5.0*10^4$
800 °C-CMS	$1.2*10^6$	$3.9*10^4$	$3.7*10^5$	$7.2*10^4$
800 °C-precrosslinked-CMS	$3.9*10^5$	$1.4*10^4$	$1.1*10^5$	$1.9*10^4$

6.3.3 Temperature dependence of sorption coefficients

CO_2, CH_4, O_2, and N_2 sorption uptakes of 550 ^oC-CMS, 800 ^oC-CMS, and 800 ^oC-precrosslinked-CMS as well as polymeric membranes derived from 6FDA/DETDA:DABA(3:2) were measured at 35 ^oC, 42.5 ^oC, and 50 ^oC. Figures 6.12-6.15 show the CO_2, CH_4, O_2, and N_2 sorption isotherms of these four types of membranes at the three temperatures along with the Langmuir mode fitting. The fitted parameters are listed in Tables 6.20-6.23. As mentioned in Section 6.2, for consistency, the sorption coefficients reported here correspond to a sorption pressure of 30 psia, which equals to the permeation feed pressure. It can be seen that the Langmuir sorption capacity in the various types of membranes increases with gas critical temperature in the order: $N_2 < O_2 < CH_4 < CO_2$, and decreases as temperature increases.

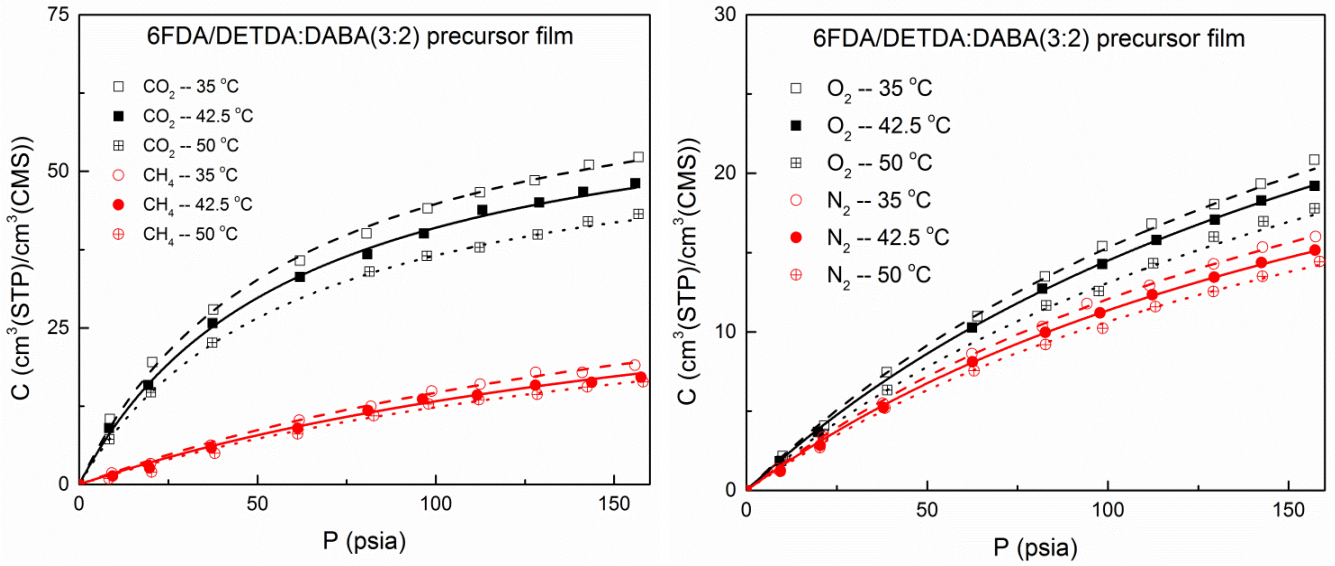

Figure 6.12: CO_2, CH_4, O_2, and N_2 sorption isotherms of 6FDA/DETDA:DABA(3:2) polymeric membrane at 35 ^oC, 42.5 ^oC, and 50 ^oC.

Table 6.20: CO_2, CH_4, O_2, and N_2 Langmuir mode parameters of 6FDA/DETDA:DABA(3:2) polymeric membrane at 35 ^oC, 42.5 ^oC, and 50 ^oC.

6FDA/DETDA:DABA(3:2) polymeric membrane						
	35 ^oC		42.5 ^oC		50 ^oC	
	CO_2	CH_4	CO_2	CH_4	CO_2	CH_4
$C_H^{'}$ [cm^3(STP) /cm^3]	71.1	47.3	65.8	42.9	58.6	39.9
b [1/psia]	0.017	0.004	0.017	0.005	0.017	0.004
	O_2	N_2	O_2	N_2	O_2	N_2
$C_H^{'}$ [cm^3(STP) /cm^3]	46.9	37.8	45.4	35.6	41.0	33.3
b [1/psia]	0.005	0.005	0.005	0.005	0.005	0.005

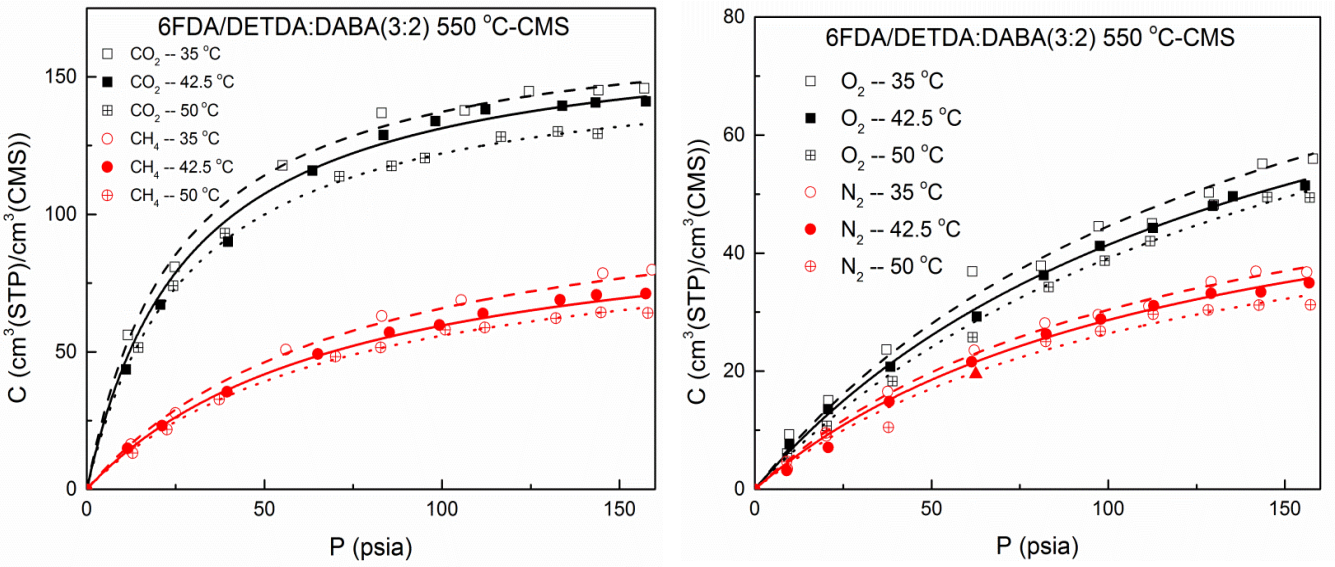

Figure 6.13: CO_2, CH_4, O_2, and N_2 sorption isotherms of 6FDA/DETDA:DABA(3:2) 550 ^oC- CMS membrane at 35 ^oC, 42.5 ^oC, and 50 ^oC.

Table 6.21: CO_2, CH_4, O_2, and N_2 Langmuir mode parameters of 6FDA/DETDA:DABA(3:2) 550 ^oC- CMS membrane at 35 ^oC, 42.5 ^oC, and 50 ^oC.

6FDA/DETDA:DABA(3:2) 550 ^oC- CMS						
	35 ^oC		42.5 ^oC		50 ^oC	
	CO_2	CH_4	CO_2	CH_4	CO_2	CH_4
$C_H^{'}$ [cm^3 (STP) /cm^3]	172.2	114.3	168.8	96.6	157.0	92.8
b [1/psia]	0.039	0.014	0.035	0.014	0.035	0.014
	O_2	N_2	O_2	N_2	O_2	N_2
$C_H^{'}$ [cm^3 (STP) /cm^3]	108.3	65.2	100.8	63.1	98.5	58.1
b [1/psia]	0.007	0.009	0.007	0.008	0.007	0.008

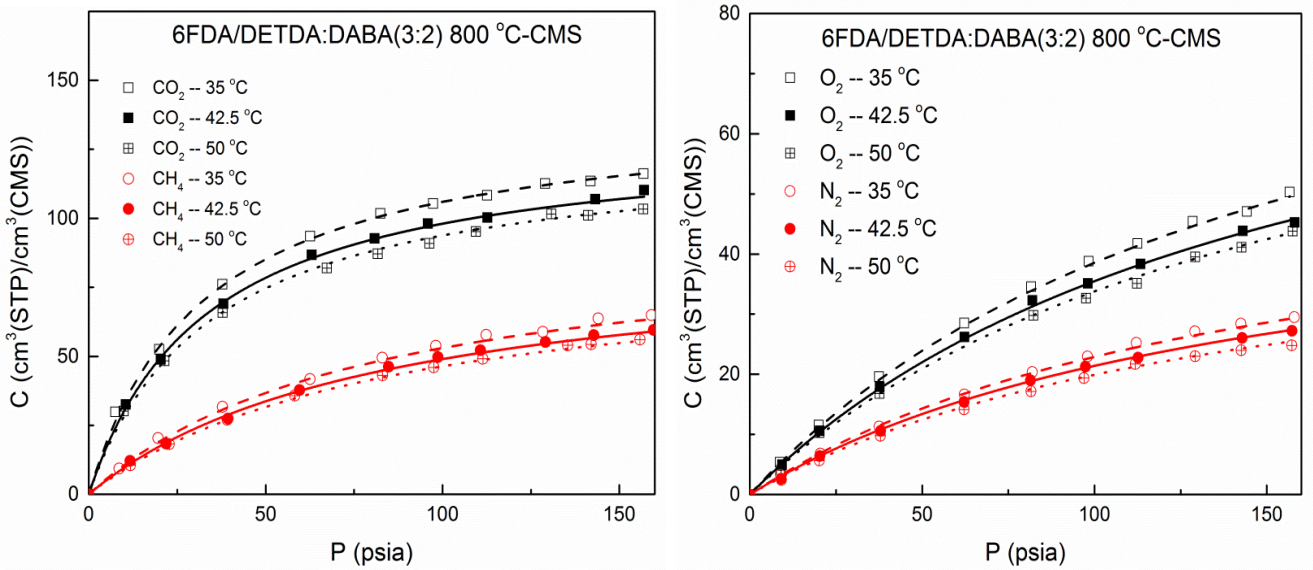

Figure 6.14: CO_2, CH_4, O_2, and N_2 sorption isotherms of 6FDA/DETDA:DABA(3:2) 800 ^oC- CMS membrane at 35 ^oC, 42.5 ^oC, and 50 ^oC.

Table 6.22: CO_2, CH_4, O_2, and N_2 Langmuir mode parameters of 6FDA/DETDA:DABA(3:2) 800 ^oC- CMS membrane at 35 ^oC, 42.5 ^oC, and 50 ^oC.

6FDA/DETDA:DABA(3:2) 800 ^oC-CMS						
	35 ^oC		42.5 ^oC		50 ^oC	
	CO_2	CH_4	CO_2	CH_4	CO_2	CH_4
C_H' [cm^3 (STP) /cm^3]	140.1	95.2	130.8	89.8	126.2	86.4
b [1/psia]	0.031	0.013	0.030	0.012	0.029	0.012
	O_2	N_2	O_2	N_2	O_2	N_2
C_H' [cm^3 (STP) /cm^3]	99.7	57.0	91.7	53.3	87.3	49.6
b [1/psia]	0.006	0.006	0.006	0.007	0.006	0.006

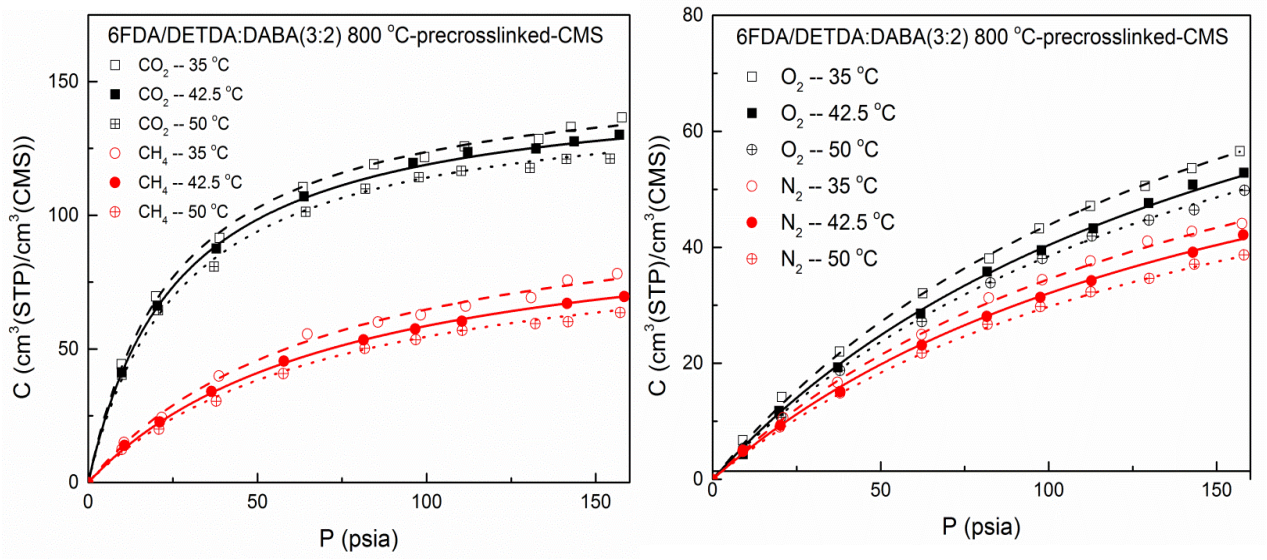

Figure 6.15: CO_2, CH_4, O_2, and N_2 sorption isotherms of 6FDA/DETDA:DABA(3:2) 800 °C-precrosslinked-CMS membrane at 35 °C, 42.5 °C, and 50 °C.

Table 6.23: CO_2, CH_4, O_2, and N_2 Langmuir mode parameters of 6FDA/DETDA:DABA(3:2) 800 °C-precrosslinked-CMS membrane at 35 °C, 42.5 °C, and 50 °C.

6FDA/DETDA:DABA(3:2) 800 °C-precrosslinked-CMS						
	35 °C		42.5 °C		50 °C	
	CO_2	CH_4	CO_2	CH_4	CO_2	CH_4
C_H' [cm^3(STP)/cm^3]	155.4	110.7	150.2	102.7	145.3	94.9
b [1/psia]	0.039	0.014	0.038	0.013	0.036	0.013
	O_2	N_2	O_2	N_2	O_2	N_2
C_H' [cm^3(STP)/cm^3]	110.3	88.9	107.7	84.1	102.8	78.1
b [1/psia]	0.007	0.006	0.006	0.006	0.006	0.006

Sorption uptakes of the CMS membranes for various gases are all much higher than the precursor membranes, indicating a much more open and porous structure in CMS membranes. Among the three CMS membrane, the 800 ^{o}C- CMS membranes presents the lowest sorption capacity, implying its most compact structures.

Figure 6.16 shows the least squares fit of sorption coefficients of four gases versus inverse absolute temperature for the four membrane materials. The apparent heats of sorption and the corresponding sorption pre-exponential factors for CO_2, CH_4, O_2, and N_2 are tabulated in Table 6.24 and Table 6.25. As described by Van't Hoff relationship (Eq.2.26), sorption coefficients of all gases decrease with increasing temperature, reflecting a negative heat of sorption.

By observing Table 6.24, one can see that the heat of sorption of polymeric membrane is more negative than those of CMS membranes. As has been explained in Section 6.2, in flexible polymers, the heat of sorption is comprised of two energetic contributions: one energetic contribution reflects the enthalpy change of a gas molecule to transfer from gas phase into a more stablized sorbed phase, and it is mainly governed by the gas critical temperature. The other energetic contribution is a combined result from the formation of a sorption site and the extent of interaction between sorbed molecule and the formed site [11, 12]. In rigid porous CMS media, the need to form a sorption site is absent. Furthermore with almost pure carbon structure, CMS membranes interact with gas molecules to a much smaller extent comparing with polymeric membranes. This is presumably why CMS membranes present lower heats of sorption. Table 6.24 also illustrates that in all types of membranes, the heat of sorption increases follows the order: $N_2 < O_2 < CH_4 < CO_2$, which is the order of gas critical temperature listed in Table 3.2. This general trend reflects that the first energetic contribution is dominant in both polymeric and CMS membranes.

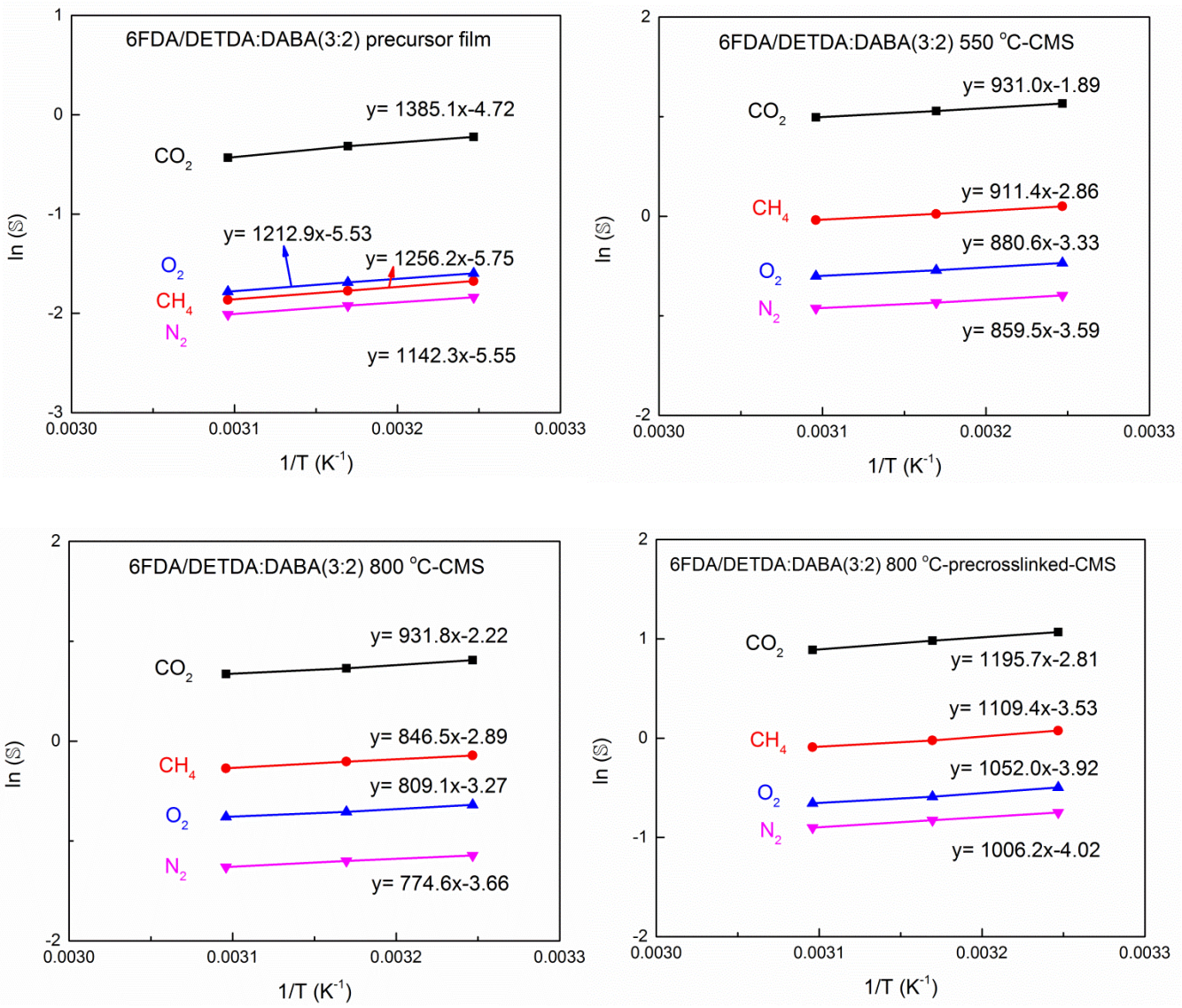

Figure 6.16: Temperature dependence of sorption coefficients for various gases in 550 °C-CMS, 800 °C-CMS, and 800 °C-precrosslinked-CMS as well as precursor membranes derived from 6FDA/DETDA:DABA(3:2) at 30 psia in the temperature range from 35 °C to 50 °C.

Table 6.24: Apparent heats of sorption of four gases in 550 °C-CMS, 800 °C-CMS, and 800 °C-precrosslinked-CMS as well as precursor membranes derived from 6FDA/DETDA:DABA(3:2) at 30 psia in the temperature range from 35 °C to 50 °C.

	H_S [kJ/mol]			
	CO_2	CH_4	O_2	N_2
Precursor membrane	-11.5 ±0.4	-10.4 ±0.1	-10.1 ±0.2	-9.5 ±0.3
550 °C-CMS	-7.7 ±0.0	-7.6 ±0.1	-7.3 ±0.2	-7.1 ±0.0
800 °C-CMS	-7.7 ±0.3	-7.0 ±0.2	-6.7 ±0.2	-6.4 ±0.1
800 °C-precrosslinked-CMS	-9.9 ±0.3	-9.2 ±0.2	-8.7 ±0.1	-8.4 ±0.1

Table 6.25: Sorption pre-exponential factors of four gases in 550 °C-CMS, 800 °C-CMS, and 800 °C-precrosslinked-CMS as well as precursor membranes derived from 6FDA/DETDA:DABA(3:2) at 30 psia in the temperature range from 35 °C to 50 °C.

	$\mathbb{S}_0$ [cc(STP)/cm^3/psia]			
	CO_2	CH_4	O_2	N_2
Precursor membrane	$9.0*10^{-3}$	$3.1*10^{-3}$	$3.9*10^{-3}$	$3.9*10^{-3}$
550 °C-CMS	$1.5*10^{-1}$	$5.7*10^{-2}$	$3.6*10^{-2}$	$2.8*10^{-2}$
800 °C-CMS	$1.1*10^{-1}$	$5.6*10^{-2}$	$3.8*10^{-2}$	$2.6*10^{-2}$
800 °C-precrosslinked-CMS	$6.0*10^{-2}$	$2.9*10^{-2}$	$2.0*10^{-2}$	$1.8*10^{-2}$

6.3.4 Temperature dependence of diffusion coefficients

Again, average diffusion coefficients of CO_2, CH_4, O_2, and N_2 at 35 ^oC, 42.5 ^oC, and 50 ^oC were calculated from the permeability and sorption coefficients. Temperature dependence of diffusion coefficients follows an Arrhenius relationship. Figure 6.17 illustrates the least squares fit of the diffusion coefficients for the four gases versus inverse absolute temperature for the four membranes derived from 6FDA/DETDA:DABA(3:2). The activation energies of diffusion and the corresponding diffusion pre-exponential factors are calculated and tabulated in Table 6.26 and Table 6.27.

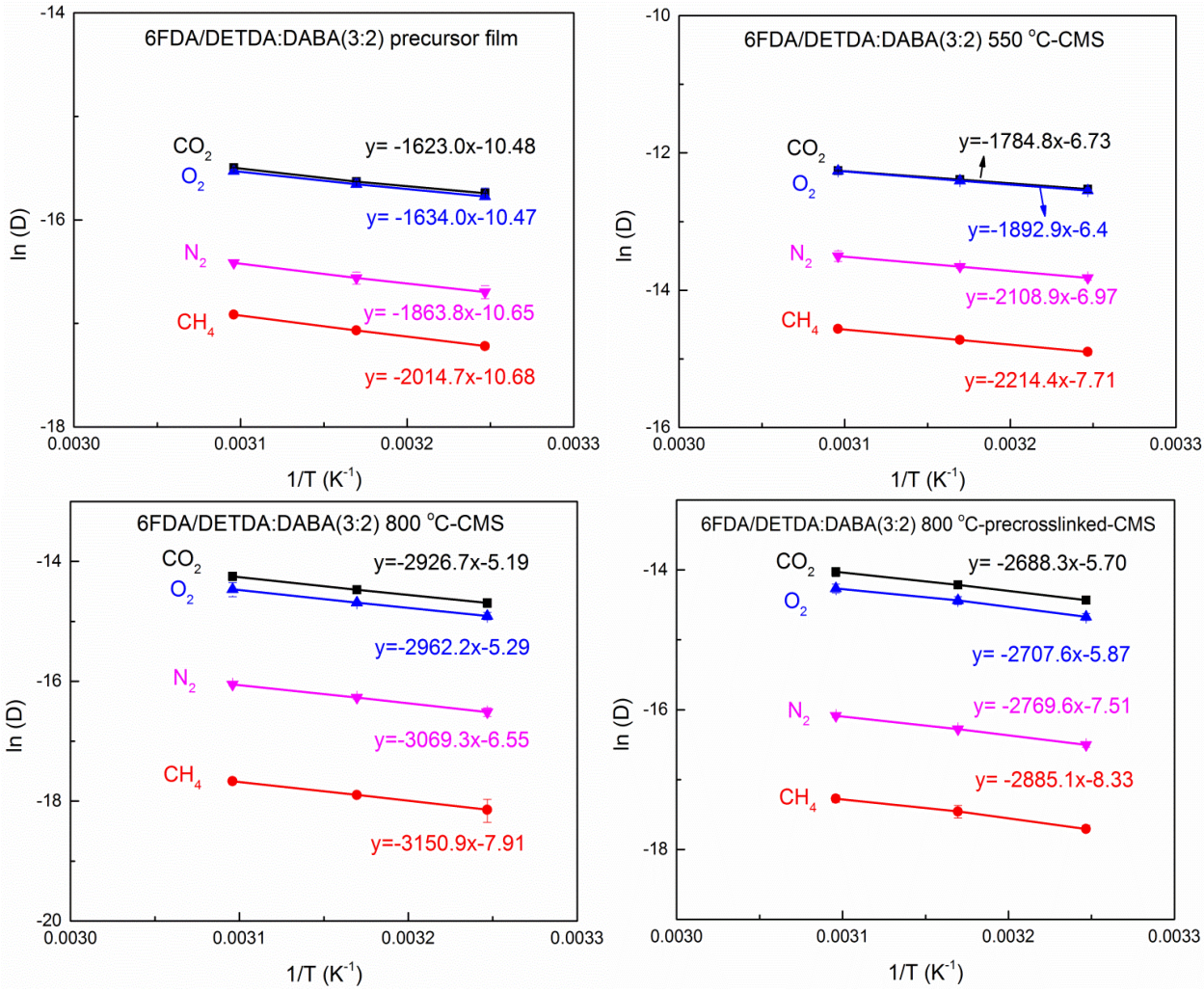

Figure 6.17: Temperature dependence of diffusion coefficients for 550 °C-CMS, 800 °C-CMS, and 800 °C-precrosslinked-CMS as well as precursor membranes derived from 6FDA/DETDA:DABA(3:2) at 30 psia in the temperature range from 35 °C to 50 °C. (All data points are presented with error bars, some of the error bars are too small to be seen)

Table 6.26: Diffusion activation energies of four gases for 550 °C-CMS, 800 °C-CMS, and 800 °C-precrosslinked-CMS as well as precursor membranes derived from 6FDA/DETDA:DABA(3:2) at 30 psia in the temperature range from 35 °C to 50 °C.

	E_D [kJ/mol]			
	CO_2	CH_4	O_2	N_2
Precursor membrane	13.5 ±0.2	16.8 ±0.1	13.6 ±0.2	15.5 ±0.4
550 °C-CMS	14.8 ±0.0	18.4 ±0.1	15.7 ±0.5	17.6 ±0.3
800 °C-CMS	24.3 ±0.3	26.2 ±0.2	24.6 ±0.0	25.5 ±0.3
800 °C-precrosslinked-CMS	22.4 ±0.2	24.0 ±0.4	22.5 ±0.0	23.0 ±0.1

Table 6.27: Diffusion pre-exponential factors of four gases for 550 °C-CMS, 800 °C-CMS, and 800 °C-precrosslinked-CMS as well as precursor membranes derived from 6FDA/DETDA:DABA(3:2) at 30 psia in the temperature range from 35 °C to 50 °C.

	D_0 [cm^2/s]			
	CO_2	CH_4	O_2	N_2
Precursor membrane	$2.8*10^{-5}$	$2.3*10^{-5}$	$2.8*10^{-5}$	$2.4*10^{-5}$
550 °C-CMS	$1.2*10^{-3}$	$4.5*10^{-4}$	$1.7*10^{-3}$	$9.3*10^{-4}$
800 °C-CMS	$5.6*10^{-3}$	$3.7*10^{-4}$	$5.0*10^{-3}$	$1.4*10^{-3}$
800 °C-precrosslinked-CMS	$3.3*10^{-3}$	$2.4*10^{-4}$	$2.8*10^{-3}$	$5.5*10^{-4}$

By comparing Table 6.24 and Table 6.25, we validaed our previous statement that diffusion activation energy outweighs the heat of sorption in affecting permeation activation energy. Again as shown in Table 6.26, larger penetrants (CH_4, N_2) require higher diffusion activation energies to enable passage than smaller penetrants (CO_2, O_2). 6FDA/DETDA:DABA(3:2) polymer membrane shows lower diffusion activation energy than the other three CMS memranes，reflecting a less hindered flexible matrix. The critical difference in the activation step between rigid CMS vs. flexible polymeric matrices relies upon the motion of the membrane matrix. The higher diffusive selectivities in CMS materials are fundamentally related to the rigid size discriminating ultramicropores. Table 6.26 also shows among the three types of CMS membranes, the diffusion activation energy follows the opposite order of gas permeability. The comparison between 550 ^{o}C-CMS and 800 ^{o}C-CMS shows that the diffuson activation energy increases with pyrolysis temperature, indicating greater resistance to gas transport due to the "tighter" CMS structure. Through precrosslinking, the 800 ^{o}C-precrosslinked-CMS gained a somewhat open framework and a drop in diffusion activation energy compared with 800 ^{o}C-CMS.

Maxwell-Stefan diffusion coefficients were also calculated for these four membrane materials. Again, similar conclusions can be drawn based on the results for average transport diffusion coefficients and Maxwell-Stefan diffusion coefficients. Figure 6.18 shows the temperature dependence of Maxwell-Stefan diffusivities for various gases of 550 ^{o}C-CMS; 800 ^{o}C-CMS; and 800 ^{o}C-precrosslinked-CMS as well as precursor membranes derived from 6FDA/DETDA:DABA(3:2) at 30 psia in the temperature range from 35 ^{o}C to 50 ^{o}C. Table 6.28 and Table 6.29 tabulate the Maxwell-Stefan diffusion activation energies and the corresponding Maxwell-Stefan diffusion pre-exponential factors. The general trends we observed from the results based on average transport diffusion coefficients are also valid for Maxwell-Stefan diffusion coefficients. By comparing Figure 6.17 and Figure 6.18, clearly, as for the average transport diffusivities,

the Maxwell-Stefan diffusivities increase with temperature. Table 6.27 shows that, similar to the trend observed in average diffusion activation energy, the 6FDA/DETDA:DABA(3:2) polymeric membrane with the flexble polymer chains, shows the lowest Maxwell-Stefan diffusion activation energy. Other three CMS membranes show higher Maxwell-Stefan diffusion activation energy, and the higher the pyrolysis temperature, the higher the Maxwell-Stefan diffusion activation energy becomes.

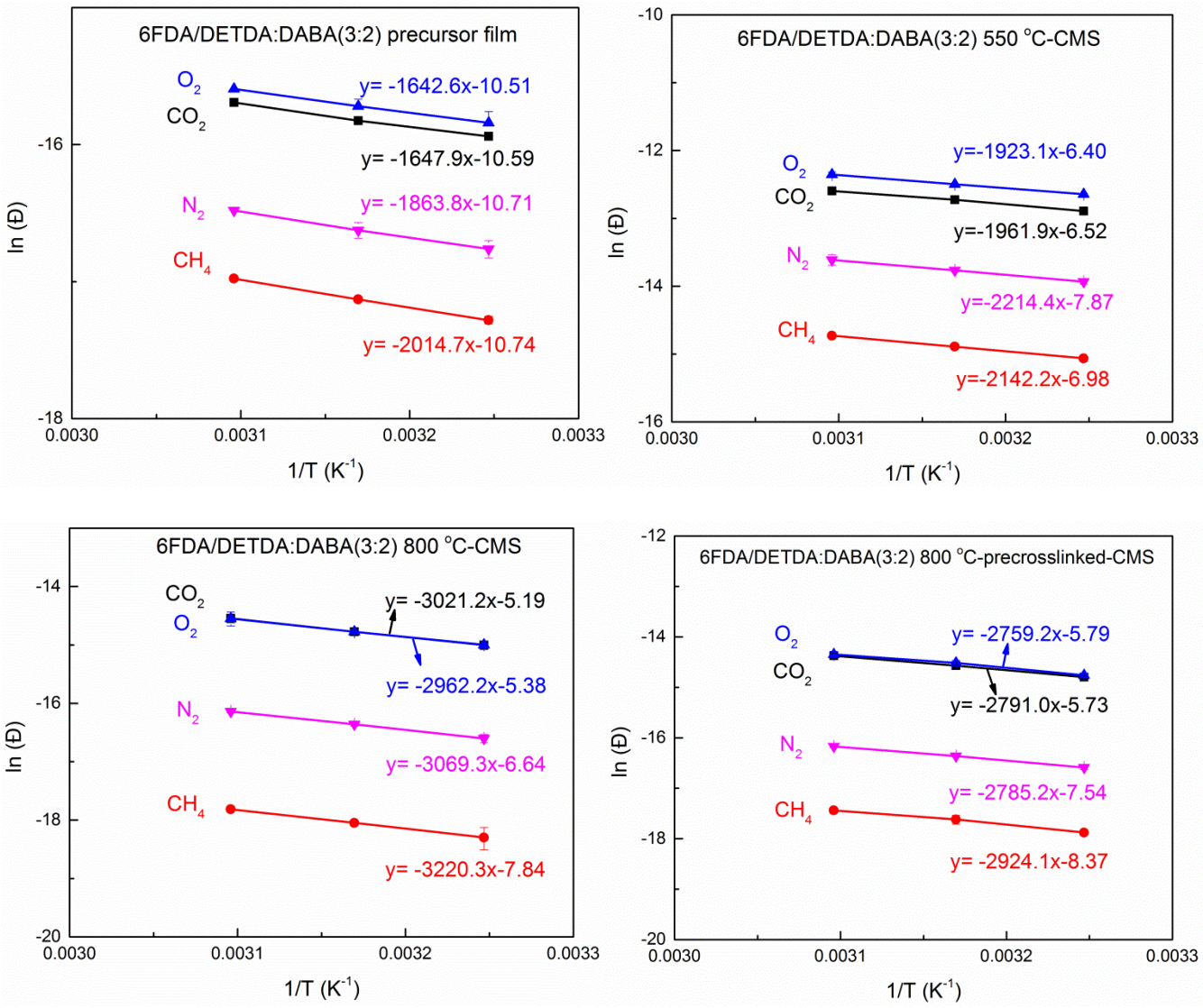

Figure 6.18: Temperature dependence of Maxwell-Stefan diffusivities for various gases in 550 °C-CMS, 800 °C-CMS, and 800 °C-precrosslinked-CMS as well as precursor membranes derived from 6FDA/DETDA:DABA(3:2) at 30 psia in the temperature range from 35 °C to 50 °C. *(In accordance with Figure 6.17).*

Table 6.28: Diffusion activation energies, based on Maxwell-Stefan diffusivity, of four gases for 550 ^{o}C-CMS, 800 ^{o}C-CMS, and 800 ^{o}C-precrosslinked-CMS as well as precursor membranes derived from 6FDA/DETDA:DABA(3:2) at 30 psia in the temperature range from 35 ^{o}C to 50 ^{o}C. *(In accordance with Table 6.26).*

	$E_Đ$ [kJ/mol]			
	CO_2	CH_4	O_2	N_2
Precursor membrane	13.7 ±0.2	16.8 ±0.2	13.7 ±0.2	15.5 ±0.4
550 ^{o}C-CMS	16.3 ±0.0	18.4 ±0.0	16.0 ±0.5	17.8 ±0.3
800 ^{o}C-CMS	25.1 ±0.2	26.8 ±0.2	24.6 ±0.0	25.5 ±0.1
800 ^{o}C-precrosslinked-CMS	23.2 ±0.2	24.3 ±0.3	22.9 ±0.4	23.2 ±0.1

Table 6.29: Diffusion pre-exponential factors, based on Maxwell-Stefan diffusivity, of four gases for 550 ^{o}C-CMS, 800 ^{o}C-CMS, and 800 ^{o}C-precrosslinked-CMS as well as precursor membranes derived from 6FDA/DETDA:DABA(3:2) at 30 psia in the temperature range from 35 ^{o}C to 50 ^{o}C. *(In accordance with Table 6.27).*

	$Đ_0$ [cm^2/s]			
	CO_2	CH_4	O_2	N_2
Precursor membrane	$2.5*10^{-5}$	$2.2*10^{-5}$	$2.8*10^{-5}$	$2.2*10^{-5}$
550 ^{o}C-CMS	$1.5*10^{-3}$	$9.3*10^{-4}$	$1.7*10^{-3}$	$3.8*10^{-4}$
800 ^{o}C-CMS	$5.5*10^{-3}$	$4.0*10^{-4}$	$4.6*10^{-3}$	$1.3*10^{-3}$
800 ^{o}C-precrosslinked-CMS	$3.2*10^{-3}$	$2.3*10^{-4}$	$3.1*10^{-3}$	$5.3*10^{-4}$

6.3.5 Diffusion selectivity: energetic selectivity vs. entropic selectivity

Table 6.30 summarizes at 30 psia and in the temperature range from 35 ^{o}C to 50 ^{o}C, the energetic and entropic selectivities of gas pairs CO_2/CH_4, O_2/N_2, and N_2/CH_4 for four types membranes derived from 6FDA/DETDA:DABA(3:2). Energetically for each gas pair, four membranes showed similar discriminating ability with polymeric and 550 ^{o}C-CMS membranes a little bit higher than 800 ^{o}C- and 800 ^{o}C-precrosslinked-CMS. Nevertheless, the energetic selectivities for these membrane materials for CO_2/CH_4, O_2/N_2, and N_2/CH_4 separations are all within the range of 1~4. On the other hand entropically, polymeric membrane behaves differently from CMS membranes. The entropic selectivity of precursor polymeric membrane for three gas pairs are all around unity, suggesting that polymeric membrane is not capable of discriminating between the configurational differences of penetrants. All three CMS membranes showed larger than unity entropic discriminations for these gas pairs and the discrimination ability depends on the limiting ultramicropore sizes. The three CMS membranes derived from 6FDA/DETDA:DABA(3:2) show increasing entropic selectivity for all gas pairs following the order: 550 ^{o}C-CMS < 800 ^{o}C-precrosslinked-CMS < 800 ^{o}C-CMS, which is the opposite of their permeability order for the various penetrants. As has been discussed in Chapter 5, the increase in pyrolysis temperature leads to a tightened pore structures in the resulting CMS membrane, which gives better discrimination between the shapes and configurational degrees of freedom of the penetrants. Table 6.30 shows clearly that the main contribution to the increased diffusion selectivity from 550 ^{o}C-CMS to 800 ^{o}C-CMS comes from the entropic selection factor (2.65 to 15.2 for CO_2/CH_4, 1.77 to 3.50 for O_2/N_2, and 2.08 to 3.92 for N_2/CH_4), while the energetic selectivity even drops in all cases (~4 to ~2 for CO_2/CH_4, ~2 to ~1.4 for O_2/N_2, and ~1.4 to ~1.3 for N_2/CH_4). What's more, the 800 ^{o}C-CMS is capable of such high selectivities (88.3 for CO_2/CH_4 and 7.6 for O_2/N_2) dues to its exceptional high entropic selectivity (15.2 for CO_2/CH_4 and 3.50 for

O_2/N_2). After precrosslinking, comparing with 800 ^oC-CMS, the 800 ^oC-precrosslinked-CMS gains some free volume and the entropic selectivity drops somewhat (with the exception of an increase for O_2/N_2). Nevertheless, it still holds much higher entropic selectivity compared with 550 ^oC-CMS.

Table 6.30: Summary of energetic and entropic selectivities of gas pairs CO_2/CH_4, O_2/N_2, and N_2/CH_4 for 550 ^oC-CMS, 800 ^oC-CMS, and 800 ^oC-precrosslinked-CMS as well as precursor membranes derived from 6FDA/DETDA:DABA(3:2) at 30 psia in the temperature range from 35 ^oC to 50 ^oC.

	Energetic selectivity		
	CO_2/CH_4	O_2/N_2	N_2/CH_4
Precursor membrane	3.5 ±0.2	2.1 ±0.4	1.6 ±0.3
550 ^oC-CMS	4.0 ±0.1	2.1 ±0.5	1.4 ±0.3
800 ^oC-CMS	2.1 ±0.3	1.4 ±0.3	1.3 ±0.2
800 ^oC-precrosslinked-CMS	1.8 ±0.4	1.2 ±0.1	1.4 ±0.3
	Entropic selectivity		
	CO_2/CH_4	O_2/N_2	N_2/CH_4
Precursor membrane	1.1 ±0.3	1.2 ±0.4	1.0 ±0.3
550 ^oC-CMS	2.7 ±0.2	1.6 ±0.4	2.1 ±0.1
800 ^oC-CMS	14.6 ±0.4	3.5 ±0.4	3.9 ±0.3
800 ^oC-precrosslinked-CMS	14.2 ±0.2	5.4 ±0.2	2.3 ±0.4

Overall, the higher than unity entropic selectivity in CMS membranes is a result of the rigid pore structures, which polymer chains lack, and it is also the reason that CMS membranes can outperform polymeric membrane, and more importantly, surpass the polymeric upper bound. The results shown in this study are consistent with previous studies. Rungta et al. [16] discussed the C_2H_4/C_2H_6 separation with polymeric and CMS membranes derived from Matrimid®. She observed that the polymeric Matrimid® membrane lacks entropic selectivity (~1) while CMS Matrimid® membranes possessed higher entropic selectivity, which also increased as the final pyrolysis temperature increases. Singh and Koros [15] have discussed the significance of entropic selectivity in molecular sieving materials， including 4A zeolite and carbon molecular sieve, for the O_2/N_2 pair. They also showed that in polypyrrolone polymeric membranes, despite quite rigid chains, entropic selectivity is close to unity, while in CMS membranes, a much higher entropic selectivity is observed.

Table 6.31 summarizes at 30 psia and in the temperature range from 35 ^oC to 50 ^oC, the energetic and entropic selectivities of gas pairs CO_2/CH_4, O_2/N_2, and N_2/CH_4 for 550 ^oC-CMS; 800 ^oC-CMS; and 800 ^oC-precrosslinked-CMS as well as precursor membranes derived from 6FDA/DETDA:DABA(3:2) based on Maxwell-Stefan diffusion coefficients.

Table 6.31: Summary of energetic and entropic selectivities of gas pairs CO_2/CH_4, O_2/N_2, and N_2/CH_4 for 550 ^oC-CMS, 800 ^oC-CMS, and 800 ^oC-precrosslinked-CMS as well as precursor membranes derived from 6FDA/DETDA:DABA(3:2) based on Maxwell-Stefan diffusion coefficients at 30 psia in the temperature range from 35 ^oC to 50 ^oC. *(In accordance with Table 6.30).*

	Energetic selectivity		
	CO_2/CH_4	O_2/N_2	N_2/CH_4
Precursor membrane	3.3±2.3	2.0±0.4	1.6±0.4
550 ^oC-CMS	2.2±0.0	2.0±0.5	1.3±0.3
800 ^oC-CMS	1.9±0.3	1.4±0.1	1.6±0.2
800 ^oC-precrosslinked-CMS	1.5±0.3	1.1±0.4	1.5±0.3
	Entropic selectivity		
	CO_2/CH_4	O_2/N_2	N_2/CH_4
Precursor membrane	1.1±0.3	1.2±0.2	1.0±0.1
550 ^oC-CMS	4.8±0.3	1.7±0.3	2.3±0.3
800 ^oC-CMS	13.8±0.3	3.5±0.2	3.4±0.3
800 ^oC-precrosslinked-CMS	14.0±0.4	5.6±0.5	2.4±0.3

Also as expected, the energetic and entropic selectivities of gas pairs CO_2/CH_4, O_2/N_2, and N_2/CH_4 for the four CMS membranes calculated based on Maxwell-Stefan diffusivity shows consistent trends as obtained from calculation based on average diffusivity.

6.4 Summary

Seven types of membranes were studied in this chapter: four CMS membranes derived from 6FDA-based precursor polyimides: 6FDA/DETDA, 6FDA:BPDA(1:1)/DETDA, 6FDA/1,5-ND:ODA(1:1), and 6FDA/DETDA:DABA(3:2) and three types of membranes derived from 6FDA/DETDA:DABA(3:2) including polymeric-; 800^{o}C-; and 800^{o}C-precrosslinked CMS membranes. The effects of testing temperature on gas permeation, sorption, and diffusion of these membranes were analyzed to provide insights into the factors governing gas separation properties in CMS membrane materials. The temperature dependence study was shown to be not only practically important, but also fundamentally valuable in evaluating the transport trends based on different CMS precursor structures. As expected, an increase in permeability as well as diffusivity and a decrease in sorption occur with increasing testing temperature. This study also clearly emphasizes the significance of entropic selectivity in CMS membranes vs. polymeric membranes for gas separation.

6.5 References

[1] L. Xu, M. Rungta, M.K. Brayden, M.V. Martinez, B.A. Stears, G.A. Barbay, W.J. Koros, Olefins-selective asymmetric carbon molecular sieve hollow fiber membranes for hybrid membrane-distillation processes for olefin/paraffin separations, J. Membr. Sci., 423-424 (2012) 314-323.

[2] D.Q. Vu, W.J. Koros, S.J. Miller, High pressure CO_2/CH_4 separation using carbon molecular sieve hollow fiber membranes, Ind. Eng. Chem. Res., 41 (2002) 367-380.

[3] N. Tanihara, H. Shimazaki, Y. Hirayama, S. Nakanishi, T. Yoshinaga, Y. Kusuki, Gas permeation properties of asymmetric carbon hollow fiber membranes prepared from asymmetric polyimide hollow fiber, J. Membr. Sci, 160 (1999) 179-186.

[4] K.M. Steel, W.J. Koros, Investigation of porosity of carbon materials and related effects on gas separation properties, Carbon, 41 (2003) 253-266.

[5] M. Rungta, L. Xu, W.J. Koros, Structure–performance characterization for carbon molecular sieve membranes using molecular scale gas probes, Carbon, 85 (2015) 429-442.

[6] C.M. Zimmerman, W.J. koros, Polypyrrolones for membrane gas separations. II. activation energies and heats of sorption, J. Polym. Sci. Polym. Phys. Ed., 37 (1999) 1251-1265.

[7] L.M. Costello, W.J. Koros, Temperature dependence of gas sorption and transport properties in polymers: measurement and applications, Ind. Eng. Chem. Res., 31 (1992) 2708-2714.

[8] M. Rungta, L. Xu, W.J. Koros, Carbon molecular sieve dense film membranes derived from Matrimid® for ethylene/ethane separation, Carbon, 50 (2012) 1488-1502.

[9] X. Ning, W.J. Koros, Carbon molecular sieve membranes derived from Matrimid® polyimide for nitrogen/methane separation, Carbon, 66 (2014) 511-522.

[10] W.J. Koros, D.R. Paul, CO_2 sorption in poly(ethylene terephthalate) above and below the glass transition, J. Polym. Sci. Polym. Phys. Ed., 37 (1978) 1251-1265.

[11] G.J. Van Amerongen, Diffusion in elastomers, Rubber Chem. Technol., 37 (1964) 1065-1152.

[12] W.J. Koros, Simplified analysis of gas/polymer selective solubility behavior, J. Polym. Sci. Polym. Phys. Ed., 23 (1985) 1611-1628.

[13] J. Karger, D.M. Ruthven, Diffusion in zeolites and other microporous solids, John Wiley, New York, USA, 1992.

[14] D.W. Breck, Zeolite Molecular Sieves, Structure, Chemistry and Use, John Wiley & Sons, New York, London, Sydney, Toronto, 1974.

[15] A. Singh, W.J. Koros, Significance of entropic selectivity for advanced gas separation membranes, Ind. Eng. Chem. Res., 35 (1996) 1231-1234.

[16] M. Rungta, Carbon molecular sieve dense film membranes for ethylene/ethane separations, in, Georgia Institute of Technology, Atlanta, GA, 2012.

[17] S. Fu, E.S. Sanders, S.S. Kulkarni, G.B. Wenz, W.J. Koros, Temperature dependence of gas transport and sorption in carbon molecular sieve membranes derived from four 6FDA based polyimides: Entropic selectivity evaluation, Carbon, 95 (2015) 995-1006.

CHAPTER 7

DEVELOPMENT OF ASYMMETRIC POLYMERIC AND CMS HOLLOW FIBER MEMBRANES DERIVED FROM 6FDA/DETDA:DABA(3:2)

7.1 Overview

This project not only focused on the development of novel CMS membrane materials, but also the translation of homogeneous dense film work to asymmetric hollow fibers, since as has been noted in Chapter 1 and Chapter 2, hollow fibers are industrially favored form of membrane [1]. Such membranes provide good mechanical strength due to the combination of a thin skin layer supported by a microporous support layer. What's more, higher surface area-to-volume ratio and higher packing density make fibers more practical compared with dense film membranes. In Chapter 4, 6FDA/DETDA:DABA(3:2) CMS membranes pyrolyzed at 550 ^{o}C have been shown to offer the greatest practical potential with the highest permeability. Moreover, in Section 4.2, 6FDA/DETDA:DABA(3:2) showed the smallest Δ (defined as T_d-T_g), which could potentially give the smallest degree of substructure collapse in the resulting CMS hollow fiber membranes. Thus, in this chapter, we focused on the development of defective free asymmetric polymeric and CMS hollow fiber membranes derived from 6FDA/DETDA:DABA(3:2). Section 7.2 confirms our statement that 6FDA/DETDA:DABA(3:2) CMS fibers showed the least substructure collapse during the high temperature pyrolysis by comparing the skin layer thicknesses of polymeric as well as CMS syringed extruded fibers derived from various precursor polymers. Section 7.3

discusses in detail the development of a potential spinning dope via a method of binodal line construction. Section 7.4 demonstrates a 6FDA/DETDA:DABA(3:2) defective free polymeric and CMS hollow fiber membrane is achievable.

7.2 Substructure collapse study in asymmetric CMS membranes

Previous studies have explained a phenomenon called substructure collapse in CMS hollow fiber membranes, as shown in Figure 7.1 [2, 3]. Xu found in his study that based on the permeability of Matrimid® CMS dense films, the permeance of Matrimid® CMS hollow fibers was much lower than expected, due to a thickened separation layer in the resulting CMS hollow fibers. It is well accepted that a thickened separation layer is unwanted since it decreases the productivity of a hollow fiber membrane. To confirm, Xu took SEM images of a Matrimid® polymer fiber and a Matrimid® CMS fiber as shown in Figure 7.1. Figure 7.1 (a) and (c) show the overall morphology of the precursor fiber and the resulting CMS fiber. It can be seen that compared with the precursor fiber, the cross-section of the carbon fiber is smoother and featureless. Figure 7.1 (b) and (d) show the asymmetric skin morphology of the same precursor fiber and the CMS fiber. It is quite obvious that in the precursor fiber, the skin layer thickness is < 2 μm and the support layer is very porous and occupied most of the fiber structure. On the other hand in the Figure 7.1 (d), in Matrimid® CMS fiber, the skin layer is not distinguishable, and even near the bore side the structure appears to be dense.

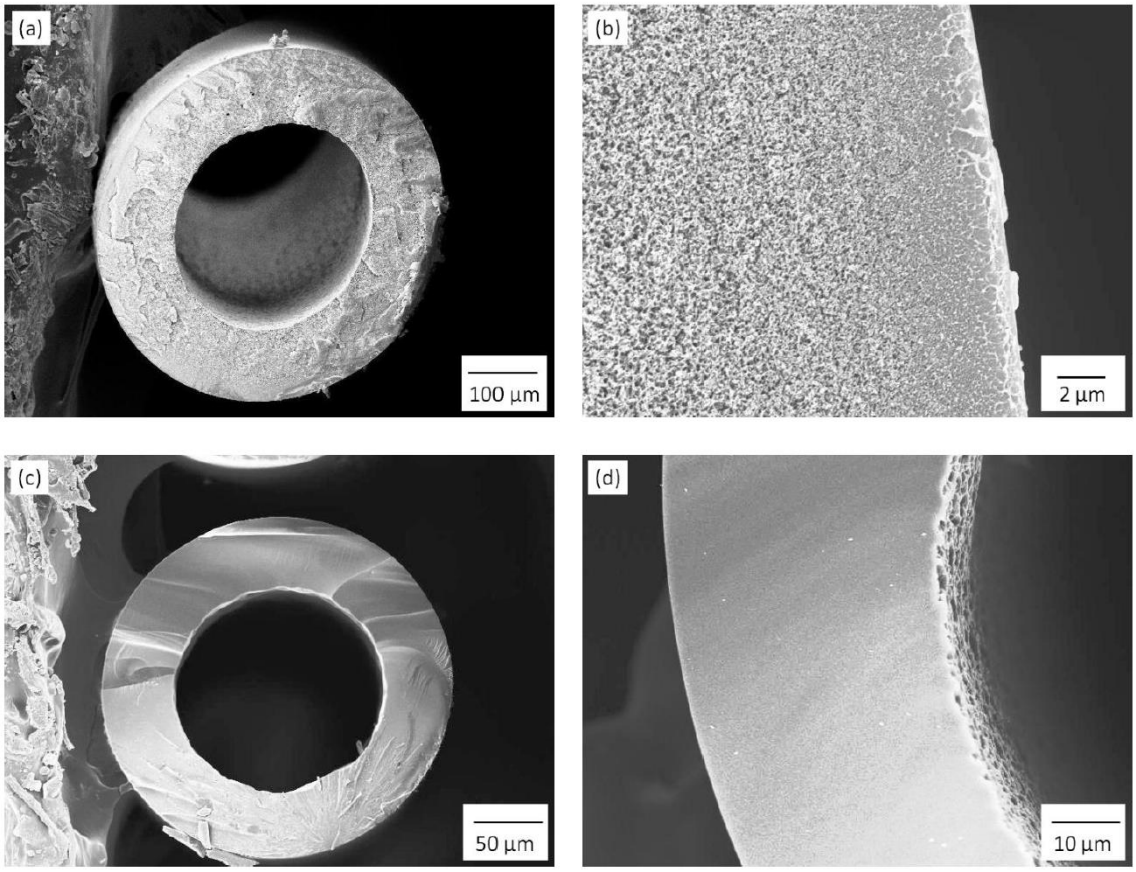

Figure 7.1: SEM images of Matrimid® precursor and CMS hollow fibers: a) cross-section of a precursor fiber; b) skin region of the precursor fiber; c) cross-section of a CMS fiber; d) fiber wall of the CMS fiber [2].

To explain this, Xu hypothesized that this substructure collapse is closely related to the rigidity of the material and exceeding the T_g of the material triggers the collapse. When temperature is higher than T_g, the thermal energy is sufficient to overcome segmental motional hindrance, and the polymer chains enter a soft viscous state instead of being rigid and tough [4]. Until temperature reaches T_d, the polymer remains in this

softened state, and the increased chain mobility enables easier chain interactions, and morphology densification occurs.

Identifying membrane materials with less tendency to collapse during pyrolysis, as noted in Chapter 4, can be guided using the parameter of Δ (defined as T_d-T_g). Our ideas from Chapter 4 suggest that 6FDA/DETDA: DABA(3:2), with the smallest Δ of 82 ^oC shown in Table 7.1, is the best choice for the next generation material to extend beyond 6FDA/BPDA-DAM for hollow fiber membrane formation. The SEM images of precursor and CMS fibers derived from 6FDA/DETDA, 6FDA:BPDA(1:1)/DETDA, and 6FDA/DETDA:DABA(3:2) formed by syringe tests were taken and compared. The 6FDA/1,5-ND:ODA(1:1) was not included in this part of study because of its poor solubility and unsuitability for forming a homogeneous solution with concentration up to 25%.

Table 7.1: Δ (defined as T_d-T_g) of the three polymers investigated in this chapter. T_d was measured with TGA and T_g is measured with DSC.

Polymer	T_d (^oC)	T_g(^oC)	$\Delta = T_d - T_g$ (^oC)
6FDA/DETDA	495	378	117
6FDA:BPDA(1:1)/DETDA	505	401	104
6FDA/DETDA:DABA(3:2)	470	388	82
6FDA:BPDA/DAM	492	424	68 [5]

Syringe test, instead of real spinning process, was applied to form mimic fibers since it is more economical. It has been successfully used as a screening tool to identify the influences of dope formulation and spinning conditions on resulting fibers [6]. In this

study, dopes made from three polymers with compositions listed in Table 7.2 were formed. This dope composition was chosen because it has been proven to give good 6FDA-DAM hollow fiber membranes [2, 7]. The dope consists of polymer, solvents (NMP (N-Methyl-2-pyrrolidone), and THF (tetrahydrofuran)), and non-solvent (Ethanol). NMP has a strong interaction with the polymer, and its relatively benign nature is favored over dimethylacetamide (DMAc). THF is a volatile solvent which assists skin layer formation. Ethanol is a weak non-solvent that allows a greater compositional window for tuning dope formulation compared with water.

Table 7.2: Dope composition used in this study for syringe tests.

Component	Weight percent (%)
Polymer	25
NMP	43
THF	10
Ethanol	22

Homogeneous dopes were loaded into disposable syringes and extruded at room temperature through a certain length of air gap into a water quench bath. To mimic real spinning process, we controlled the air gap to be between 5-10 cm and the temperature of the water bath to be around 50 ^{o}C. After being collected, the fibers were rinsed in water baths at least three times during 48 hours. The fibers were then solvent exchanged with three separate 20 min methanol baths followed by three separate 20 min hexane baths and finally dried under vacuum at 75 ^{o}C for about 3 hours. This protocol is equivalent to that used in typical fiber spinning. CMS fibers were made by pyrolyzing these syringe-formed precursor fibers following protocol 1 listed in Chapter 3 with a pyrolysis temperature up

to 550 ^{o}C in an inert argon atmosphere. The wall morphologies of these mimic precursor as well as CMS solid fibers were examined with SEM and are shown in Figure 7.2. The asymmetric structures of three polymeric fibers are quite similar as demonstrated in Figure 7.2, each consists of a dense skin layer (about 1-2 μm) and a porous support substructure. However, after being pyrolyzed into CMS fibers, the morphology of these materials changed. Most obviously, 6FDA/DETDA and 6FDA:BPDA(1:1)/DETDA CMS fibers lost their asymmetry during pyrolysis, the cross-section is smooth and featureless compared with polymeric fibers. This substructure collapse is undesirable because it tends to increase separation layer thickness in hollow fibers and to decrease permeance. On the other hand, 6FDA/DETDA: DABA(3:2) CMS fibers, although the skin layer almost doubled after pyrolysis, maintained the asymmetry. From this aspect, as expected from the Δ parameter analysis, 6FDA/DETDA: DABA(3:2) was a promising novel precursor material in forming high performance hollow fibers.

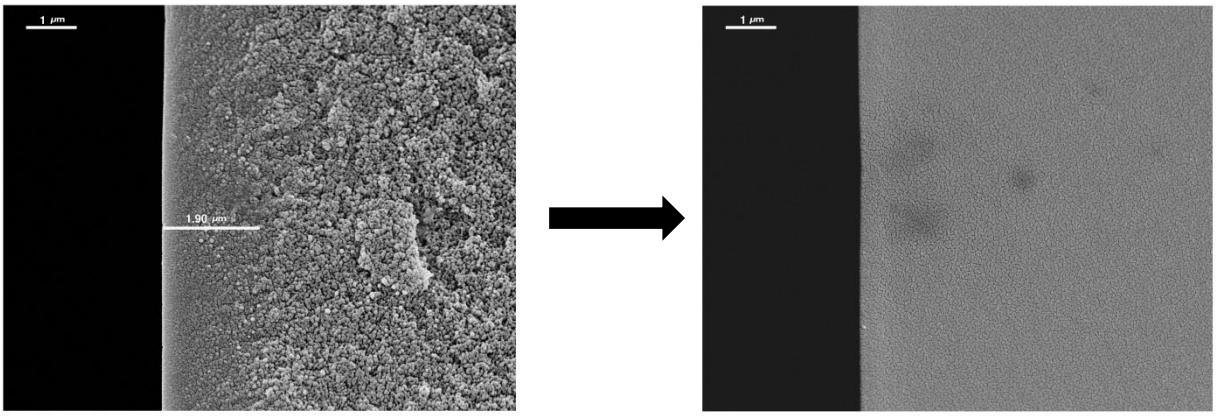

(a) 6FDA/DETDA polymer fiber

(d) 6FDA/DETDA CMS fiber

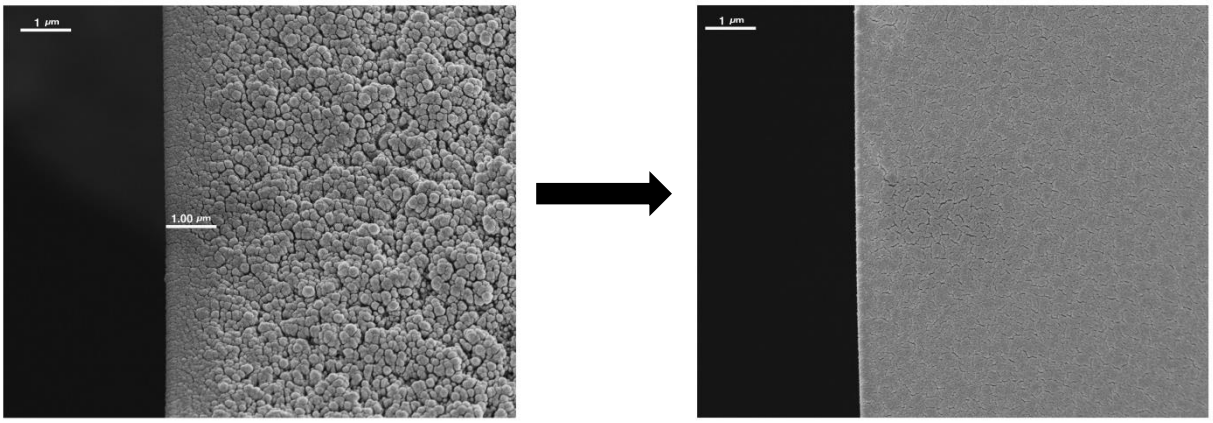

(b) 6FDA:BPDA(1:1)/DETDA polymer fiber

(e) 6FDA:BPDA(1:1)/DETDA CMS fiber

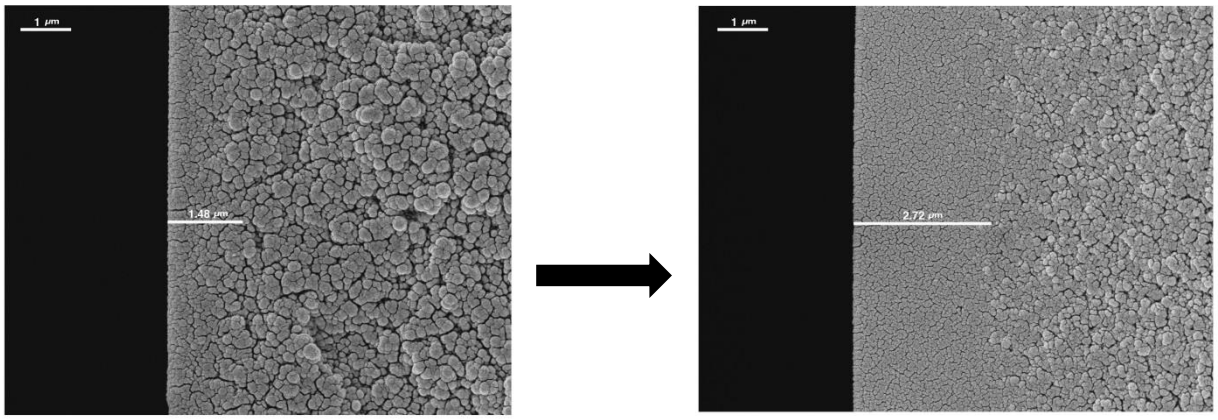

(c) 6FDA/DETDA:DABA(3:2) polymer fiber

(f) 6FDA/DETDA:DABA(3:2) CMS fiber

Figure 7.2: SEM images of cross-sections of syringe formed precursor and the resultant CMS fibers fabricated from 6FDA/DETDA, 6FDA:BPDA(1:1)/DETDA, and 6FDA/DETDA: DABA(3:2).

7.3 Exploration of potential dope formulation and spinning conditions

7.3.1 Polymer properties

Homogeneous dense film study requires a small amount of polymer (~0.5 g/sample), so the polymer used in dense film study was in-house synthesized. However, for asymmetric hollow fiber study, one spinning consumes ~ 30 g of the polymer. To ensure the consistency of the result, the polymer used in hollow fiber formation was custom synthesized by Akron Polymer System, Inc. Table 7.3 shows the molecular weights and polydispersity indices of both of the in-housed synthesized and the custom synthesized 6FDA/DETDA:DABA(3:2). The same T_g of both samples indirectly proves these two samples have similar structure properties. High molecular weight has been proven to be important to enhance spinnability and the ability to form defect-free skin layers [6, 8, 9]. The polymer purchased from Akron Polymer System, Inc has a high molecular weight (>100 kDa) and thus good spinnability, which allows spinning speeds greater than 50 m/min.

Table 7.3: The molecular weights, polydispersity indices, and the T_gs of in-house synthesized and custom synthesized 6FDA/DETDA:DABA(3:2).

Polymer 6FDA/DETDA:DABA(3:2)	Mw (kDa)	PDI (Mw/Mn)	T_g (^oC)
In-house synthesized (for homogeneous dense film study)	~ 95	2.5	388
Custom synthesized (for asymmetric hollow fiber study)	~140	2.0	388

7.3.2 Potential dope formulation

Since 6FDA/DETDA:DABA(3:2) is a novel polymer that has not been studied in hollow fiber membrane formation before, there is no existing dope formulation to refer to. Thus, the first step is to determine the potential spinning dope. In 2004, Wallace [10] constructed the binodal line for a related polymer 6FDA-DAM:DABA(4:1) as shown in Figure 7.3 (2). In 2011, Chen studied another DABA containing polyimide 6FDA-DAM:DABA (3:2), and showed a very similar binodal line as the one of 6FDA-DAM:DABA(4:1) (Figure 7.3 (3)). Ma et al. [11] in 2015, trying to deal with the issue of plasticization in polymer fibers, constructed the binodal line for PDMC (propane-diol monoesterified crosslinkable) polyimide, shown as (4) in Figure 7.3. They demonstrated this PDMC, containing carboxylic group as well, was even more hydrophilic than the previous two types of DABA containing polyimides. Figure 7.3 (1) represents the binodal line of Matrimid®, a well-studied commercial polyimide widely used for gas separation [12-15]. It can be seen that compared with Matrimid®, all DABA containing polyimides have binodal lines that shift towards the non-solvent side. This more hydrophilic nature, meaning more non-solvents are required for phase separation on the same level of polymer concentration, of these DABA containing polymers, results from the carboxylic acid group in DABA, tends to increase the phase separation time inside the water quench bath. Inadequate phase separation may lead to oval or crushed fibers that are not vitrified before contacting guide rolls. Thus, it is important to select the optimized dope formulation to produce hollow fibers with defect-free selective skin layers on a porous support substructure to provide a final robust membrane.

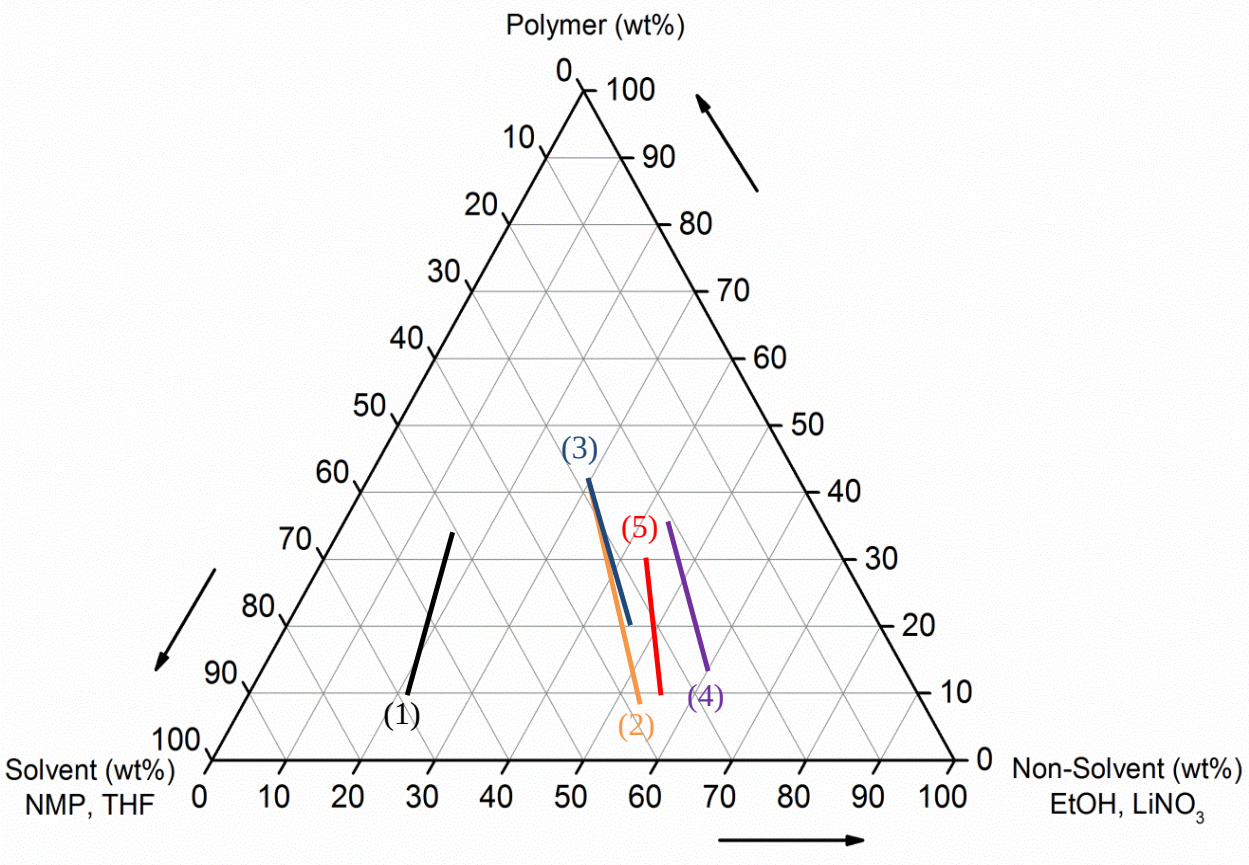

Figure 7.3: Ternary phase diagram depicting the binodal lines of polymers of: (1) Matrimid® [2]; (2) 6FDA-DAM:DABA(4:1) [10]; (3) 6FDA-DAM:DABA (3:2) [16]; (4) PDMC [11], and (5) 6FDA/DETDA:DABA(3:2) in this work.

Based on these valuable previous studies, we constructed the binodal line for 6FDA/DETDA:DABA(3:2) via a cloud point technique [17]. In this technique, at a fixed polymer concentration, a series of dope samples with increasing non-solvent amounts (accordingly solvent amounts were reduced) were made. With increasing non-solvent amount, the dope changes from one-phase into two-phase. The composition on the phase

boundary is called “cloud points”, and these cloud points at different polymer concentrations together form the binodal line. In essence, a spinnable dope composition should sit in the one-phase region and be close to the binodal line. During the air gap, the spinning conditions should drive the dope composition to the vitrified region, rapidly without crossing the two-phase region to the left of the binodal, or defective porous skinned fibers would be produced.

To select a workable dope, the polymer concentration must be identified, since dope viscosity is highly dependent on the polymer concentration. A higher concentration is preferred for the skin layer formation, however if too high, it may lead to excessive skin layers or substrate resistance in the support. Based on previous studies, in this study we decided to construct the binodal line of 6FDA/DETDA:DABA(3:2) based on the cloud points at the polymer concentrations of 15 wt%, 18 wt%, 22 wt %, 24 wt %, and 28 wt %.

The binodal lines were determined by presetting: (1) volatile solvent THF at 10 wt% to aid skin formulation during air gap [7]; (2): lithium nitrate ($LiNO_3$) at 6.5 wt% to accelerate phase separation during quenching, and adjusting NMP and ethanol concentration. Five series of dopes with the polymer concentrations listed above were prepared and observed. Figure 7.4 shows an example with polymer concentration fixed at 15 wt% and varying the ethanol concentrations from 35% to 50%. As shown, for this polymer concentration, the dopes are: (1) clear when the ethanol concentrations are lower than 46 wt%; (2) cloudy when ethanol concentration reaches 46 wt%; (3) phase separated when the ethanol concentration is higher than 46 wt%. Thus, the cloud point for the 15 wt% case is set to be: 15 wt% polymer – 52.5 (46 ethanol + 6.5 $LiNO_3$) wt% non-solvent – 32.5 wt% solvent. Based on this framework, the resulting binodal line is shown as (5) in Figure 7.3. As expected, the binodal line of 6FDA/DETDA:DABA(3:2) is similar with the other DABA-containing polyimides, and also shift towards the non-solvent side compared with Matrimid®.

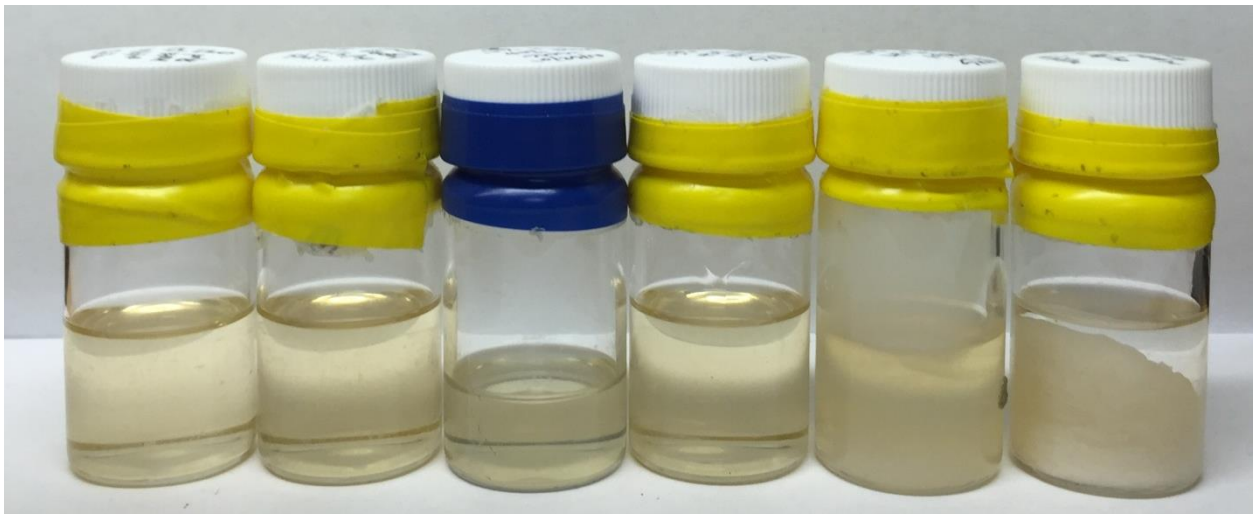

Figure 7.4: A series of 6FDA/DETDA:DABA(3:2) dopes with polymer concentrations fixed at 15 wt% and varying the ethanol concentrations from left to right: 35 wt%, 38 wt%, 40 wt%, 42 wt%, 46 wt%, 50 wt%. At 46 wt% of ethanol, the dope became cloudy and was set as the cloud point.

To determine the optimal polymer concentration in the potential spinning dope, besides the guideline related with solution viscosity described above, extensive syringes tests were also conducted to simulate real fibers. By observing the homogeneity and viscosity of polymer dopes, we decided 24 wt% or 28 wt% dopes offer sufficient viscosity. By observing the SEM images of syringed solid fibers formed from 24 wt% and 28 wt% dopes, as shown in Figure 7.5, one can see in both solid fibers, there is clearly a dense separation layer on top of a porous support layer. Since a thinner skin layer is preferred in hollow fiber application, 24 wt% polymer dope, which showed a thinner skin layer in Figure 7.5, was chosen.

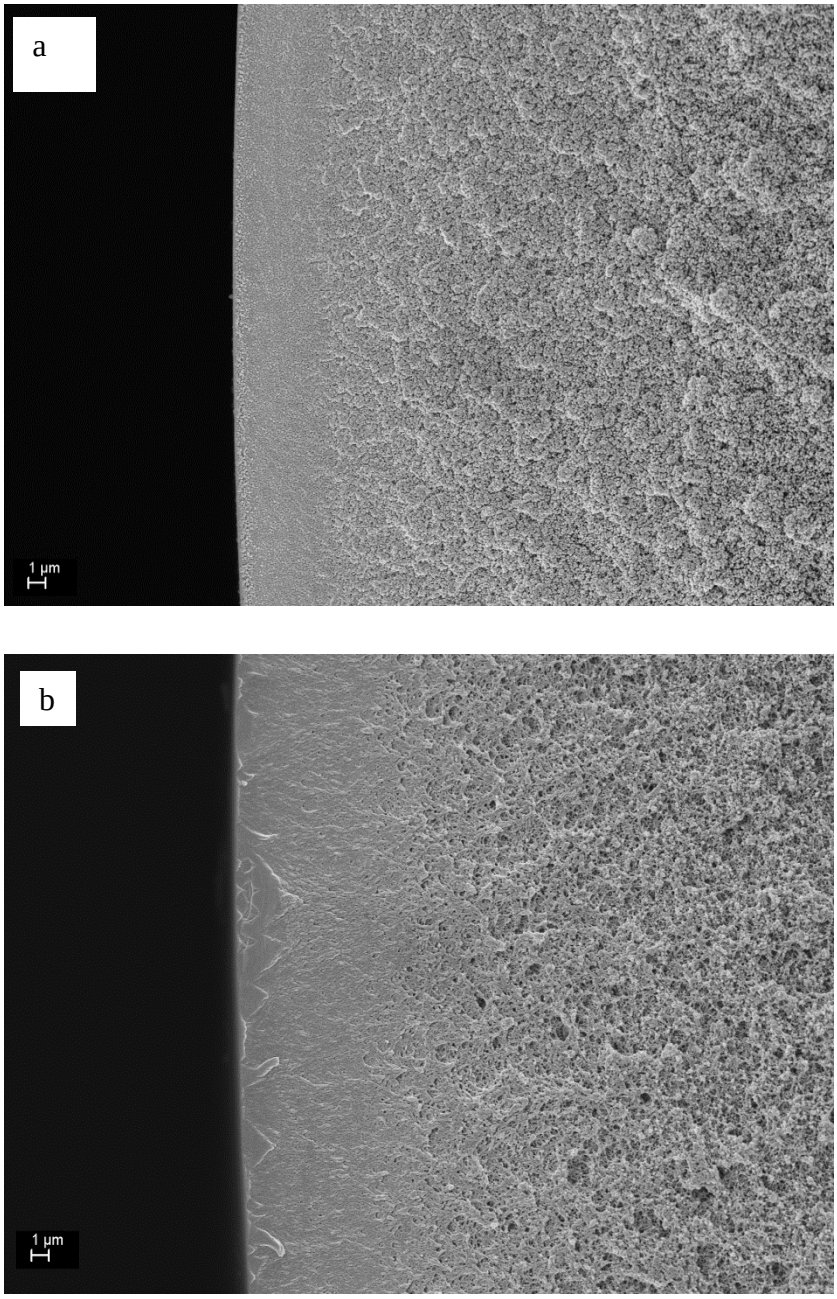

Figure 7.5: SEM images of syringed solid fibers prepared from: a) 24 wt% polymer dope; b) 28 wt% polymer dope.

Based on the above results and discussions, the initial dope formulation for spinning is listed in Table 7.4 and shown in the ternary phase diagram of 6FDA/DETDA:DABA(3:2) in Figure 7.6.

Table 7.4: Dope composition of 6FDA/DETDA:DABA(3:2) hollow fiber spinning.

Component	wt%
6FDA/DETDA:DABA(3:2)	24
NMP	29.5
THF	10
Ethanol	30
$LiNO_3$	6.5
total	100

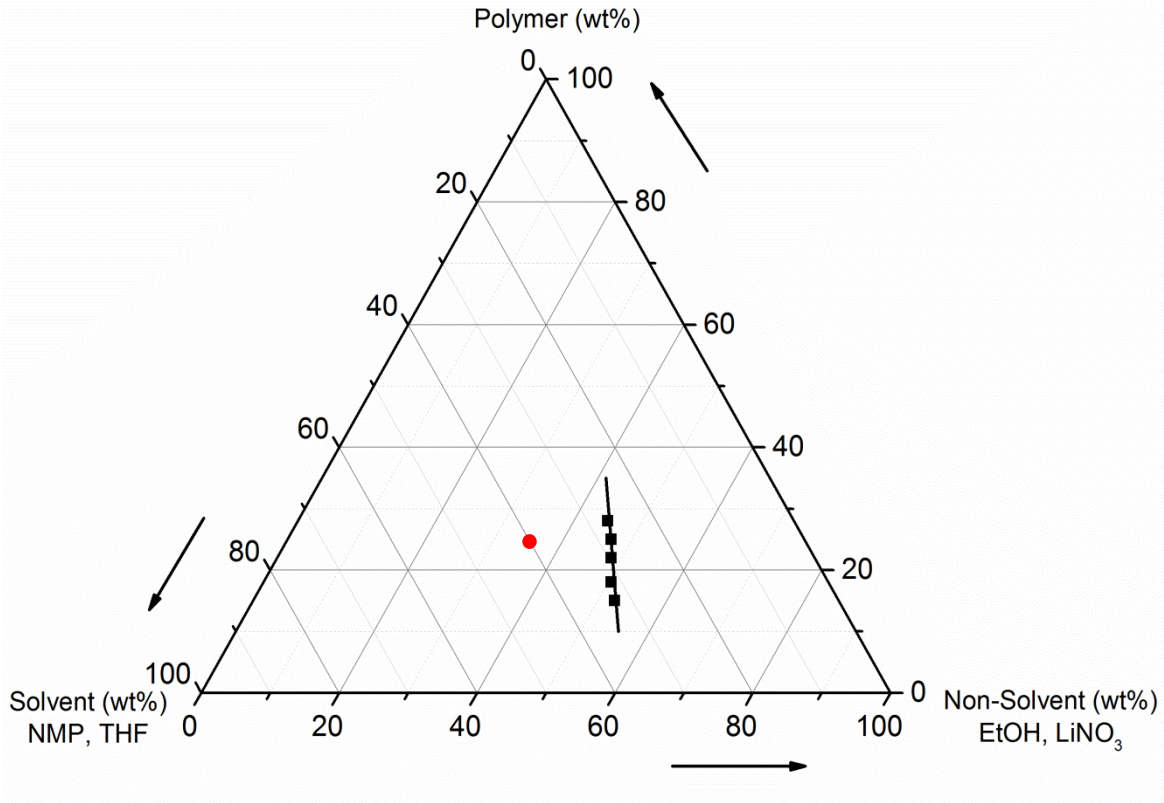

Figure 7.6: Ternary phase diagram of 6FDA/DETDA:DBA(3:2). Black square: dope compositions on the phase boundary; liner line: constructed binodal line; red dot: spinning dope composition.

7.3.3 Potential spinning conditions

The spinning conditions are listed in Table 7.5. The conditions were designed to (1) keep the neutral nature of the bore fluid, so the composition of bore fluid was set as 80 wt% NMP/20 wt% H_2O; (2) accelerate the evaporation rate of volatiles in the air gap, so a high spinneret temperature as 70 ^oC was used; (3) accelerate phase separation during quenching, so a 50 ^oC water quench temperature was used.

Table 7.5: Spinning conditions of 6FDA/DETDA:DABA(3:2) hollow fiber membranes.

Spinning parameter	value
Dope extrusion rate	180 mL/h
Bore fluid	60 mL/h, 80/20 (NMP/water)
Spinneret temperature	70 ^{o}C
Air gap	3-20 cm
Quench bath	50 ^{o}C
Take-up rate	27.2-50.9 m/min

7.4 6FDA/DETDA:DABA(3:2) hollow fiber membranes results

7.4.1 Precursor hollow fiber membranes

7.4.1.1 Morphology

The 6FDA/DETDA:DABA(3:2) precursor hollow fiber membranes were spun with the dope formulation and spinning conditions described in Section 7.3. A total of 18 states were formed in this spinning campaign. Figure 7.7 shows that multiple states were gathered on one drum.

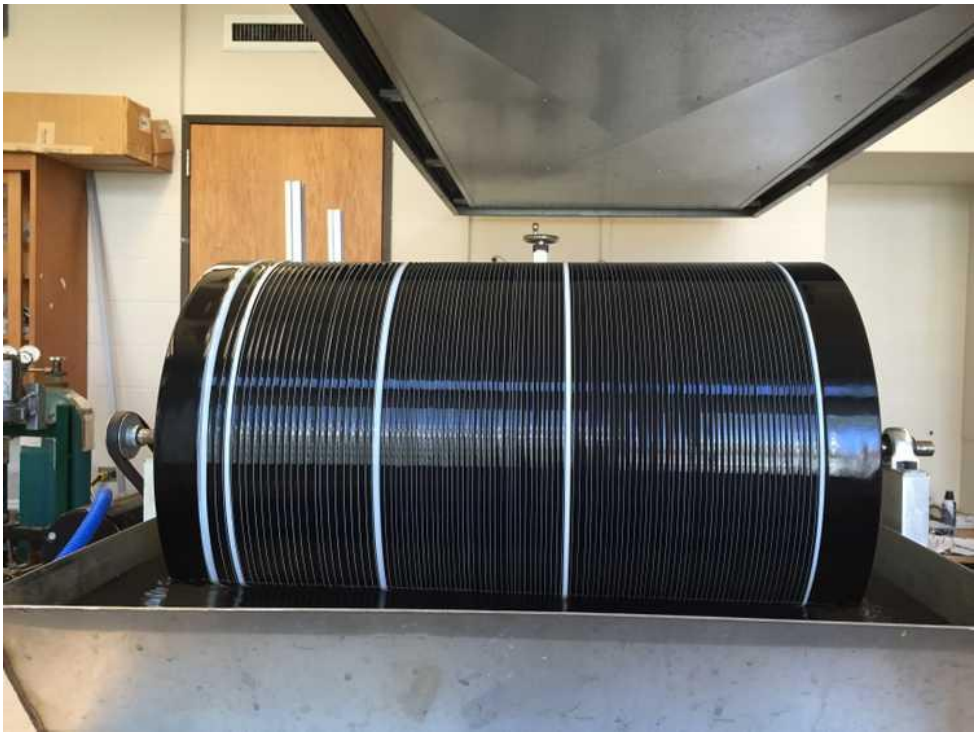

Figure 7.7: 3 states of 6FDA/DETDA:DABA(3:2) hollow fiber membranes collected on one drum. Each state was separated by “waste” rolls of hollow fibers.

SEM pictures of all spinning states were taken and Figure 7.8 shows one example of state 15. Figure 7.8 (a) shows the overall cross-section of a hollow fiber membrane, as can be seen, the fiber is circular and the overall macroscopic properties were reasonable. Figure 7.8 (b) shows the skin layer and the thickness of the skin layer was ~1.5 μm from the SEM observation.

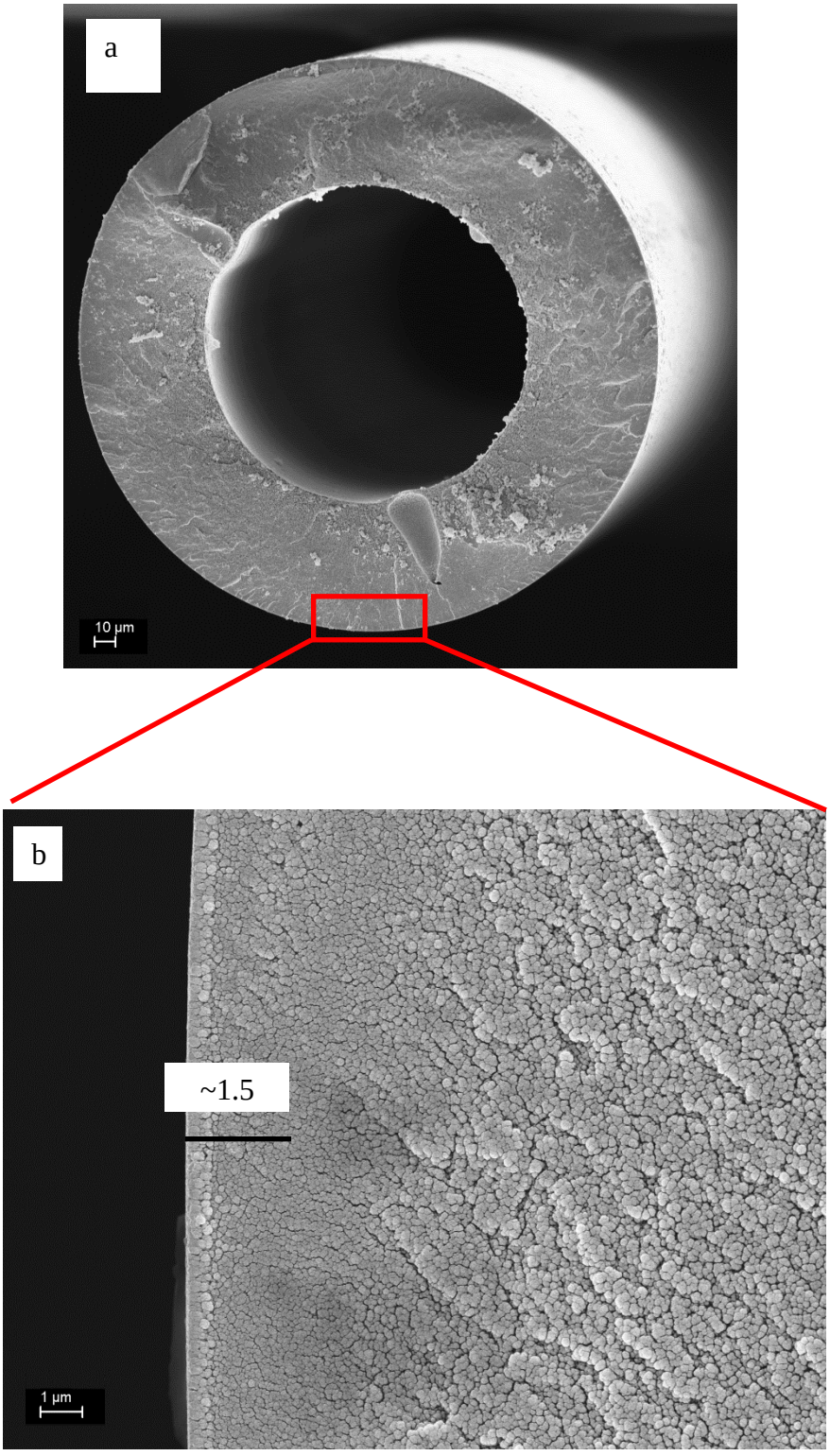

Figure 7.8: SEM pictures of a 6FDA/DETDA:DABA(3:2) hollow fiber membrane: a) overall cross-section morphology; b) skin layer morphology.

7.4.1.2 Pure gas separation performance

The transport properties and defect-free properties of these 18 states precursor hollow fiber membranes were characterized by pure gas permeation at 35 ^{o}C and 30 psia and the results are shown in Table 7.6. As noted in Chapter 3, when testing polymeric hollow fibers, multiple fibers, usually 4 to 6, were put in one module to build up the flux. Thus, the results shown here are the averages of 4 to 6 fibers. Table 7.6 also lists the pure gas selectivity of the homogeneous dense film fabricated from 6FDA/DETDA:DABA(3:2). By comparing with the selectivity of dense films, one can tell whether the fibers are defective free or not.

The intrinsic 6FDA/DETDA:DABA(3:2) O_2/N_2 and CO_2/CH_4 selectivity are 3.5 and 22 respectively. The fibers show similar or higher (may be attributed to shear induced molecular orientation on the skin layer [8, 18-20]) gas selectivity are considered to be defective free; otherwise, the fiber are defective. Based on this category, 9 states: 5, 8-10, 12, 14-15, and 17-18 are defective-free fibers; 7 states: 1-2, 4, 6-7, 11, and 16 are defective fibers with very low gas selectivities. On the other hand, other 2 states: 3 and 13, they showed somewhat gas selectivity but not as high as the intrinsic selectivity. For this type of fibers, we consider them to be with minor defects, which may be healed by PDMS (silicon rubber) coating [10].

Table 7.6: Pure gas permeation of 6FDA/DETDA:DABA(3:2) polymeric hollow fiber membranes. Testing conditions: 35 ^{o}C and 30 psia.

State #	Air gap (cm)	Take up rate (m/min)	Permeance (GPU)			Selectivity		
			O_2	CO_2	He	O_2/N_2	CO_2/CH_4	He/N_2
1	5	27.2	45	160	262	1.5	4.2	8.8
2	5	39.1	50	330	330	2.2	8.6	14.2
3	5	50.9	21	170	210	3.0	20	29.5
4	10	27.2	30	250	210	2.8	12	20.2
5	10	39.1	33	220	280	4.8	32	40.2
6	10	50.9	340	390	1000	1.0	1	3.0
7	15	27.2	750	1250	1660	1.0	0.8	2.1
8	15	39.1	27	173	230	4.4	30	37.0
9	15	50.9	33	190	260	3.7	21	29.0
10	20	27.2	17	141	140	4.8	29.1	38.2
11	20	39.1	15	42	60	3.9	8.2	16.0
12	20	50.9	13	145	110	4.7	32	40.6
13	3	27.2	63	358	470	2.9	13.5	21.5
14	3	39.1	63	335	500	4.1	25	33.0
15	3	50.9	39	150	305	3.4	20	27.5
16	7.5	27.2	700	750	2000	1.3	0.8	3.9
17	7.5	39.1	18	131	170	5.0	44.5	47.0
18	7.5	50.9	38	220	300	3.1	24	25.0
film	-	-	-	-	-	3.5	22	-

An extensive hollow fiber study is not within the scope of this work, since our main goal is to simply demonstrate that 6FDA/DETDA:DABA(3:2) defect-free polymeric and CMS hollow fibers can be achieved. Nevertheless as expected, based on Table 7.6, one can see lower air gap (3 cm) and faster take up rate (50.9 m/min) might be favored for future spinning since they provide higher chance of giving defective-free polymeric hollow fiber membranes, which is consistent with Chen's finding [16].

7.4.2 CMS hollow fiber membranes

7.4.2.1 Morphology

CMS hollow fiber membranes were also pursued in this work. Polymer hollow fiber membrane state 15, with spinning condition of air gap of 3 cm and take up rate of 50.9 m/min that has been discussed above to be very promising, was chosen as the precursor. The pyrolysis protocol used here is protocol 1 (550 ^{o}C under inert argon). SEM images, shown in Figure 7.9, were used to examine the morphologies of the resulting CMS hollow fiber membranes.

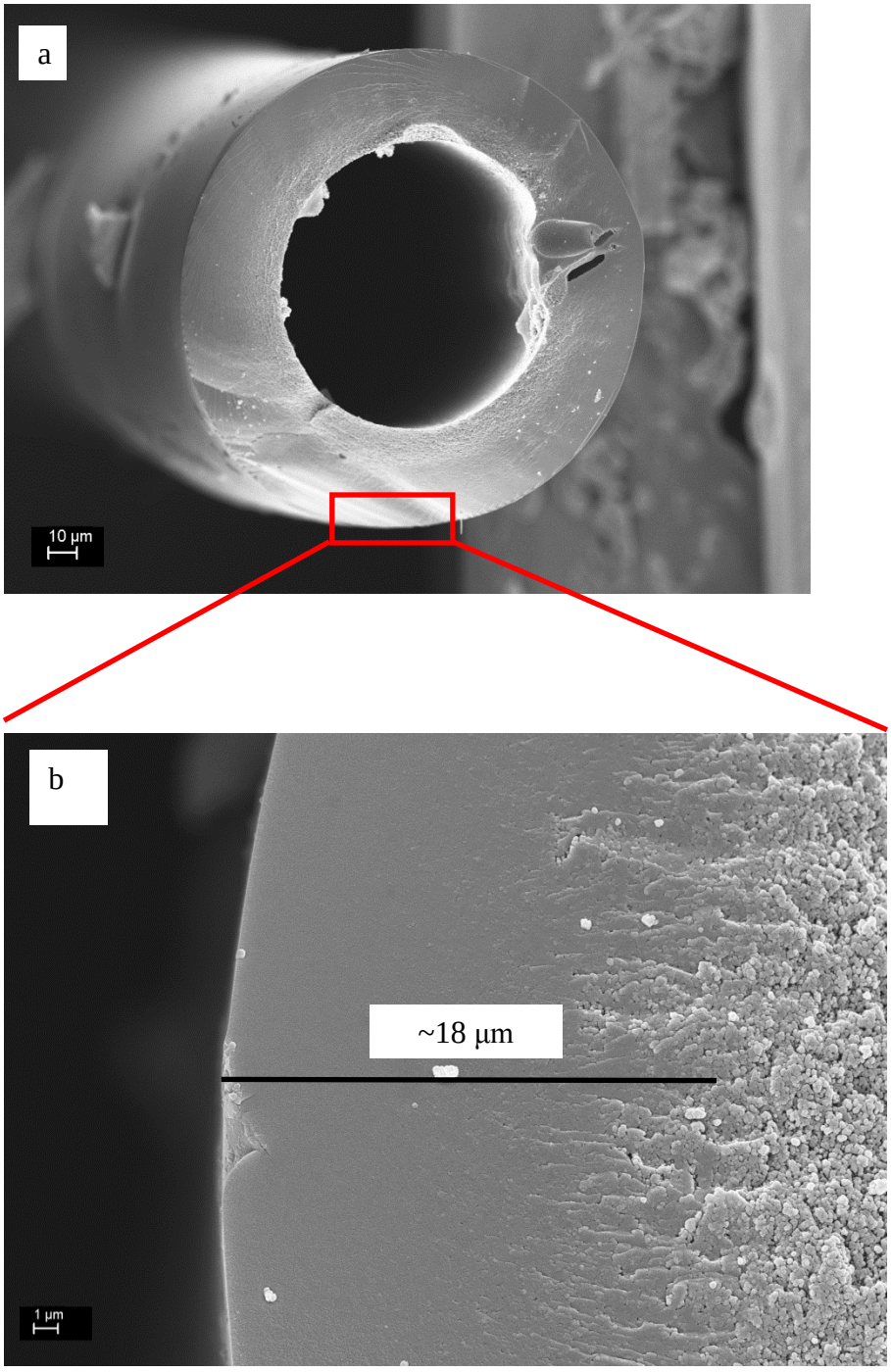

Figure 7.9: SEM pictures of a 6FDA/DETDA:DABA(3:2) CMS hollow fiber membrane: a) overall cross-section morphology; b) skin layer morphology.

Figure 7.9 (a) shows the overall cross-section of the CMS hollow fiber membrane, compared with the cross-section of the polymer hollow fiber membrane as shown in Figure 7.8 (a), the diameter of the CMS fiber shrank about 35%. Figure 7.9 (b) shows the CMS fiber skin layer and the thickness of the skin layer was ~18 μm. Comparing with the skin layer of the precursor hollow fiber (Figure 7.8 (b)), which was ~5 μm, one can know that some substructure collapse happened. This much thicker skin layer also dramatically decreased the productivity of this CMS hollow fiber as will be seen in the next section. Bhuwania [21] has found recently that a method called V-treatment can effectively restrict substructure morphology collapse in 6FDA:BPDA-DAM CMS hollow fibers. In this technique, a sol-gel reaction was used to induce vinyl crosslinked silica on precursor fiber pore walls, which restricts the ability of the porous support to collapse during pyrolysis. This technique might be a very attractive future work to improve the separation performance of 6FDA/DETDA:DABA(3:2) CMS hollow fiber membranes; however, it is out of the scope of this work.

7.4.2.2 Pure gas separation performance

The 6FDA/DETDA:DABA(3:2) polymeric hollow fiber membrane state 15 was pyrolyzed at 550 ^{o}C under inert argon to form CMS hollow fibers, and two single-fiber modules were prepared and tested with pure gases at 35 ^{o}C and 30 psia. Results are shown in Table 7.7 along with the pure gas separation performance of 6FDA/DETDA:DABA(3:2) CMS dense film. The intrinsic 6FDA/DETDA:DABA(3:2) CMS dense film showed O_2/N_2 and CO_2/CH_4 selectivity as 4.9 and 30.1 respectively. 6FDA/DETDA:DABA(3:2) CMS hollow fiber #1 showed somewhat lower but somewhat gas selectivity, indicating some minor defects in the separation skin layer. On the other hand, CMS #2 showed much higher selectivity than the intrinsic property, indicating its defect-free nature. However, at this point, the reason why the selectivity was much higher

is still unknown; we suspect there might be some trace contaminants (such as O_2) during the pyrolysis might have doped the membrane structure. This is consistent with the work of Kiyono on CMS hollow fibers from other precursors [22].This also might be another reason for the low permeance of these CMS fibers apart from the densified skin layer.

Table 7.7: Pure gas permeation of 6FDA/DETDA:DABA(3:2) CMS hollow fiber membranes. Testing conditions: 35 ^{o}C and 30 psia.

CMS #	Permeance (GPU)		Selectivity	
	O_2	CO_2	O_2/N_2	CO_2/CH_4
1	31	153	2.5	12.0
2	15	116	6.8	65.1
film	-	-	4.9	30.1

In this study, we showed 6FDA/DETDA:DABA(3:2) defective CMS hollow fiber membranes are achievable. However, the ultimate goal for CMS membrane development is to obtain excellent transport properties (high permeance and high selectivity). As an extension of this work, several techniques might need to be applied to optimize the 6FDA/DETDA:DABA(3:2) defective-free CMS hollow fiber membranes separation performance, including altering spinning conditions, V-treatment, altering pyrolysis temperature and atmosphere, etc..

7.5 Summary

In this chapter, we investigated the possibility of extending the promising separation performance obtained from 550 ^{o}C and inert argon pyrolyzed 6FDA/DETDA:DABA(3:2) CMS dense film into hollow fiber morphology. The translation from dense films to fibers is inevitable for commercial scale up. A spinnable 6FDA/DETDA:DABA(3:2) doped was formulated via a method of binodal line construction. The 6FDA/DETDA:DABA(3:2) polymeric hollow fiber membranes were successfully spun and pure gas permeation tests showed defective-free polymeric fibers were achieved. Through pyrolysis of the defective-free polymeric hollow fiber, good performanced CMS hollow fibers were also obtained. However, more in-depth optimization work needs to be done before thorough understanding of this particular type of CMS hollow fiber membranes can be achieved.

7.6 References

[1] R.W. Baker, Future directions of membrane gas separation technology, Ind. Eng. Chem. Res., 41 (2002) 1393-1411.

[2] L. Xu, Carbon molecular sieve hollow fiber membranes for olefin/paraffin separations, in, Georgia Institute of Technology, 2012.

[3] X. Ning, Carbon molecualr sieve membranes for nitrogen/methane separation, in, Georgia Institute of Technology, 2014.

[4] R.W. Baker, Membrane technology and applications, 2nd ed., John Wiley & Sons Ltd., West Sussex, England, 2004.

[5] L. Xu, M. Rungta, M.K. Brayden, M.V. Martinez, B.A. Stears, G.A. Barbay, W.J. Koros, Olefins-selective asymmetric carbon molecular sieve hollow fiber membranes for hybrid membrane-distillation processes for olefin/paraffin separations, J. Membr. Sci., 423-424 (2012) 314-323.

[6] S.B. Carruthers, Integral-skin formation in hollow fiber membranes for gas separations, in, The University of Texas at Austin, Austin, TX, 2001.

[7] C.-C. Chen, W. Qiu, S.J. Miller, W.J. Koros, Plasticization-resistant hollow fiber membranes for CO_2/CH_4 separation based on a thermally crosslinkable polyimide, J. Membr. Sci., 382 (2011) 212-221.

[8] I.C. Omole, Crosslinked Polyimide Hollow Fiber Membranes for Aggressive Natural Gas Feed Streams, in, Georgia Institute of Technology, Atlanta, GA, 2008.

[9] I.C. Omole, S.J. Miller, W.J. Koros, Increased Molecular Weight of a Cross-Linkable Polyimide for Spinning Plasticization Resistant Hollow Fiber Membranes, Macromolecules, 41 (2008) 6367-6375.

[10] D.W. Wallace, Crosslinked Hollow Fiber Membranes for Natural Gas Purification and Their Manufacture from Novel Polymers, in, The University of Texas at Austin, Austin, TX, 2004.

[11] C. Ma, C. Zhang, Y. Labreche, S. Fu, L. Liu, W.J. Koros, Thin-skinned intrinsically defect-free asymmetric mono-esterified hollow fiber precursors for crosslinkable polyimide gas separation membranes, Journal of Membrane Science, 493 (2015) 252-262.

[12] M. Rungta, L. Xu, W.J. Koros, Carbon molecular sieve dense film membranes derived from Matrimid® for ethylene/ethane separation, Carbon, 50 (2012) 1488-1502.

[13] X. Ning, W.J. Koros, Carbon molecular sieve membranes derived from Matrimid® polyimide for nitrogen/methane separation, Carbon, 66 (2014) 511-522.

[14] J. Barsema, S. Klijnstra, J. Balster, N. Vandervegt, G. Koops, M. Wessling, Intermediate polymer to carbon gas separation membranes based on Matrimid PI, Journal of Membrane Science, 238 (2004) 93-102.

[15] L. Xu, M. Rungta, W.J. Koros, Matrimid® derived carbon molecular sieve hollow fiber membranes for ethylene/ethane separation, J. Membr. Sci., 380 (2011) 138-147.

[16] C.-C. Chen, THERMALLY CROSSLINKED POLYIMIDE HOLLOW FIBER MEMBRANES FOR NATURAL GAS PURIFICATION, in, Georgia Institute of Technology, Atlanta, GA, 2011.

[17] S.B. Carruthers, G.L. Ramos, W.J. Koros, Morphology of integral-skin layers in hollow-fiber gas-separation membranes, J. Appli. Polym. Sci., 90 (2003) 399-411.

[18] S.A. Gordeyev, S.J. Shilton, Forced convection spinning of gas separation hollow fibre membranes: some underlying factors, mechanisms and effects, Journal of Membrane Science, 229 (2004) 225-233.

[19] A.F. Ismail, I.R. Dunkin, S.L. Gallivan, S.J. Shilton, Production of super selective polysulfone hollow fiber membranes for gas separation, Polymer, 40 (1999) 6499-6506.

[20] M. Niwa, Surface orientation effect of asymmetric polyimide hollow fibers on their gas transport properties, Journal of Membrane Science, 230 (2004) 141-148.

[21] N. Bhuwania, Engineering the morphology of carbon molecular sieve (CMS) hollow fiber membranes, in, Georgia Institute of Technology, 2013.

[22] M. Kiyono, Carbon molecular sieve membranes for natural gas separations, in, Georgia Institute of Technology, Atlanta, Georgia, 2010.

CHAPTER 8

CONCLUSIONS & RECOMMENDATIONS

8.1 Summary and conclusions

The overarching goal of this work is to develop a framework to understand the material science options to fabricate novel, high performing separation CMS membranes. Moreover, the translation of high-performance CMS dense film work to asymmetric hollow fiber membranes was also pursued. The objectives described in Chapter 1 are summarized and the progress toward these objectives are reviewed below.

Research objective 1: Analysis of different polymers as precursors to CMS dense film membranes for pure gas CO_2/CH_4 and O_2/N_2 separations (Chapters 4).

Former studies have shown that ultimate CMS properties are strongly influenced by polymer precursor properties [1-3]. Here we considered the separation performance of CMS membranes formed by pyrolysis under argon at 550 ^{o}C for four novel polyimide precursors referred to as 6FDA/DETDA, 6FDA:BPDA(1:1)/DETDA, 6FDA/DETDA:DABA(3:2) and 6FDA/1,5-ND:ODA(1:1). Various characterization techniques including Thermogravimetric Analysis (TGA), Differential Scanning Calorimetry (DSC), and Wide-angle X-ray Diffraction (WAXD) have been used to characterize the thermal and structural properties of these precursor polymers. The 6FDA/DETDA: DABA(3:2) precursor has been proven to be most favored in the formation of hollow fibers based on its smallest $\Delta(defined\ as\ T_d - T_g)$ among the four.

The separation performance of precursor polymer films formed from these polymers was studied using CO_2, CH_4, O_2 and N_2 pure gases. As expected, higher FFV in the polyimide led to higher permeability of the polymeric film. The separation performance, as well as the time dependent behavior, of the resulting CMS membranes pyrolyzed under pure argon at 550 ^oC was also examined. 6FDA/DETDA and 6FDA:BPDA(1:1)/DETDA carbon membranes showed somewhat lower permeability, but moderate aging tendencies. On the other hand, 6FDA/DETDA:DABA(3:2) and 6FDA/1,5-ND:ODA(1:1) CMS films displayed much higher permeability and comparable selectivity but were subject to larger aging-related phenomenon. The 6FDA/DETDA:DABA(3:2) derived CMS membranes showed the highest permeability (above 20,000 Barrer for CO_2 and above 4000 Barrer for O_2 at 35 ^oC), however, its larger time-dependent properties need to be addressed before using in practical applications. An active feed of mixed gas 50% CO_2/50% CH_4 was shown to suppress physical aging in 6FDA/DETDA: DABA(3:2) CMS, with only 4% CO_2 permeability loss and 6% CO_2/CH_4 selectivity gain.

Considering the separation performance, 6FDA/DETDA: DABA(3:2) and 6FDA/1,5-ND:ODA(1:1) CMS membranes showed the greatest potential for future study. The smallest T_d-T_g of 6FDA/DETDA: DABA(3:2) made it favorable in the formation of hollow fiber membranes. Thus, 6FDA/DETDA: DABA(3:2) CMS membrane is recommended for later studies.

Research objective 2: Investigation of pyrolysis conditions on gas separation properties of 6FDA/DETDA:DABA(3:2) derived CMS membranes for both pure and mixed gases separations (Chapter 5).

Separation performance of CMS membranes depends on the critical pore sizes and the pore size distribution, and several parameters have been studied to tailor the pore structures of CMS membranes including the pyrolysis temperature, pyrolysis atmosphere and heating protocol [4-12]. The 6FDA/DETDA:DABA(3:2) polyimide, which was shown to offer the greatest practical potential with the highest permeability, was pyrolyzed under different protocols to produce CMS dense film membranes for separation of important gas pairs including pure gases CO_2/CH_4, O_2/N_2 and mixture gases 50% CO_2/50% CH_4 and 50% C_3H_6/50% C_3H_8.

The effects of pyrolysis conditions, including pyrolysis temperature; O_2 doping; and precrosslinking were reported. It was shown that increased pyrolysis temperatures tend to give lower permeable but higher selective membranes. Oxygen doping provides a fine tuning method for altering the separation performance of CMS membranes by increasing the selectivity without a significant loss in permeability. Finally, CMS membranes derived from a novel method proposed in this study, referred to as precrosslinking, was proven to be very attractive with significantly improved gas permeability and slightly drop in selectivity. The results reported in this chapter serves as a guide for future optimization study on CMS membranes; the combination of different tuning methods might be attractive for some specific applications.

Research objective 3: Temperature dependence of gas transport and sorption in CMS membranes derived from 6FDA based polyimides: entropic selectivity evaluation (Chapter 6).

CMS fiber membranes have been proven to be able to maintain stability under high pressure up to 1000 psi without undergoing plasticization [13-15]; however, temperature effects on CMS membranes need more systematic investigations. Analysis of the effects of testing temperature on CMS membrane performance is of importance not only just from a practical purpose, but also for a fundamental understanding of CMS materials. In this objective, seven types of membranes were studied: four CMS membranes derived from 6FDA-based precursor polyimides: 6FDA/DETDA, 6FDA:BPDA(1:1)/DETDA, 6FDA/1,5-ND:ODA(1:1), and 6FDA/DETDA:DABA(3:2), and three types of membranes derived from 6FDA/DETDA:DABA(3:2) including polymeric-; 800 ^{o}C-; and 800 ^{o}C-precrosslinked CMS membranes. Temperature dependences of gas transport and sorption properties on these CMS membranes were examined over the temperature range from 35 ^{o}C to 50 ^{o}C. The permeability, sorption and diffusivity were reported, and activation energies of permeation and diffusion as well as heats of sorption for gases CO_2, CH_4, O_2, and N_2 of these materials are compared. Moreover, the diffusion selectivity was factored into "energetic" and "entropic" selectivity contributions to clarify the importance of entropic factors as tools to tailor membrane performance.

The study of the four similar yet diverse CMS materials derived from 6FDA-based precursor polyimides provides a tool to identify structural characteristics that affect permeability and selectivity. On the other hand, the study on the three membranes derived from 6FDA/DETDA:DABA(3:2) provides fundamental insights into the reason for CMS membranes to outperform polymeric membranes.

Research objective 4: Create "first generation" asymmetric hollow fiber CMS membranes with 6FDA/DETDA:DABA(3:2) (Chapter 7).

Asymmetric hollow fiber membranes are the industrially favored membrane morphology, considering the high surface area to volume ratio and scalability in manufacturing they can provide. In this objective, we investigated the possibility of extending the promising separation performance obtained from 550 ^{o}C and inert argon pyrolyzed 6FDA/DETDA:DABA(3:2) CMS dense film into hollow fiber morphology. The 6FDA/DETDA:DABA(3:2) polymeric hollow fiber membranes were successfully spun and pure gas permeation tests showed defect-free polymeric fibers were achieved. Through pyrolysis of the defect-free polymeric hollow fibers, good performance CMS hollow fibers were also obtained.

This part of study serves as a guide for future study by showing the viability of spinning the first generation of 6FDA/DETDA:DABA(3:2) hollow fiber membranes and efficacy in achieving defect-free CMS hollow fiber membranes. Extensive and more in-depth optimization work needs to be done before thorough understanding of this particular type of CMS hollow fiber membranes can be achieved.

8.2 Recommendations

The research objectives of the current project have been successfully achieved. During the development, however, there remain several opportunities for further investigation. Below outlines several potential research areas.

8.2.1 Optimizing CMS membranes for specific applications

As mentioned in Chapter 1, natural gas consists of various impurities including heavy hydrocarbons, moisture, H_2S and etc.. There are many other potential applications of CMS membranes in natural gas processing. One can imagine for different applications, the dominant factors and the corresponding requirement for a membrane can be significantly different. For example for the separation of N_2 and CH_4, due to the small size difference between N_2 and CH_4, higher pyrolysis temperature might be essential to achieve high-performing N_2-selective CMS membranes. On the other hand when considering separating CO_2 and CH_4, of C_3H_6 and C_3H_8, gas pairs with relatively larger sizes, a relatively lower pyrolysis temperature might be favored to enhance gas permeability.

Moreover, corresponding to different starting precursor polymers, different pyrolyzing conditions would be preferred to meet a certain separation requirement. When polymers like Matrimid® are to be used, denser and more compact CMS structures would be anticipated. Thus, pyrolysis conditions with relatively lower pyrolysis temperature and lower amount of doping should be applied to avoid reducing the productivity. On the other hand, when starting with polymers like 6FDA/DETDA:DABA(3:2) as discussed in this study, higher pyrolysis temperature (>1000 ^oC for instance) and higher doping amount must be used if higher selectivity is a must.

In this study, the effects of precursor polymer, pyrolysis temperature, O_2-doping, and precrosslinking on the resulting CMS membranes have been demonstrated. Of course,

there are various other parameters including soaking time, ramping rate that can be altered to tune the structure of CMS membranes. All these parameters, separate or combined, must be optimized according to the specific application.

8.2.2 Further investigation of entropic contributions to CMS membrane separation performance

The importance of entropic selectivity, which stems from the shape and subtle configurational difference between the penetrants, has been illustrated. In this study, the work been done has been focusing on separating the relatively small gases of CO_2, CH_4, O_2 and N_2. Rungta [16] previously demonstrated the importance of entropic selectivity in C_2H_4/C_2H_6 in Matrimid® and 6FDA:BPDA-DAM derived CMS membranes. Results showed the somewhat planar shape of C_2H_4 allows it to have an entropic advantage over the bulkier C_2H_6. What's more, she also compared C_2H_4, which has several degrees of rotational and vibrational freedom, against Kr, which has essentially the same critical size but lacks any configurational degrees of freedom.

Xu et al. [13] proposed the use of CMS membranes in separations in cracked gas processing including olefins (C_2H_4 and C_3H_6) from paraffins (C_2H_6 and C_3H_8), between H_2, acetylene (C_2H_2), methylacetylene (MA) and propadiene (PD). The spacing-filling models of these molecules are shown in Figure 8.1. The "slit-shaped" pore structures of CMS membranes may enable effective discrimination between linear molecules (H_2, C_2H_2, MA, PD), somewhat planar olefins (C_2H_4 and C_3H_6), and the bulky paraffins (C_2H_6 and C_3H_8). Furthering the understanding of these entropic contributions would be beneficial for the practical application of CMS membranes. In addition to the experimental results as achieved in this study, theoretical predictions and molecular simulations on these extended separation processes may be required to facilitate better understanding.

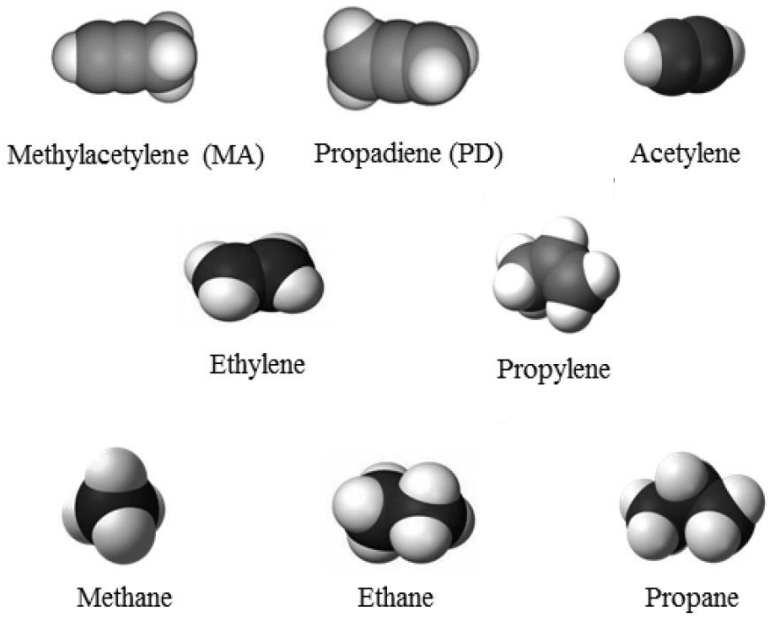

Figure 8.1: Space filling models of C1, C2, and C3 hydrocarbons [13].

8.2.3 Performance evaluation under realistic conditions and scale up of CMS hollow fibers

The focus of the current work was to investigate the separation performance of CMS membranes for pure gases under mild temperatures and pressures. In practical applications, however, mixture gases and harsh temperatures and pressures might be of interest. It would be wise to perform more systematic studies of CMS membranes under practical testing conditions and several parameters must be considered carefully. These parameters include feed gas pressure, feed gas composition, and testing temperature and etc.. Results in Chapter 5 showed that mixture gases 50% CO_2/50% CH_4 tests exhibited lower CO_2 permeabilities and higher CO_2/CH_4 selectivities comparing with pure gas tests. Results in Chapter 6 showed at higher testing temperature, membranes gas permeability

increased while selectivity decreased. The separation performance of CMS membranes under high feed pressures, which is not discussed in this study, is also of great practical potential worth systematic investigation.

Another issue for CMS hollow fiber membrane applications is the scale up issue. While our current pyrolysis set-up allows production of 5-20 fibers in one batch, Dr. Oguz Karvan has successfully demonstrated preliminary CMS hollow fiber scale-up to 200 fiber capacity in a larger pyrolysis furnace. Preliminary results are encouraging and it is speculated that the impact of scale-up on pyrolysis, module construction and permeation behaviors are all important areas for future developments.

8.2.4 Further investigation of optimization of hollow fiber membrane formation

Chapter 7 revealed that 6FDA/DETDA:DABA(3:2) defective free polymeric and CMS hollow fibers can be achieved without extensive optimization on the fiber spinning and formation process. The 6FDA/DETDA:DABA(3:2) polymer fibers achieved in Chapter 7 exhibited thicker skin layer than desired. Several parameters need to be optimized to lower the skin thickness. For example, lower THF content in the dope formulation, lower spinneret temperature, and lower air gas all can help to achieve this goal. Several more optimizing spinning trials would be required before satisfying thin-skin-layered polymer hollow fibers can be achieved.

Defective polymer hollow fiber membranes can be treated to "plug" minor defects in the fiber skin. This post treatment usually involves coating the fibers with a second layer of a highly permeable, flexible polymer that can prevent Knudsen flow through the fibers as outline previously [17]. A crosslinkable polydimethylsiloxane (PDMS) Sylgard 184® has been widely used. The successful application of this PDMS treatment can help

to tell whether a fiber is defective free or not by comparing the gas selectivity before and after the treatment.

In order to transform the thin-skin-layered polymer hollow fibers into thin-skin-layered CMS fibers, the V-treatment mentioned in Chapter 7 needs to be used [18]. The detailed V-treatment effect on restricting substructure collapse in 6FDA/DETDA:DABA(3:2) CMS hollow fiber and its side effect of changing intrinsic separation property in the skin layer needs systematic understanding.

Lastly, for the commercial application to reduce the cost of polymer precursor in CMS hollow fiber membranes, composite hollow fiber membranes can be a future path to pursue. A typical composite hollow fiber membrane may comprise of a low-cost core layer precursor, with a more intrinsically open 6FDA based precursor as a sheath layer. The morphology of a typical dual-layer composite hollow fiber membrane and its spinning set-up is shown in Figure 8.2.

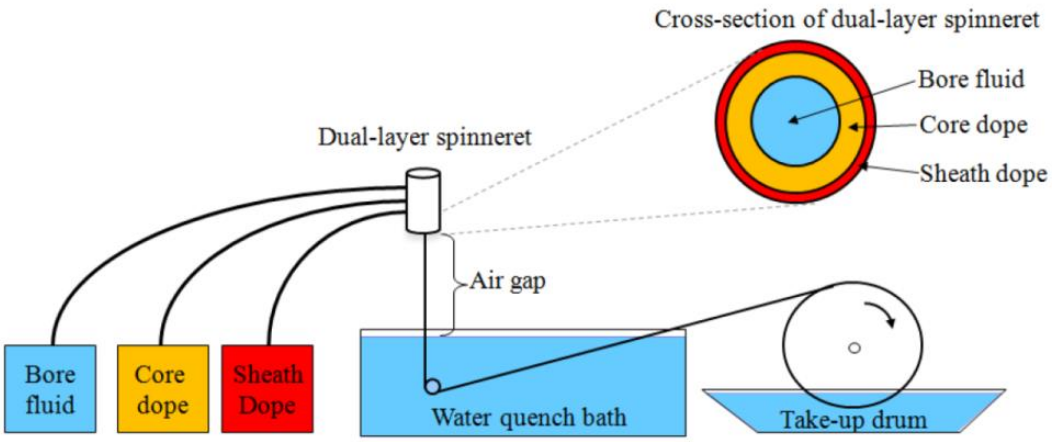

Figure 8.2: Dry-jet/wet-quench set-up for spinning dual-layer composite hollow fiber membranes [19].

8.3 References

[1] Y.K. Kim, J.M. Lee, H.B. Park, Y.M. Lee, The gas separation properties of carbon molecular sieve membranes derived from polyimides having carboxylic acid groups, J. Membr. Sci., 235 (2004) 139-146.

[2] H.B. Park, Y.K. Kim, J.M. Lee, S.Y. Lee, Y.M. Lee, Relationship between chemical structure of aromatic polyimides and gas permeation properties of their carbon molecular sieve membranes, J. Membr. Sci., 229 (2004) 117-127.

[3] M. Kiyono, P.J. Williams, W.J. Koros, Effect of polymer precursors on carbon molecular sieve structure and separation performance properties, Carbon, 48 (2010) 4432-4441.

[4] V.C. Geiszler, W.J. Koros, Effects of Polyimide Pyrolysis Conditions on Carbon Molecular Sieve Membrane Properties, Ind. Eng. Chem. Res., 35 (1996) 2999-3003.

[5] M. Kiyono, P.J. Williams, W.J. Koros, Generalization of effect of oxygen exposure on formation and performance of carbon molecular sieve membranes, Carbon, 48 (2010) 4442-4449.

[6] M. Kiyono, P.J. Williams, W.J. Koros, Effect of pyrolysis atmosphere on separation performance of carbon molecular sieve membranes, J. Membr. Sci., 359 (2010) 2-10.

[7] M. Rungta, L. Xu, W.J. Koros, Carbon molecular sieve dense film membranes derived from Matrimid® for ethylene/ethane separation, Carbon, 50 (2012) 1488-1502.

[8] X. Ning, W.J. Koros, Carbon molecular sieve membranes derived from Matrimid® polyimide for nitrogen/methane separation, Carbon, 66 (2014) 511-522.

[9] Y.-J. Fu, K.-S. Liao, C.-C. Hu, K.-R. Lee, J.-Y. Lai, Development and characterization of micropores in carbon molecular sieve membrane for gas separation, Microporous Mesoporous Mater., 143 (2011) 78-86.

[10] K.M. Steel, W.J. Koros, An investigation of the effects of pyrolysis parameters on gas separation properties of carbon materials, Carbon, 43 (2005) 1843-1856.

[11] P.S. Tin, T.-S. Chung, Y. Liu, R. Wang, Separation of CO2/CH4 through carbon molecular sieve membranes derived from P84 polyimide, Carbon, 42 (2004) 3123-3131.

[12] W. Qiu, K. Zhang, F.S. Li, K. Zhang, W.J. Koros, Gas separation performance of carbon molecular sieve membranes based on 6FDA-mPDA/DABA (3:2) polyimide, ChemSusChem, 7 (2014) 1186-1194.

[13] L. Xu, M. Rungta, M.K. Brayden, M.V. Martinez, B.A. Stears, G.A. Barbay, W.J. Koros, Olefins-selective asymmetric carbon molecular sieve hollow fiber membranes for

hybrid membrane-distillation processes for olefin/paraffin separations, J. Membr. Sci., 423-424 (2012) 314-323.

[14] D.Q. Vu, W.J. Koros, S.J. Miller, High pressure CO_2/CH_4 separation using carbon molecular sieve hollow fiber membranes, Ind. Eng. Chem. Res., 41 (2002) 367-380.

[15] N. Tanihara, H. Shimazaki, Y. Hirayama, S. Nakanishi, T. Yoshinaga, Y. Kusuki, Gas permeation properties of asymmetric carbon hollow fiber membranes prepared from asymmetric polyimide hollow fiber, J. Membr. Sci, 160 (1999) 179-186.

[16] M. Rungta, Carbon molecular sieve dense film membranes for ethylene/ethane separations, in, Georgia Institute of Technology, Atlanta, GA, 2012.

[17] J.M.S. HENIS, M.K. TRIPODI, Composite hollow fiber membranes for gas separation: the resistance model approach, J. Membr. Sci., 8 (1981) 233-246.

[18] N. Bhuwania, Engineering the morphology of carbon molecular sieve (CMS) hollow fiber membranes, in, Georgia Institute of Technology, 2013.

[19] C. Zhang, Zeolitic imidazolate framework (ZIF)-based membranes and sorbens for advanced olefin/paraffin separations, in, Georgia Institute of Technology, 2014.

APPENDIX A

POLYMER SYNTHESIS PROCEDURE

As noted in Chapter 3, all four novel polyimides investigated in this study: 6FDA/DETDA, 6FDA:BPDA(1:1)/DETDA, 6FDA/1,5-ND:ODA(1:1), and 6FDA/DETDA:DABA(3:2) were synthesized by a two-step polycondensation reaction. The procedure for this type of reaction is outlined as follows:

1) Monomer and Solvent Drying

(Start ~3 days before synthesis).

- Dry both Dianhydride and Diamine in separate vacuum ovens ~20 ^{o}C below their actual sublimation temperature overnight.
- Dry molecular sieves in different flasks under vacuum in an oven for at least one day at 150 ^{o}C.
- Seal the flasks with rubber septum, needle transfer ~1.5 times of calculated amount of NMP and Acetic Anhydride (AcAn) solvents to the flasks 2~3 days before synthesis.
- Seal flasks with parafilm.

2) Synthesis Reaction

2.1) Polyamic Acid Formation

- Assemble synthesis reactor. Glassware, stirrer, and thermometer should be very clean.

- After the whole assembly is done, purge it with dry inert gas for 1~2 hours to get rid of moisture.
- Flame the whole reactor with propane torch under purging for 2 times.
- Needle transfer ~60% of required NMP to the reactor with a syringe (Rest of it will be required after monomer addition step).
- Carefully weigh the amount of Diamines required.
- Under stirring and purging, add diamines into the reactor, rinse the neck of the reactor with NMP using a syringe, and seal the neck with rubber septum.
- Cool the reactor with an ice-water bath.
- Wait until diamines are dissolved, and temperature reaches below 5 ^{o}C.
- Carefully weigh ~1/4 amount of required dianhydride, add it to reactor quickly, rinse the neck with NMP, and seal with rubber septum.
- Keep temperature below 5 ^{o}C, wait till all the dianhydride dissolves.
- Repeat this step, added all the pre-calculated dianhydride partially in 3~4 times.
- Keep the reaction below 5 ^{o}C for several hours till viscosity rise significantly, let reaction go at room temperature.
- After total reaction continues for 24 hours under purging, starting imidization process.

2.2) Chemical Imidization

- Add calculated amount of Beta-Picoline via syringe into the reactor.
- Let it dissolve in the solution completely.
- Add calculated amount of acetic anhydride (AcAn) slowly with a syringe.
- Let the reaction go for 24 hours at room temperature under purging.

3) Precipitation

- Pour Methanol in a large container.
- Pour the polyimide solution into methanol slowly, polyimide will phase separate easily.
- Blend polymer, and collect the polymer with pressure filtration.
- Soak polyimide in methanol overnight.
- Filtrate polymer, wash the polymer with methanol 2~3 times.
- Dry the polymer in a hood at room temperature until most solvents were volatilized.
- Dry the polymer in the vacuum oven at 210 ^{o}C for 24 hours.

APPENDIX B

GAS SEPARATION PERFORMANCE OF CMS MEMBRANES FABRICATED FROM DIFFEENT-SOLVENT-CASTED PRECURSOR FILMS

As has been discussed in Chapter 3, because of the different solubilities of the four polymers, different solvents have to be used. Here in Appendix B, I showed the separation performance of CMS membranes fabricated from different-solvent-casted precursor films to confirm my former statement that these CMS membranes exhibited essentially equivalent performance.

Three strategies have been applied throughout this work. Strategy 1: solvent: DCM and solvent removal strategy: annealing temperature of 120 ℃ in vacuum oven for 24 hours; Strategy 2: solvent: THF and solvent removal strategy: methanol solvent exchange for 24 hours followed by annealing in vacuum oven under 210 ℃ for 24 hours; Strategy 3: solvent: NMP and solvent removal strategy: methanol solvent exchange for 24 hours followed by annealing in vacuum oven under 210 ℃ for 24 hours.

Table B.1 shows the separation performance for pure gas pairs CO_2/CH_4 and O_2/N_2 of 6FDA/DETDA and 6FDA: BPDA(1:1)/DETDA CMS films fabricated with strategy 1 and strategy 2. Table B.2 shows the separation performance for pure gas pairs CO_2/CH_4 and O_2/N_2 of 6FDA/DETDA:DABA(3:2) CMS films fabricated with strategy 2 and strategy 3.

Table B.1: Pure gas CO_2/CH_4 and O_2/N_2 separation performance of 6FDA/DETDA and 6FDA: BPDA(1:1)/DETDA CMS films fabricated with: a) strategy 1: solvent: DCM and solvent removal strategy: annealing temperature of 120 ℃ in vacuum oven for 24 hours; b) strategy 2: solvent: THF and solvent removal strategy: methanol solvent exchange for 24 hours followed by annealing in vacuum oven under 210 ℃ for 24 hours.

	6FDA/DETDA		6FDA:BPDA(1:1)/DETDA	
	Strategy 1	Strategy 2	Strategy 1	Strategy 2
P_{CO2} (Barrer)	2735	2822	4663	5893
P_{CO2}/P_{CH4}	48.0	45.2	24.0	26.5
P_{O2} (Barrer)	641	685	1074	1244
P_{O2}/P_{N2}	7.0	7.7	4.7	5.1

Table B.2: Pure gas CO_2/CH_4 and O_2/N_2 separation performance of 6FDA/DETDA:DABA(3:2) CMS films fabricated with: a) strategy 2: solvent: THF and solvent removal strategy: methanol solvent exchange for 24 hours followed by annealing in vacuum oven under 210 ℃ for 24 hours; b) strategy 3: solvent: NMP and solvent removal strategy: methanol solvent exchange for 24 hours followed by annealing in vacuum oven under 210 ℃ for 24 hours.

	6FDA/DETDA:DABA(3:2)	
	Strategy 2	Strategy 3
P_{CO2} (Barrer)	22680	24283
P_{CO2}/P_{CH4}	33	30
P_{O2} (Barrer)	4340	4507
P_{O2}/P_{N2}	4.8	4.3

APPENDIX C

DENSITIES OF POLYMERIC AND CMS MEMBRANES

In this study, all density values were acquired from $Ca(NO_3)_2$ density column. Table C.1 shows the density values of polymeric as well as CMS membranes pyrolyzed at 550 ^oC with UHP argon atmosphere derived from 6FDA/DETDA, 6FDA:BPDA(1:1)/DETDA, 6FDA/DETDA:DABA(3:2) and 6FDA/1,5-ND:ODA(1:1). Table C.2 tabulates the density values of various CMS membranes pyrolyzed with different protocols derived from 6FDA/DETDA:DABA(3:2).

Table C.1: Density values of polymeric as well as CMS membranes pyrolyzed at 550 ^oC with UHP argon atmosphere derived from 6FDA/DETDA, 6FDA:BPDA(1:1)/DETDA, 6FDA/DETDA:DABA(3:2) and 6FDA/1,5-ND:ODA(1:1).

Polymer	Density (g/cm^3)	
	Polymer	CMS
6FDA/DETDA	1.3126	1.3415
6FDA:BPDA(1:1)/DETDA	1.2319	1.3498
6FDA/DETDA:DABA(3:2)	1.3764	1.3498
6FDA/1,5-ND:ODA(1:1)	1.4471	1.4086

Table C.2: Density values of various CMS membranes pyrolyzed with different protocols derived from 6FDA/DETDA:DABA(3:2).

Pyrolysis conditions	Density (g/cm^3)
	CMS
550 ^oC-/ pure argon	1.3498
675 ^oC-/ pure argon	1.5107
800 ^oC-/ pure argon	1.5408
550 ^oC-/ 30ppm O_2 doped argon	1.3721
550 ^oC-/ 50ppm O_2 doped argon	1.3768
800 ^oC-/ pure argon/precrosslinked	1.5340

APPENDIX D

GAS COMPRESSIBILITY FACTORS

The compressibility factors (Z) were used to account for the deviance in the properties of a real gas from the idea gas law. The calculation is as follows:

$$Z=\frac{pV}{RT} \tag{D.1}$$

where p is the gas pressure, V is the molar volume, T is the absolute temperature, and R is the universal gas constant. The deviation from ideal gas behavior is observed to be higher at higher gas pressures, which must be accounted for in the calculations.

The pressure dependent compressibility factor equation is given in equation D.2:

$$Z=1+(A)p+(B)p^2+(C)p^3+\cdots \tag{D.2}$$

where A, B, C etc. are constants. The higher order terms in the equation are negligible in our case, and thus ignored.

The pressure dependent compressibility factor equations of pure gases CO_2, CH_4, O_2, and N_2 were obtained from the National Institute of Standards and Technology (NIST) Software Standard Reference Database 12, Version 5.0 and NIST WebBook, Standard Reference Database Number 69, These are shown in Table D.1 below

Table D.1: Compressibility factor equations of pure gases CO_2, CH_4, O_2, and N_2, with pressure, p in psia.

Gas	Temperature (^oC)	Compressibility Equation
CO_2	35	$1+(-3.21E-11)p+(-5.03E-08)p^2+(-3.41E-04)p^3$
	42.5	$1+(-2.12E-11)p+(-4.03E-08)p^2+(-3.16E-04)p^3$
	50	$1+(-1.38E-11)p+(-3.17E-08)p^2+(-2.94E-04)p^3$
CH_4	35	$1+(4.54E-12)p+(1.66E-08)p^2+(-1.37E-04)p^3$
	42.5	$1+(4.03E-12)p+(1.67E-08)p^2+(-1.26E-04)p^3$
	50	$1+(3.50E-12)p+(1.66E-08)p^2+(-1.16E-04)p^3$
O_2	35	$1+(2.15E-13)p+(1.15E-08)p^2+(-5.52E-05)p^3$
	42.5	$1+(4.64E-14)p+(1.01E-08)p^2+(-4.96E-05)p^3$
	50	$1+(-5.95E-14)p+(1.05E-08)p^2+(-4.45E-05)p^3$
N_2	35	$1+(-6.43E-13)p+(1.52E-08)p^2+(-2.43E-05)p^3$
	42.5	$1+(-8.11E-13)p+(1.42E-08)p^2+(-1.98E-05)p^3$
	50	$1+(-7.98E-13)p+(1.32E-08)p^2+(-1.57E-05)p^3$

APPENDIX E

UNCERTAINTYIES IN ACTIAVTION ENERGIES AND HEATS OF SORPTION

In Chapter 2, the temperature dependence of gas permeability, diffusivity and sorption have been given as Eq. 2.24-26 as following:

$$P_i = P_{0i} \exp\left(\frac{-E_{Pi}}{RT}\right) \tag{2.24}$$

$$D_i = D_{0i} \exp\left(\frac{-E_{Di}}{RT}\right) \tag{2.25}$$

$$\mathbb{S}_i = \mathbb{S}_{0i} \exp\left(\frac{-H_{\mathbb{S}i}}{RT}\right) \tag{2.26}$$

These equatios can be rearranged to obtain Eq. E.1-3:

$$\ln P_i = \ln P_{0i} + \frac{-E_{Pi}}{R} * \frac{1}{T} \tag{E.1}$$

$$\ln D_i = \ln D_{0i} + \frac{-E_{Di}}{R} * \frac{1}{T} \tag{E.2}$$

$$\ln \mathbb{S}_i = \ln \mathbb{S}_{0i} + \frac{-H_{\mathbb{S}i}}{R} * \frac{1}{T} \tag{E.3}$$

These equations can be described by the generalized relation:

$$y_i = A + Bx_i \tag{E.4}$$

where

$$y_i = \ln P,\ \ln D,\ \ln \mathbb{S}$$
$$x_i = \frac{1}{T}$$
$$A = \ln P_0,\ \ln D_0,\ \ln \mathbb{S}_0$$
$$B = \frac{-E_P}{R}, \frac{-E_D}{R}, \frac{-H_{\mathbb{S}}}{R}$$

For linear regression of n data points, the uncertainty in the constant B can be calculated using the following expression [1]

$$\sigma_B^{\,2} = n\sigma_y^{\,2}/\Delta \tag{E.5}$$

where

$$\sigma_y^{\,2} = \frac{1}{n-2}\Sigma(y_i - A - Bx_i)^2$$
$$\Delta = n(\Sigma x_i^{\,2}) - (\Sigma x_i)^2$$

Thus, the uncertainty of E_P and $H_{\mathbb{S}}$ can be calculated using the following equation:

$$\sigma_{E_P} = \sigma_{H_S} = R\sigma_B \tag{E.6}$$

The uncertainty of E_D can then be calculated according to:

$$\frac{\sigma_{E_D}}{E_D} = \frac{\sigma_{E_P}}{E_P} + \frac{\sigma_{H_S}}{H_S} \tag{E.7}$$

The resulting uncertainties for the activation energies of permeation and diffusion and the heats of sorption are tabulated in Chapter 6.

References:

[1] J.R. Taylor, An Introduction to Error Analysie, University Science Books, Oxford, 1982.